HIGH FIDELITY FLUID-STRUCTURE TURBULENCE MODELLING USING AN IMMERSED-BODY METHOD

Pan Yang
Supervised by:
Dr. Jiansheng Xiang
Dr. FangXin Fang
Prof. Christopher C. Pain

Submitted for the degree of Doctor of Philosophy
and the Diploma of Imperial College

Applied Modelling and Computation Group
Department of Earth Science and Engineering
Imperial College London

January, 2018

Abstract

There is an increasing need for turbulence models with fluid-structure interaction (FSI) in many industrial and environmental high Reynolds number flows. Since the complicated structure boundaries move in turbulent flows, it is quite challenging to numerically apply boundary conditions on these moving fluid-structure interfaces. To achieve accurate and reliable results from numerical FSI simulations in turbulent flows, a high fidelity fluid-structure turbulence model is developed using an immersed-body method in this thesis. It does this by coupling a finite element multiphase fluid model and a combined finite-discrete element solid model via a novel thin shell mesh surrounding solid surfaces.

The FSI turbulence model presented has four novelties. Firstly, an unsteady Reynolds-averaged Navier-Stokes (URANS) $k-\varepsilon$ turbulence model is coupled with an immersed-body method to model FSI by using this thin shell mesh. Secondly, to reduce the computational cost, a log-law wall function is used within this thin shell to resolve the flow near the boundary layer. Thirdly, in order to improve the accuracy of the wall function, a novel shell mesh external-surface intersection approach is introduced to identify sharp solid-fluid interfaces. Fourthly, the model has been extended to simulate highly compressible gas coupled with fracturing solids.

This model has been validated by various test cases and results are in good agreement with both experimental and numerical data in published literature. This model is capable to simulate the aerodynamic and hydrodynamic details of fluids and the stress, vibration, deformation and motion of structures simultaneously. Finally, this model has been applied to several industrial applications including a floating structure being moved around by complex hydrodynamic flows involving wave breaking; a blasting engineering simulation with shock waves, fracture propagation, gas-solid in-

teraction and flying fragments; fluid dynamics, flow-induced vibrations, flow-induced fractures of a full-scale vertical axis turbine. Some useful conclusions, e.g. how to model them, how to make them stable and how to predict when they will break, are obtained by this FSI model when applying it to the above applications.

Copyright Declaration

The copyright of this thesis rests with the author and is made available under a Creative Commons Attribution Non-Commercial No Derivatives licence. Researchers are free to copy, distribute or transmit the thesis on the condition that they attribute it, that they do not use it for commercial purposes and that they do not alter, transform or build upon it. For any reuse or redistribution, researchers must make clear to others the licence terms of this work.

Declaration

I hereby certify that the work presented in this dissertation is the result of my own investigations during the PhD project. Text and results obtained from other sources are referenced and properly acknowledged.

Pan Yang
January, 2018

The greatest wealth is to live content with little.
Plato

If I have seen further than others, it is by standing upon the shoulders of giants.
Isaac Newton

Education is what remains after one has forgotten what one has learned in school.
Albert Einstein

Acknowledgements

Dr Jiansheng Xiang, Dr Fangxin Fang and Prof. Christopher Pain are incredible supervisors. Prof. Pain introduced me to the Applied Modelling and Computation Group (AMCG) at Imperial College London. During my PhD training, Prof. Pain has encouraged me with a variety of amazing ideas and suggestions. Some of these ideas I have already implemented, some of them provide me possible solutions to do further investigation. In particular, I am deeply grateful to Dr Xiang. Dr Xiang has provided me tremendous help, suggestions and encourages. Without his supervision, I could not complete the research in this thesis. Every time when I despaired, he always provided encouragement and advise. I would also like to express my appreciation to Dr Fang. Without her suggestions to do research efficiently, I would not have completed this thesis in time. She helped me immensely to improve the quality and efficiency of my PhD research. They deserve my greatest gratitude.

I am grateful for the funding support provided by my sponsor-the China Scholarship Council. This funding gave me the opportunity to study at Imperial College London. Without the funding support, I would not have had the chance to do my PhD research.

Also, I deeply thank all those who have helped me with the work and research in this thesis, and supported my life during my PhD training. First of all, I would like to thank all the fellow PhD students and AMCG staff who helped me to learn research skills and obtain passion in scientific research. For instance, Dr Gerard Gorman, Prof. Matthew D Piggott and Prof. Peter A Allison are full of passion and scientific ideas to complete fantastic research tasks. I am grateful for the colleagues in AMCG: Dr Dimitrios Pavlidis, Dr John-Paul Latham, Dr Dunhui Xiao, Dr Frank Milthaler, Dr James R Percival, Dr Zhihua Xie, Dr Pablo Salinas, Dr Alexandros

Avdis, Dr Timothy M B Greaves, Rong Hu, Asiri Obeysekara, Dr Qinghua Lei, Dr Ado Farsi, Prof. Matthew D Jackson, Dr Liang Yang, Wei Pan, Zehao Lyu, and other AMCG members. The discussions with them have supplied me the source to do research.

Furthermore, I thank Dr Axelle C Viré from the Delft University of Technology for providing me with some data and code to validate my model. She provided me with a number of suggestions about the fluid-structure interaction in the field of renewable energy. I would like to express my appreciation to Prof. Ming Chen at Wuhan University who helped me to apply my fluid-structure interaction model to the blasting applications. I am grateful to those researchers from Institute of Atmospheric Physics Chinese Academy of Sciences (IAP): Prof. Xiaobao You, Prof. Lijing Cheng, Dr Jinxi Li. Prof. Lijing Cheng helped to implement the 3D fluid-structure interaction model. Prof. Xiaobao You and Dr Jinxi Li helped to discuss some of the problems in my research field. Moreover, I would like to thank Dr Gang Yao for the discussions regarding parallel algorithms in high-performance computing (HPC). Importantly, I also thank Miten Patel for the proofreading.

Finally, I would like to give my indeed thanks to my parents Yang and Guo. They have supported me with constant encouragement, patience and help over the years. Particularly, I would like to give my sincere appreciation to my wife Yu who I cannot thank enough for her unlimited support, patience and encouragement in these years. This helped me maintain a strong mind and a brave heart to achieve my dreams. They are all the reasons I am fighting to achieve my goals and dreams in science and life. Their encouragement and support have helped me significantly in both of my research and life.

Table of Contents

1 Introduction **35**

1.1 Research motivation . . . 36

1.2 Literature review of FSI in CFD . . . 39

1.2.1 Incompressible flow FSI . . . 39

1.2.2 Compressible flow FSI model within fractured solids . . . 41

1.2.3 Turbulence flow FSI model . . . 43

1.2.4 FSI application in renewable energy . . . 45

1.3 Original contributions . . . 47

1.4 Thesis outline . . . 49

2 A fluid-structure interaction model for incompressible, compressible and turbulent flows **53**

2.1 Introduction . . . 54

2.2 Governing equations . . . 55

2.2.1 Equations for solid dynamics . . . 55

2.2.2 The constitutive model for deformable solids . . . 56

2.2.3 Equations for fluid dynamics of incompressible flows . . . 56

2.2.4 Equations for fluid dynamics of compressible flows . . . 58

2.3 The $k - \varepsilon$ turbulence model 58
2.3.1 Standard $k - \varepsilon$ turbulence model 58
2.3.2 Wall functions 59
2.3.3 The wall distance in the immersed-body method 64
2.4 Spatial discretization 67
2.5 Mesh adaptivity 70
2.5.1 Mesh adaptivity geometric operations 70
2.5.2 Hessian matrix 71
2.5.3 Consistent and Galerkin projections 72
2.6 Coupling methodology between the fluid and solid dynamics 72
2.6.1 Form of the coupling term $\boldsymbol{s}_c$ 72
2.6.2 Projections between fluid, solid and shell meshes 76
2.6.3 The theory behind the semi-implicit coupling approach 78
2.7 The coupling algorithm for turbulent flows 80
2.7.1 The exchange forces on the solid surface 80
2.7.2 The coupling steps 80
2.8 Concluding remarks 82

3 Incompressible flow FSI model **83**
3.1 Introduction 84
3.2 A free falling circular cylinder in a fluid at rest 85
3.2.1 The test case set up and the semi-empirical solution 85
3.2.2 The results for different fluid-solid density ratios and Reynolds numbers 87
3.2.3 Mesh size sensitivity analysis 88
3.2.4 Vortex shedding behind a circular cylinder 89

3.3 A free falling sphere 92

3.3.1 A free falling sphere at Re = 7, 20 and 100 92

3.3.2 A free falling sphere at Re = 450, 620, 1200 and 1800 94

3.4 A collapsing column of water moving an initially stationary solid square 97

3.5 An elastic membrane 101

3.6 The water-air interface with a floating solid square 105

3.7 Concluding remarks 108

4 Compressible flow FSI model with a fracture model 109

4.1 Introduction 110

4.2 Solid fracture model 111

4.2.1 Joint element 111

4.2.2 Combined tensile and shear failure criterion 111

4.3 The equation of state 113

4.4 Coupled gas-solid interaction 115

4.4.1 The coupling term $\boldsymbol{s}_c$ and the exchange force $\boldsymbol{F}_v$ and $\boldsymbol{F}_p$ including the Q-scheme 115

4.4.2 Update of solid boundary after fracturing 116

4.4.3 The theory behind the coupling approach 118

4.5 Results 119

4.5.1 Blasting cylinder 119

4.5.2 Projectile 121

4.5.3 Masonry block fragmentation due to an internal explosion . . 128

4.6 Concluding remarks 133

5 Turbulence flow FSI model 135

5.1 Introduction . . . 136
5.2 Flow over a circular cylinder at $Re = 3900$ . . . 137
5.3 Turbulent flow over a static NACA0015 aerofoil with an attack angle of $\alpha = 60°$ at $Re = 5200$ . . . 142
5.4 A free rising circular cylinder in a fluid at rest with $Re = 5000$ and $Re = 3800$ . . . 152
5.5 A free rising sphere in a fluid at rest with $Re = 6000$ and 10000 . . . 156
5.6 Flow bending a 3D elastic plate . . . 159
5.7 Computational time . . . 167
5.8 Concluding remarks . . . 168

6 Application: FSI model for tidal turbine **169**
6.1 Introduction . . . 170
6.2 Flow past a 2D rotating vertical axis turbine . . . 171
  6.2.1 The setup of the vertical axis turbine . . . 171
  6.2.2 The fluid dynamics of the flow past a 2D rotating vertical axis turbine . . . 173
6.3 Flow past a 3D rotating vertical axis turbine . . . 180
6.4 Flow past a 3D flexible vertical axis turbine . . . 184
6.5 Flow-induced fractures in a 3D vertical axis turbine . . . 190
6.6 Concluding remarks . . . 197

7 Discussion and Conclusion & Future Work **199**
7.1 Discussion and Conclusion . . . 199
7.2 Future Work . . . 202
  7.2.1 Further validation . . . 202
  7.2.2 Numerical model improvement . . . 202

7.2.3 Moving mesh 203
7.2.4 Possible applications 203

Bibliography **205**

Appendices **227**

A Third party material permissions **228**

List of Figures

2.1 Computational domain V (*left*), fluid mesh adapted to the volume fraction of the shell (*centre*) and the solid mesh (*right*). The method to generate the shell mesh can be found in Section 2.6.2. 57

2.2 Law of the wall. The blue line is the real relationship between u^+ and y^+. The red lines are the approximations of this relationship by using log law and $u^{+}_{=}y^{+}$. 60

2.3 Definitions of fluid, solid and intersection cells. Fluid-cell: ○, Solid-Cell: ●, Fluid Intersection-Cell: □, Solid Intersection-Cell: ◊.The grey part is the solid. 64

2.4 Definitions of fluid, solid and intersection cells.○: Fluid-cell, ●: Solid-Cell, □: Fluid Intersection-Cell, ◊: Solid Intersection-Cell. The grey part is the solid. 65

2.5 Definitions of fluid, solid and intersection cells.○: Fluid-cell, ●: Solid-Cell, □: Fluid Intersection-Cell, ◊ Solid Intersection-Cell. The grey part is the solid and the green part is the shell. 66

2.6 Mesh adaptivity geometric operations. (a) node insertion or edge split, (b) node deletion or edge collapse, (c) edge swap, (d) node movement (Piggott *et al.*, 2009). 71

2.7 Left: the solid mesh with its surrounding shell mesh; right: a 2D solid element with its shell mesh. Δr is the shell thickness. The method to generate the shell mesh can be found in Section 2.6.2. . . . 75

2.8 The flow chart of the immersed-body method. 79

2.9 The flow chart of the immersed-body URANS model. The left part is the loop in fluid solver (Fluidity-Multiphase), and the right part is the loop in solid solver (Solidity). 81

3.1 The computational domain of the free falling circular cylinder case. . 86

3.2 Relative errors between the terminal velocities calculated by the immersed-body method, U_t^{is}, and semi-empirical value U_t^{sf} for different mesh sizes of the free falling circular cylinder cases. 88

3.3 Falling circular cylinder: $\rho_s/\rho_f = 2.0$, Re=195.23, mesh (left), velocity (middle-left), velocity in y direction (middle-right), non-hydrostatic pressure (right). This test case is dimensionless. The velocity bar here represents ds/dt, where ds is the spatial motion length in a finite time period dt. 90

3.4 (a) Falling circular cylinder: $\rho_s/\rho_f = 4.0$, Re=192.41, mesh (left), velocity (middle-left), velocity in y direction (middle-right), non-hydrostatic pressure (right). (b) The velocity in the y direction of the falling circular cylinder cases: $\rho_s/\rho_f = 2.0$, Af20-200 (left), Yf20-200 (right). This test case is dimensionless. The velocity bar here represents ds/dt, where ds is the spatial motion length in a finite time period dt. 91

3.5 (a) The computational domain of the falling sphere test case, (b) The computational mesh of the falling sphere test case. 93

3.6 The comparison of the sphere velocity history between the semi-analytical solutions and the simulation results obtained by the present method. The solid back continuous lines are the semi-analytical solutions and the blue plus symbols are numerical results using the present model. (a) Velocity histories at $m^* = 2.0$, (b) Velocity histories at $m^* = 4.0$. 94

3.7 The terminal velocity against the Reynolds number for the falling sphere test cases. The solid black line is the empirical solution and the blue star line is the results obtained from the presented model. . . 95

3.8 Wakes of freely falling spheres in the experiment (Horowitz & Williamson, 2010). (a) $Re = 450$. (b) $Re = 620$. (c) $Re = 1200$. (d) $Re = 1800$. 96

3.9 Wakes of freely falling spheres obtained by the present model. The weaks shown here are Q-criterion. (a) $Re = 450$. (b) $Re = 620$. (c) $Re = 1200$. (d) $Re = 1800$. 97

3.10 Wave pressure acting on the initially stationary solid square. The black solid line represents the computational results of the immersed-body method in this thesis. The blue dash line and asterisk line are simulation results and experimental data from literature (Kawasaki & Mizutani, 2007). P1, P2 and P3, refer to 0.01 m, 0.02 m and 0.03 m from the bottom on the left wave impacted surface of the initially stationary solid square. 99

3.11 The snapshots of the collapsing column of water moving an initially stationary solid square. The blue grids are the adapted meshes; the green parts refer to the air; the red parts represents the water; the blue vectors are the velocity vectors of the fluids; the white square is the solid square. Figure (a), (b), (c), (d), (e), (f), (g) and (h) refer to the snapshots at 0.000 s, 0.200 s, 0.300 s, 0.390 s, 0.500 s, 0.627 s, 0.700 s and 0.800 s respectively. 100

3.12 Initial, resting and equilibrium shapes of the elastic membrane. 102

3.13 Elastic membrane test cases: the fluid mesh at different times: (a) $t = 0.19\,\mathrm{s}$, (b) $t = 0.80\,\mathrm{s}$, and (c) $t = 1.47\,\mathrm{s}$. 103

3.14 Elastic membrane test cases: the fluid velocity fields at different times: (a) $t = 0.19\,\mathrm{s}$, (b) $t = 0.80\,\mathrm{s}$, and (c) $t = 1.47\,\mathrm{s}$. 104

3.15 Elastic membrane test cases: the fluid pressure profiles at different times: (a) $t = 0.19\,\mathrm{s}$, (b) $t = 0.80\,\mathrm{s}$, and (c) $t = 1.47\,\mathrm{s}$. 104

3.16 Elastic membrane test cases: the fluid pressure profiles ($y = 0.0$) with three different shell mesh thicknesses at different times: (a) $t = 0.19\,\mathrm{s}$, (b) $t = 0.80\,\mathrm{s}$, and (c) $t = 1.47\,\mathrm{s}$. 104

3.17 The snapshots of the water-air interface with a floating solid square. The blue grids are the adapted meshes; the green parts refer to the air; the red parts represents the water; the blue vectors are the velocity vectors of the fluids; the white square is the solid square. Figure (a), (b), (c) and (d) refer to the snapshots at 0.000 s and 0.150 s, respectively. 106

3.18 The snapshots of the water-air interface with a floating solid square. The blue grids are the adapted meshes; the green parts refer to the air; the red parts represents the water; the blue vectors are the velocity vectors of the fluids; the white square is the solid square. Figure (e), (f), (g) and (h) refer to the snapshots at 0.705 s and 0.910 s, respectively. 107

4.1 Six solid discontinuous elements with joint elements. Elements 1–6 are six adjacent discontinuous elements, and elements 7–12 are the six joint elements added among them. 112

4.2 The stress for different displacements. 113

4.3 Different zones in a single mode I fracture tip. δ_{np} and δ_{nc} represent δ_p and δ_c, respectively. The left open white area refers to a physically discrete fracture; the middle light-blue area is the plastic zone; the top and bottom white area represent the continuous solid without any cracks; the short vertical pink bars between the pink and blue lines represent the magnitudes of the normal stress σ. 114

4.4 Six solid continuous elements with cracks in different broken patterns: (a) only joint element 9 is broken, (b) both joint element 9 and 12 are broken, (c) all the joint elements $7-12$ are broken. 118

4.5 The geometry of the cylindrical chamber. Point A is where the gas pressure is measured. 120

4.6 The pressure and density history at point A of the blasting cylinder test. 121

4.7 The geometry of the firing system. 122

4.8 The snapshots of projectile position and gas velocity when the mass of the explosive material is 0.005 kg. Figure (a), (b), (c), (d), (e), (f), (g) and (h) refer to the snapshots at 1.70 ms, 3.00 ms, 4.00 ms, 5.55 ms, 6.60 ms ,7.63 ms , 7.81 ms and 8.10 ms, respectively. 123

4.9 Thermodynamic quantity histories for different values of M_e in the projectile system. 124

4.10 The snapshots of projectile stress and gas pressure when the mass of the explosive material is 0.005 kg. Figure (a), (b), (c), (d), (e), (f), (g) and (h) refer to the snapshots at 0.01 ms, 0.02 ms, 0.03 ms, 0.04 ms, 0.05 ms, 0.06 ms, 0.07 ms and 0.08 ms, respectively. 126

4.11 The snapshots of projectile stress and gas pressure when the mass of the explosive material is 0.005 kg. Figure (i), (j), (k), (l), (m), (n), (o) and (p) refer to the snapshots at 1.70 ms, 3.00 ms, 4.00 ms, 5.55 ms, 6.60 ms 7.63 ms, 7.81 ms and 8.10 ms, respectively. 127

4.12 The geometry and mesh for the square rock block, and the gas mesh. 129

4.13 (a) The black line and the blue star line represent the numerical results of the immersed-body method and Mohammadi two-mesh coupled model (Mohammadi & Pooladi, 2012), respectively. (b) The black, blue, red lines stand for three different initial pressures: $p_0 = 1.0 \times 10^9$ Pa, $p_0 = 1.8 \times 10^8$ Pa and $p_0 = 1.0 \times 10^8$ Pa, respectively.130

4.14 The snapshots of the crack and solid velocity inside the square rock block for test case $p_0 = 1.8 \times 10^8$ Pa. Figure (a), (b), (e) and (f) refer to the snapshots at 0.14 ms, 0.30 ms, 0.64 ms and 5.70 ms. Figure (c) and (d) show different fracture type at 0.30 ms and 0.64 ms, where blue and red crack stand for the tensile and shear failure, respectively. 131

4.15 The snapshots of the crack and solid velocity inside the square rock block for test case $p_0 = 1.0 \times 10^9$ Pa. Figure (a), (b), (e) and (f) refer to the snapshots at 0.14 ms, 0.30 ms, 0.64 ms and 1.86 ms. Figure (c) and (d) show different fracture type at 0.30 ms and 0.64 ms, where blue and red crack stand for the tensile and shear failure, respectively. 132

5.1 The computational domain and settings of the flow over a cylinder at $Re = 3900$. 137

5.2 The computational mesh of the flow over a cylinder at $Re = 3900$. . . 138

5.3 (a) The instantaneous vorticity field of the turbulent wake behind the cylinder at $Re = 3900$. (b) Pressure coefficient C_p around the circular cylinder surface from the stagnation point where $\theta = 0$ at $Re = 3900$; □: Norberg (1987) (experiment); – –: Kravchenko & Moin (2000) (LES); –: Present immersed-body URANS model. . . . 138

5.4 Comparison of velocity fields with experimental data and numerical results in literature for the flow over a circular cylinder at $Re = 3900$ test case. (a) Mean streamwise velocity along the centreline of the circular cylinder; (b) Mean streamwise velocity along four different vertical lines at $x/D = 0.58$, $x/D = 1.06$, $x/D = 1.54$ and $x/D = 2.02$, respectively; (c) Mean transverse velocity along three different vertical lines at $x/D = 1.06$, $x/D = 1.54$ and $x/D = 2.02$, respectively; (d) Streamwise velocity fluctuations along four different vertical lines at $x/D = 0.58$, $x/D = 1.06$, $x/D = 1.54$ and $x/D = 2.02$, respectively; in the wake of the flow over circular cylinder at $Re = 3900$. □: Lourenco & Shih (1993) (experiment); ○: Ong & Wallace (1996) (experiment); ◇: Parnaudeau *et al.* (2008) (experiment, PIV); △: Parnaudeau *et al.* (2008) (experiment, HWA); – –: Kravchenko & Moin (2000) (LES); –: Present immersed-body URANS model. 140

5.5 The computational domain and settings of the flow over a static NACA0015 aerofoil with an attack angle of $\alpha = 60°$ at $Re = 5200$. . . 143

5.6 The fluid mesh at different times of the flow over a NACA0015 aerofoil at $Re = 5200$ and attack angle $\alpha = 60°$: (a) $t = \frac{25}{64}$ s, (b) $t = \frac{27}{64}$ s, (c) $t = \frac{35}{64}$ s, (d) $t = \frac{40}{64}$ s, (e) $t = \frac{45}{64}$ s, (f) $t = \frac{52}{64}$ s, (g) $t = \frac{55}{64}$ s and (h) $t = \frac{58}{64}$ s. 144

5.7 The pressure contours of flow over a NACA0015 aerofoil at $Re = 5200$ and attack angle $\alpha = 60°$ obtained from the present model in different times: (a) $t = \frac{25}{64}$ s, (b) $t = \frac{27}{64}$ s, (c) $t = \frac{35}{64}$ s, (d) $t = \frac{40}{64}$ s, (e) $t = \frac{45}{64}$ s, (f) $t = \frac{52}{64}$ s, (g) $t = \frac{55}{64}$ s and (h) $t = \frac{58}{64}$ s. Similar results have been found in Figure 14 in the literature (Sengupta *et al.*, 2007) and Fig. 4.5 in the literature (Milthaler, 2014). 145

5.8 Comparison of present streamlines (right) of flow over a NACA0015 aerofoil at $Re = 5200$ and attack angle $\alpha = 60°$ with the numerical streamlines in (Sengupta *et al.*, 2007) at different times: (a) $t = \frac{25}{64}$ s, (b) $t = \frac{27}{64}$ s, (c) $t = \frac{35}{64}$ s and (d) $t = \frac{40}{64}$ s. . Similar results have been found in Fig. 4.6 in (Milthaler, 2014). 147

5.9 Comparison of present streamlines (right) of flow over a NACA0015 aerofoil at $Re = 5200$ and attack angle $\alpha = 60°$ with the numerical streamlines in (Sengupta *et al.*, 2007) at different times: (e) $t = \frac{45}{64}$ s, (f) $t = \frac{52}{64}$ s, (g) $t = \frac{55}{64}$ s and (h) $t = \frac{58}{64}$ s. Similar results have been found in Fig. 4.6 in (Milthaler, 2014). 148

5.10 The turbulent kinetic energy profiles of flow over a NACA0015 aerofoil at $Re = 5200$ and attack angle $\alpha = 60°$ obtained from the present model in different times: (a) $t = \frac{25}{64}$ s, (b) $t = \frac{27}{64}$ s, (c) $t = \frac{35}{64}$ s, (d) $t = \frac{40}{64}$ s, (e) $t = \frac{45}{64}$ s, (f) $t = \frac{52}{64}$ s, (g) $t = \frac{55}{64}$ s and (h) $t = \frac{58}{64}$ s. . . . 149

5.11 Comparison of present vorticity contours (right) of flow over a NACA0015 aerofoil at $Re = 5200$ and attack angle $\alpha = 60°$ with visualization pictures (left) from the literature (Freymuth, 1985) at different times: (a) $t = \frac{25}{64}$ s, (b) $t = \frac{27}{64}$ s, (c) $t = \frac{35}{64}$ s and (d) $t = \frac{40}{64}$ s. Similar results have been found in Fig. 12 in the literature (Sengupta *et al.*, 2007) and Fig. 4.7 in (Milthaler, 2014). 150

5.12 Comparison of present vorticity contours (right) of flow over a NACA0015 aerofoil at $Re = 5200$ and attack angle $\alpha = 60°$ with visualization pictures (left) from the literature (Freymuth, 1985) at different times: (e) $t = \frac{45}{64}$ s, (f) $t = \frac{52}{64}$ s, (g) $t = \frac{55}{64}$ s and (h) $t = \frac{58}{64}$ s. Similar results have been found in Fig. 12 in Sengupta et al. (Sengupta *et al.*, 2007) and Fig. 4.7 in (Milthaler, 2014). 151

5.13 The computational domain and settings of the rising cylinder. 153

5.14 (a) The fluid mesh of a free rising cylinder at $m^* = 0.78$, (b) The fluid mesh of a free rising cylinder at $m^* = 0.45$. 153

5.15 Comparison of present vorticity contours (b) of free rising cylinder at $Re = 5000$ with experimental measurements (a) from the literature (Horowitz & Williamson, 2006) when $m* = 0.78$. 154

5.16 Comparison of present vorticity contours (b) of free rising cylinder at $Re = 3800$ with experimental measurements (a) from the literature (Horowitz & Williamson, 2006) when $m* = 0.45$. 155

5.17 The blue lines with circles are experimental data from Ref. (Horowitz & Williamson, 2006), and the black solid lines are trajectories of the rising cylinders in the simulations obtained from the present immersed-body URANS model. (a) The trajectories of a rising cylinder at $m^* = 0.78$, (b) The trajectories of a rising cylinder at $m^* = 0.45$. 155

5.18 (a) The contours of eddy viscosity for a free rising cylinder at $m^* = 0.78$, (b) The contours of eddy viscosity for a free rising cylinder at $m^* = 0.45$. 156

5.19 (a) The computational domain of the rising sphere test case, (b) The computational mesh of the rising sphere test case. 157

5.20 The Q-criterion of the free rising sphere cases: (a) Rising-sphere-r41: $m^* = 0.55$ and $Re = 6000$, (b) Rising-sphere-r42: $m^* = 0.55$ and $Re = 10000$, and (c) Rising-sphere-r43 $m^* = 0.8$ and $Re = 6000$. . . . 158

5.21 Different free rising sphere near weak patterns on the $\{m^*, Re\}$ plane from Ref. (Horowitz & Williamson, 2010). 158

5.22 (a) Schematic of a flexible plate. (b) The comparison of baselines computed by the present model with the numerical data in (Tian *et al.*, 2014) and experimental data in (Luhar & Nepf, 2011). 160

5.23 (a) The mesh the flow bending a flexible plate case. (b) The computational domain and boundary settings of the flow bending a flexible plate case. 161

5.24 The bending plate positions at different times: (a) $t = 0$, (b) $t = 40$, (c) $t = 80$, (d) $t = 155$, (e) $t = 170$, (f) $t = 265$, (g) $t = 330$, (h) $t = 470$, (i) $t = 575$, (j) $t = 590$, (k) $t = 625$, (l) $t = 675$, (m) $t = 700$, (n) $t = 750$, (o) $t = 800$ and (p) $t = 840$. 162

5.25 The pressure contour of the flow bending a 3D elastic plate case at different times: (a) $t = 0$, (b) $t = 40$, (c) $t = 80$, (d) $t = 155$, (e) $t = 170$, (f) $t = 265$, (g) $t = 330$, (h) $t = 470$ and (i) $t = 575$. 163

5.26 The pressure contour of the flow bending a 3D elastic plate case at different times: (j) $t = 590$, (k) $t = 625$, (l) $t = 675$, (m) $t = 700$, (n) $t = 750$, (o) $t = 800$ and (p) $t = 840$. 164

5.27 The streamline of the flow bending a 3D elastic plate case at different times: (a) $t = 0$, (b) $t = 40$, (c) $t = 80$, (d) $t = 155$, (e) $t = 170$, (f) $t = 265$, (g) $t = 330$ and (h) $t = 470$. 165

5.28 The streamline of the flow bending a 3D elastic plate case at different times: (i) $t = 575$, (j) $t = 590$, (k) $t = 625$, (l) $t = 675$, (m) $t = 700$, (n) $t = 750$, (o) $t = 800$ and (p) $t = 840$. 166

6.1 The computational domain and settings of flow past a 2D rotating vertical axis turbine. 172

6.2 (a) The incidence angle α_i of the flow past a 2D rotating vertical axis turbine at different blade position θ_b at $\lambda = 2.0$. (b) Velocities triangles and forces in a vertical axis turbine. 173

6.3 The vorticity of flow past a rotating vertical axis turbine obtained by the presented model at $\lambda = 2$ at different blade positions. (a) The positions of the three blades are $\theta_b = 0°$, $\theta_b = 120°$ and $\theta_b = 240°$. (b) The positions of the three blades are $\theta_b = 90°$, $\theta_b = 210°$ and $\theta_b = 330°$. (c) The positions of the three blades are $\theta_b = 180°$, $\theta_b = 300°$ and $\theta_b = 60°$. (d) The positions of the three blades are $\theta_b = 270°$, $\theta_b = 30°$ and $\theta_b = 150°$. 176

6.4 The vorticity contours of flow past a rotating vertical axis turbine obtained by the presented model at $\lambda = 2$ at different blade positions. (a) The positions of the three blades are $\theta_b = 0°$, $\theta_b = 120°$ and $\theta_b = 240°$. (b) The positions of the three blades are $\theta_b = 90°$, $\theta_b = 210°$ and $\theta_b = 330°$. (c) The positions of the three blades are $\theta_b = 180°$, $\theta_b = 300°$ and $\theta_b = 60°$. (d) The positions of the three blades are $\theta_b = 270°$, $\theta_b = 30°$ and $\theta_b = 150°$. 176

6.5 The meshes of flow past a rotating vertical axis turbine obtained by the presented model at $\lambda = 2$ at different blade positions. (a) The positions of the three blades are $\theta_b = 0°$, $\theta_b = 120°$ and $\theta_b = 240°$. (b) The positions of the three blades are $\theta_b = 90°$, $\theta_b = 210°$ and $\theta_b = 330°$. (c) The positions of the three blades are $\theta_b = 180°$, $\theta_b = 300°$ and $\theta_b = 60°$. (d) The positions of the three blades are $\theta_b = 270°$, $\theta_b = 30°$ and $\theta_b = 150°$. 177

6.6 The pressure contours of flow past a rotating vertical axis turbine obtained by the presented model at $\lambda = 2$ at different blade positions. (a) The positions of the three blades are $\theta_b = 0°$, $\theta_b = 120°$ and $\theta_b = 240°$. (b) The positions of the three blades are $\theta_b = 90°$, $\theta_b = 210°$ and $\theta_b = 330°$. (c) The positions of the three blades are $\theta_b = 180°$, $\theta_b = 300°$ and $\theta_b = 60°$. (d) The positions of the three blades are $\theta_b = 270°$, $\theta_b = 30°$ and $\theta_b = 150°$. 178

6.7 The turbulent kinetic energy of flow past a rotating vertical axis turbine obtained by the presented model at $\lambda = 2$ at different blade positions. (a) The positions of the three blades are $\theta_b = 0°$, $\theta_b = 120°$ and $\theta_b = 240°$. (b) The positions of the three blades are $\theta_b = 90°$, $\theta_b = 210°$ and $\theta_b = 330°$. (c) The positions of the three blades are $\theta_b = 180°$, $\theta_b = 300°$ and $\theta_b = 60°$. (d) The positions of the three blades are $\theta_b = 270°$, $\theta_b = 30°$ and $\theta_b = 150°$. 179

6.8 The comparison of total power coefficient C_{pow} of flow past a rotating vertical axis turbine at $\lambda = 2$. The black solid line is the simulation result obtained from the present model. The green dash line is the experimental data in (Maître *et al.*, 2013). The blue circle line is the simulation result of $k-\omega$ SST model in (McNaughton *et al.*, 2014). The purple star line is the simulation result of $k-\omega$ SST LRE model in (McNaughton *et al.*, 2014). 180

6.9 (a) The geometry of the vertical axis turbine. (b) The solid mesh of the vertical axis turbine. 181

6.10 The computational domain and settings of flow past a 3D rotating vertical axis turbine. 181

6.11 The velocity and adaptive mesh of flow past a 3D rotating vertical axis turbine obtained by the presented model at $\lambda = 2$ at different blade positions. (a) The positions of the three blades are $\theta_b = 0°$, $\theta_b = 120°$ and $\theta_b = 240°$. (b) The positions of the three blades are $\theta_b = 90°$, $\theta_b = 210°$ and $\theta_b = 330°$. (c) The positions of the three blades are $\theta_b = 180°$, $\theta_b = 300°$ and $\theta_b = 60°$. (d) The positions of the three blades are $\theta_b = 270°$, $\theta_b = 30°$ and $\theta_b = 150°$. 182

6.12 The Q-criterion of flow past a 3D rotating vertical axis turbine obtained by the presented model at $\lambda = 2$ at different blade positions. (a) The positions of the three blades are $\theta_b = 0°$, $\theta_b = 120°$ and $\theta_b = 240°$. (b) The positions of the three blades are $\theta_b = 90°$, $\theta_b = 210°$ and $\theta_b = 330°$. (c) The positions of the three blades are $\theta_b = 180°$, $\theta_b = 300°$ and $\theta_b = 60°$. (d) The positions of the three blades are $\theta_b = 270°$, $\theta_b = 30°$ and $\theta_b = 150°$. 183

6.13 The comparison of total power coefficient C_{pow} of flow past a 3D rotating vertical axis turbine at $\lambda = 2$. The black solid line is the simulation result obtained from the present model. The green dash line is the experimental data in (Maître *et al.*, 2013). The blue circle line is the simulation result of $k - \omega$ SST model in (McNaughton *et al.*, 2014). The purple star line is the simulation result of $k - \omega$ SST LRE model in (McNaughton *et al.*, 2014). 184

6.14 (a) The geometry of the vertical axis turbine with tower. (b) The solid mesh of the vertical axis turbine with tower. 185

6.15 The 3D computational domain of a tower bottom fixed vertical axis turbine. 186

6.16 The velocity and adaptive mesh of the vibrating vertical axis turbine at different times: (a) t=0.2 s, (b) t=0.25 s, (c) t=0.3 s and (d) t=0.35 s. 187

6.17 (a)The displacement of the vertical axis turbine compared to the initial position. The yellow one without mesh is the initial position. The white one with blue mesh is the position at the largest displacement. (b) The displacement measurement points on each blade. The three red points on each blade are the points where the displacement is plotted out in Fig. 6.18. 188

6.18 The displacements of three points marked in Fig. 6.17b. 188

6.19 The Q-criterion of the vibrating vertical axis turbine at different times: (a) t=0.2 s, (b) t=0.25 s, (c) t=0.3 s and (d) t=0.35 s. 189

6.20 The streamline of the vibrating vertical axis turbine at different times: (a) t=0.2 s, (b) t=0.25 s, (c) t=0.3 s and (d) t=0.35 s. 189

6.21 Different fracture patterns of wind turbines damaged by the super typhoon Usagi in 2013. (a) Tower collapse at the bottom. (b) Fractured blades. (c) Intact wind turbine. (d) Two fractured blades in one turbine. (e) The details at the collapsed tower location. This figure is from Ref. (Chen & Xu, 2016). 191

6.22 The fluid velocity and adaptive mesh of the fracturing vertical axis turbine at different times: (a) t=0.0 s, (b) t=0.1 s, (c) t=0.2 s and (d) t=0.277 s. 192

6.23 The solid velocity of the fracturing vertical axis turbine at different times: (a) t=0.0 s, (b) t=0.1 s, (c) t=0.2 s and (d) t=0.277 s. 193

6.24 The solid stress component σ_1 of the fracturing vertical axis turbine at different times: (a) t=0.0 s, (b) t=0.1 s, (c) t=0.2 s and (d) t=0.277 s.194

6.25 The solid cracks of the fracturing vertical axis turbine at different times. (a) t=0.0 s, (b) t=0.1 s, (c) t=0.2 s and (d) t=0.277 s. The blue parts are fractured and the yellow parts are intact. Here, the fracture bar value=-1 means preexisting boundaries or fractures, the fracture bar value=2 means shear failure, while the fracture bar value=2 means tensile failure. 195

6.26 The displacements of three points marked in Fig. 6.17b. 195

6.27 The stress measurement points on each blade.The three red points on each blade are the points where the stress is plotted out in Fig. 6.28. 196

6.28 The stress component σ_1 of three points marked in Fig. 6.27. The black solid line is the stress component σ_1 on the joint between the tower and the arm which links the tower and the Blade No. 1. The green dash line is the stress component σ_1 on the joint between the tower and the arm which links the tower and the Blade No. 2. The blue dash line is the stress component σ_1 on the joint between the tower and the arm which links the tower and the Blade No. 3. 196

List of Tables

3.1 Incompressible flow test cases 84

3.2 Free falling circular cylinder test cases for different ρ_s/ρ_f. 87

3.3 Free falling circular cylinder test cases for mesh sensitivity analysis. . 88

3.4 Free falling circular cylinder test cases for vortex comparison. 89

3.5 Free falling sphere test cases for different m^*. 93

3.6 Initial values of materials from literature (Kawasaki & Mizutani, 2007). 98

3.7 The properties of the membrane. 102

3.8 Elastic membrane test cases with different shell mesh thicknesses. . . 103

4.1 Compressible flow test cases 110

4.2 The density, maximum gas pressure, maximum projectile velocity and maximum kinetic energy for three different masses of explosives. 122

5.1 Turbulence flow test cases 136

5.2 Global flow quantity comparisons for the flow over a cylinder at $Re = 3900$ test case. This table includes mean pressure drag coefficient C_D. mean base pressure coefficient (bulk suction coefficient) C_{pb}, mean separation angle θ_{sep}, mean recirculation bubble length L_r/D, Strouhal number S_t, and minimum mean streamwise velocity U_{min}. The first group is the experimental data. The second and third groups are the LES and DNS model data in the previous literature, respectively. The last group is simulation results of present immersed-body URANS model. 141

5.3 Free rising sphere test cases for different m^*. 157

5.4 The time cost in different functions in percentage. 167

6.1 Tidal turbine test cases 170

6.2 The relationship between the blade position θ_b and the attack angle α_i.175

6.3 The material properties of the turbine. 186

Chapter

ONE

Introduction

The research motivation is given in this introductory chapter. The progress of fluid-structure interaction (FSI) in computational fluid dynamics (CFD) is reviewed. The contributions and outline of this thesis are presented.

1.1 Research motivation

The increase in computational power has enabled complex problems and situations to be simulated, numerical simulations are widely used in a variety of research areas including cosmology, physics, biology, chemistry, engineering etc. In the field of computational physics, many applied problems involve multi-physics, for instance, fluid-structure interaction (FSI), acoustic disturbances inside elastic structures, magneto-hydrodynamics, and chemical reactions in fluid flow etc. (Alotto *et al.*, 2013). FSI is a multidisciplinary study involving solid mechanics and fluid dynamics. In numerical FSI, the structural mechanics and fluid dynamics are numerically solved together to obtain the stress, deformation, motion and multi-body contact for solids, and the pressure, velocity and density for fluids.

Recently, the fluid-structure coupling methods have been applied to various fields, ranging from civil engineering, marine engineering to bioengineering. The applications of FSI are successful in many fields including urban pollution (García *et al.*, 2011), road vehicle aerodynamics (Jindal *et al.*, 2005), blasting (Mohammadi & Pooladi, 2012), turbulent flow in wind and tidal turbines (Kang *et al.*, 2012) and cardiac blood flows (Peskin, 1972). In these various engineering applications, FSI plays a significant role to understand these problems and to improve the new design methods in these applications. Thus, high fidelity and trustable FSI models are in high demand in numerous research fields and industrial applications.

However, there are several challenges in FSI modelling (Bungartz & Schäfer, 2006):

- Coupling of different types of partial differential equations (PDEs) in structural mechanics and fluid dynamics;

- Moving structural boundaries, especially when dealing with fast-moving or large deformable solids;

- Coupling different mesh systems typically occurs when coupling continuum mechanics;

- Turbulence modelling with moving interaction boundaries;

- Complex boundaries and stabilities;

- Speed and efficiency of the coupling system.

To overcome these challenges, a large number of numerical FSI models have been developed. These models can be divided into different groups depending on different criteria. Based on coordinate systems, they are divided into three groups: Lagrangian-Eulerian (ALE) scheme (Van Loon *et al.*, 2007; Farhat *et al.*, 1998), Lagrangian formulation (Idelsohn *et al.*, 2003; Ryzhakov *et al.*, 2010; Rafiee & Thiagarajan, 2009) and Eulerian formulation (Dunne & Rannacher, 2006; Coquerelle & Cottet, 2008; Yang, 2017; Yang *et al.*, 2018). The Lagrangian-Eulerian (ALE) scheme is one of the most common models for FSI since Lagrangian solid solvers and Eulerian fluid solvers have been developed separately for several decades. The coupling procedures can keep the advantages in both the Lagrangian solid solver and the Eulerian fluid solver. However, special treatments at the fluid-structure interfaces are required to make it stable. In the Lagrangian formulation FSI model, the descriptions of both the fluid and the structure are in one Lagrangian form. Most of these Lagrangian formulation FSI approaches are meshless e.g. Smoothed Particle Hydrodynamics (SPH) (Idelsohn *et al.*, 2003; Rafiee & Thiagarajan, 2009) methods. It is easy to implement Lagrangian formulation FSI models since the fluid and solid are in one form. However, there could be some limitations when applying them to compressible flow FSI situations. In the Eulerian formulation, both the fluid and the solid are described in Eulerian formulation and the level set functions are used to represent the fluid-structure interfaces. The Eulerian formulation FSI models are able to treat large solid deformations. This is the main advantage compared to the ALE schemes. However, this makes it more computationally expensive than ALE schemes. Additionally, it could be difficult for Eulerian formulation FSI models to handle fracture propagations inside the solid.

Based on the temporal algorithm which performs the coupling between the solid mechanics and fluid dynamics, the FSI models can be sorted into two types: strong coupling models (Hübner *et al.*, 2004; Ryzhakov *et al.*, 2010; Michler *et al.*, 2004) and weak coupling models (Viré *et al.*, 2012, 2015; Farhat *et al.*, 1998; Jaiman *et al.*, 2006). The strong coupling approaches solve the fluid and solid equations in a coupled matrix implicitly at the same time, while the weak coupling models apply different approaches to fluids and solids. Strong coupling approaches are more stable and accurate than weak coupling models because of the same system used in them. However, this makes them computationally more expensive. The weak coupling approach enables existing advanced solid mechanics solvers couple with complex fluid solvers. Different meshes and time steps can be used in the solid and fluid solvers to boost the coupling system (detailed review of these two kinds of FSI models can be seen in Section 1.2.1).

In this work, a weak coupling FSI model has been built developed on an immersed-body method (Kajishima *et al.*, 2001). The original immersed-body method relaxes the fluid velocities towards solid velocities inside the solid domain. It only couples incompressible flow with rigid particles in 2D. The present FSI model has been rebuilt and extended based on the original immersed-body method. It relaxes the fluid velocity to the solid velocity inside a thin shell mesh surrounding the solid surface. Additionally, it has combined a URANS turbulence model, a cohesive zone fracture model and an equation of state for compressible flow. Therefore, the present 2D & 3D FSI model aims at coupling incompressible, compressible and turbulent flows with the moving, deforming and fracturing solids. The details of the model are given in chapters 2 - 6.

Applications of the FSI model for engineering is extremely important in industries. The FSI model developed in this work is applicable in three fields of engineering: moving structure coupled with the multiphase flow, fracturing solids coupled with compressible gas and tidal turbine operating in a turbulent flow. Moving structures in multiphase flows are popular in coastal and ocean engineering. Modelling of structures floating in fresh or sea water requires that the air-water interface as well as the solid-air, solid-water interfaces are modelled, especially for the case of breaking waves. The solid-air and the solid-water interfaces are the positions where the fluid-structure interaction occurs. The understanding of wave-structure interactions is very important in ocean dynamics, for instance, the impacts of ocean waves on ships, floating wind turbine platforms, and ocean oil platforms. The immersed-body method which combines with an advanced interface capturing method is a good choice for these applications. In rock blasting, cutting, mining and tunnelling industries, a highly compressible gas model is implemented and the immersed-boy method can simulate shock waves, fracture propagation, gas-solid interaction and flying fragments. Importantly, in the field of the renewable energy industry and research, wind and tidal turbines have been widely used in the past decade. In order to design the turbines and optimize the performance of these energy generators, the numerical fluid-structure interaction models have been introduced to simulate the rotating turbine in the water and air. In these simulations, complex moving structures in turbulent air and water flow convert the wind and tide energy to electricity. To ensure these turbines operate stably with high power efficiency, the detailed FSI models are required to simulate the real-scale wind and tidal turbines to predict the unstable operating conditions and give suggestions to increase the power generation efficiency.

1.2 Literature review of FSI in CFD

The literature review of FSI on incompressible flow, compressible flow coupling with fracture models, turbulent flow, and renewable energy is presented in this section. The literature in these fields of FSI is extensive. However, this review is limited to my experiences and perspective, therefore, it may not include all relevant literature.

1.2.1 Incompressible flow FSI

The modelling of FSI for incompressible viscous flows is of great relevance in various fields of engineering, such as civil engineering, marine engineering and bioengineering, etc. Its applications include urban pollution (García *et al.*, 2011), offshore wind turbines (Rasheed *et al.*, 2014; Hsu & Bazilevs, 2012), nuclear energy (Buchan *et al.*, 2014; Jewer *et al.*, 2014), coastal engineering (Latham *et al.*, 2009), cardiac blood flows (Peskin, 1972; Van Loon *et al.*, 2006), and particulate flows (Feng & Michaelides, 2005; Apte *et al.*, 2009; Uhlmann, 2005; Kempe & Fröhlich, 2012). Two types of approaches in the area of computational FSI have been developed to couple both the solid and fluid equations. One is the strong coupling approach referred to here as the monolithic coupling method (Gibou & Min, 2012; Feng & Michaelides, 2005; Apte *et al.*, 2009; Hübner *et al.*, 2004; Ryzhakov *et al.*, 2010; Michler *et al.*, 2004), in which both equations are solved in a coupled fashion by forming matrix equations implicitly containing the coupling terms. Compared with other existing approaches, monolithic approaches are more stable and more accurate. However, they often require the same mesh and time step size for both the fluid and solid models. An alternative is to use weak coupling models (Viré *et al.*, 2012, 2015; Farhat *et al.*, 1998; Jaiman *et al.*, 2006), in which different approaches are used for fluids and solids. These weak coupling models are also called partitioned or staggered methods due to the solid and fluid equations being solved separately with explicitly represented coupling terms. A key advantage of staggered approaches is that they readily enable different meshes and time steps to be used in the solid and fluid models. Among weak coupling methods, the volume penalization method is used in the literature (Viré *et al.*, 2012, 2015; Gibou & Min, 2012; Engels *et al.*, 2015) to ensure that the action-reaction force is balanced at the interface between the solids and fluids. This approach has similarities with the approach introduced here as both approaches relax the solid and fluid velocities towards one another at the solid-fluid interface.

Based on different mesh schemes, these FSI models can be divided into Arbitrary Lagrangian-Eulerian (ALE) schemes and immersed boundary/body methods. The ALE method couples a Eulerian to a Lagrangian formulation to solve fluid-structure interaction and multiphase flow problems via a body conforming Cartesian grid. However, a non body conforming Cartesian grid is used in immersed boundary/body methods. It is worth to notice that there are some differences between the immersed boundary and immersed-body methods. The immersed boundary method uses a spring force term and a delta function (Peskin, 1972) in fluid momentum equation to ensure the force balance between the fluids and solids. while the immersed-body method relaxes the fluid velocities towards solid velocities inside the solid domain to solve the fluid-structure interaction problem (Kajishima *et al.*, 2001). ALE approaches (Van Loon *et al.*, 2007; Farhat *et al.*, 1998) ensure that the velocities of solids and fluids are matched at the interface, whilst both the fluid and solid simulations share the same mesh. Despite the algorithm being robust for the small movements of solids, it requires a high computational cost and may cause numerical instabilities when dealing with large deformations or displacements of solids. To tackle this problem, the immersed body method has been developed that allows us to use different meshes for the solid and fluid models (Peskin, 1972; Griffith *et al.*, 2007; Viré *et al.*, 2012, 2015; Glowinski *et al.*, 1994; Van Loon *et al.*, 2007). This idea can be seen in the original immersed boundary method, which was used to resolve flow patterns around heart valves by Peskin (1972). In this method, an immersed boundary was employed to link moving solid and fluid boundaries. (Griffith *et al.*, 2007) enabled the adaptive mesh for the original immersed boundary method. Moreover, fictitious domain methods were developed and tested in (Glowinski *et al.*, 1994; Van Loon *et al.*, 2007). The fictitious domain methods are based on the idea of original immersed boundary method. Sometimes, the fictitious domain methods are called as domain embedding methods. Because different solvers for the fluid and solid are allowed in fictitious domain methods, they are flexible and easy to choose fast solvers. Recently, the separate solver concept has been extended, then a weak coupling immersed body method has been developed by Viré *et al.* (2012). This method is built based on dual meshes: a fluid and a solid mesh. The fluid mesh covers the entire computational domain including both the fluid and solid areas while the solid mesh is used only in the solid area. This versatile algorithm enables distinct finite element models to be used in fluid and solid equations. In this approach, to ensure that the projection of the force is equal and opposite to the solid and fluid equations, a novel Galerkin projection algorithm was introduced(Viré *et al.*, 2012). Viré *et al.* (2015) also have further developed a new immersed-body method, in which a penalty force was added to the momentum equation as a source term to relax the fluid velocity to the structural velocity. In this method, the force exchange between solid and fluid models is resolved within a thin shell mesh surrounding the structures. Despite the fact that these two immersed-body methods were successful in many applications involving FSI, they only deal with single phase flow coupled with solids, i.e. where solid bodies were totally immersed inside a single fluid phase.

1.2.2 Compressible flow FSI model within fractured solids

In this section, the compressible flow FSI models within fractured solids for blasting are reviewed. Blasting and explosives have played an important role in rock blasting, cutting, mining and tunnelling industries through centuries. In such applications, the damage and other effects due to blasts are mainly predicted by experiments and numerical analysis. The earliest developments in the numerical analysis of blasting process began with very simple empirical formulae. These primitive formulae date back to the nineteenth century (Chapman, 1899; Jouguet, 1905) and more or less depend on users' experience. However, they are very effective for obtaining a realistic estimate for engineering use.

A large number of models have been developed for modelling blast-induced fracture processes. They can be divided into two groups: the distinct phase models and the complete blast models (Mohammadi & Pooladi, 2012). For the distinct phase models, there are two phases: the fragmentation phase with shock waves (Banadaki & Mohanty, 2012; Ai & Ahrens, 2006; Larcher, 2009) and the burden movement phase (Firth & Taylor, 2001; Preece *et al.*, 1996; Yan *et al.*, 2016). Fragmentation models only simulate the beginning stage of explosions, which is mainly the fracture propagation and shock wave reflection. After the first stage, the fracture extension and fragmentation movements are described by the burden movement models. The distinct phase models are easily built, but they are not able to simulate blasting processes realistically. In order to resolve this problem, several complete blast models (Mohammadi & Pooladi, 2012; Ning *et al.*, 2011; Morris *et al.*, 2006) have been developed to simulate the fragmentation and burden movement phases in one model. The ultimate goal of the complete models is to simulate the entire blasting process including detonation, shock waves, compressible flow, fracture propagation and gas-solid interaction in one model.

In blast-induced fracture modelling, there are three parts involved: gas modelling, solid fracture modelling and the gas-solid coupling. In simple gas models, user-defined or empirical pressure profiles are applied on the cracks and the walls of blasting holes (Zhu *et al.*, 2007; Nilson, 1986). In sophisticated gas models, pressure distributions in the blast process are determined by solving the fluid governing equations. Munjiza *et al.* (2000, 1999) proposed a gas model based on a combined finite-discrete element method (FEMDEM) for accurate simulation of pressure within cracks and fractures. The FEMDEM is a combination of both discrete and finite element methods which can model problems with the deformability in one entire solid body, a large number of discrete bodies, or a solid body with existing fractures (Munjiza, 2004). The gas flow in this model is assumed as an equivalent one-dimensional duct flow with a constant duct area. Based on this idea, Mohammadi & Pooladi (2007) further applied the model to non-uniform isentropic gas flows (Mohammadi & Pooladi, 2012). From a different point of view, Preece *et al.* (1996) and Preece & Taylor (1989) proposed gas models based on porous media flows. In these models, the fractured rock mass is replaced with an equivalent porous medium. This type of models was further developed by Mohammadi & Pooladi (2007, 2012) and Su *et al.* (2015). Mohammadi & Pooladi (2007) first introduced a non-uniform isentropic gas model, and used a two-mesh method (Mohammadi & Pooladi, 2012) to couple porous media flows and FEMDEM. Su *et al.* (2015) extended this method to multiphase flows.

As far as fracture models are concerned, a variety of numerical methods have been developed. The earliest are continuum-based fracture models, which are used at the starting stage of an explosion. Firstly, cracking models, which depend on stress wave propagation, were introduced into the finite element or finite difference methods to resolve small fractures inside solids (Field & Ladegaard-Pedersen, 1971; Sanchidrian *et al.*, 2007; Farnam *et al.*, 2010). Continuum fracture models were then developed to adapt to various rock blasting problems (Wang *et al.*, 2009; Hao *et al.*, 2002b,a; Renani *et al.*, n.d.). Despite the widespread use of continuum damage models, they are not suitable for simulating extensive solid cracks and fragmentation since there are significant discontinuities in the solid mass. To resolve intense fractures, discontinuum based methods were introduced into the burden movement models. These methods treat the fractured solids as discontinuous separate smaller parts, which impact each other via contacts and collisions (Ning *et al.*, 2011; Li *et al.*, 2007; Gui *et al.*, 2016; Saharan & Mitri, 2008; Versino *et al.*, 2015). In order to simulate complete blasting processes, FEMDEM was proposed by Munjiza (1992).

FEMDEM has been used recently in complete blast models (Munjiza *et al.*, 1999, 2000; Munjiza, 2004; Rougier *et al.*, 2014).

With regard to the gas-solid interaction modelling, two types of numerical methods have been developed. One is local influence gas flow modelling, whilst the other group is general gas flow modelling in porous media. In local gas flow models, flow in cracks and fractures is simulated as a uniform gas flow in pipes and channels (Munjiza *et al.*, 2000). On the other hand, porous media models treat the gas flow in cracks and fractures as flow in equivalent porous media (Mohammadi & Pooladi, 2007, 2012). In the coupled gas-solid interaction model developed by Mohammadi & Pooladi (2012), two separate meshes were introduced for representing the rock and gas, respectively. These two meshes were coupled to each other to complete the simulation of the entire blast process. In this model, the porous, media gas flow was coupled with the FEMDEM (Mohammadi & Bebamzadeh, 2005) to resolve both the gas flow behaviour and the solid fracturing process. However, there is a gap between the model and real blasting problems, most notable being the simplified gas equation of state and the structured coarse gas mesh used in this model.

1.2.3 Turbulence flow FSI model

There is a need for turbulence models with FSI in many industrial and environmental high Reynolds number flows e.g. the turbulent flow in the wind and tidal turbines (Milthaler, 2014; Kang *et al.*, 2012), flow in impeller stirred tanks (Tyagi *et al.*, 2007), road vehicle aerodynamics (Jindal *et al.*, 2005), atmospheric flows (Tseng & Ferziger, 2003; Yang & Balaras, 2006) and stator-rotor interaction (Tyagi & Acharya, 2005). Immersed-boundary/body methods for FSI are very promising due to their strengths in dealing with complicated geometries and moving structures. Their application ranges from civil engineering to medical science, such as complex geometries (Löhner *et al.*, 2008; Le *et al.*, 2008), particulate flows (Luo *et al.*, 2007; Uhlmann, 2005), flexible structures (Hesch *et al.*, 2012; Wiens & Stockie, 2015; Xiao *et al.*, 2016), multi-phase flows (Yang *et al.*, 2016), compressible flows (Yang *et al.*, 2017b; Ghias *et al.*, 2007; Xiao *et al.*, 2017), cardiac mechanics (Borazjani, 2013) etc.

The interface representation in turbulent FSI models is important because there is a need to know the exact wall distances from the fluid to the structural surfaces. Thus this section reviews the interface representation for FSI models. In immersed-boundary/body methods, the methodologies for representation of the fluid-structure interface can be classified into two groups: diffused and sharp interface methods (Sotiropoulos & Yang, 2014). Diffused interface immersed-boundary/body methods smear the exchange forces between solids and fluids on the background grid of the interfaces by applying discrete functions or mask functions for penalization methods. There are three kinds of diffused interface immersed-boundary/body methods: classic immersed-boundary/body, direct forcing immersed-boundary/body and penalization methods. The main weakness of the diffused interface immersed-boundary/body method is that the immersed boundaries are not sharp and as such resolving boundary layers in turbulent flows becomes problematic. Sharp interface method does not suffer from this drawback. Four kinds of sharp interface methods have been developed, that is, the cut-cell, immersed interface, hybrid Cartesian-immersed boundary and curvilinear immersed boundary methods.

Among these sharp interface methods coupling with various turbulent models, the hybrid Cartesian-immersed boundary method is the most popular, including the ghost cell method (Ghias *et al.*, 2007; Ghosh *et al.*, 2010; Tseng & Ferziger, 2003; Ikeno & Kajishima, 2007; Yang & Stern, 2009) and the boundary reconstruction method (Johnson *et al.*, 2014; De Tullio *et al.*, 2007; Kang *et al.*, 2009; Cristallo & Verzicco, 2006; Tessicini *et al.*, 2002; Roman *et al.*, 2009). For the boundary reconstruction method, the Reynolds-averaged Navier-Stokes (RANS) model was used for turbulent flows in FSI, see (Johnson *et al.*, 2014; De Tullio *et al.*, 2007), while the large eddy simulation (LES) model in (Kang *et al.*, 2009; Cristallo & Verzicco, 2006; Tessicini *et al.*, 2002; Roman *et al.*, 2009). The boundary reconstruction method can provide high degree and accuracy solutions in the vicinity of the solid-fluid interface. However, wiggles and spurious extrema could be introduced by high order polynomial interpolations and this may cause numerical instabilities. This method is suitable for fixed solids coupled with turbulent flows, but it is difficult to apply to moving and deforming solids because of instabilities when dealing with moving interfaces. Among these references using the ghost cell method, the direct numerical simulation (DNS) is used in (Ghias *et al.*, 2007), RANS in (Ghosh *et al.*, 2010), and LES in (Tseng & Ferziger, 2003; Ikeno & Kajishima, 2007; Yang & Stern, 2009). The ghost cell method may generate some non-physical force oscillations due to the fact that nodes change in time from solid to fluid (or fluid to solid) near a moving interface. This could result in a very small mesh edge length and time step being used in order to stabilise this method.

There are few approaches that couple turbulent flows with diffused interface immersed-boundary/body methods. A wall-layer model (WLM) (Ji *et al.*, 2012) and RANS model (De Palma *et al.*, 2006; Ghosh *et al.*, 2008; Capizzano, 2011) have been used to simulate the turbulence for FSI by using direct forcing immersed-boundary/body methods. Discrete delta functions are used in the direct forcing immersed-boundary methods to ensure the force balance between solids and fluids. However, it makes the interface more diffusive due to the fact that these delta functions are normally smeared across several grid nodes. This makes it difficult to apply turbulent wall functions at the solid-fluid interface. Regarding the penalization methods, only RANS has been used to couple with FSI (Cho *et al.*, 2007, 2006). However, there are some numerical oscillations in the penalization methods when large penalization terms are applied. Nevertheless, the numerical oscillations can be stabilized by smearing the penalization terms into several grid nodes. In spite of the weakness of the diffused interface method, it is relatively easier than the sharp interface method when dealing with fast moving and deforming solids in turbulent flows.

1.2.4 FSI application in renewable energy

As reasonable renewable energy choices, the wind & tidal turbines have been widely used over the past decade. Low carbon emission in wind & tidal turbines makes them more likely to be acceptable to the public. Nowadays, the onshore wind turbines have been extensively studied. This type of wind turbines is normally horizontal axis wind turbines (HAWT) with three blades configuration upwind. In order to increase the renewable energy's shares of wind turbines in global energy production, the vertical axis wind turbines (VAWT) have been introduced in the offshore and urban environment. Inspired by the VAWT, the vertical axis tidal turbines to collect the energy of the ocean currents or tides are also being implemented. Comparing with the research in HAWT, the study of VAWT is relatively less.

For flow models, five main aerodynamic models have been developed for simulating the VAWTs in the literature. They are blade element momentum (BEM) model, cascade model, vortex model (Islam *et al.*, 2008), panel model (Smith *et al.*, 1996), and computatinal fluid dynamics (CFD) model. The BEM model uses Bernoulli's equation to compute the mass flow rate and the velocity change through every streamtube. The force on the blades in this streamtube is computed by the velocity change multiplying the mass flow rate. The cascade model has been widely used for turbomachinaries where the blades are periodic equidistant arranged on. Hirsch

& Mandal (1987) proposed the cascade model to VAWTs for the first time. For the vortex models, the velocity field is computed in the wake of the blades by using the vorticity (Strickland *et al.*, 1979; Cardona, 1984). The vortex models are also called as the potential flow models. The panel model is an extension of the vortex model. In the panel model, a potential flow regime is defined in the discretised 3D surface via a number of panels (Borg *et al.*, 2014). In CFD models, the fluid governing equations are solved on discretised meshes using different numerical methods, e.g. finite-difference methods (FDM) and finite-element methods (FEM). There are relatively fewer assumptions and simplifications in CFD models than these in BEM models, cascade models, vortex models, and panel models. Since there are some simplifications in BEM models, cascade models, vortex models, and panel models, these models have high computational efficiency. They are suitable for a conceptual and preliminary design of VAWTs. When dealing with the details of VAWT aerodynamics, for instance, dynamic stall (Rezaeiha *et al.*, 2017), tip and junction losses (Nobari *et al.*, 2016), turbulent incident wind (Danao *et al.*, 2014), the CFD model is required. Especially for the turbulent flow modelling in wind turbines, CFD models are demanded to simulate the unsteady flows (Danao *et al.*, 2014; Maître *et al.*, 2013; McNaughton *et al.*, 2014).

To perform aeroelastic modelling for wind turbine and hydroelastic modelling for tide turbine, structure models need to be coupled with flow models to simulate the structural deformations and motions of turbine blades and tower. There are two groups of these structural models: 1D equivalent beam model (Oñate, 2013; Bauchau & Craig, 2009; Hodges, 2003) and 3D FEM model (ANSYS, 2013; Version, 2013; Berg & Resor, 2012). In 1D equivalent beam model, the whole structure is discretized into a number of 1D beam elements. For 3D FEM model, 3D composite shell elements are used to discretize the wind turbine composite blades. The 3D FEM model is able to simulate the layer characteristics of composites throughout the shell thickness. The 1D equivalent beam models can be categorized into two groups: linear and nonlinear. The Timoshenko beam model (Oñate, 2013) and the Euler-Bernoulli beam model (Bauchau & Craig, 2009) are widely used linear beam models since they are easy to implement. Linear beam models are designed for small deflections, thus, nonlinear beam models (Hodges, 2003) are required when large deformation is generated. The accuracy for beam models are acceptable, while 3D FEM models (ANSYS, 2013; Version, 2013; Berg & Resor, 2012) are used to obtain more accurate results although that the meshing for 3D FEM models is time-consuming and tedious.

For the fluid-structure interaction models, Guerri *et al.* (2008) built a model based on finite volume Arbitrary Lagrangian-Eulerian (ALE) method and moving mesh to model a 2D wind turbine airfoil. This model is able to simulate the flow-induced vibrations for a 2D wind turbine, while this model cannot give detailed structural analysis. However, it only applied a 2D incompressible low Reynolds number flow model. Moreover, the commercial CFD software CFX (ANSYS, 2013) was coupled with ANSYS Mechanical software to simulate a morphed wind turbine blade via an ALE method by Krawczyk *et al.* (2013). This coupled model is a pressure coupled system with the focus on 2D applications. This model has the ability to model elastic blade aerodynamics, but it is limited in 2D simulations. A 3D coupled model was proposed by Lee *et al.* (2012) to evaluate the response of wind turbine blades under aerodynamic pressure. This model combined a BEM model and a finite element analysis (FEA) structural model via the pressure coupling. This model provides detailed structural analysis inside the blades and has a relatively high computational speed. However, the fluid dynamic details, e.g. the accurate pressure and velocity profiles are not available in this model. A 3D wind turbine blade vibration caused by wind was modelled by combining ALE and ANSYS by Zhang *et al.* (2014). This model is suitable for small deformation in the blades since the deformable fluid mesh is used. It is not able to simulate structural collapse and large deformation of the blades. In contrast to these 3D models (Lee *et al.*, 2012; Zhang *et al.*, 2014), which only simulate the 3D wind turbine blades, a full-scale wind turbine FSI model was developed by Bazilevs *et al.* (2011a,b) based on the finite element method (FEM) and ALE with the Deforming-Spatial-Domain/Stabilized Space-Time (DSD/SST) formulation (Tezduyar *et al.*, 1992b,a). This model was applied to a full-scale 3D horizontal axis wind turbine (the NREL 5MW offshore baseline wind turbine rotor). The moving/sliding meshes are used in this model (Bazilevs *et al.*, 2011a,b) to enable the wind turbine to rotate compared to the static tower. However, this model may have some limitations when applying to large deformation situations. Additionally, this model is incapable to model flow-induced fractures in the turbines.

1.3 Original contributions

A novel immersed-body method is developed here to model fluid-structure interaction for incompressible viscous flows. It does this by coupling a finite element multiphase fluid model and a combined finite-discrete element solid model. A coupling term containing the fluid stresses is introduced within a thin shell mesh surrounding the solid surface. In order to reduce the computational costs, the thin shell mesh acts as a numerical delta function in order to help apply the solid-fluid boundary conditions. In combination with an advanced interface capturing method, the immersed-body method has the capability to solve problems with fluid-solid interfaces in the presence of multiphase fluid-fluid interfaces. Importantly, the solid-fluid coupling terms are treated implicitly to enable larger time steps for fluids to be used.

The second significant contribution of this thesis is the implementation of the equation of state for high compressible gas in this immersed-body method combining with a cohesive zone fracture model. The equation of state implemented here is the John-Wilkins-Lee equation of state. This enables blast-induced fractures to be simulated by this novel gas-solid interaction model. This model is fully coupled and simulates the whole blasting process including gas pressure impulse, shock wave propagation, gas expansion, fragmentation and flying fragments. A Q-scheme is used to stabilise the model when solving extremely high-pressure situations.

The most important contribution of this thesis is the novel combination of the immersed-body method with an unsteady Reynolds-averaged Navier-Stokes (URANS) turbulence model. Particular attention is paid to the application of suitable turbulent flow boundary conditions with the immersed-body method. The thin shell mesh surrounding the solid surface is used as a delta function to apply the interface boundary conditions for both the turbulence model and the momentum equation. In order to reduce the computational cost, a log-law wall function is used within this thin shell to resolve the flow near the solid surface. To improve the accuracy of the wall function, a novel shell mesh external-surface intersection approach is introduced to identify sharp solid-fluid interfaces. More importantly, an unstructured anisotropic mesh adaptivity is used to refine the mesh according to the interface and the velocity, which improves the accuracy of this immersed-body URANS turbulence model with use of a limited number of fluid cells.

The developed FSI models are validated by a variety of test cases. For the immersed-body method coupled with incompressible flow, three numerical test cases: a free falling circular cylinder in a fluid at rest, an elastic membrane and a collapsing column of water moving an initially stationary solid square, are used to validate the model. To validate the compressible flow FSI model coupling with a cohesive zone fracture model, two benchmark tests, blasting cylinder and projectile fire, are presented. The results of these tests are in good agreement with experimental data.

For the FSI model coupled with URANS turbulence model, three test cases flow over a circular cylinder at $Re = 3900$ and turbulent flow past a static NACA0015 aerofoil with an attack angle of $\alpha = 60^\circ$ at $Re = 5200$, a free rising circular cylinder in a fluid at rest with $Re = 5000$ and $Re = 3800$, are used to validate the model. Detailed validation of 3D FSI model is presented in this thesis, i.e. free falling sphere test cases, free rising sphere test cases, flow cross a full scale vertical tidal turbine, and flow bending a flexible plate benchmark test case.

Finally, a variety of applications are simulated by this FSI model. The FSI model is applied to a water-air interface with a floating solid square being moved around by complex hydrodynamic flows including wave breaking in Chapter 2. In addition, a blasting engineering simulation with shock waves, fracture propagation, gas-solid interaction and flying fragments is simulated in Chapter 3. More importantly, flow-induced vibration and flow-induced fractures of a vertical axis tidal turbine are presented to demonstrate the model ability in analysing the elasticities and fractures for tidal turbines in Chapter 5.

1.4 Thesis outline

Chapter 1 is a brief introduction including a literature review of FSI in CFD, motivation, original contributions and outline of the thesis. Some contents of this Chapter is reorganised from:

Yang, P., Xiang, J., Fang, F., Pavlidis, D., Latham, J.P. and Pain, C.C., 2016. Modelling of fluid-structure interaction with multiphase viscous flows using an immersed-body method. Journal of Computational Physics, 321, pp.571-592.

Yang, P., Xiang, J., Chen, M., Fang, F., Pavlidis, D., Latham, J.P. and Pain, C.C., 2017. The immersed-body gas-solid interaction model for blast analysis in fractured solid media. International Journal of Rock Mechanics and Mining Sciences, 91, pp.119-132.

Yang, P., Xiang, J., Fang, F., Pavlidis, D. and Pain, C.C., 2018. Modelling of fluid-structure interaction for moderate Reynolds number flows using an immersed-body method. Computers & Fluids, Under Review.

Yang, P., Xiang, J., Fang, F. and Pain, C.C., 2018. A fidelity fluid-structure interaction model for vertical axis tidal turbines in turbulence flows. Applied Energy, Under Review.

A novel immersed-body method is developed in Chapter 2 to model fluid-structure interaction for incompressible flow, compressible flow and turbulent flow.

This Chapter is derived from:
Yang, P., Xiang, J., Fang, F., Pavlidis, D., Latham, J.P. and Pain, C.C., 2016. Modelling of fluid-structure interaction with multiphase viscous flows using an immersed-body method. Journal of Computational Physics, 321, pp.571-592.
Yang, P., Xiang, J., Chen, M., Fang, F., Pavlidis, D., Latham, J.P. and Pain, C.C., 2017. The immersed-body gas-solid interaction model for blast analysis in fractured solid media. International Journal of Rock Mechanics and Mining Sciences, 91, pp.119-132.
Yang, P., Xiang, J., Fang, F., Pavlidis, D. and Pain, C.C., 2018. Modelling of fluid-structure interaction for moderate Reynolds number flows using an immersed-body method. Computers & Fluids, Under Review.
Yang, P., Xiang, J., Fang, F. and Pain, C.C., 2018. A fidelity fluid-structure interaction model for vertical axis tidal turbines in turbulence flows. Applied Energy, Under Review.

In Chapter 3, the FSI model for incompressible flow is validated by four numerical test cases: a free falling circular cylinder in a fluid at rest, a free falling sphere, an elastic membrane and a collapsing column of water moving an initially stationary solid square. The application in this Chapter is a floating object being moved around by complex hydrodynamic flows including wave breaking. This Chapter is based on:
Yang, P., Xiang, J., Fang, F., Pavlidis, D., Latham, J.P. and Pain, C.C., 2016. Modelling of fluid-structure interaction with multiphase viscous flows using an immersed-body method. Journal of Computational Physics, 321, pp.571-592.

In Chapter 4, the FSI model is extended to highly compressible flow coupling with a cohesive zone fracture model. The compressible flow FSI model is applied to blasting engineering problems with shock waves, fracture propagation, gas-solid interaction and flying fragments. This Chapter is expanded from:
Yang, P., Xiang, J., Chen, M., Fang, F., Pavlidis, D., Latham, J.P. and Pain, C.C., 2017. The immersed-body gas-solid interaction model for blast analysis in fractured solid media. International Journal of Rock Mechanics and Mining Sciences, 91, pp.119-132.

In Chapter 5, the FSI model for turbulent flow is validated by five benchmark test cases: flow over a circular cylinder at $Re = 3900$, turbulent flow past a static

NACA0015 aerofoil with an attack angle of $\alpha = 60°$ at $Re = 5200$, a free rising circular cylinder in a fluid at rest with $Re = 5000$ and $Re = 3800$, a free rising sphere in turbulent flow at $Re = 6000$ and 10000, and flow bending a 3D plate. This Chapter is derived from:
Yang, P., Xiang, J., Fang, F., Pavlidis, D. and Pain, C.C., 2018. Modelling of fluid-structure interaction for moderate Reynolds number flows using an immersed-body method. Computers & Fluids, Under Review.

In Chapter 6, the FSI model is applied to the field of renewable energy.

This Chapter is expanded from:
Yang, P., Xiang, J., Fang, F. and Pain, C.C., 2018. A fidelity fluid-structure interaction model for vertical axis tidal turbines in turbulence flows. Applied Energy, Under Review.

Finally, Chapter 7 discusses the strengths and weaknesses of the URANS immersed-body model and draw conclusions and findings of this thesis. Certain future research works for turbulent FSI modelling and its application are proposed.

Chapter

TWO

A fluid-structure interaction model for incompressible, compressible and turbulent flows

An immersed-body method is developed here to model fluid-structure interaction for incompressible, compressible and turbulent flows. This model couples a combined finite-discrete element solid model (a solid solver 'Solidity ') and a finite element fluid model with the standard $k - \varepsilon$ turbulence model (a fluid solver 'Fluidity-Multiphase'). A coupling term containing the fluid stresses is introduced within a thin shell mesh surrounding the solid surface. The thin shell mesh surrounding the solid surface is first used as a delta function to apply the interface boundary conditions for both the turbulence model and the momentum equation. A large number of fluid mesh elements are required to resolve the fluid details near the solid surface. In order to reduce the computational cost, a log-law wall function representation is used within this thin shell to help resolve the flow near the solid surface. To improve the accuracy of the wall function, a novel shell mesh external-surface intersection approach is introduced to identify sharp solid-fluid interfaces. More importantly, an unstructured anisotropic mesh adaptivity is used to refine the mesh according to the interface and the velocity, which improves the accuracy of this immersed-body URANS turbulence model with the use of a limited number of fluid cells. Additionally, since

the solid solver 'Solidity ' is explicit and fluid solver 'Fluidity-Multiphase'is implicit, the solid-fluid coupling terms are treated implicitly in the solid solver to enable larger time steps for fluids to be used.

2.1 Introduction

This chapter describes a new solid-fluid coupling model for incompressible, compressible and turbulent flows. The proposed algorithm proceeds as follows. Firstly, in the fluids, a viscous term is added to the momentum equation, which is similar to the penalty force (Viré *et al.*, 2012; Engels *et al.*, 2015). Secondly, in the solid model, this viscous term is used to construct the drag force. Then the model developed here couples the immersed-body approach with the $k - \varepsilon$ URANS turbulence model. The interface boundary conditions for both the turbulence model and the fluid momentum equation are solved on the thin shell mesh. A log-law wall function is also implemented within this thin shell to help resolve the fluid friction velocity and stress within the first off-wall fluid cell. This reduces the computational cost since it does not require a very fine mesh near the solid wall. A novel shell mesh external-surface intersection approach is introduced to identify sharp solid-fluid interfaces. This improves the accuracy of the wall function and also overcomes the weakness of the diffused interface method. In order to further increase the computational efficiency of the present model, the anisotropic mesh adaptivity (Pain *et al.*, 2001b) is used to refine the mesh according to the interface and the velocity fields.

The remainder of this chapter is organised as follows. Section 2.2 presents the governing fluid and solid equations. The standard $k - \varepsilon$ model is presented at Section 2.3.1. The wall functions and the algorithms to compute the wall distance for the immersed-body method are given at Sections 2.3.2 and 2.3.3. Section 2.4 gives out the spatial discretization. The theory behind the semi-implicit coupling approach; and the projection between fluid, solid and shell meshes are detailed in Section 2.6. The coupling process for turbulent flow is described in detail in Section 2.7. I discuss the strength and weaknesses of this approach and draw conclusions in Section 2.8.

2.2 Governing equations

2.2.1 Equations for solid dynamics

For solid modelling, the combined finite-discrete element method (FEMDEM) is used here. It combines deformable fracturing arbitrary shaped solid body interactions modelled by finite-element method (FEM) with discrete solid motion modelled by discrete element method (DEM). For its FEM part, it uses a finite strain formulation for solving the solid dynamics equations. This model has the capability of computing the vibration modes, stresses, and fracture networks of any shape and stiffness (Xiang *et al.*, 2012; Latham *et al.*, 2013b). The governing equations for the dynamics of deformable structures on the solid mesh are given by Xiang *et al.* (2009):

$$\boldsymbol{M}_s \frac{D\boldsymbol{u}_s}{Dt} + \boldsymbol{F}_{int} = \boldsymbol{F}_{ext} + \boldsymbol{F}_c + \boldsymbol{F}_v + \boldsymbol{F}_p, \tag{2.1}$$

where, the nodal mass matrix $\boldsymbol{M}_s$ is given by:

$$\boldsymbol{M}_s = \int_V \rho_s \boldsymbol{N}_s \boldsymbol{N}_s^T dV, \tag{2.2}$$

where, the ρ_s is the solid density, and the $\boldsymbol{N}_s$ is the basis functions of the solid finite elements. The internal nodal forces $\boldsymbol{F}_{int}$ are given by:

$$\boldsymbol{F}_{int} = \int_{v^{(n)}} \frac{\partial \boldsymbol{N}_s}{\partial \boldsymbol{x}} \boldsymbol{T} dv, \tag{2.3}$$

where, $\boldsymbol{T}$ is the Cauchy stress. The external nodal forces $\boldsymbol{F}_{ext}$ are given by:

$$\boldsymbol{F}_{ext} = \int_{v^{(e)}} \boldsymbol{N}_s \boldsymbol{b} dv + \int_{v^{(e)}} \boldsymbol{N}_s \boldsymbol{t}_s dv, \tag{2.4}$$

where $\boldsymbol{b}$ is body force, defined by $\boldsymbol{b} = [b_x \ b_y \ b_z]$, $\boldsymbol{t}_s$ is surface traction force. $\boldsymbol{F}_c$ is the contact force when multiple solids impact on each other. $\boldsymbol{F}_v$ and $\boldsymbol{F}_p$ are the exchange forces between the solid and fluid due to the viscous terms and fluid pressure respectively. In this work, a solid FEMDEM solver 'Solidity ' (Xiang *et al.*, 2012; Latham *et al.*, 2013b) is coupled with a fluid solver 'Fluidity-Multiphase'. The approach to forming the exchange forces are going to be described in Section 2.6 in detail. When using equation 2.1 to model the rigid body, the material stiffness is increased to its real value.

2.2.2 The constitutive model for deformable solids

The constitutive model used here to model large deformable solids is the Neo-Hookean material model (Xiang *et al.*, 2009). This model is an extension of Hooke's law to large nonlinear deformations. The Cauchy stress $\boldsymbol{T}$ can be computed by the following equation:

$$\boldsymbol{T} = \frac{\mu}{J}(\boldsymbol{B} - \boldsymbol{I}) + \frac{\lambda}{J}(\mathrm{In}J)\boldsymbol{I}, \tag{2.5}$$

where $\boldsymbol{I}$ is the identity matrix. The Cauchy-Green tensor $\boldsymbol{B} = \boldsymbol{F}\boldsymbol{F}^T$, and the Jacobian determinant $J = det(\boldsymbol{F})$. Here, $\boldsymbol{F}$ is the deformation gradient tensor, μ and λ are Lamé constants,

$$\mu = \frac{E}{2(1+\nu)}, \tag{2.6}$$

and

$$\lambda = \frac{\nu E}{(1+\nu)(1-2\nu)}, \tag{2.7}$$

where ν is the Possion ratio and E is the Young's modulus.

2.2.3 Equations for fluid dynamics of incompressible flows

The fluid dynamics model 'Fluidity-Multiphase' is a finite-element open-source numerical tool that solves the Navier-Stokes equations on fully unstructured mesh for multiphase flows. It has the ability to dynamically change its resolution (adapt the mesh) in response to the physical demands (Pain *et al.*, 2001b, 2005; Piggott *et al.*, 2009). Since it is difficult to embed the solid equations into the fluids equations, I achieve the coupling with the introduction of the supplementary equation:

$$\hat{\sigma}\left(\hat{\boldsymbol{u}}^f - \boldsymbol{u}_f^f\right) = \hat{\sigma}\left(\boldsymbol{u}_s^s - \boldsymbol{u}_f^s\right), \tag{2.8}$$

in which $\hat{\sigma} = \frac{\rho_f}{\Delta t}$, where ρ_f is the fluid density, and the bulk velocity $\hat{\boldsymbol{u}}^f$ is defined:

$$\hat{\boldsymbol{u}}^f = \alpha_f \boldsymbol{u}_f^f + \alpha_s \boldsymbol{u}_s^f = \hat{\boldsymbol{u}}_f^f + \hat{\boldsymbol{u}}_s^f, \tag{2.9}$$

where α_f is the fluid volume fraction and α_s is the solid volume fraction. The subscripts f and s represent the value of the fluid and solid respectively, whilst the superscripts f and s refer the value on the fluid and solid mesh respectively. For example, $\boldsymbol{u}_f^f$ is the fluid velocity on the fluid mesh, and $\boldsymbol{u}_s^f$ is the solid velocity on the fluid mesh.

In this work, the Navier-Stokes equations are solved on an extended domain $V = V_f \cup V_s$, where the computing domain include fluids in V_f and structures in V_s (see Fig. 2.1). Hence the continuity equation in the extended domain V can then be expressed as:

$$\nabla \cdot \hat{\boldsymbol{u}}^f = 0. \tag{2.10}$$

Notice that if $\boldsymbol{u}_s^s$ is mapped from the solid mesh to the fluid mesh we get $\hat{\boldsymbol{u}}_s^f$. Thus from equation 2.8 when $\alpha_f = 1$, $\alpha_s = 0$ then $\hat{\boldsymbol{u}}^f = \boldsymbol{u}_f^f$ and when $\alpha_f = 0$, $\alpha_s = 1$ then $\hat{\boldsymbol{u}}^f = \boldsymbol{u}_s^f$.

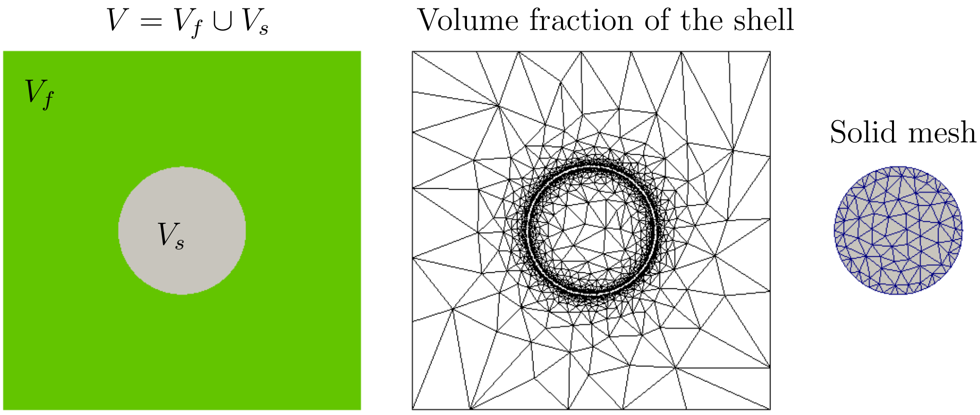

Figure 2.1 Computational domain V (*left*), fluid mesh adapted to the volume fraction of the shell (*centre*) and the solid mesh (*right*). The method to generate the shell mesh can be found in Section 2.6.2.

In order to represent the effect of the solids on the fluids, a coupling term $\boldsymbol{s}_c$ is introduced into the momentum equation. This coupling term is only added into a thin shell mesh surrounding the solid surface (see section 2.6.2) by using a shell concentration α_{sh}. The momentum equation is written:

$$\rho_f \frac{D\boldsymbol{u}_f}{Dt} + \nabla(p - \tau) = \boldsymbol{F}_b + \boldsymbol{s}_c, \tag{2.11}$$

where p is fluid pressure, τ is fluid shear stress, $\boldsymbol{F}_b$ represents body forces (e.g. the gravity force), and $\boldsymbol{s}_c$ is the coupling term. The coupling term contains exchange forces between the solid and fluid due to the viscous terms. The algorithm to form the coupling term will be presented in Section 2.6.

2.2.4 Equations for fluid dynamics of compressible flows

In the fluid model 'Fluidity-Multiphase', the continuity equation for the compressible flow can be expressed as:

$$\frac{\partial \rho_f}{\partial t} + \nabla \cdot (\rho_f \boldsymbol{u}_f) = 0, \tag{2.12}$$

where, ρ_f and $\boldsymbol{u}_f$ denote the fluid density and velocity; t is the time.

For the momentum equation, it can be written as,

$$\frac{\partial}{\partial t}(\rho_f \boldsymbol{u}_f) + \nabla \cdot (\rho_f \boldsymbol{u}_f \otimes \boldsymbol{u}_f + p - \tau) = \rho_f \boldsymbol{F}_b + \boldsymbol{s}_c. \tag{2.13}$$

The energy equation is given as,

$$\frac{\partial}{\partial t}(\rho_f E) + \nabla \cdot (\rho_f E \boldsymbol{u}_f - \tau \boldsymbol{u}_f + \boldsymbol{q}) = \rho_f \boldsymbol{F}_b \boldsymbol{u}_f, \tag{2.14}$$

where $\boldsymbol{q}$ represents the rate of volumetric heat addition per unit mass, $E = e + \mid \boldsymbol{u} \mid^2 /2$ is the total specific energy, e is the internal energy per unit mass, more details about e can be see in Section 4.3.

2.3 The $k - \varepsilon$ turbulence model

2.3.1 Standard $k - \varepsilon$ turbulence model

The $k - \varepsilon$ model described here is an unsteady RANS (URANS). The $k - \varepsilon$ model is first proposed by Launder & Spalding (1974). It consists of two transport equations for turbulent kinetic energy (k_f) and turbulent dissipation rate (ε_f), respectively.

For turbulent kinetic energy (k_f) (Versteeg & Malalasekera, 2007):

$$\frac{\partial k_f}{\partial t} + \bar{u}_i \frac{\partial k_f}{\partial x_i} = \Pi - \varepsilon_f + \frac{\partial}{x_j}\left[\left(\nu + \frac{\nu_T}{\sigma_k}\right)\frac{\partial k_f}{x_i}\right] + \boldsymbol{s}_k. \tag{2.15}$$

For turbulent dissipation rate (ε_f) determining the rate of dissipation of the turbulent kinetic energy:

$$\frac{\partial \varepsilon_f}{\partial t} + \bar{u}_i \frac{\partial \varepsilon_f}{\partial x_i} = C_{\varepsilon 1}\frac{\varepsilon_f}{k}\Pi - C_{\varepsilon 2}\frac{\varepsilon_f^2}{k} + \frac{\partial}{x_j}\left[\left(\nu + \frac{\nu_T}{\sigma_\varepsilon}\right)\frac{\partial \varepsilon_f}{x_i}\right] + \boldsymbol{s}_\varepsilon, \tag{2.16}$$

where u_i stands velocity component in corresponding direction, ν is kinematic viscosity, ν_T is the kinematic eddy viscosity, $\nu_T = C_\mu k_f^2/\varepsilon_f$, and Π is given as follow:

$$\Pi = \left(\tau_{ij} - \frac{1}{3}\tau_{ii}\right) \cdot \nabla \bar{\boldsymbol{u}}_f = \left[\nu_T\left(\nabla \bar{\boldsymbol{u}}_f + (\nabla \bar{\boldsymbol{u}}_f)^T - \frac{2}{3}k_f \mathrm{I}\right)\right] \cdot \nabla \bar{\boldsymbol{u}}_f, \tag{2.17}$$

where I is the identity matrix. The adjustable constants C_μ, σ_k , σ_ε , $C_{\varepsilon 1}$ and $C_{\varepsilon 2}$ are empirically obtained by data fitting of unbounded turbulent flows (Launder & Spalding, 1974) and their values are: $C_\mu = 0.09$, $\sigma_k = 1.00$, $\sigma_\varepsilon = 1.30$, $C_{\varepsilon 1} = 1.44$, $C_{\varepsilon 2} = 1.92$. $\boldsymbol{s}_k$ and $\boldsymbol{s}_\varepsilon$ are the coupling terms of the immersed-body URANS model. They are used to implement the turbulent boundary conditions for the solid surface. More details on $\boldsymbol{s}_k$ and $\boldsymbol{s}_\varepsilon$ can be found in Section 2.3.2.4.

2.3.2 Wall functions

In order to reduce the computational cost, a log-law wall function is used within the thin shell to help resolve the flow near the solid surface (Bull, 2013).

2.3.2.1 The definition of wall distance y^+

Taking into account a fully developed pipe flow, the no-slip wall condition $\boldsymbol{u}_f = 0$ is applied at $y = 0$. The corresponding fluctuation $u_i'u_j' = 0$ (u' is the fluctuation velocity) and the Reynolds stresses at $y = 0$ are thus zeros. The total viscous stress at $y = 0$ is:

$$\tau_w = \rho_f \nu \left(\frac{\partial u_f}{\partial y}\right)_{y=0}. \tag{2.18}$$

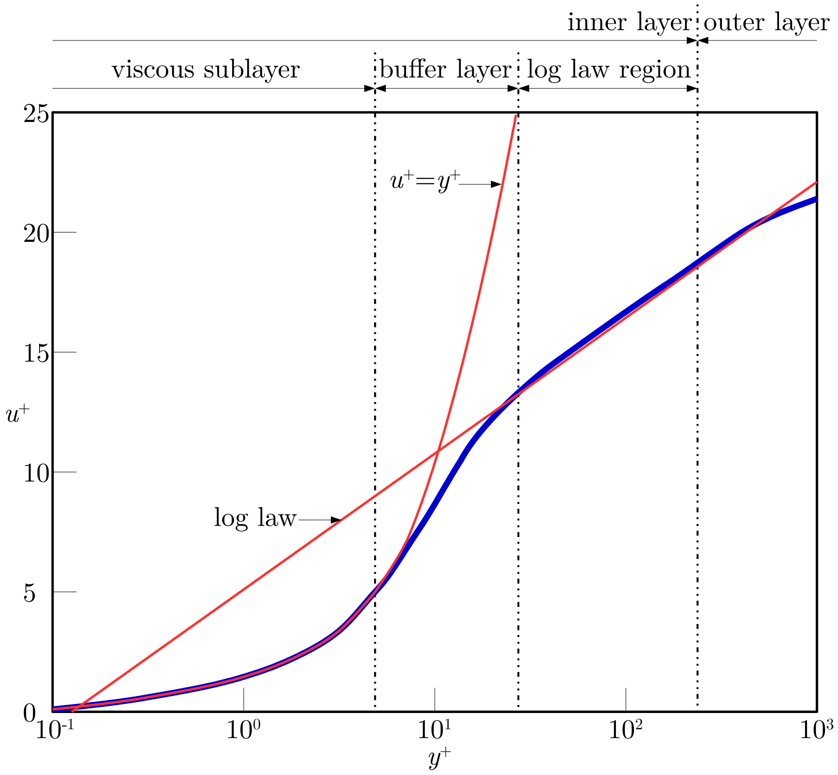

Figure 2.2 Law of the wall. The blue line is the real relationship between u^+ and y^+. The red lines are the approximations of this relationship by using log law and $u^{+}_{=}y^{+}$.

The friction velocity u_τ is defined as:

$$u_\tau = \sqrt{\frac{\tau_w}{\rho_f}}. \tag{2.19}$$

The normalized wall distance and velocity are defined as:

$$y^+ = \frac{u_\tau y}{\nu}, \tag{2.20}$$

$$u_f^+ = \frac{u_f}{u_\tau}, \tag{2.21}$$

where y is the distance to the wall.

The relationship between u_f^+ and y^+ is:

$$\begin{cases} u_f^+ = y^+ & , \textit{when} \quad y^+ < 5 \quad , \\ u_f^+ \to \frac{1}{C_\kappa} \ln y^+ + B & , \textit{when} \quad 5 < y^+ < 30 \quad , \\ u_f^+ = \frac{1}{C_\kappa} \ln y^+ + B & , \textit{when} \quad y^+ > 30 \quad , \end{cases} \tag{2.22}$$

where C_κ is the von Kármán constant and B is the smallest value of u_f^+, commonly taken as 0.41 and 5.2 respectively (Wilcox *et al.* , 1998). From Eq. 2.22 (Pope, 2000), the near wall region can be divided into three parts: viscous sublayer, buffer layer and log law region (see Fig. 2.2).

2.3.2.2 Wall functions

The wall functions proposed in the literature (Launder & Spalding, 1974) are used within the log-law region. The distance in wall units y^+ is usually set to a value larger than 30 to ensure that the log-law wall functions are valid. However, in order to calculate y^+, the wall shear stress τ_w should be solved first. Since the wall shear stress is not known for most real flows, a scalable method is needed to avoid this situation.

When $y^+ > 30$, combining Eq. 2.20, 2.21 and 2.22 yields:

$$u_f = u_\tau \left[\frac{1}{C_\kappa} \ln(u_\tau y/\nu) + B \right]. \tag{2.23}$$

From Eqs. 2.19 and 2.18, it can be seen that the friction velocity u_τ depends on the shear stress τ_w, whilst τ_w depends on the velocity gradient, thus the equation is indeterminate. To resolve this, Pope (2000) introduced the nominal friction velocity u_τ^*:

$$u_\tau^* = C_\mu^{1/4} k_f^{1/2}, \tag{2.24}$$

where k_f is the fluid turbulent kinetic energy of the near-wall nodes. Substituting Eq. 2.24 into Eq. 2.23, then the nominal mean velocity u_f^* is

$$u_f^* = u_\tau^* \left[\frac{1}{C_\kappa} \ln(u_\tau^* y/\nu) + B \right]. \tag{2.25}$$

Thus the wall shear stress can be given as:

$$\tau_{wf} = (u_\tau^*)^2 \frac{u_f}{u_f^*}. \tag{2.26}$$

2.3.2.3 Weakly enforced wall boundary conditions for the immersed-body method

The shear stress (see Eq. 2.26) is weakly enforced in the momentum equation using Green's Theorem for a computational domain Ω with solid walls Γ:

$$\begin{aligned}\int_{\Omega} N \bigtriangledown \cdot \tau_f d\Omega &= -\int_{\Omega} \bigtriangledown N \cdot \tau_f d\Omega + \int_{\Gamma_s} N\boldsymbol{n} \cdot \tau_s d\Gamma_s, \\ &= \int_{\Omega} N \bigtriangledown \cdot \tau_f d\Omega + \underbrace{\int_{\Gamma_s} N\boldsymbol{n} \cdot \tau_s d\Gamma_s}_{\text{viscous sublayer}} - \underbrace{\int_{\Gamma} N\boldsymbol{n} \cdot \tau_f d\Gamma}_{\text{log-law region}} \end{aligned} \tag{2.27}$$

where τ is the instantaneous stress tensor and $\boldsymbol{n}$ is the unit normal to the wall. By using $\tau_w = \boldsymbol{n} \cdot \tau$, then:

$$\underbrace{\int_{\Gamma_s} N\boldsymbol{n} \cdot \tau_s d\Gamma_s}_{\text{viscous sublayer}} - \underbrace{\int_{\Gamma} N\boldsymbol{n} \cdot \tau_f d\Gamma}_{\text{log-law region}} = \underbrace{\int_{\Gamma_s} N\tau_{ws} d\Gamma_s}_{\text{viscous sublayer}} - \underbrace{\int_{\Gamma} N\tau_{wf} d\Gamma}_{\text{log-law region}}. \tag{2.28}$$

For the viscous sublayer term, by using Eqs. 2.19, 2.20, 2.21 and 2.22, then:

$$\tau_{ws} = \rho\nu \frac{u_s}{y_s}, \tag{2.29}$$

where y_s is the wall distance of the fluid element that u_s is based on. Substituting Eqs. 2.26 and 2.29 into Eq. 2.28, and defining $q = \frac{(u_\tau^*)^2}{u_f^*}$, Eq. 2.28 can be becomes:

$$\underbrace{\int_{\Gamma_s} N\boldsymbol{n} \cdot \tau_s d\Gamma_s}_{\text{viscous sublayer}} - \underbrace{\int_{\Gamma} N\boldsymbol{n} \cdot \tau_f d\Gamma}_{\text{log-law region}} = \int_{\Gamma_s} N\rho\nu \frac{u_s}{y_s} d\Gamma_s - \int_{\Gamma} N q u_f d\Gamma. \tag{2.30}$$

Considering the thin shell mesh on the solid surface in the immersed-body method (Yang *et al.*, 2016), by converting the surface integral on the solid surface to the volume integral on the thin shell mesh, Eq. 2.30 can be written as:

$$\underbrace{\int\limits_{\Gamma_s} N\boldsymbol{n}\cdot\tau_s d\Gamma_s}_{\text{viscous sublayer}} - \underbrace{\int\limits_{\Gamma} N\boldsymbol{n}\cdot\tau_f d\Gamma}_{\text{log-law region}} = \int\limits_{V_{shell}} N\frac{\rho\nu u_s}{y_s\Delta r}dV_{shell} - \int\limits_{V_{shell}} N\frac{q u_f}{\Delta r}dV_{shell}, \tag{2.31}$$

where Δr is the shell mesh thickness. More details about the shell mesh can be found in (Yang *et al.*, 2016). Thus, the coupling term $\boldsymbol{s}_c$ is:

$$\boldsymbol{s}_c = \int\limits_{V_{shell}} N\frac{\rho\nu u_s}{y_s\Delta r}dV_{shell} - \int\limits_{V_{shell}} N\frac{q u_f}{\Delta r}dV_{shell}. \tag{2.32}$$

2.3.2.4 Wall function for the $k-\varepsilon$ model

After the simplification of k_f and ε_f equations in the log-law region, they can be expressed as :

$$k_f = \frac{u_\tau^2}{C_\mu^{1/2}}, \tag{2.33}$$

$$\varepsilon_f = \frac{u_\tau^3}{C_\kappa y}. \tag{2.34}$$

These are commonly used as Dirichlet boundary conditions for the $k-\varepsilon$ model at high Reynolds numbers (Ferziger & Peric, 2012).

The coupling term $\boldsymbol{s}_k$ is given as:

$$\boldsymbol{s}_k = \beta\alpha_{sh}\left(k_s - k_f\right). \tag{2.35}$$

The coupling term $\boldsymbol{s}_\varepsilon$ is:

$$\boldsymbol{s}_\varepsilon = \beta\alpha_{sh}\left(\varepsilon_s - \varepsilon_f\right), \tag{2.36}$$

where α_{sh} denotes the shell mesh volume fraction; k_s and ε_s are the k and ε on solid surface, which is given by Eqs. 2.33 and 2.34; k_f and ε_f represent the values of k and ε on the fluid mesh at the shell mesh part; β is given as: $\beta = \gamma \max\left(\frac{\rho_f}{\Delta t}, \frac{\nu}{L}\right)$, where ρ_f is the fluid density, L represents the edge length of the fluid cell near the shell mesh, and γ is given as: $\gamma = l_e/\Delta$, where l_e is the minimum fluid mesh edge length and Δ is the shell mesh thickness.

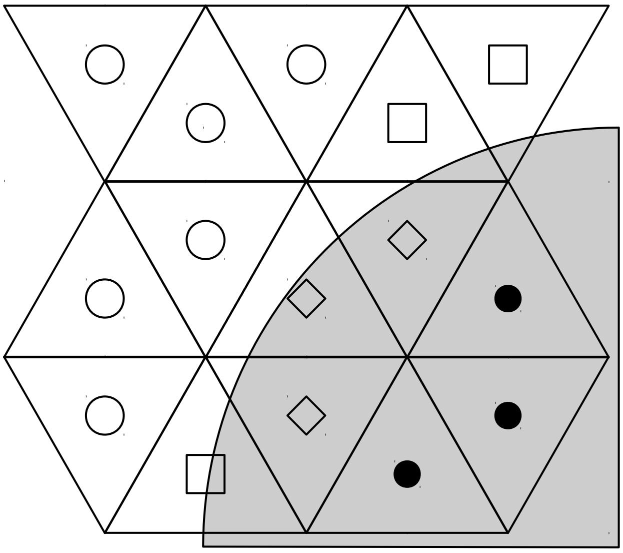

Figure 2.3 Definitions of fluid, solid and intersection cells. Fluid-cell: ○, Solid-Cell: •, Fluid Intersection-Cell: □, Solid Intersection-Cell: ◊.The grey part is the solid.

2.3.3 The wall distance in the immersed-body method

To calculate the wall distance y accurately, one has to identify the exact position of the fluid-solid interface. In this section, three approaches used for locating the interface fluid cells are provided.

2.3.3.1 Intersection cells

The first one is the intersection cells by using the Galerkin projection of the solid volume fraction α_s on the fluid mesh. When on the interface, $0 < \alpha_s < 1$. The cells with $0 < \alpha_s < 0.5$ are assumed as the intersection cells (see Fig. 2.3). And the solid surface information (including the coordinates and direction $\boldsymbol{n}_s$) is projected on these intersection cells to compute the wall distance y.

2.3.3.2 Neighbour cell reconstruction

The second is the neighbour cell reconstruction approach. Based on the intersection cells, searching all the neighbour cells these sharing at least one node or one face

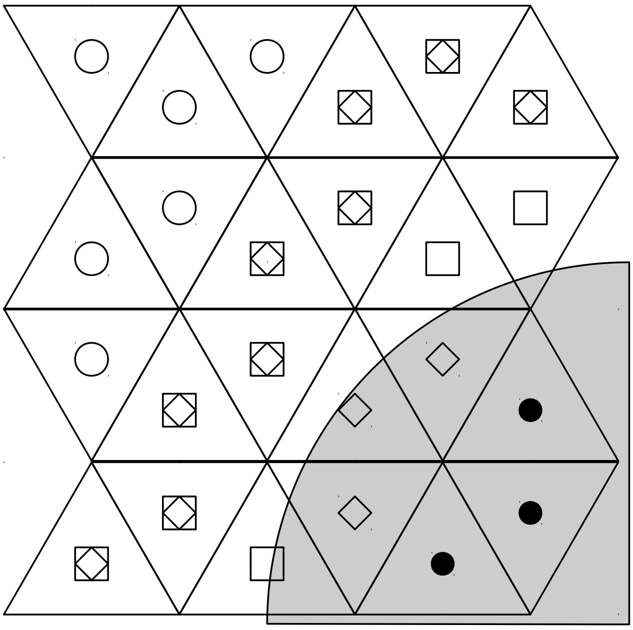

Figure 2.4 Definitions of fluid, solid and intersection cells.○: Fluid-cell, ●: Solid-Cell, □: Fluid Intersection-Cell, ◇: Solid Intersection-Cell. The grey part is the solid.

with them. These neighbour cells are used to reconstruct the intersection cell (see Fig. 2.4):

$$\phi_{i,j} = \sum_n \beta_n \phi_n. \tag{2.37}$$

The reconstruction intersection cells will be used to calculate the wall distance y.

2.3.3.3 Shell mesh external-surface intersection

The third one is the shell mesh external-surface intersection approach. This approach considers both the interaction cells and their shell mesh neighbour cells (see Fig. 2.5). The method to generate the shell mesh can be found in Section 2.6.2. The shell volume fraction α_{sh} on the shell external-surface is also taken into account. Fluid cells with the $\alpha_{sh} < 1$ on the shell external-surface are also considered to calculate the wall distance y.

The intersection cells method can introduce negative wall distances that make the

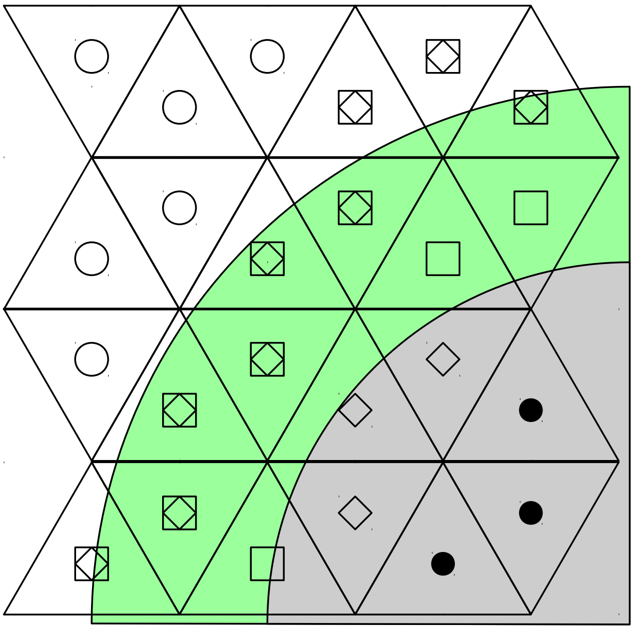

Figure 2.5 Definitions of fluid, solid and intersection cells.○: Fluid-cell, •: Solid-Cell, □: Fluid Intersection-Cell, ◊ Solid Intersection-Cell. The grey part is the solid and the green part is the shell.

wall function invalid. The neighbour cell reconstruction method requires the system to store all the neighbour cell information during the calculation. This increases the computational cost. Since the shell mesh external-surface intersection method does not have these two disadvantages, it is used in this immersed-body URANS model.

2.3.3.4 The calculation of the wall distance

By using the shell mesh external-surface intersection approach, the locations of the intersection cells are known. The coordinate $(x_i,\, y_i,\, z_i)$ of the intersection cell is projected to the shell mesh, then from the shell mesh to the solid surface. As the normal vector $(nx_j,\, ny_j,\, nz_j)$ and the coordinate $(xs_j,\, ys_j,\, zs_j)$ of the solid surface are already known in the solid. The wall distance y_i can be computed by using the following equation:

$$y_i = \frac{nx_{S_i}x_i + ny_{S_i}y_i + nz_{S_i}z_i - (nx_{S_i}xs_{S_i} + ny_{S_i}ys_{S_i} + nz_{S_i}zs_{S_i})}{\sqrt{(nx_{S_i})^2 + (ny_{S_i})^2 + (nz_{S_i})^2}}, \tag{2.38}$$

where, S_i is the index of the solid surface coordinate (xs_j, ys_j, zs_j), which has the shortest point to point distance to the intersection cell coordinate (x_i, y_i, z_i).

2.4 Spatial discretization

The finite element method is used in both the fluid and solid models. The Crank-Nicolson scheme is used in the fluid dynamics model while a backward Euler scheme in the solid dynamics model. Details of these methods are described in the literature (Gresho & Sani, 1998; Zienkiewicz & Taylor, 2000; Piggott *et al.*, 2008).

The continuity equation 2.10 for incompressible solid can be written as:

$$\frac{\alpha_s^{n+1} - \alpha_s^n}{\Delta t} + \nabla \cdot \alpha_s^{n+1} \boldsymbol{u}_s^{n+1} = 0, \tag{2.39}$$

and for each fluid phase, k with $k \in \{1, 2, ..., \mathcal{P}\}$, equation 2.39 is re-written:

$$\frac{\rho_k^{n+1}\alpha_k^{n+1} - \rho_k^n \alpha_k^n}{\rho_k^{n+1}\Delta t} + \frac{1}{\rho_k^{n+1}} \nabla \cdot \left[\theta \rho_k^{n+1} \alpha_k^{n+1} \boldsymbol{u}_k^{n+1} + (1-\theta)\rho_k^n \alpha_k^n \boldsymbol{u}_k^n\right] = 0, \tag{2.40}$$

where the superscripts refer to the time level. Summing all these equations the global continuity equation is and using the fact that $\alpha_s^{n+1} + \sum_k \alpha_k^{n+1} = 1$ in the time derivative and using $\alpha_s^{n+1}\boldsymbol{u}_s^{n+1} = \hat{\boldsymbol{u}}_f^{n+1} - \sum_k \alpha_k^{n+1}\boldsymbol{u}_k^{n+1}$ then yields:

$$\begin{aligned}
\mathcal{R}_{cty} = \frac{1-\alpha_s^n}{\Delta t} &+ \frac{1}{\Delta t}\sum_k \frac{-\alpha_k^n \rho_k^n}{\rho_k^{n+1}} \\
&+ \{\frac{1}{\rho_k^{n+1}} \nabla \cdot \left[\theta \rho_k^{n+1} \alpha_k^{n+1} \boldsymbol{u}_k^{n+1} + (1-\theta)\rho_k^n \alpha_k^n \boldsymbol{u}_k^n\right] \\
&+ \left(\nabla \cdot \hat{\boldsymbol{u}}_f^{n+1} - \sum_k \nabla \cdot \alpha_k^{n+1} \boldsymbol{u}_k^{n+1}\right)\} = 0.
\end{aligned} \tag{2.41}$$

The first term on the left and the last terms on the right are the new terms introduced into the solid-fluid coupling equations. Alternatively, one may assume that the solid phase continuity equation 2.39 has been enforced by the solid mechanics model. This can be obtained by a compromise defined variable: $\theta_{solid-cty}$, in which $\theta_{solid-cty} = 1$ is the method outlined by equation 2.41 and $\theta_{solid-cty} = 0$ enforces this new method where:

$$\begin{aligned}\mathcal{R}_{cty} = \frac{1 - \theta_{solid-cty}\alpha_s^n - (1 - \theta_{solid-cty})\alpha_s^{n+1}}{\Delta t} + \frac{1}{\Delta t}\sum_k \frac{-\alpha_k^n \rho_k^n}{\rho_k^{n+1}} \\ + \{\frac{1}{\rho_k^{n+1}} \nabla \cdot \left(\theta \rho_k^{n+1} \alpha_k^{n+1} \boldsymbol{u}_k^{n+1} + (1-\theta)\rho_k^n \alpha_k^n \boldsymbol{u}_k^n\right) \\ + \theta_{solid-cty}\left(\nabla \cdot \hat{\boldsymbol{u}}_f^{n+1} - \sum_k \nabla \cdot \alpha_k^{n+1} \boldsymbol{u}_k^{n+1}\right)\} = 0, \quad (2.42)\end{aligned}$$

in which $a_k^{n+1} = \alpha_k^{n+1}$. However, for compressible flow, by using the limit as the fluid volume fraction, we get a pure solid. Hence the system of equations for density/-pressure of the fluid can become ill-posed. For instance, if one considers the system of equations for an ideal gas, in which the negative pressures that could be formed in the solid will result in negative densities. This is easily avoided by setting:

$$a_k^{n+1} = \frac{\alpha_k^{n+1}}{1 - \alpha_s^{n+1}}. \quad (2.43)$$

For single phase flow this becomes:

$$a_k^{n+1} = 1. \quad (2.44)$$

Then the system of equation becomes well posed and there is no longer this issue.

In matrix form equation 2.42 becomes:

$$\underline{\boldsymbol{r}}_{cty}^{*} = \tilde{\boldsymbol{B}}^T \hat{\underline{\boldsymbol{u}}}_f^{n+1} + \boldsymbol{B}^T \underline{\boldsymbol{u}}^{n+1} + \underline{\boldsymbol{res}}_{cty}, \quad (2.45)$$

where, the velocity field is expressed as

$$\boldsymbol{u} \approx \sum_{i=1}^{N} \boldsymbol{u}_i N_i(\boldsymbol{x}), \quad (2.46)$$

in which, the N_i are the basis functions of the fluid finite elements. Thus in this multi-phase flow case the coupling matrix $\boldsymbol{M}_c$ between $\underline{\boldsymbol{u}}$ and $\hat{\underline{\boldsymbol{u}}}_f$:

$$\boldsymbol{M_c}\begin{pmatrix}\underline{\boldsymbol{u}}^{n+1} \\ \hat{\underline{\boldsymbol{u}}}_f^{n+1}\end{pmatrix} = \begin{pmatrix}\boldsymbol{M}_\rho & \boldsymbol{0} \\ -\hat{\boldsymbol{N}} & \boldsymbol{I}\end{pmatrix}\begin{pmatrix}\underline{\boldsymbol{u}}^{n+1} \\ \hat{\underline{\boldsymbol{u}}}_f^{n+1}\end{pmatrix}, \quad (2.47)$$

where,

$$\boldsymbol{M}_{\rho_{ij}} = \int \rho_f N_i(\boldsymbol{x}) N_j(\boldsymbol{x}) dV \quad \text{is the mass matrix,} \tag{2.48}$$

defining,

$$\boldsymbol{M}_c^{-1} = \begin{pmatrix} \boldsymbol{M}_\rho^{-1} & \boldsymbol{0} \\ \hat{\boldsymbol{N}} \boldsymbol{M}_\rho^{-1} & \boldsymbol{I} \end{pmatrix}, \tag{2.49}$$

and $\underline{\boldsymbol{u}}^{n+1}$ is the vector containing the solution variables for each phase $\boldsymbol{u}_k^{n+1}$, that is:

$$\underline{\boldsymbol{u}}^{n+1} = \left(\boldsymbol{u}_1^{n+1}, \boldsymbol{u}_2^{n+1}, \ldots, \boldsymbol{u}_{\mathcal{P}}^{n+1} \right)^T. \tag{2.50}$$

Thus the pressure equation becomes:

$$\left(\boldsymbol{B}^T \;\; \hat{\boldsymbol{B}}^T \right) \boldsymbol{M}_c^{-1} \begin{pmatrix} \boldsymbol{C} \\ \boldsymbol{0} \end{pmatrix} \underline{\Delta \boldsymbol{p}} = \left(\boldsymbol{B}^T + \tilde{\boldsymbol{B}}^T \hat{\boldsymbol{N}} \right) \boldsymbol{M}_\rho^{-1} \boldsymbol{C} \underline{\Delta \boldsymbol{p}} = -\underline{\boldsymbol{r}}_{cty}^*, \tag{2.51}$$

where,

$$\boldsymbol{C}_{ij} = \int N_i(\boldsymbol{x}) \nabla N_{p_j}(\boldsymbol{x}) dV \quad \text{is the pressure gradient matrix,} \tag{2.52}$$

in which, N_{p_j} are the pressure basis functions. Here we replace $\tilde{\boldsymbol{B}}^T \hat{\boldsymbol{N}}$ with $\hat{\boldsymbol{B}}^T$ which is an approximation and thus the pressure matrix equation becomes:

$$\left(\boldsymbol{B}^T + \hat{\boldsymbol{B}}^T \right) \boldsymbol{M}_\rho^{-1} \boldsymbol{C} \underline{\Delta \boldsymbol{p}} = -\underline{\boldsymbol{r}}_{cty}^*, \tag{2.53}$$

in which $\hat{\boldsymbol{B}}^T \underline{\boldsymbol{u}}^{n+1}$ is a discretization of $\sum_k \left(\nabla \cdot \hat{\alpha}_k^{n+1} \boldsymbol{u}_k^{n+1} \right)$ and $\hat{\alpha}_k^{n+1} = \frac{max\left(\epsilon, \alpha_k^{n+1}\right)}{\sum_k max\left(\epsilon, \alpha_k^{n+1}\right)}$ and thus $\sum_{k=1}^{\mathcal{P}} \hat{\alpha}_k^{n+1} = 1$. Here $\epsilon = 1 \times 10^{-7}$. In addition,

$$\hat{\boldsymbol{N}} = \left(\underline{\underline{\hat{\alpha}}}_1^{n+1} \quad \underline{\underline{\hat{\alpha}}}_2^{n+1} \quad \ldots \quad \underline{\underline{\hat{\alpha}}}_{\mathcal{P}}^{n+1} \right), \tag{2.54}$$

in which $\underline{\underline{\hat{\alpha}}}_k^{n+1}, \forall k \in \{1, 2, ..., \mathcal{P}\}$ are diagonal matrices with entries equal to the control volume values of $\hat{\alpha}_k^{n+1}$ and $\mathcal{P}$ is the number of phases. For a single phase system $\hat{\boldsymbol{N}} = \boldsymbol{I}$.

2.5 Mesh adaptivity

In order to resolve the fluid details in specific areas and without the increase of the computational cost globally, an unstructured anisotropic mesh adaptivity (Mostaghimi *et al.*, 2015) is used here. The mesh is adapted to the solid-fluid interface, fluid-fluid interface and velocity fields.

2.5.1 Mesh adaptivity geometric operations

The mesh adaptivity in 'Fluidity-Multiphase' is based on optimisation, which aims to obtain a new mesh with high quality and low solution error. To define the mesh quality for each individual mesh element Δ_e, a function $Q_m(\Delta_e)$ is introduced. $Q_m(\Delta_e)$ is the function of the mesh edge length and the shape (anisotropy) for each element (Mostaghimi *et al.*, 2015):

$$\boldsymbol{Q}_m(\Delta_e) = \sum_{i \in edges} \left(\boldsymbol{v}_i^T \boldsymbol{M} \boldsymbol{v}_i - 1 \right), \tag{2.55}$$

where, i are the mesh element indices, v_i are vectors representing the edges connecting the vertices of the finite element mesh, and $\boldsymbol{M}$ is the matrix defining the approximate anisotropic interpolation error metric along each element edge (Chen *et al.*, 2007; Loseille & Alauzet, 2011b). The $\boldsymbol{M}$ is given by the following equation:

$$\boldsymbol{M}_{ij} = (det(\boldsymbol{H}))^{-\frac{1}{2\gamma+\chi}} \frac{\boldsymbol{H}_{ij}}{\eta}, \tag{2.56}$$

where $\boldsymbol{H}$ is the Hessian matrix (details can be found in section 2.5.2), γ is the polynomial degree of an element for the chosen norm, χ is the dimension of the mesh, and η represents the expected normalizing tolerance factor in the chosen field.

To generate a mesh with high quality, the $Q_m(\Delta_e)$ is required to reach its minimum value, which represents the mesh thus approximately has a minimum interpolation error. Additionally, some other constraints, such as total mesh node number, mesh node number increase ratio, maximum mesh element edge length, minimum mesh edge length, etc., are implemented in this mesh adaptivity as strong or weak conditions on the function $Q_m(\Delta_e)$ (Farrell, 2011; Pain *et al.*, 2001a).

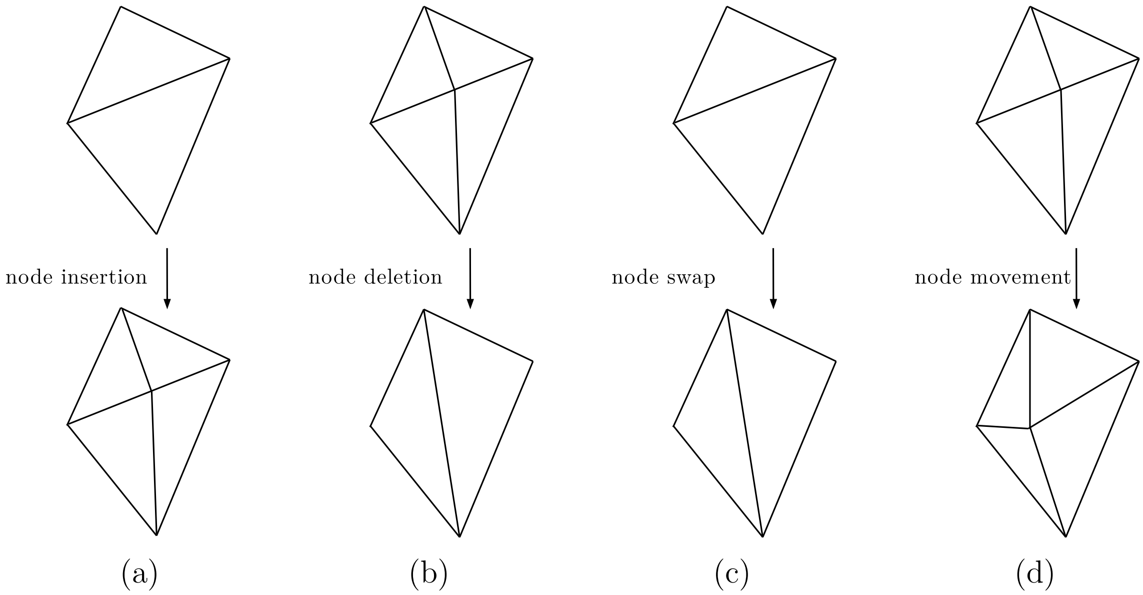

Figure 2.6 Mesh adaptivity geometric operations. (a) node insertion or edge split, (b) node deletion or edge collapse, (c) edge swap, (d) node movement (Piggott *et al.*, 2009).

In order to obtain the minimum interpolation error, four dynamic mesh operations during the mesh adaptivity are implemented. They are node insertion/edge splitting, node deletion/edge collapse, edge swap and node movement (see Fig. 2.6).

2.5.2 Hessian matrix

The Hessian matrix is used in the mesh adaptivity to bound the interpolation error between a smooth field and its piecewise linear interpolation over a fixed mesh. The smooth field and its piecewise linear interpolation over a fixed mesh are represented by $q(x_1, x_2, x_3)$ and $\tilde{q} = \sum_a \tilde{q}_a N_a$, respectively. The Hessian matrix is defined as (Loseille & Alauzet, 2011a):

$$\boldsymbol{H}_{ij} = \frac{\partial^2 q}{\partial x_i \partial x_j}. \tag{2.57}$$

The iterative Galerkin projection of the linear interpolation is used to approximate the Hessian matrix:

$$\sum_a \int N_a N_b dV \frac{\partial \tilde{q}_b}{\partial x_i} = \sum_a \int N_a \frac{\partial}{\partial x_i} \left(N_c \tilde{q}_c\right) DV, \tag{2.58}$$

$$\sum_a \int N_a N_b dV[\tilde{\boldsymbol{H}}_b]_{x_i x_j} = \sum_a \int N_a \frac{\partial}{\partial x_i}\left(N_c \frac{\partial \tilde{q}_c}{\partial x_i}\right) DV. \tag{2.59}$$

The same as Loseille & Alauzet (2011b) have implemented in their work, the mass matrix has been row lumped in equation 2.59.

2.5.3 Consistent and Galerkin projections

The adaptivity geometric operations are used to improve the mesh quality till the quality criterion is as desired. Once the quality criterion based on $Q_m(\Delta_e)$ is obtained, a new mesh is generated. All the variables on the existing mesh will be projected to this new mesh (Farrell, 2011) via consistent projection or Galerkin projections. In the consistent projection, the nodal values are to be the same as the old finite element representation, for instance, at node (x_1, x_2, x_3):

$$\tilde{q}^{new} = \sum_b \tilde{q}_b^{old} N_b^{old}(x_1, x_2, x_3). \tag{2.60}$$

The consistent projection is non-conservative method but bounded. However the Galerkin projection is conservative. It can be expressed as:

$$\int N_a^{new} N_b^{new} \tilde{q}_b^{new} = \int N_a^{new} N_b^{old} \tilde{q}_b^{old}, \tag{2.61}$$

where supermeshing method is used to ensure the projection error is acceptable (Farrell *et al.*, 2009). More details about anisotropic mesh adaptivity can be found in Mostaghimi *et al.* (2015); Pain *et al.* (2001b); Piggott *et al.* (2009); Bull (2013).

2.6 Coupling methodology between the fluid and solid dynamics

2.6.1 Form of the coupling term $\boldsymbol{s}_c$

In order to form the coupling term $\boldsymbol{s}_c$, the momentum equation 2.11 should be written in a discretized form as:

$$\alpha_f \left[\rho_f \left(\frac{\boldsymbol{u}_f^{n+1} - \boldsymbol{u}_f^n}{\Delta t}\right) + \rho_f \boldsymbol{u}_f \cdot \nabla \boldsymbol{u}_f + \nabla(p - \tau) - \boldsymbol{s}_c - \rho_f g k\right] = 0, \tag{2.62}$$

in which, $\rho_f gk$ is the body force $\boldsymbol{B}_f$, and τ is the shear stress. The solid-fluid coupling term can be expressed as $\alpha_f \boldsymbol{s}_c$. This coupling term has the form expressed as a discretized equation for the shell surrounding the solid surface as:

$$\int\limits_{V_s} N_i^s \left(\alpha_f \boldsymbol{s}_c\right)^s dV = \int\limits_{\Gamma_s} N_i^s \tau d\Gamma, \tag{2.63}$$

with say $\left(\alpha_f \boldsymbol{s}_c\right)^s = \sum_j N_j^s \left(\alpha_f \boldsymbol{s}_c\right)_j^s$ and τ just contains the viscous components of force on the surface of the solid. The force $\left(\alpha_f \boldsymbol{s}_c\right)^s$ is then mapped onto the fluid mesh forming $\left(\alpha_f \boldsymbol{s}_c\right)^f = \alpha_s \left(\alpha_f \boldsymbol{s}_c\right)^s$.

Applying the divergence theorem to the product of a scalar function, f, and a non-zero constant vector $\boldsymbol{c}$, the following theorem can be proven:

$$\int\limits_{V} \boldsymbol{c} \cdot \nabla f \, dV = \int\limits_{\Gamma} (\boldsymbol{c} f) \cdot d\Gamma - \int\limits_{V} f (\nabla \cdot \boldsymbol{c}) \, dV. \tag{2.64}$$

By using Equation 2.64, the stress conditions can be discretized as:

$$\begin{aligned} \int\limits_{V} N_i \nabla \cdot \underline{\underline{\tau}} dV &= -\int\limits_{V} N_i \nabla \cdot \underline{\underline{\tau}} dV + \int\limits_{\Gamma_{solid}} N_i n \cdot \underline{\underline{\tau}}_{solid} d\Gamma \\ &= \int\limits_{V} N_i \nabla \cdot \underline{\underline{\tau}} dV + \int\limits_{\Gamma_{solid}} N_i n \cdot \left(\underline{\underline{\tau}}_{solid} - \underline{\underline{\tau}} \right) d\Gamma. \end{aligned} \tag{2.65}$$

Consider for example the part of the $\underline{\underline{\tau}}$ term:

$$\int\limits_{\Gamma} N_i n_x \mu \left(\frac{\partial \boldsymbol{u}}{\partial x}|_{solid} - \frac{\partial \boldsymbol{u}}{\partial x} \right) d\Gamma, \tag{2.66}$$

in which, $\frac{\partial \boldsymbol{u}}{\partial x}|_{solid}$ is the gradient of the fluid velocity in x direction on solid surfaces, and $\frac{\partial \boldsymbol{u}}{\partial x}$ is the gradient of the fluid velocity in x direction in the fluid area near solid surfaces. We can approximate the fluid derivatives next to the solid boundary using:

$$\int\limits_{V} N_{walli} \frac{\partial \boldsymbol{u}}{\partial x}|_{solid} dV = -\int\limits_{V} \frac{\partial N_{walli}}{\partial x} \boldsymbol{u} dV + \int\limits_{\Gamma_{solid}} N_{walli} \boldsymbol{u} d\Gamma. \tag{2.67}$$

Using the solid velocity $\boldsymbol{u}_s$ on the boundary:

$$\int\limits_V N_{walli}\frac{\partial \boldsymbol{u}}{\partial x}|_{solid}dV = -\int\limits_V \frac{\partial N_{walli}}{\partial x}\boldsymbol{u}dV + \int\limits_{\Gamma_{solid}} N_{walli}\boldsymbol{u}_s d\Gamma. \tag{2.68}$$

Then using equation 2.67 in equation 2.68 to obtain:

$$\int\limits_V N_{walli}\frac{\partial \boldsymbol{u}}{\partial x}|_{solid}dV = \int\limits_V N_{walli}\frac{\partial \boldsymbol{u}}{\partial x}|_{solid}dV - \int\limits_{\Gamma_{solid}} N_{walli}n_x\left(\boldsymbol{u}-\boldsymbol{u}_s\right)d\Gamma. \tag{2.69}$$

Using very simplest constant basis functions N_{walli} with Δx_{wall} being the fluid element length scale around the wall and normal to it, then:

$$\frac{\partial \boldsymbol{u}}{\partial x}|_{solid} = \frac{\partial \boldsymbol{u}}{\partial x} - \frac{n_x\left(\boldsymbol{u}-\boldsymbol{u}_s\right)}{\Delta x_{wall}}. \tag{2.70}$$

We can evaluate the terms in equation 2.66 over a thin shell V_{shell} using equation 2.70 to obtain:

$$\int\limits_\Gamma N_i n_x \mu\frac{\partial \boldsymbol{u}}{\partial x}|_{solid}d\Gamma \approx \int\limits_{V_{shell}} N_i n_x\frac{1}{\Delta r}\mu\frac{\partial \boldsymbol{u}}{\partial x}|_{solid}dV \tag{2.71}$$

$$\approx \int\limits_{V_{shell}} N_i n_x\frac{1}{\Delta r}\mu\frac{\partial \boldsymbol{u}}{\partial x}dV + \int\limits_{V_{shell}} N_i n_x n_x\frac{1}{\Delta r\Delta x_{wall}}\mu\left(\boldsymbol{u}_{solid}-\boldsymbol{u}\right)dV. \tag{2.72}$$

Thus

$$\int\limits_\Gamma N_i n_x \mu\left(\frac{\partial \boldsymbol{u}}{\partial x}|_{solid} - \frac{\partial \boldsymbol{u}}{\partial x}\right)d\Gamma \approx \int\limits_{V_{shell}} N_i n_x n_x\frac{1}{\Delta r\Delta x_{wall}}\mu\left(\boldsymbol{u}_{solid}-\boldsymbol{u}\right)dV, \tag{2.73}$$

in which Δr is the width of the thin shell surrounding the solid (see Fig. 2.7).

For the viscous term, by using the slip velocity $\boldsymbol{u}_{sl} = \boldsymbol{u}_s - \boldsymbol{u}$, and gathering the contributions to each velocity component u and v, when the viscosity is isotropic

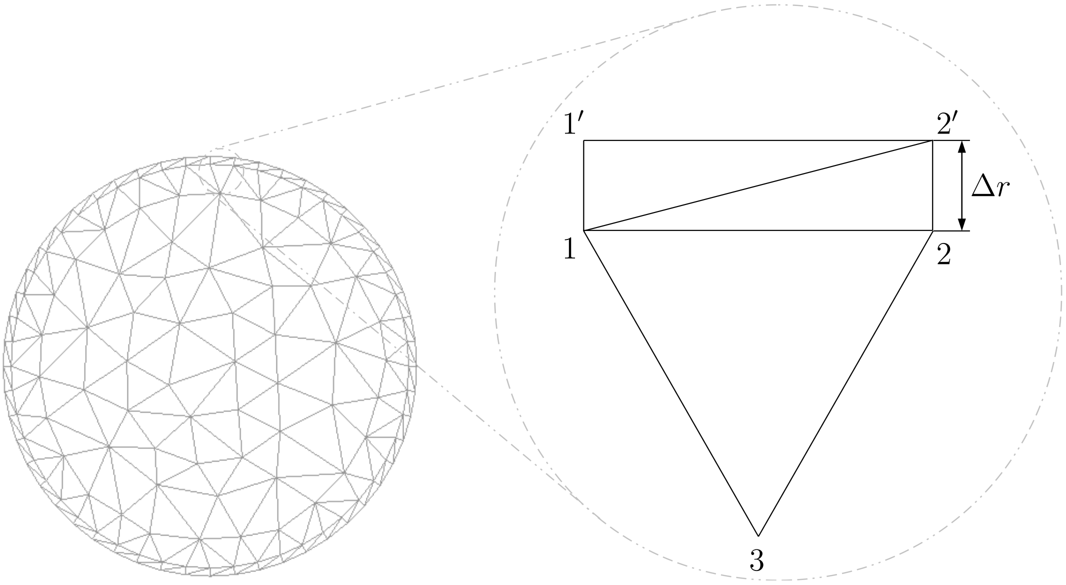

Figure 2.7 Left: the solid mesh with its surrounding shell mesh; right: a 2D solid element with its shell mesh. Δr is the shell thickness. The method to generate the shell mesh can be found in Section 2.6.2.

$\mu = \mu_{xx} = \mu_{xy}...$, it can be expanded for the (u_{sl}, v_{sl}, w_{sl}) as:

$$\begin{aligned}
&\int\limits_{V_{shell}} N_i \frac{\mu}{\Delta r \Delta x_{wall}} \{ \left[n_x \left(2 - \frac{2}{3} \right) n_x + n_y n_y + n_z n_z \right] u_{sl} + \left(-n_x \frac{2}{3} n_y + n_y n_x \right) v_{sl} \\
&\qquad\qquad + \left(-n_x \frac{2}{3} n_z + n_z n_x \right) w_{sl} \} dV; \\
&\int\limits_{V_{shell}} N_i \frac{\mu}{\Delta r \Delta x_{wall}} \{ \left(n_x n_y - n_y \frac{2}{3} n_x \right) u_{sl} + \left[n_x n_x + n_y \left(2 - \frac{2}{3} \right) n_y + n_z n_z \right] v_{sl} \\
&\qquad\qquad + \left(-n_y \frac{2}{3} n_z + n_z n_y \right) w_{sl} \} dV; \\
&\int\limits_{V_{shell}} N_i \frac{\mu}{\Delta r \Delta x_{wall}} \{ \left(n_x n_z - n_z \frac{2}{3} n_x \right) u_{sl} + \left(n_y n_z - n_z \frac{2}{3} n_y \right) v_{sl} \\
&\qquad\qquad + \left[n_x n_x + n_y n_y + n_z \left(2 - \frac{2}{3} \right) n_z \right] w_{sl} \} dV. \qquad (2.74)
\end{aligned}$$

Or in more condensed form - also serving as a definition of coupling viscous coefficients: $a_{xx}, a_{xy}, a_{xz}, ...$ - for (u, v, w):

$$\begin{aligned} f_x^s &= \int\limits_{V_{shell}} N_i \left(a_{xx} u_{sl} + a_{xy} v_{sl} + a_{xz} w_{sl}\right) dV; \\ f_y^s &= \int\limits_{V_{shell}} N_i \left(a_{yx} u_{sl} + a_{yy} v_{sl} + a_{yz} w_{sl}\right) dV; \\ f_z^s &= \int\limits_{V_{shell}} N_i \left(a_{zx} u_{sl} + a_{zy} v_{sl} + a_{zz} w_{sl}\right) dV. \end{aligned} \tag{2.75}$$

Defining,

$$\begin{aligned} f_x^f &= a_{xx} u_s + a_{xy} v_s + a_{xz} w_s; \\ f_y^f &= a_{yx} u_s + a_{yy} v_s + a_{yz} w_s; \\ f_z^f &= a_{zx} u_s + a_{zy} v_s + a_{zz} w_s. \end{aligned} \tag{2.76}$$

then the solid-fluid coupling term $\boldsymbol{s}_c = \left(f_x^f, f_y^f, f_z^f\right)^T$.

2.6.2 Projections between fluid, solid and shell meshes

The fluid velocity, pressure and viscosity coefficient are computed on the fluid mesh, whilst the solid velocity, the coupling term $\boldsymbol{s}_c$, and the coupling viscous coefficients $a_{xx}, a_{xy}, a_{xz}, ...$ are computed on the solid mesh in Section 2.2. In order to complete the coupling algorithm, the fields (fluid velocity, pressure and viscosity coefficient) need to be projected from the fluid mesh onto the shell mesh, and then from there to the solid surface mesh. Meanwhile, the fields (the solid velocity, the coupling term $\boldsymbol{s}_c$, and the coupling viscous coefficients $a_{xx}, a_{xy}, a_{xz}, ...$ need to be projected from the solid surface mesh onto the shell mesh, and then from there onto the fluid mesh. The projection technique between these three meshes is shown in this section.

A supermeshing method (Farrell & Maddison, 2011) is employed, in order to project a field from the shell to fluid mesh. The interactions between the shell and fluid mesh have to be identified when the supermesh method is used (Viré *et al.*, 2015). A Galerkin projection is used to complete the mesh-to-mesh projection. Given a donor mesh D and a target mesh T on a domain Ω, a Galerkin projection on a field q from D to T ensures that:

$$\int\limits_{\Omega} q_D dV = \int\limits_{\Omega} q_T dV, \tag{2.77}$$

by minimizing the L_2 norm of the interaction error (Farrell & Maddison, 2011). Take the solid velocity $\boldsymbol{u}_s$ as an example, by solving the following linear equation:

$$\int\limits_{V} \sum_{j=1}^{n_f} (\boldsymbol{u}_s)_j^f \, N_j^f N_k^f dV = \int\limits_{V_{sh}} \sum_{i=1}^{n_{sh}} (\boldsymbol{u}_s)_i^{sh} \, N_i^{sh} N_k^f dV. \tag{2.78}$$

The projection method used in this thesis is the same as those used in the immersed-body method (Viré *et al.*, 2012, 2015).

After the fluid viscosity being passed to the shell mesh, it needs to be applied on the solid surface. Then the coupling term $\boldsymbol{s}_c$ and the viscosity force $\boldsymbol{F}_v$ can be computed by using equation 2.76 and 2.81 on the solid surface. Similarly, once the solid quantities at the solid surface are mapped to the shell, they need to be projected to the fluid mesh. The following will describe these processes in detail. A shell mesh is constructed directly from the surface of the solid mesh. We can see it from Fig. 2.7, where the triangular element 1-2-3 is a 2D solid element, and 1-2 is its surface. By extruding the surface 1-2 in its normal direction with a shell thickness Δr, the shell mesh is formed. Thus for each surface element at the solid surface in two dimensions, two triangular elements are added to form the shell area mesh, for example, element $1 - 2 - 2'$ and element $1 - 1' - 2'$. In order to ensure that the projection between the inner and outer shell nodes is conservative, the shell thickness is set to be smaller than the solid mesh size. However, for the projection from a shell to a solid surface in two dimensions, the condition is

$$\int\limits_{S_{sh}} q^{sh} dS_{sh} = \int\limits_{L_s} q^{surf} dL_s, \tag{2.79}$$

where L_s presents the surface of the solid. The superscripts notations 'sh' and 'surf' denote the shell mesh and the solid surface mesh respectively. More details of the projection method can be seen in the literature (Viré *et al.*, 2012, 2015).

2.6.3 The theory behind the semi-implicit coupling approach

The coupling is achieved by the coupling term $\boldsymbol{s}_c$. In order to evaluate the coupling term force contribution $\boldsymbol{s}_c$ on the fluid, each of f_x^f, f_y^f, f_z^f is mapped to the fluid mesh. In addition, each of the coupling viscous coefficients $a_{xx}, a_{xy}, a_{xz}, ...$ is mapped to the fluid mesh in order to form the implicit treatment of the fluid velocity.

The discretized force on the solid surface is evaluated from:

$$\boldsymbol{F}_v^s + \boldsymbol{F}_p^s = \int\limits_{\Gamma_{solid}} N_i n \cdot \left(\underline{\underline{\tau}}_{solid} + Ip\right) d\Gamma, \tag{2.80}$$

in which $\underline{\underline{\tau}}_{solid}$ contains just the viscous contributions to the stress term.

As shown in equation 2.72 the individual gradients (that make up the viscous stress tensor $\underline{\underline{\tau}}_{solid}$) can be calculated from:

$$\begin{aligned}\int\limits_{\Gamma_{solid}} N_i n_x \mu \frac{\partial \boldsymbol{u}}{\partial x}|_{solid} d\Gamma &\approx \int\limits_{V_{shell}} N_i n_x \frac{1}{\Delta r} \mu \frac{\partial \boldsymbol{u}}{\partial x} dV + \int\limits_{V_{shell}} N_i n_x n_x \frac{1}{\Delta r \Delta x_{wall}} \mu \left(\boldsymbol{u}_{solid} - \boldsymbol{u}\right) dV \\ &\approx \int\limits_{\Gamma_{solid}} N_i n_x \mu \frac{\partial \boldsymbol{u}}{\partial x} d\Gamma + \int\limits_{\Gamma_{solid}} N_i n_x n_x \frac{1}{\Delta x_{wall}} \mu \left(\boldsymbol{u}_{solid} - \boldsymbol{u}\right) d\Gamma. \end{aligned} \tag{2.81}$$

This integral is used as a discretized surface force in the solid equations.

The steps to implement the two-way solid-fluid coupling for multiphase viscous flows are shown in Fig. 2.8.

As we can see from the coupling steps, the shell mesh play a crucial role in transporting solid consideration, velocity; and fluid velocity, pressure, viscous coefficients between the fluid mesh and the solid mesh. It is a thin intermediate mesh surrounding the solid surface. Since it only includes a layer of mesh, when transporting these coupling fields between the solid mesh and the fluid mesh, the computational costs can be reduced extremely. Moreover, this layer thin shell mesh is very promising for resolving the boundary-layer for flows with high Reynolds numbers between these three meshes (Viré *et al.*, 2015).

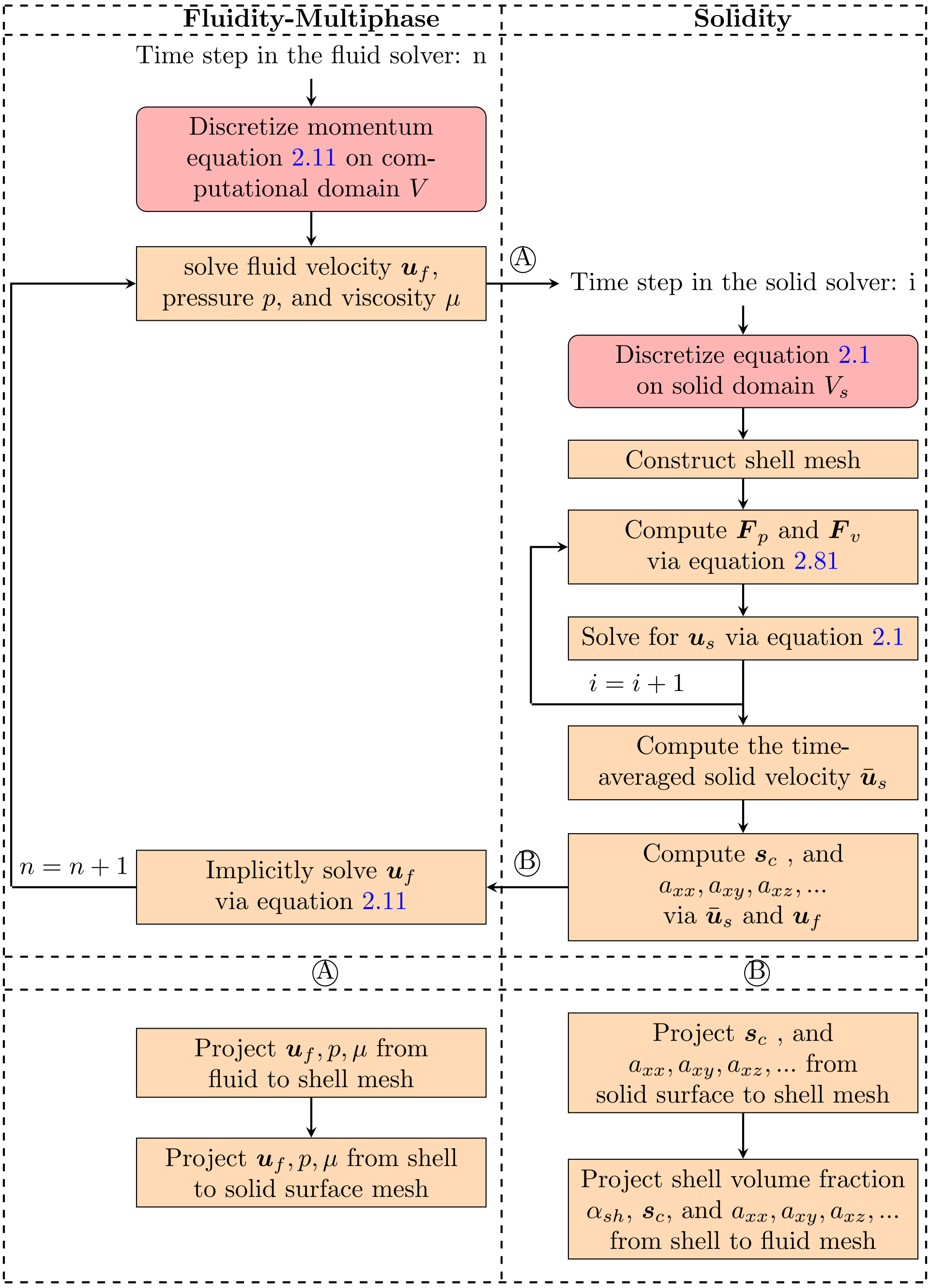
Fluidity-Multiphase
Solidity
Time step in the fluid solver: n
Discretize momentum equation 2.11 on computational domain V
solve fluid velocity $\boldsymbol{u}_f$, pressure p, and viscosity μ
Ⓐ
Time step in the solid solver: i
Discretize equation 2.1 on solid domain V_s
Construct shell mesh
Compute $\boldsymbol{F}_p$ and $\boldsymbol{F}_v$ via equation 2.81
Solve for $\boldsymbol{u}_s$ via equation 2.1
$i = i + 1$
Compute the time-averaged solid velocity $\bar{\boldsymbol{u}}_s$
Compute $\boldsymbol{s}_c$, and $a_{xx}, a_{xy}, a_{xz}, ...$ via $\bar{\boldsymbol{u}}_s$ and $\boldsymbol{u}_f$
Ⓑ
$n = n + 1$
Implicitly solve $\boldsymbol{u}_f$ via equation 2.11
Ⓐ
Ⓑ
Project $\boldsymbol{u}_f, p, \mu$ from fluid to shell mesh
Project $\boldsymbol{u}_f, p, \mu$ from shell to solid surface mesh
Project $\boldsymbol{s}_c$, and $a_{xx}, a_{xy}, a_{xz}, ...$ from solid surface to shell mesh
Project shell volume fraction α_{sh}, $\boldsymbol{s}_c$, and $a_{xx}, a_{xy}, a_{xz}, ...$ from shell to fluid mesh

Figure 2.8 The flow chart of the immersed-body method.

2.7 The coupling algorithm for turbulent flows

2.7.1 The exchange forces on the solid surface

The exchange forces on the solid surface contain the pressure force and shear stress:

$$\boldsymbol{F}_v^s + \boldsymbol{F}_p^s = \int\limits_{\Gamma_{solid}} N_i n \cdot \left(\underline{\underline{\tau}}_{solid} + Ip \right) d\Gamma. \tag{2.82}$$

Combined with the wall function (see section 2.3.2.3), it can be rewritten as

$$\boldsymbol{F}_v^s + \boldsymbol{F}_p^s = \int\limits_{V_{shell}} N \frac{\rho \nu u_s}{y_s \Delta r} dV_{shell} - \int\limits_{V_{shell}} N \frac{q u_f}{\Delta r} dV_{shell} + \int\limits_{\Gamma_{solid}} Ipd\Gamma. \tag{2.83}$$

2.7.2 The coupling steps

The coupling steps for the immersed-body URANS model are shown in the flow chart in Fig. 2.9.

Step 1: Solve the fluid governing Eqs. 2.10 and 2.11 for fluid velocity $\boldsymbol{u}_f$ and pressure p;

Step 2: Solve the $k - \varepsilon$ model at the nonlinear iteration stage, for k and ε. Then update eddy viscosity υ_T;

Step 3: By using the shell mesh external-surface intersection approach (see Section 2.3.3.3), locate the intersection cells. Then get the intersection cell coordinate (x_i, y_i, z_i);

Step 4: Project fluid velocity $\boldsymbol{u}_f$, pressure p, k_f , ε_f, and the intersection cell coordinate (x_i, y_i, z_i) to the shell mesh, and then from here to the solid surface;

Step 5: Compute the wall distance via Eqs. 2.38;

Step 6: Calculate the fluid force on solid by using Eq. 2.83;

Step 7: Solve the solid velocity $\boldsymbol{u}_s$, stress and displacement by using Eq. 2.1;

Step 8: Form the coupling term $\boldsymbol{s}_c$, $\boldsymbol{s}_k$ and $\boldsymbol{s}_\varepsilon$ via Eq. 2.32, 2.35 and 2.36 ;

Step 9: Project the coupling term $\boldsymbol{s}_c$, $\boldsymbol{s}_k$ and $\boldsymbol{s}_\varepsilon$ from solid surface to the shell mesh, and then from here to the fluid mesh. Then go to Step 1.

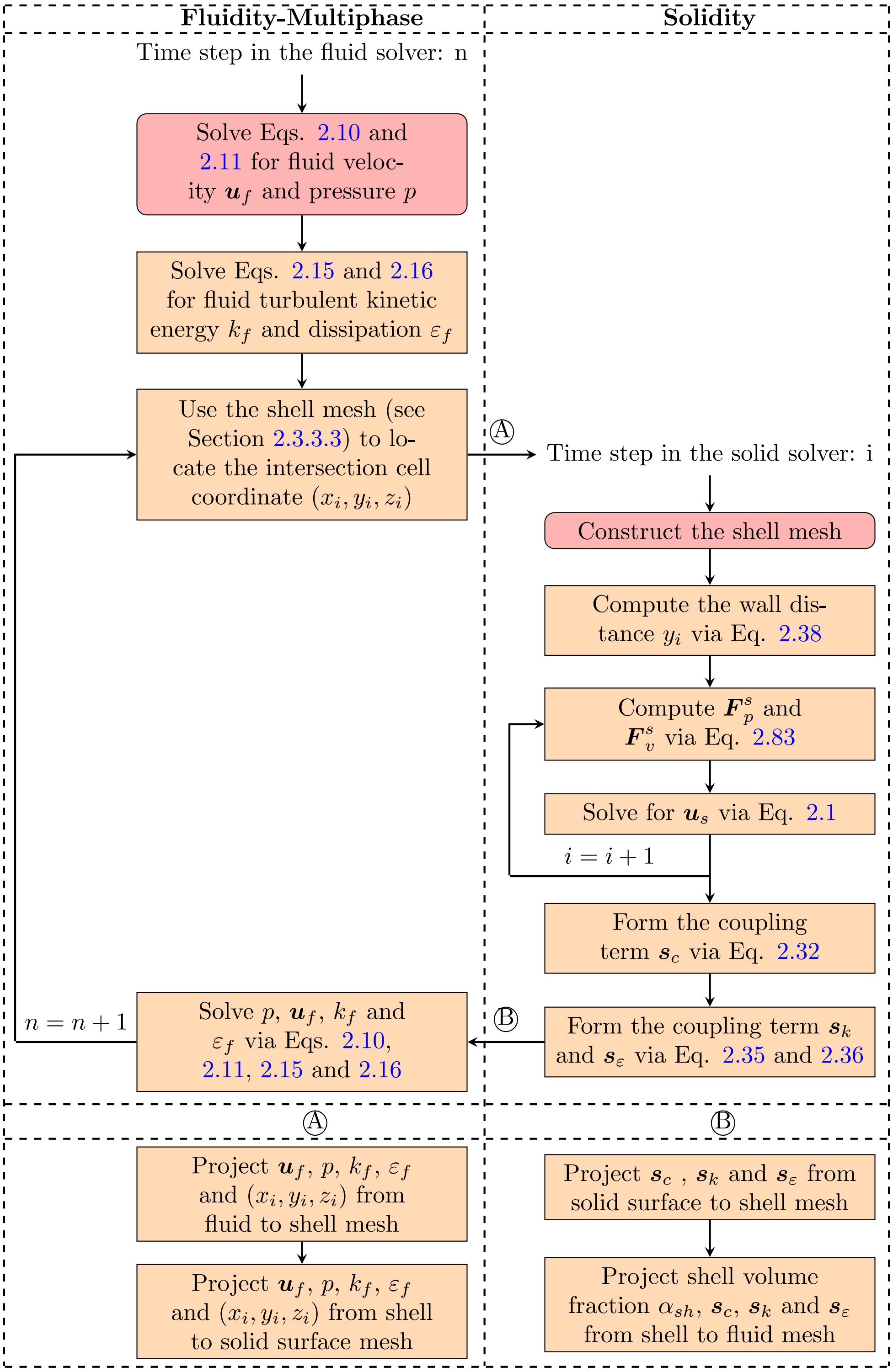
Fluidity-Multiphase
Solidity
Time step in the fluid solver: n
Solve Eqs. 2.10 and 2.11 for fluid velocity $\boldsymbol{u}_f$ and pressure p
Solve Eqs. 2.15 and 2.16 for fluid turbulent kinetic energy k_f and dissipation ε_f
Use the shell mesh (see Section 2.3.3.3) to locate the intersection cell coordinate (x_i, y_i, z_i)
Ⓐ
Time step in the solid solver: i
Construct the shell mesh
Compute the wall distance y_i via Eq. 2.38
Compute $\boldsymbol{F}_p^s$ and $\boldsymbol{F}_v^s$ via Eq. 2.83
Solve for $\boldsymbol{u}_s$ via Eq. 2.1
$i = i + 1$
Form the coupling term $\boldsymbol{s}_c$ via Eq. 2.32
Form the coupling term $\boldsymbol{s}_k$ and $\boldsymbol{s}_\varepsilon$ via Eq. 2.35 and 2.36
Ⓑ
$n = n + 1$
Solve p, $\boldsymbol{u}_f$, k_f and ε_f via Eqs. 2.10, 2.11, 2.15 and 2.16
Ⓐ
Project $\boldsymbol{u}_f$, p, k_f, ε_f and (x_i, y_i, z_i) from fluid to shell mesh
Project $\boldsymbol{u}_f$, p, k_f, ε_f and (x_i, y_i, z_i) from shell to solid surface mesh
Ⓑ
Project $\boldsymbol{s}_c$, $\boldsymbol{s}_k$ and $\boldsymbol{s}_\varepsilon$ from solid surface to shell mesh
Project shell volume fraction α_{sh}, $\boldsymbol{s}_c$, $\boldsymbol{s}_k$ and $\boldsymbol{s}_\varepsilon$ from shell to fluid mesh

Figure 2.9 The flow chart of the immersed-body URANS model. The left part is the loop in fluid solver (Fluidity-Multiphase), and the right part is the loop in solid solver (Solidity).

2.8 Concluding remarks

This chapter presents a novel immersed-body model, which combined a dynamic solid model (FEMDEM) and a multiphase viscous fluid model (Fluidity-Multiphase). This model is capable of resolving FSI for incompressible, compressible and turbulent flows. In this model, a coupling term containing the fluid stresses is introduced within a thin shell mesh surrounding the solid surface. In this shin shell, the boundary conditions of the solid surface for the turbulence model and the momentum equation are implemented. As well as a log-law wall function is used in this thin shell to reduce the computational cost when resolving the boundary layers near the solid surface. A novel shell mesh external-surface intersection approach is introduced to produce the sharp interfaces between the solids and fluids, which ensures the accuracy of the wall function. An advanced anisotropic mesh adaptivity is applied in unstructured meshes to improve the performance of the presented immersed-body URANS turbulence model by using relatively less number of cells compared to those methods that are using fixed meshes. The following chapters are going to present the benchmark, validation and application cases for the developed FSI model from incompressible, compressible to turbulent flows.

Chapter

THREE

Incompressible flow FSI model

In the previous chapter, the FSI model for incompressible flows has been developed. In order to validate this model for incompressible flows, several test cases are set up and described in this chapter. Two benchmark test cases, a free falling circular cylinder in a fluid at rest and a free falling sphere, are set up at first. Then a collapsing column of water moving an initially stationary solid square and an elastic membrane test cases are presented. The mesh sensitivity analysis is given out in test cases: a free falling circular cylinder in a fluid at rest and an elastic membrane. Finally, the fifth simulation example is of a water-air interface with a floating solid square being moved around by complex hydrodynamic flows including wave breaking. The results show that the immersed-body method is an effective approach for two-way solid-fluid coupling in multiphase viscous flows.

3.1 Introduction

This chapter focuses on solid-fluid coupling validation and application for incompressible flows. By using an advanced interface capturing method here (Pavlidis *et al.*, 2016), the overall method has the capability to tackle problems with fluid-solid interfaces and multiphase flow interfaces.

The remainder of this chapter is organised as follows. Section 3.2 presents the test case: a free falling circular cylinder in a fluid at rest. A free falling sphere test case is given in section 3.3. A collapsing column of water moving an initially stationary solid square is presented in Section 3.4. Section 3.5 shows the mesh sensitivity analysis test case: an elastic membrane. A floating solid square simulation is also presented in Section 3.6. The list of the test cases in this chapter is shown in Table 3.1. The mesh sensitivity analysis is given out in section 3.2 and 3.5. I discuss the strength and weaknesses of this approach and draw conclusions in Section 3.7.

In all the test cases, the finite element pair, $P1_{DG} - P2$ (Cotter *et al.*, 2009), is used. This means the velocity is approximated by discontinuous linear finite element functions, whilst the pressure is approximated by continuous quadratic finite element functions. This makes the velocity has the first order spatial-discretization accuracy, whilst the pressure has the second order spatial-discretization accuracy.

Table 3.1 Incompressible flow test cases

Section	Case name	Case purpose
Section 3.2	A free falling circular cylinder in a fluid at rest	Validation & Mesh sensitivity analysis
Section 3.3	A free falling sphere	Validation
Section 3.4	A collapsing column of water moving an initially stationary solid square	Validation
Section 3.5	An elastic membrane	Mesh sensitivity analysis
Section 3.6	The water-air interface with a floating solid square	Application

3.2 A free falling circular cylinder in a fluid at rest

The benchmark test case, a free falling circular cylinder with density ρ_s in a fluid with density ρ_f and viscosity μ at rest is revisited since there are many available references in the literature (Gibou & Min, 2012; Glowinski *et al.*, 1999; Robinson-Mosher *et al.*, 2011; Cate *et al.*, 2004; Wang *et al.*, 2008; Glowinski *et al.*, 2001; Jayaweera & Mason, 1965).

3.2.1 The test case set up and the semi-empirical solution

In this validation test case, an infinite section of the solid cylinder perpendicular to the motion direction, this problem is easy to be treated in two-dimension. The fluid domain is 2.5×18.5, and the radius of the circular cylinder r =0.125 (see Fig. 3.1). The centre of the circular cylinder is located at (1.25, 18). The falling circular cylinder reaches the terminal velocity when gravitational force is balanced by the buoyancy and drag force. The buoyancy force is calculated by the pressure integral over the surface of the solid. The drag force is formed by equation 2.81.

For the drag force, the drag coefficient C_D is employed to evaluate it. There are many experiments measuring the C_D of flow passing long cylinders in the literature (Pruppacher *et al.*, 1970). Clift *et al.* (2005) approximated these experimental data using the following equations:

$$\begin{aligned}
C_D &= 9.689Re^{-0.78}\left(1+0.147Re^{0.82}\right), && 0.1 \leq Re \leq 5;\\
C_D &= 9.689Re^{-0.78}\left(1+0.227Re^{0.55}\right), && 5 \leq Re \leq 40;\\
C_D &= 9.689Re^{-0.78}\left(1+0.0838Re^{0.82}\right), && 40 \leq Re \leq 400. \qquad (3.1)
\end{aligned}$$

Gabitto & Tsouris (2008) introduced an expression of the relationship between terminal velocities and C_D for non-spherical particles as:

$$U_t = \sqrt{\frac{2m_s g\left(\rho_s - \rho_f\right)}{\rho_f \rho_s A_s C_D}}, \qquad (3.2)$$

where U_t is the terminal velocity, C_D is the solid particle drag coefficient based on the projection area, m_s is the particle mass, ρ_s is the solid particle density, ρ_f

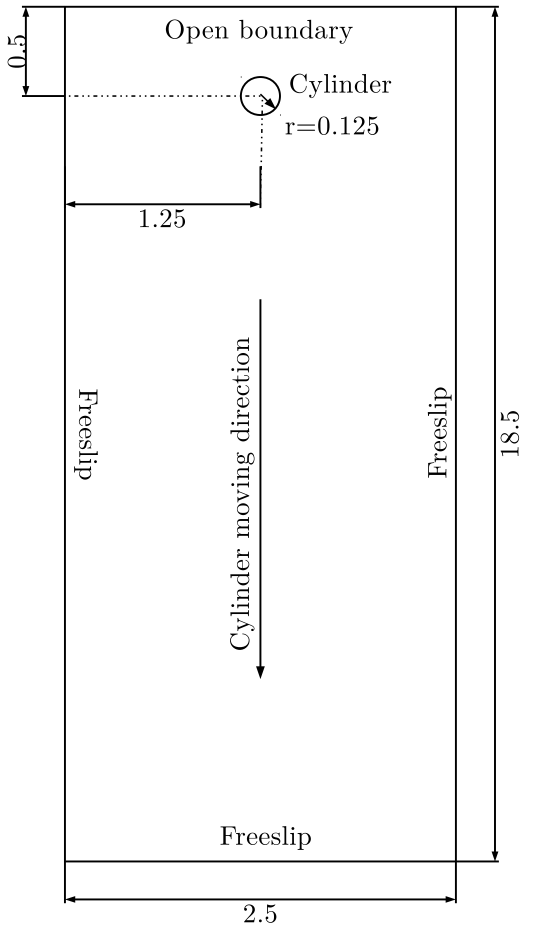
Open boundary
0.5
Cylinder
r=0.125
1.25
Cylinder moving direction
Freeslip
Freeslip
18.5
Freeslip
2.5

Figure 3.1 The computational domain of the free falling circular cylinder case.

is the density of the surrounding fluid, A_s is the projected area of the particle in the direction of motion, and g is the gravitational acceleration constant. In this benchmark test case, $m_s = \rho_s \pi r^2$ and $A_s = 2r$, where the circular cylinder axis remains horizontal during falling and has unit length ($L = 1$). The Reynolds number for the circular cylinder is expressed as

$$Re = \frac{2rU_t}{\nu}, \tag{3.3}$$

where ν is the kinematic viscosity of the fluid.The terminal velocity U_t, Reynolds number Re and drag coefficient C_D can be computed by combining equations 3.1 , 3.2, and 3.3. This semi-empirical solution is used to validate current results obtained by the present immersed-body method.

3.2.2 The results for different fluid-solid density ratios and Reynolds numbers

In Table 3.2, Δr is the shell mesh thickness and l_e is the minimum fluid mesh size. For all the cases, the maximum fluid mesh size L_e is set as 0.06. The relative error between the terminal velocities calculated by the immersed-body method, U_t^{is}, and semi-empirical value U_t^{sf} is defined as

$$E_r^{Ut} = \frac{U_t^{is} - U_t^{sf}}{U_t^{sf}}. \tag{3.4}$$

For all the cases, the Courant number is fixed at $CFL = u\Delta t/\Delta l = 0.5$. As we can see, at the beginning of the simulation, the fluid velocity u is very small. When the CFL number is fixed at 0.5, the Δt can be very large. This will result in large initial values. In order to avoid this situation, the largest time step is limited to $\Delta t = 10^{-2}$. For $\rho_s/\rho_f = 2.0$ (Y020 series in Table 3.2), the relative errors are +0.0456 (Re=21.21), -0.0044 (Re=99.52), and -0.0232 (Re=195.23). As the Reynolds number increases, the relative error becomes bigger. This situation is more obvious in the larger fluid-solid density ratio cases (Y040 and Y060 series in Table 3.2). This difference could be caused by the lack of turbulence models, which results in the overestimation of the drag force on the solid surface. In return, the larger drag force causes the lower terminal velocities. However, despite the absence of turbulence models, the relative errors in all the cases are between -0.0368 and +0.0456.

Table 3.2 Free falling circular cylinder test cases for different ρ_s/ρ_f.

Case	ρ_s/ρ_f	ν	Re	Δr	l_e	U_t^{sf}	U_t^{is}	E_r^{Ut}
Y020-020	2.0	0.017173	21.21	0.0005	0.005	1.3935	1.4570	+0.0456
Y020-100	2.0	0.004401	99.52	0.0005	0.005	1.7599	1.7522	-0.0044
Y020-200	2.0	0.002278	195.23	0.0005	0.005	1.8216	1.7793	-0.0232
Y040-020	4.0	0.029673	20.69	0.0005	0.005	2.3991	2.4552	+0.0234
Y040-100	4.0	0.007621	98.34	0.0005	0.005	3.0457	2.9982	-0.0156
Y040-200	4.0	0.003946	192.41	0.0005	0.005	3.1534	3.0373	-0.0368
Y060-020	6.0	0.038404	20.76	0.0005	0.005	3.0998	3.1883	+0.0286
Y060-100	6.0	0.009852	98.53	0.0005	0.005	3.9325	3.8831	-0.0126
Y060-200	6.0	0.005096	194.60	0.0005	0.005	4.0727	3.9666	-0.0261

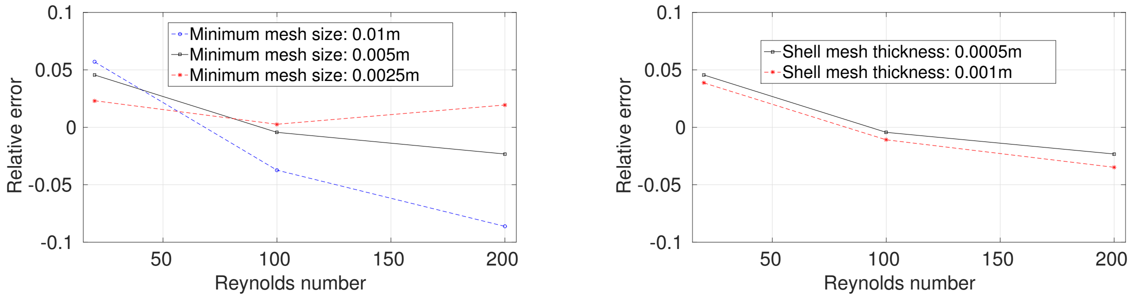

(a) Relative errors for different fluid mesh sizes

(b) Relative errors for different shell mesh thicknesses

Figure 3.2 Relative errors between the terminal velocities calculated by the immersed-body method, U_t^{is}, and semi-empirical value U_t^{sf} for different mesh sizes of the free falling circular cylinder cases.

3.2.3 Mesh size sensitivity analysis

In order to evaluate the effect of fluid mesh size on numerical solutions, two series of tests (Yc20 and Yf20) have been performed. In the series Yf20, the fluid mesh size is smaller than that in Y020 series, whilst the fluid mesh size in the series Yc20 is larger than that in Y020 series. Comparing results from these three series in Table 3.3, although the mesh sizes are different, the terminal velocities are almost the same (see Fig. 3.2a). The conservation of the terminal velocities for the series Yc20, Y020 and Yf20 indicate that this immersed-body method is not affected by the fluid mesh size.

Table 3.3 Free falling circular cylinder test cases for mesh sensitivity analysis.

Case	ρ_s/ρ_f	ν	Re	Δr	l_e	U_t^{sf}	U_t^{is}	E_r^{Ut}
Yc20-020	2.0	0.017173	21.51	0.0005	0.01	1.3982	1.4778	+0.0569
Yc20-100	2.0	0.004401	95.99	0.0005	0.01	1.7555	1.6900	-0.0373
Yc20-200	2.0	0.002278	182.17	0.0005	0.01	1.8169	1.6602	-0.0862
Yf20-020	2.0	0.017173	20.61	0.0005	0.0025	1.3840	1.4161	+0.0232
Yf20-100	2.0	0.004401	100.28	0.0005	0.0025	1.7608	1.7655	+0.0027
Yf20-200	2.0	0.002278	204.07	0.0005	0.0025	1.8244	1.8599	+0.0194
Yr20-020	2.0	0.017173	21.03	0.001	0.005	1.3906	1.4443	+0.0387
Yr20-100	2.0	0.004401	98.83	0.001	0.005	1.7590	1.7399	-0.0109
Yr20-200	2.0	0.002278	192.83	0.001	0.005	1.8208	1.7573	-0.0348

The shell mesh in this immersed-body method is a thin intermediate mesh between the fluid and solid meshes to transport the coupling fields, such as the fluid pressure, velocity and viscosity; and the solid velocity. This shell mesh is crucial for the coupling procedure. To evaluate the effect of the shell mesh size, test series Yr20 is introduced. As we can see from Table 3.3, the shell mesh thickness in the test series Yr20 is twice of that in test series Y020. However, the terminal velocities in these two test series are very close (see Fig. 3.2b). Moreover, the relative errors in these two series are within -0.034 and +0.0456.

3.2.4 Vortex shedding behind a circular cylinder

Figs. 3.3 and 3.4a show the mesh, velocity and non-hydrostatic pressure of Y020-200 and Y040-200 cases respectively. The vortices behind the moving circular cylinder are obvious. This indicates that this immersed-body method is able to capture the viscous behaviour of the fundamental FSIs effectively. For the non-hydrostatic pressure, it is indicated that the positive pressure appears at the front of the moving circular cylinder, whilst it is negative at the sides of the circular cylinder. This matches the fluid mechanism very well.

Table 3.4 Free falling circular cylinder test cases for vortex comparison.

Case	ρ_s/ρ_f	ν	Re	Δr	l_e	U_t^{sf}	U_t^{is}	E_r^{Ut}
Yf20-200	2.0	0.002278	204.07	0.0005	0.0025	1.8244	1.8599	+0.0194
Af20-100	2.0	0.002278	216.16	0.0005	0.0025	1.8610	2.0124	+0.0777

In this thesis, the coupling term $\boldsymbol{s_c}$ includes fluid stresses. This is more complicated than that in (Viré *et al.*, 2015). In that literature, the authors have implemented an coupling term, which is $\frac{\rho}{\Delta t}\alpha_{sh}(\boldsymbol{u}_f - \boldsymbol{u}_s)$. In order to compare our immersed-body method with the one in that literature, two more test cases are implemented. They are Yf20-200 and Af20-200. Yf20-200 is using our immersed-body approach, whilst the Af20-200 is using the immersed-body method in that literature. To make the present model be equated to the approach in that literature, the coupling term $\boldsymbol{s}_c$ in section 2.6.1 has been changed as follows. First, the a_{xy} and a_{yx} are set to 0.0. Then, the a_{xx} and $a_{yy}$are given the same value, which is $\frac{\rho}{\Delta t}$. This modified model has been used in the test case Af20-200.

In Table 3.4, the parameters for the two test cases Yf20-200 and Af20-200 are listed. For these two test cases, the CFL number is fixed at 0.5. All initial conditions for

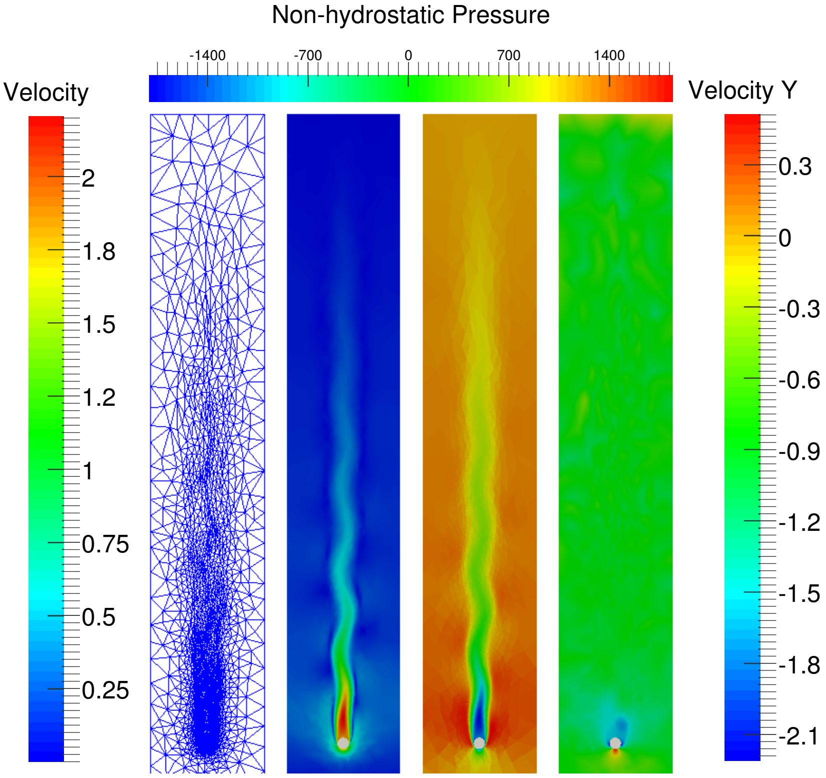

Figure 3.3 Falling circular cylinder: $\rho_s/\rho_f = 2.0$, Re=195.23, mesh (left), velocity (middle-left), velocity in y direction (middle-right), non-hydrostatic pressure (right). This test case is dimensionless. The velocity bar here represents ds/dt, where ds is the spatial motion length in a finite time period dt.

these two test cases are the same. From Table 3.4, we can see that the present model has achieved somewhat more accurate terminal velocity than that obtained by the immersed-body method in (Viré *et al.*, 2015).

Most importantly, the comparison of the vortex shedding in the two cases indicates that the fluid-stress coupling term can resolve more of the viscous behaviour than the coupling term in (Viré *et al.*, 2015). For the free falling circular cylinder in a fluid at rest test case, vortex shedding should be apparent when the Reynolds number is about 200 (Feng *et al.*, 1994; Yu *et al.*, 2002). Fig. 3.4b shows the vortex shedding for these two cases. It is clear that there is vortex shedding behind the circular cylinder in Yf20-200, whilst less in Af20-200. This implies that the use of fluid-stress coupling term $\boldsymbol{s}_c$ can improve the capture of viscous behaviour for FSIs.

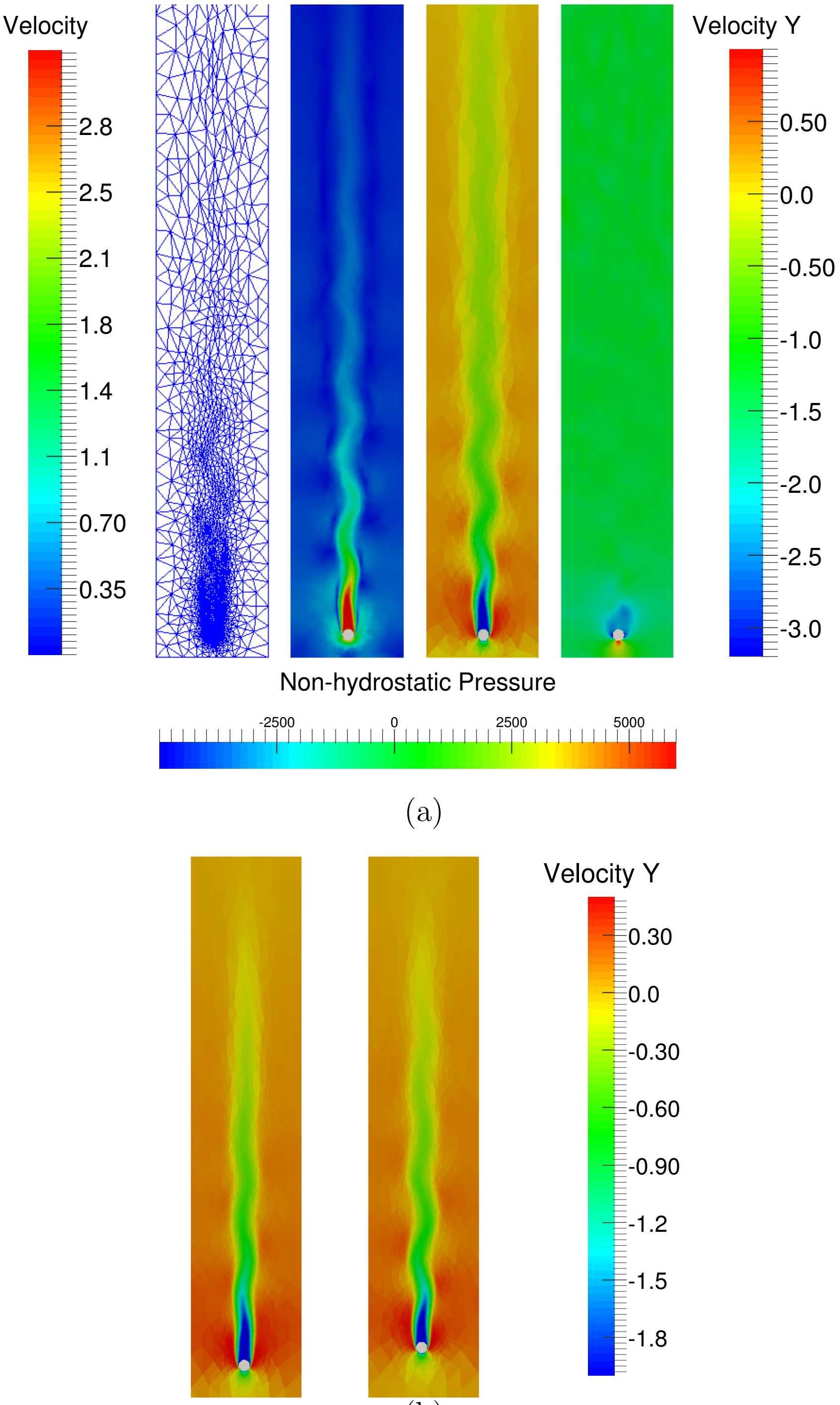

(a)

(b)

Figure 3.4 (a) Falling circular cylinder: $\rho_s/\rho_f = 4.0$, Re=192.41, mesh (left), velocity (middle-left), velocity in y direction (middle-right), non-hydrostatic pressure (right). (b) The velocity in the y direction of the falling circular cylinder cases: $\rho_s/\rho_f = 2.0$, Af20-200 (left), Yf20-200 (right). This test case is dimensionless. The velocity bar here represents ds/dt, where ds is the spatial motion length in a finite time period dt.

3.3 A free falling sphere

3.3.1 A free falling sphere at Re = 7, 20 and 100

This benchmark test case is a free falling sphere in a fluid at rest. In this case, the sphere reaches its terminal velocity when the gravity, buoyancy and drag forces are balanced with each other. The evolution of the sphere velocity can be calculated through a semi-analytical motion equation of the sphere (Clift *et al.*, 2005):

$$(\rho_f - \rho_s)gV_s = \frac{1}{2}\rho_f A C_D u_s^2 + 6\rho_f R^2\sqrt{\pi\nu}\int_0^t \frac{1}{\sqrt{t-s}}\frac{du_s(s)}{dt}ds + (m_s + m_a)\frac{du_s}{dt}, \quad (3.5)$$

where ρ_s is solid density, g is the gravity coefficient, V_s is the solid volume, A is the sphere cross-sectional area, C_D is the drag coefficient, R is the radius of the sphere, ν is the kenimatic viscosity of the fluid, s is the time between 0 and t, $u_s(s)$ is the solid velocity at $t = s$, $m_s = \rho_s V_s$ is the mass of the sphere, $m_a = C_m \rho_f V_f$ is the virtual mass, which is contributed by respected fluid to the accelerating sphere. C_m is the virtual mass coefficient and it is set to 0.5. The left term in Eq. 3.5 is the difference between buoyancy and the gravity forces. The first right-hand term in Eq. 3.5 represents the drag force on the sphere. The drag coefficient C_D is given by the following experimental data fitting equation (Brown & Lawler, 2003):

$$C_D = \frac{24}{Re}(1 + 0.15Re^{0.681}) + \frac{0.407}{1.0 + 8710/Re}. \quad (3.6)$$

The drag force balances the gravity and buoyancy forces when the sphere reaches its terminal velocity. The second right-hand term is called as the Basset force (Mei, 1994). In this work, the semi-analytical solution of the sphere velocity evolution is computed by solving Eq. 3.5 via 4th Runge-Kutta method. The presented method is validated by this semi-analytical solution at low Reynolds numbers.

The computational domain with dimensions $10D \times 10D \times 75D$ is shown in Fig. 3.5a. The centre of the sphere is initially set at $5D$ to the top, left, right, front and back of the domain. The top surface of this computational domain is given the open boundary condition, other surfaces: bottom, right, left, front and back of the domain are all given free-slip boundary conditions. Adaptive fluid meshes are used in this test case with the maximum and minimum mesh edge length $L_{max} = 5D$ and

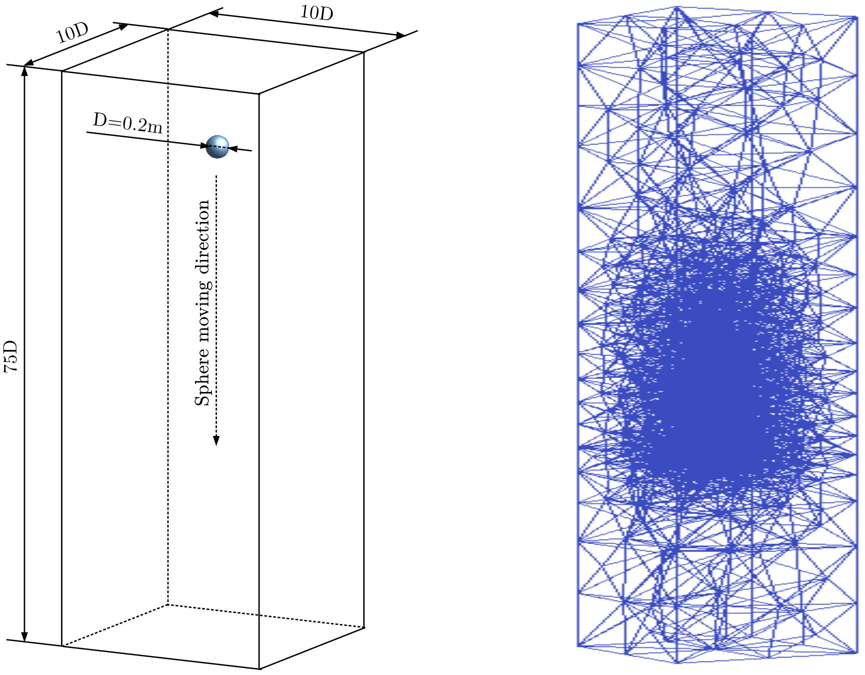

(a) (b)

Figure 3.5 (a) The computational domain of the falling sphere test case, (b) The computational mesh of the falling sphere test case.

$L_{min} = 0.025D$, respectively (see Fig. 3.5b). The Reynolds number (Re) for this case is defined as:

$$Re = \frac{U_t D}{\nu}, \tag{3.7}$$

where U_t is the terminal velocity of the sphere.

Table 3.5 Free falling sphere test cases for different m^*.

Case	m^*	ν	Re	U_t^{sf}	U_t^{is}	E_r^{Ut}
YS040-007	2.0	1.912×10^{-2}	7	-0.6396	-0.6710	0.0491
YS040-020	2.0	9.63×10^{-3}	20	-0.9216	-0.9825	0.0661
YS040-100	2.0	3.01×10^{-3}	100	-1.4508	-1.5200	0.0477
YS020-007	4.0	3.346×10^{-2}	7	-1.1324	-1.1600	0.0243
YS020-020	4.0	1.686×10^{-2}	20	-1.6313	-1.6800	0.0299
YS020-100	4.0	5.25×10^{-3}	100	-2.5602	-2.6200	0.0234

The comparison of the sphere velocity history between the semi-analytical solutions and the simulation results obtained by the present method are shown in Fig. 3.6.

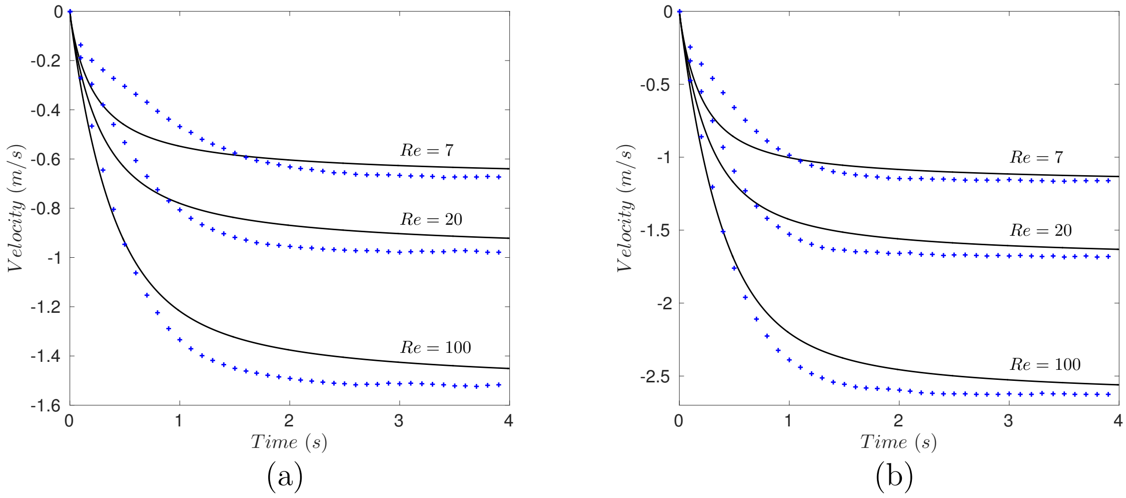

Figure 3.6 The comparison of the sphere velocity history between the semi-analytical solutions and the simulation results obtained by the present method. The solid back continuous lines are the semi-analytical solutions and the blue plus symbols are numerical results using the present model. (a) Velocity histories at $m^* = 2.0$, (b) Velocity histories at $m^* = 4.0$.

The velocity histories of three low Reynolds numbers: Re=7, 20 and 100 are given in this Figure. The relative error between the semi-analytical solutions and the simulation results

$$E_r^{Ut} = \frac{U_t^{is} - U_t^{sf}}{U_t^{sf}}, \tag{3.8}$$

where U_t^{if} is the semi-analytical terminal velocity and U_t^{is} is the simulated terminal velocity. The density ratio between the sphere and the fluid is defined as:

$$m^* = \frac{\rho_s}{\rho_f}. \tag{3.9}$$

The velocity history comparison details for $m^* = 4.0$ and $m^* = 2.0$ are listed in Table 3.5. The absolute values of all relative errors are less than 0.067. This indicates the present model has accurate computing at low Reynolds number regime.

3.3.2 A free falling sphere at Re = 450, 620, 1200 and 1800

In order to validate the performance of this model at moderate Reynolds numbers, the falling sphere test cases with Re = 450, 620, 1200 and 1800 are carried out in

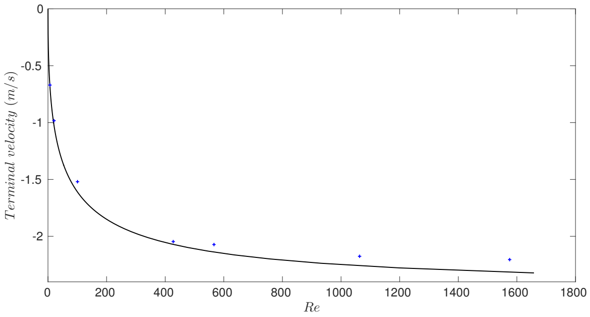

Figure 3.7 The terminal velocity against the Reynolds number for the falling sphere test cases. The solid black line is the empirical solution and the blue star line is the results obtained from the presented model.

this section.

In (Brown & Lawler, 2003), an experimental data fitting equation of the terminal velocities for setting spheres are given as:

$$U^t = \frac{\left[\left(\frac{18}{d_*^2}\right)^{((0.936d_*+1)/(d_*+1))0.898} + \left(\frac{0.317}{d_*}\right)^{0.449}\right]^{-1.114}}{\left[\frac{\rho_f}{g\nu(\rho_s-\rho_f)}\right]^{\frac{1}{3}}}, \tag{3.10}$$

where $d_* = D\left[\frac{g(\rho_s-\rho_f)}{\rho_f\nu^2}\right]^{\frac{1}{3}}$. Combining Eq. 3.10 and 3.7, an empirical relation between Reynolds numbers and sphere terminal velocities can be obtained (see Fig. 3.7). The terminal velocities for different Reynolds numbers achieved by the present model are also drawn on Fig. 3.7. They show good agreement with the empirical curve.

Additionally, the near weak structures obtained by the present model are compared with the experimental PIV measurements in (Horowitz & Williamson, 2010) (see Fig. 3.8 and 3.9) at $Re = 450$, 620, 1200 and 1800. As the Reynolds number increases, the vortex shedding pattern changes. In order to describe the vortex shedding pattern, the three-dimensional vortex criterion proposed by Hunt *et al.* (1988) is used in this work. This criterion is called as the Q-criterion and defined as:

$$Q = \frac{1}{2}\left[|\boldsymbol{\Omega}|^2 - |\boldsymbol{S}|^2\right] > 0, \tag{3.11}$$

where $\boldsymbol{\Omega}$ and $\boldsymbol{S}$ are vorticity and the rate-of-strain tensor, respectively. $\boldsymbol{\Omega}$ and $\boldsymbol{S}$

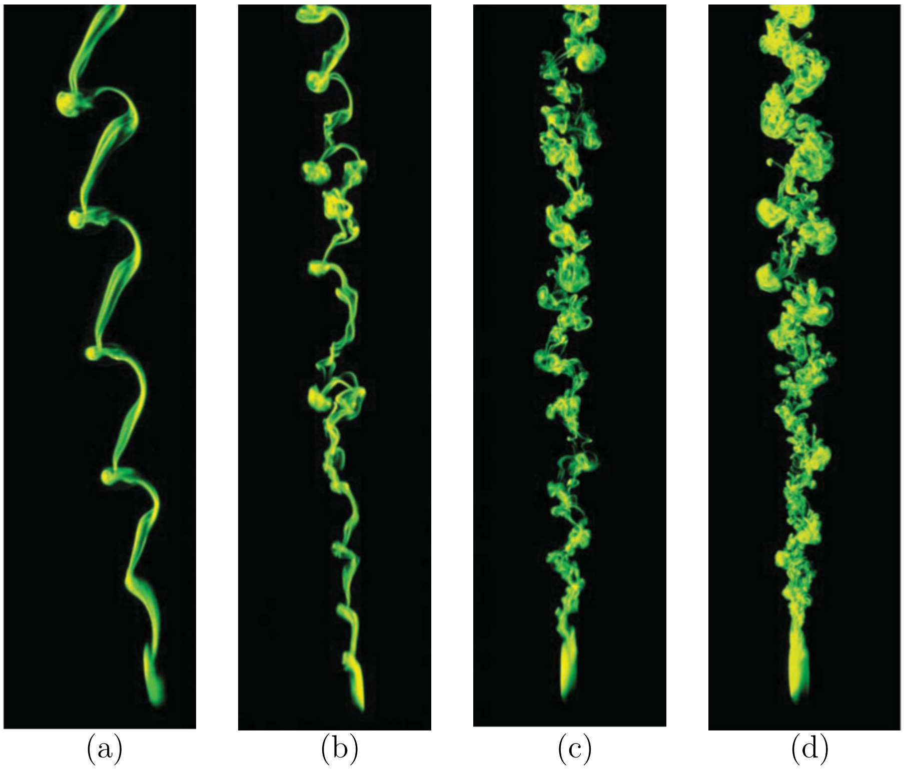
(a) (b) (c) (d)

Figure 3.8 Wakes of freely falling spheres in the experiment (Horowitz & Williamson, 2010). (a) $Re = 450$. (b) $Re = 620$. (c) $Re = 1200$. (d) $Re = 1800$.

are derived from the velocity gradient decomposition equation as follow:

$$\nabla \boldsymbol{u} = \boldsymbol{\Omega} + \boldsymbol{S}, \tag{3.12}$$

Where,

$$\begin{cases} \boldsymbol{\Omega} = \frac{1}{2}\left[\nabla \boldsymbol{u} - (\nabla \boldsymbol{u})^T\right]; \\ \boldsymbol{S} = \frac{1}{2}\left[\nabla \boldsymbol{u} + (\nabla \boldsymbol{u})^T\right]. \end{cases} \tag{3.13}$$

Fig. 3.9 shows the Q-criterion obtained by the present model. In Figs. 3.8a and 3.9a, the periodic ‘R’ mode is observed in both the PIV measurements and the simulations using the present model at $Re = 450$. The ‘R’ mode is defined as one vortex ring forming at every wavelength of wake formation (Horowitz & Williamson, 2010). When Re increases to 600, non-periodic mode appears in Fig. 3.8b and 3.9b. These non-periodic shedding also observed at $Re = 1200$ (see Fig. 3.8c and 3.9c).

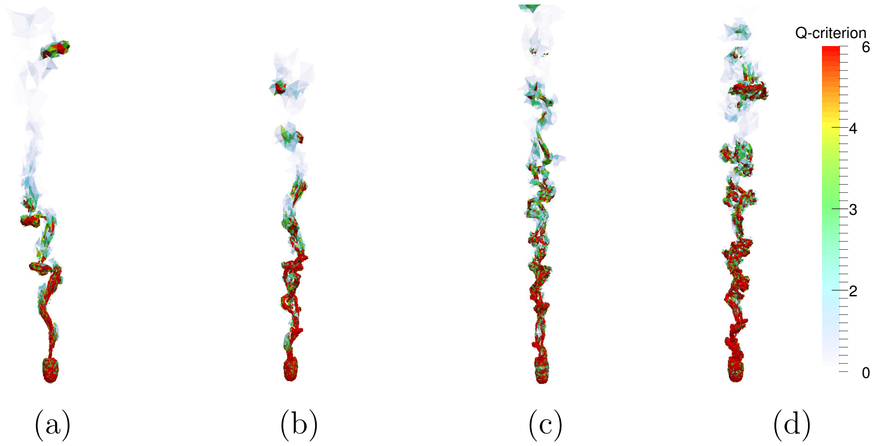

(a) (b) (c) (d)

Figure 3.9 Wakes of freely falling spheres obtained by the present model. The weaks shown here are Q-criterion. (a) $Re = 450$. (b) $Re = 620$. (c) $Re = 1200$. (d) $Re = 1800$.

However, the periodic weak appears again when the Re=1800 (see Fig. 3.8d and 3.9d). The representatives of these different weak patterns in these simulations indicate the present model is capable of accurately capturing the physics of the interaction between moving solids and flows.

Since the sphere terminal velocities match with the empirical fitting curve and the near weak patterns are comparable with the PIV measurements, the model developed here is suitable to simulate solid-fluid interaction at moderate Reynolds numbers.

3.4 A collapsing column of water moving an initially stationary solid square

For multiphase flows, the numerical results of a collapsing column of water moving an initially stationary solid square were compared with the laboratory experiment data in the literature (Kawasaki & Mizutani, 2007). This experiment demonstrated a collision between collapsing water and an initially stationary rigid solid square in an acrylic tank. The dimensions of the water tank are 1.15 m in length, 0.40 m in height and 0.20 m in width. There are two areas in the water tank, a reservoir and inundation area used to set a thin vertical gate. The initial water in the reservoir was set to 0.20 m in depth and 0.15 m in length. An initially stationary 0.04 m solid square was set at a distance of 0.70 cm from the front of the gate. In addition, there are three pressure gauges locating at 0.01 m, 0.02 m, and 0.03 m from the bottom, respectively (more details can see from literature (Kawasaki & Mizutani, 2007)). The initial values of materials are shown on Table 3.6.

Table 3.6 Initial values of materials from literature (Kawasaki & Mizutani, 2007).

Materials	Value
Water density	$1060.0\,\mathrm{kg/m^3}$
Air density	$1.20\,\mathrm{kg/m^3}$
Solid density	$1113.0\,\mathrm{kg/m^3}$
Viscosity coefficient of water	$1.0 \times 10^{-3}\,\mathrm{Pa\cdot s}$
Viscosity coefficient of air	$1.8 \times 10^{-5}\,\mathrm{Pa\cdot s}$
Gravitational acceleration	$9.80665\,\mathrm{m/s^2}$
Initial Atmospheric pressure	101325 Pa

The experiment is repeated by the simulation using the immersed-body method in two dimensions. The computational domain is $1.15\,\mathrm{m} \times 0.4\,\mathrm{m}$, and the water column is 0.15 m wide and 0.2 m high. For the left, right and bottom of the domain, free-slip boundary conditions are applied. The top of the domain is set as an open boundary. The largest fluid mesh size L_e is 0.06 m and the smallest fluid mesh size l_e is 0.002 m. The time step Δt is set as $2.5 \times 10^{-4}\,\mathrm{s}$.

Fig. 3.11 shows the time variations of the mesh, the water-air interface, and the position history of the initially stationary solid square. The water column collapses along the tank bottom under the effect of gravity. The initially stationary solid square starts to move rightwards when the collapsing water collides with it. A counterclockwise vortex is found in the air. This is similar to the results that Kawasaki & Mizutani (2007) obtained. This indicates that the water strongly drives the air to move due to the viscosity difference between water and air.

At $t = 0.390\,\mathrm{s}$, the front of the collapsing water reaches the solid square. This is the same as Kawasaki's results (Kawasaki & Mizutani, 2007). In Kawasaki's computing results, the solid square reaches the right wall at $t = 0.610\,\mathrm{s}$. However, in the present results computed by the immersed-body approach, it is at $t = 0.627\,\mathrm{s}$ when the initially stationary solid square reaches the right wall. This indicates that the present immersed-body method is more accurate than the 'DOLPHIN-2D' model that Kawasaki & Mizutani (2007) developed, since the present results is more close

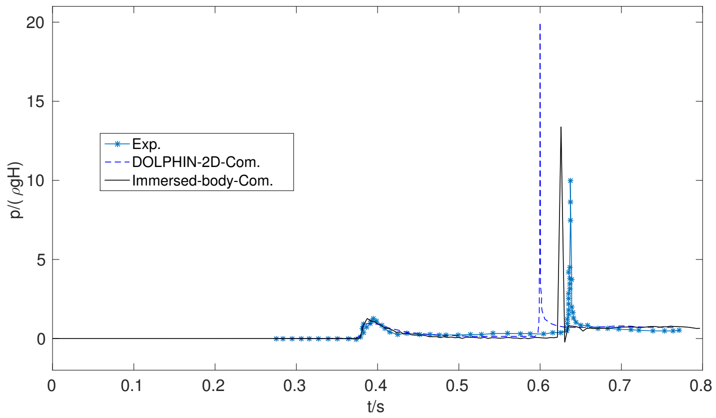

(a) P1 (0.01 m from the bottom)

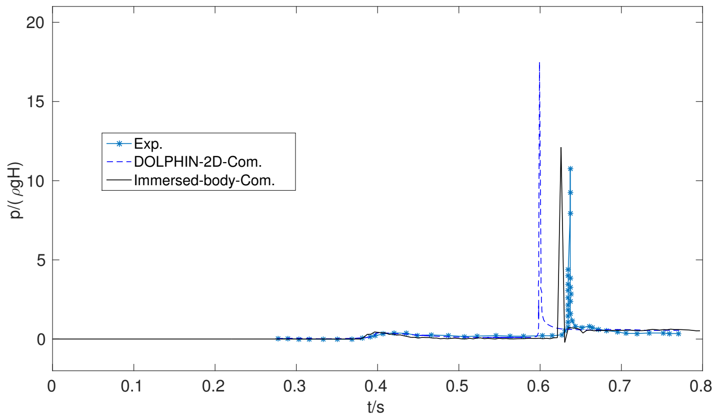

(b) P2 (0.02 m from the bottom)

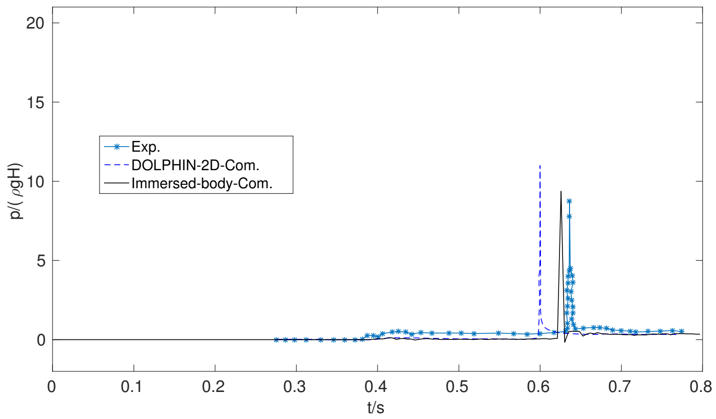

(c) P3 (0.03 m from the bottom)

Figure 3.10 Wave pressure acting on the initially stationary solid square. The black solid line represents the computational results of the immersed-body method in this thesis. The blue dash line and asterisk line are simulation results and experimental data from literature (Kawasaki & Mizutani, 2007). P1, P2 and P3, refer to 0.01 m, 0.02 m and 0.03 m from the bottom on the left wave impacted surface of the initially stationary solid square.

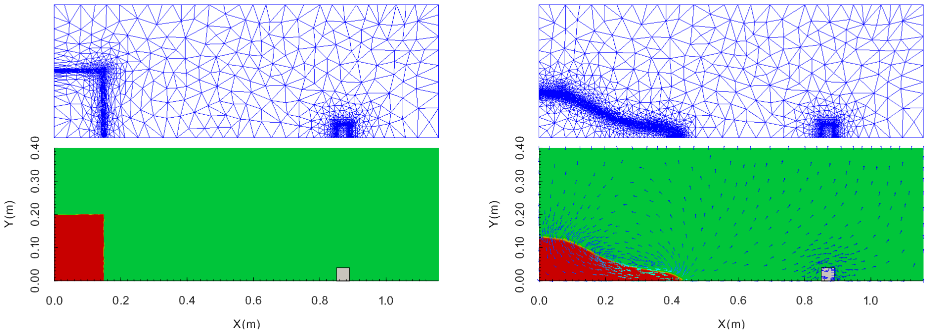

(a) 0.000 s (b) 0.200 s

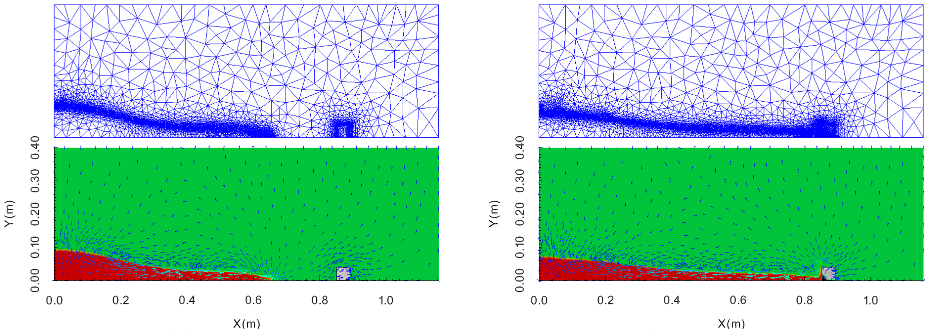

(c) 0.300 s (d) 0.390 s

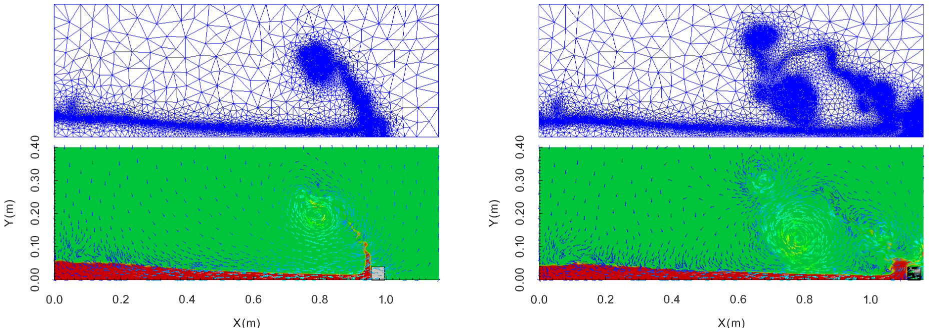

(e) 0.500 s (f) 0.627 s

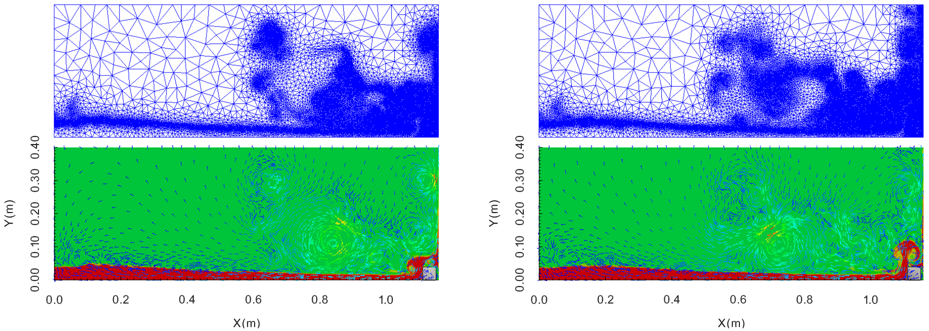

(g) 0.700 s (h) 0.800 s

Figure 3.11 The snapshots of the collapsing column of water moving an initially stationary solid square. The blue grids are the adapted meshes; the green parts refer to the air; the red parts represents the water; the blue vectors are the velocity vectors of the fluids; the white square is the solid square. Figure (a), (b), (c), (d), (e), (f), (g) and (h) refer to the snapshots at 0.000 s, 0.200 s, 0.300 s, 0.390 s, 0.500 s, 0.627 s, 0.700 s and 0.800 s respectively.

to the experimental data than simulation results calculated by the ‘DOLPHIN-2D’ model (see Fig. 3.10). It is worth noting that when the front of the collapsing water collides with the initially stationary solid square, high stress appears inside the left bottom side of the body. Additionally, when the solid square crashes into the right wall, a very high-stress peak is found in the front of the body. These two pressure peaks are the same as that obtained via the ‘DOLPHIN-2D’ model (Kawasaki & Mizutani, 2007). It can be seen that the mesh in Fig. 3.11 is adapted to the gradient of the velocities. Additionally, the mesh is intensive at the water-air interface. The adapted mesh can capture the water-air interface and the fluid vortices accurately (see Fig. 3.11 g and h).

In Fig. 3.10, the value of the impulse pressure acting on the solid square is compared with the experimental data that Kawasaki & Mizutani (2007) measured at P1, P2, and P3, which refer to 0.01 m, 0.02 m, and 0.03 m from the bottom on the left wave impacted surface of the initially stationary solid square. Pressure peaks appear when the front of the water collides with the solid square. Solid and asterisk lines in this figure represent the computed and experimental results respectively. The computed pressure magnitude matches the experimental data with high accuracy despite the small time gap between them.

In this test case, the present results computed by the immersed-body method are in good agreement with the experimental one. The immersed-body approach, therefore, would be useful in analyzing and resolving dynamic solids coupled with multiphase viscous flows.

3.5 An elastic membrane

In this test case, an elastic membrane is modelled to simulate a flexible interface problem. This case has already been used by Tu & Peskin (1992), LeVeque & Li (1997); Tan *et al.* (2008) and Lee & LeVeque (2003) to evaluate their immersed boundary and immersed interface methods. The initial shape of the membrane is an ellipse (see the red solid line in Fig. 3.12 with the label ‘Initial’). The semi-major and -minor axes of the membrane are $a = 0.75$ and $b = 0.5$ respectively. The fluid computational domain is $[-1.5, 1.5] \times [-1.5, 1.5]$, in which the membrane is situated at the centre. The membrane is modelled by the solid model with the properties listed in Table 3.7. The resting shape of the membrane is a circle with radius $r_0 = 0.5$ (see the black dash line Fig. 3.12 with the label 'Resting').

Table 3.7 The properties of the membrane.

Membrane conditions	values
Density (kg/m^3)	10.0
Young's modulus E (Pa)	1.38×10^3
Penalty number	1.38×10^5
Fracture energy release rate G_f	200.0
Poisson ratio	0.205
Tensile strength (Pa)	4.0×10^6
Shear Strength (Pa)	1.4×10^7

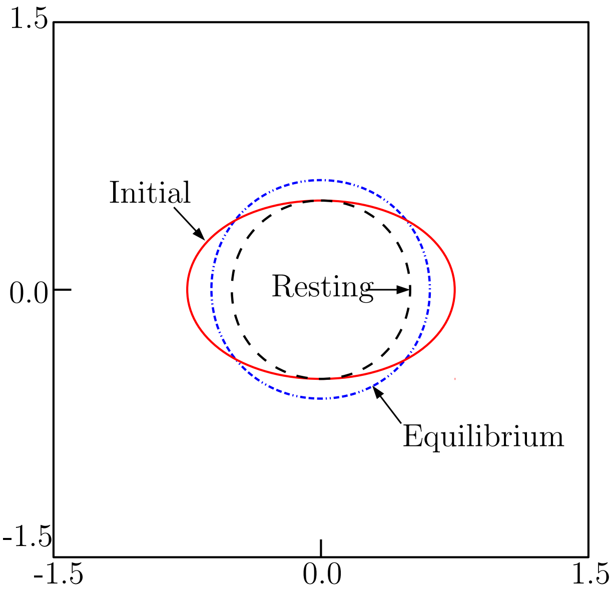

Figure 3.12 Initial, resting and equilibrium shapes of the elastic membrane.

Because the initial membrane shape is stretched from the resting circle to the ellipse, there is certain restoring force inside the ellipse. This force drives the ellipse converge to a circle with the $r_e = \sqrt{ab} \approx 0.61237$ (see the blue dash-dot line in Fig. 3.12 with the label 'Equilibrium'). The radius of the equilibrium circle is bigger than the radius of the resting circle but the equilibrium circle has the same area as the initial ellipse since the fluid is incompressible. Hence when the membrane reaches the equilibrium state, it is still stretched by the incompressible fluid inside it. This nonzero interface force is finally balanced by a fluid pressure differential. When the

Table 3.8 Elastic membrane test cases with different shell mesh thicknesses.

Case	μ	ρ_f	Δr	l_e	L_e
Elastic-membrane-y1	0.1	1.0	0.0005	0.0040	0.1
Elastic-membrane-y2	0.1	1.0	0.0010	0.0040	0.1
Elastic-membrane-y3	0.1	1.0	0.0020	0.0040	0.1

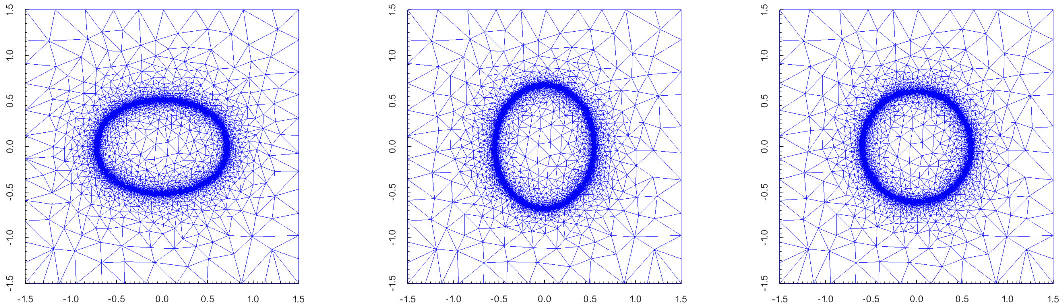

(a) $t = 0.19\,\mathrm{s}$ (b) $t = 0.80\,\mathrm{s}$ (c) $t = 1.47\,\mathrm{s}$

Figure 3.13 Elastic membrane test cases: the fluid mesh at different times: (a) $t = 0.19\,\mathrm{s}$, (b) $t = 0.80\,\mathrm{s}$, and (c) $t = 1.47\,\mathrm{s}$.

membrane reaches the equilibrium state, the fluid velocity field is zero everywhere. Meanwhile, there is a pressure differential between the inside and outside of the interface.

A zero pressure boundary condition is applied to all the sides (open boundaries). The initial conditions are zero pressure and velocity everywhere. The adaptive mesh is used in this test case. The mesh is refined around the fluid-solid interface (see Fig. 3.13). This helps to capture the interface more accurately.

The velocity field results are provided in Figs. 3.14. It is shown that the velocity becomes small as the simulated time accrues, and reaches zero at the end of the simulation. Fig. 3.15 shows the pressure profiles. In the beginning, the pressure is not constant inside the membrane. Whilst, when the membrane shape changes to a circle, the pressures inside and outside the membrane are constants with a known pressure difference.

In order to evaluate the influence of shell mesh thickness on this pressure drop. Three membrane tests with different shell mesh thicknesses are simulated in this work (see Table 3.8). In Fig. 3.16, the fluid pressure profiles along $y = 0.0$ are plotted at different time levels: (a) $t = 0.19\,\mathrm{s}$, (b) $t = 0.80\,\mathrm{s}$, and (c) $t = 1.47\,\mathrm{s}$. The blue-star,

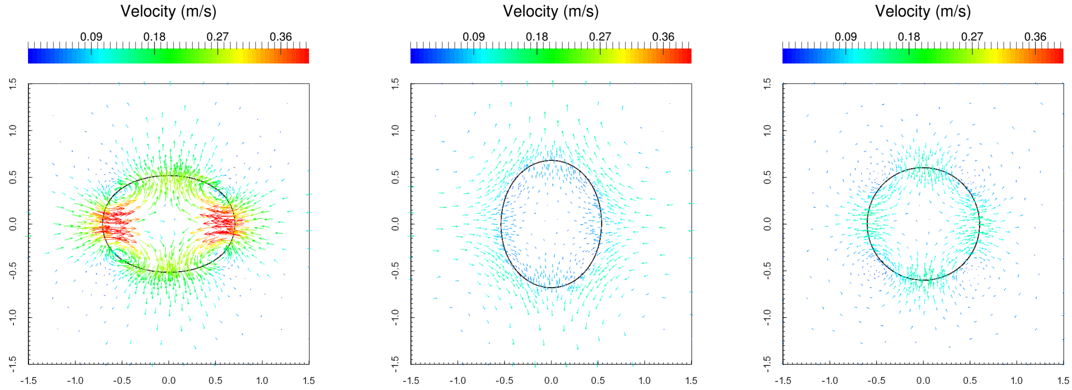

(a) $t = 0.19\,\mathrm{s}$ (b) $t = 0.80\,\mathrm{s}$ (c) $t = 1.47\,\mathrm{s}$

Figure 3.14 Elastic membrane test cases: the fluid velocity fields at different times: (a) $t = 0.19\,\mathrm{s}$, (b) $t = 0.80\,\mathrm{s}$, and (c) $t = 1.47\,\mathrm{s}$.

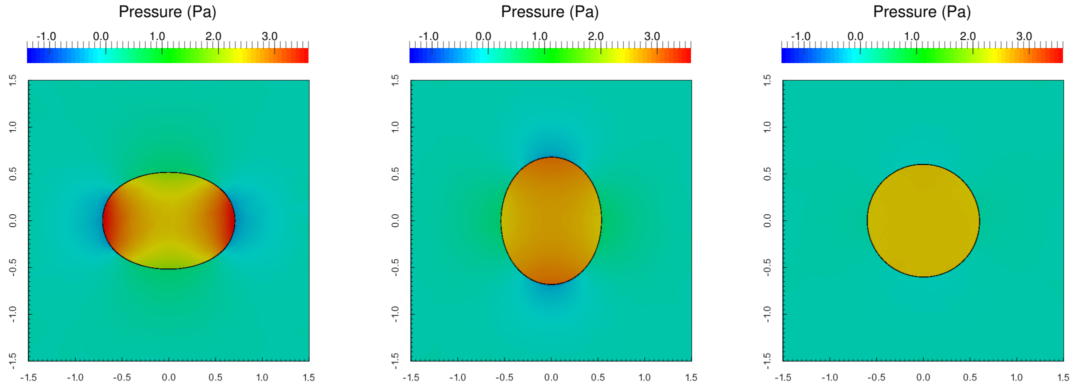

(a) $t = 0.19\,\mathrm{s}$ (b) $t = 0.80\,\mathrm{s}$ (c) $t = 1.47\,\mathrm{s}$

Figure 3.15 Elastic membrane test cases: the fluid pressure profiles at different times: (a) $t = 0.19\,\mathrm{s}$, (b) $t = 0.80\,\mathrm{s}$, and (c) $t = 1.47\,\mathrm{s}$.

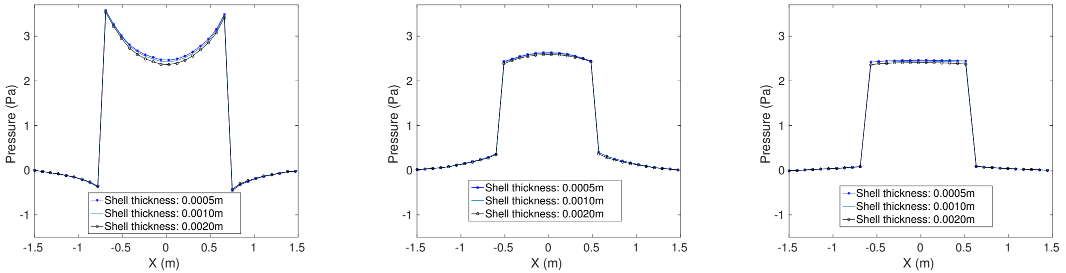

(a) $t = 0.19\,\mathrm{s}$ (b) $t = 0.80\,\mathrm{s}$ (c) $t = 1.47\,\mathrm{s}$

Figure 3.16 Elastic membrane test cases: the fluid pressure profiles ($y = 0.0$) with three different shell mesh thicknesses at different times: (a) $t = 0.19\,\mathrm{s}$, (b) $t = 0.80\,\mathrm{s}$, and (c) $t = 1.47\,\mathrm{s}$.

green and black-circle lines represent the pressure profiles with the shell thickness 0.0005 m, 0.0010 m and 0.0020 m, respectively. Despite the difference in the shell mesh thickness, the pressure profiles are almost the same at the different time levels and there are negligible differences between them. As the membrane approaches the equilibrium shape, the differences diminish (see Fig. 3.16). This implies that the shell mesh thickness does not affect the pressure drop in the membrane test.

3.6 The water-air interface with a floating solid square

Modelling of structures floating on fresh or sea water requires that the air-water interface as well as the solid-air, solid-water interface are modelled, especially for the case of breaking waves. The understanding of these wave effects is very important in ocean dynamics, for instance, the impacts of ocean waves on ships, floating wind turbine platforms, and ocean oil platforms. The following case is a simplified model of these situations. It consists of a 0.04 m solid square initially sitting stably at the top of a water column, which is 0.20 m in length and 0.195 m in depth. The centre of the floating solid square is initially located at $(0.12, 0.22)$. The viscosity of water and air are set as $\mu = 1 \times 10^{-3}\,\mathrm{Ns/m^2}$ and $\mu = 1.8 \times 10^{-5}\,\mathrm{Ns/m^2}$ respectively. The computational domain is 0.6 m in length and 0.4 m in height. For the left, right and bottom of the domain, free-slip boundary conditions are applied. The top of the domain is set as an open boundary. The maximum fluid mesh size L_e is set as 0.06 m and the minimum fluid mesh size l_e is set as 0.002 m. The time step is fixed as 0.0005 s. The density of water, air and the solid square are set as $1060.0\,\mathrm{kg/m^3}$, $1.20\,\mathrm{kg/m^3}$, and $500.0\,\mathrm{kg/m^3}$ respectively.

Fig. 3.17 and 3.18 show some snapshots of the floating solid square simulation results including the time variations of the mesh, the water-air interface, the velocity vector profile, and the position history of the floating solid square. At $t = 0.0\,\mathrm{s}$, the solid square is on the top of the water column. As the water collapses, the solid square drops into the water. At $t = 0.150\,\mathrm{s}$, near the half of the solid square sinks into the water, since the density of the solid square is almost half of water density. At $t = 0.255\,\mathrm{s}$, the front of the water reaches the right side of the computational domain. It reaches the top of the fluid domain at $t = 0.400\,\mathrm{s}$. The waterfront drops downward to the bottom at $t = 0.705\,\mathrm{s}$. Then the dropping waterfront creates a wave with

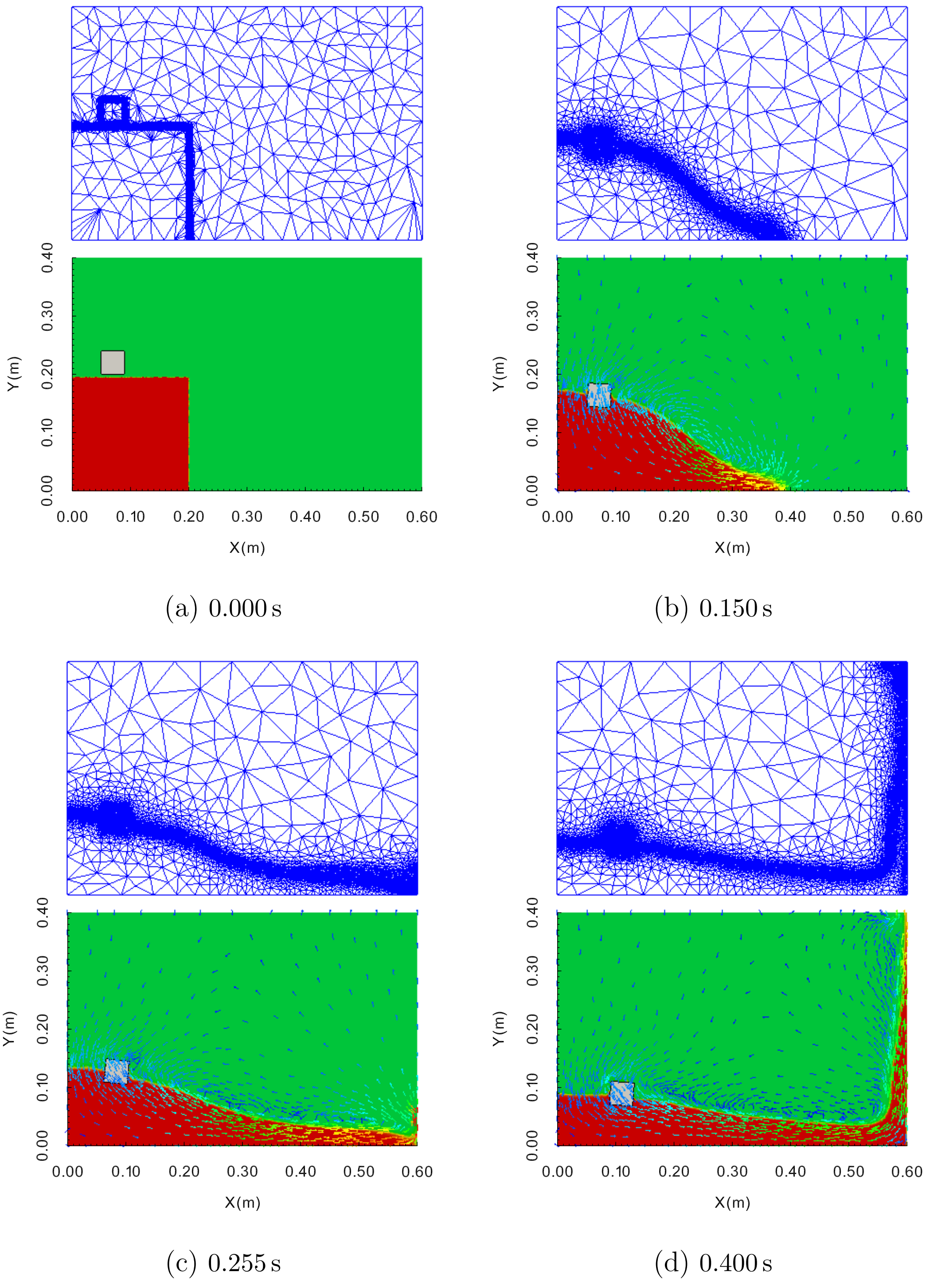

(a) 0.000 s

(b) 0.150 s

(c) 0.255 s

(d) 0.400 s

Figure 3.17 The snapshots of the water-air interface with a floating solid square. The blue grids are the adapted meshes; the green parts refer to the air; the red parts represents the water; the blue vectors are the velocity vectors of the fluids; the white square is the solid square. Figure (a), (b), (c) and (d) refer to the snapshots at 0.000 s and 0.150 s, respectively.

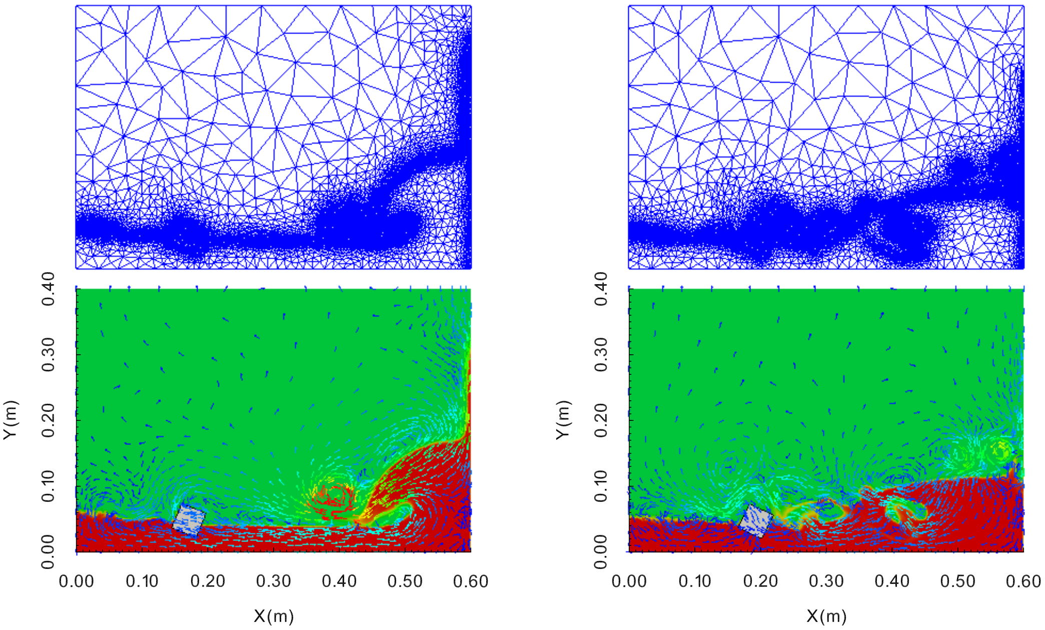

(e) 0.705 s

(f) 0.910 s

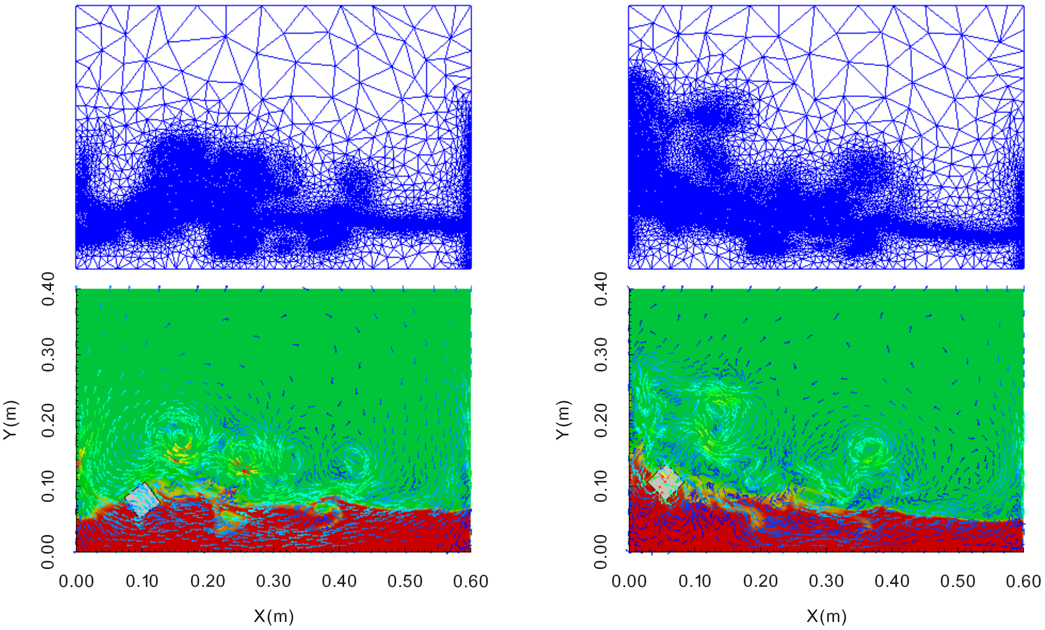

(g) 1.200 s

(h) 1.400 s

Figure 3.18 The snapshots of the water-air interface with a floating solid square. The blue grids are the adapted meshes; the green parts refer to the air; the red parts represents the water; the blue vectors are the velocity vectors of the fluids; the white square is the solid square. Figure (e), (f), (g) and (h) refer to the snapshots at 0.705 s and 0.910 s, respectively.

the characteristic form of a breaking sea wave. The front of the water wave impacts on the solid square at $t = 0.910\,\mathrm{s}$, meanwhile, complex vortex patterns are found in the bottom of the water tank. After the wave impacts on the solid square, it starts to move leftwards (see Fig. 3.18 g). It is then dragged upwards by the wave (see Fig. 3.18 h). It is worth noting that the vortices in Fig. 3.18 f and Fig. 3.18 g and h are very complex due to complicated interactions between the water-air interface and the solid-fluid interface when the wave impacts on the solid square. Indeed, the applied interface capturing method in this work, which is an alternative to the widely used volume of fluid (VOF) method, was shown to produce the full range of spilling, surging and breaking waves in previous simulation work with 'Fluidity' in the context of coastal engineering (Mindel *et al.*, 2007).

This simplified case demonstrates that the present immersed-body method for multiphase viscous flows is robust and has a wide application to ocean dynamics which involve wave-induced dynamic water-air interface FSI problems. This case is a preliminary step to the investigation of a wide range of wave-structure dynamics problems, for instance, ship structural damage and coastal damage caused by tsunamis, as well as floating wind turbine installations and oil platform protection problems.

3.7 Concluding remarks

This chapter presents the validation for the developed FSI model for incompressible flows in chapter 2. The model has been validated using a free falling circular cylinder and a free falling sphere in a fluid at rest with Reynolds number up to 1800. The benchmark case, a collapsing column of water moving an initially stationary solid square, has been used to validate this immersed-body method. The simulation results are in good agreement with the experimental data. Importantly, the mesh sensitivity analysis in this work indicates that the simulation results are converged when then fluid and shell mesh sizes are decreased. The immersed-body method is proved promising to simulate multiphase viscous flows coupled with dynamic solids, especially for phenomena with multiple-interfaces e.g solid-water, solid-air, water-air, which is useful for ocean dynamics. This immersed-body method can be applied to multiphase viscous flows, for example, the water-air flows and FSI of ships, floating wind-turbine platforms, and oil platforms. The next chapter will focus on the validation and application cases of the developed FSI model for the compressible flow with a fracture model.

Chapter

FOUR

Compressible flow FSI model with a fracture model

This chapter presents and validates the FSI model for compressible flows coupled with a cohesive zone fracture model. In order to resolve the fractures and cracks inside solids, the immersed-body method is combined with a cohesive zone fracture model. This model is fully coupled and simulates the whole blasting process including gas pressure impulse, shock wave propagation, gas expansion, fragmentation and burden movement phases. In the fluid model, the John-Wilkins-Lee equation of state is introduced to resolve the relationship between pressure and density of the highly compressible gas in blasts and explosions. A Q-scheme is used to stabilise the model when solving extremely high-pressure situations. Two benchmark tests, blasting cylinder and projectile fire, are used to validate this coupled model. The results of these tests are in good agreement with experimental data. To demonstrate the potential of the proposed method, a blasting engineering simulation with shock waves, fracture propagation, gas-solid interaction and flying fragments is simulated.

4.1 Introduction

This chapter presents the FSI model coupled with a cohesive zone fracture model. This coupled model is also validated and applied to the rock blasting. In the present model, the John-Wilkins-Lee (JWL) equation of state is used to close the gas system of equations. A Q-scheme is used to stabilise the gas model when solving extremely high-pressure situations. A fracture model using a Mohr-Coulomb failure criterion with a tension cut-off (Guo *et al.*, 2015) is employed to define the cracking and fragmentation within the solid. The fracture model employs a discontinuous mesh to complete the fracture model. The solid mesh used by the fracture model is discontinuous. By contrast, on the fluid side, a continuous representation of the pressure field is used. In order to link these two different kinds of meshes, a new mesh conversion algorithm was implemented to convert discontinuous meshes to continuous meshes.

The remainder of this chapter is organised as follows. Section 4.2 details the governing equation for discontinuum fractured solids, together with the fracture model. Section 4.3 presents the equation for the JWL equation of state. The theory behind the gas-solid interaction model is detailed in Section 4.4. The model is validated using a blasting cylinder test, and a projectile fire test in Section 4.5. A practical complicated blasting engineering simulation with shock waves, fracture propagation, gas-solid interaction and flying fragments is also presented in Section 4.5. The list of the test cases in this chapter is shown in Table 4.1. I discuss the strengths and weaknesses of this approach and draw conclusions in Section 4.6.

Table 4.1 Compressible flow test cases

Section	Case name	Case purpose
Section 4.5.1	Blasting cylinder	Validation
Section 4.5.2	Projectile	Validation
Section 4.5.3	Masonry block fragmentation due to an internal explosion	Application

4.2 Solid fracture model

The fracture model used here is based on the FEMDEM method, which was first proposed by Munjiza (2004). This model treats each solid body as a single discrete element and discrete solid motions are modelled by the discrete element method (DEM), whilst deformable fracturing arbitrary-shaped solid body interaction (stress, velocity and deformation) is modelled by finite-element method (FEM). The stresses are computed by the FEM before fracture initiation. Once the stress state meets a failure criterion, discrete fractures are generated and the DEM is used to explicitly model the discontinuous interaction between discrete surfaces. By combining the FEM and DEM parts, the fracture model is able to accurately capture the transition from continuum to discontinuum behaviour.

4.2.1 Joint element

A modified 3-noded triangular element mesh is introduced to complete the 2D fracture model. Initially, the whole solid domain is discretised by 3-noded triangular elements, and 4-noded joint elements are inserted between these triangular elements. Six adjacent discontinuous elements sharing one center point (see Fig. 4.1 left) is taken as an example to describe the joint element method. According to the joint element method mentioned in the literature (Guo *et al.*, 2015), for these six adjacent discontinuous elements (element 1–6), there should be six unbroken joint elements (element 7–12) among them (see Fig. 4.1 right).

4.2.2 Combined tensile and shear failure criterion

The constitutive model is a combined single and smeared crack model equivalent to a cohesive zone model (Guo *et al.*, 2015; Munjiza *et al.*, 1999). Both the tensile stress σ and shear stress τ in joint elements are calculated according to the basic law shown in Fig. 4.2. In Fig. 4.2, G_f is the fracture energy, which is a material property; δ_c is the critical displacement when the joint element breaks; and δ_p is the maximum elastic displacement corresponding to the peak stress f. The peak stress f is the material strength. It becomes tensile strength f_t and shear strength f_s when it represents tensile stress σ and shear stress τ, respectively. Tensile strength f_t is assumed to be constant. However, shear strength f_s is given by the Mohr-Coulomb

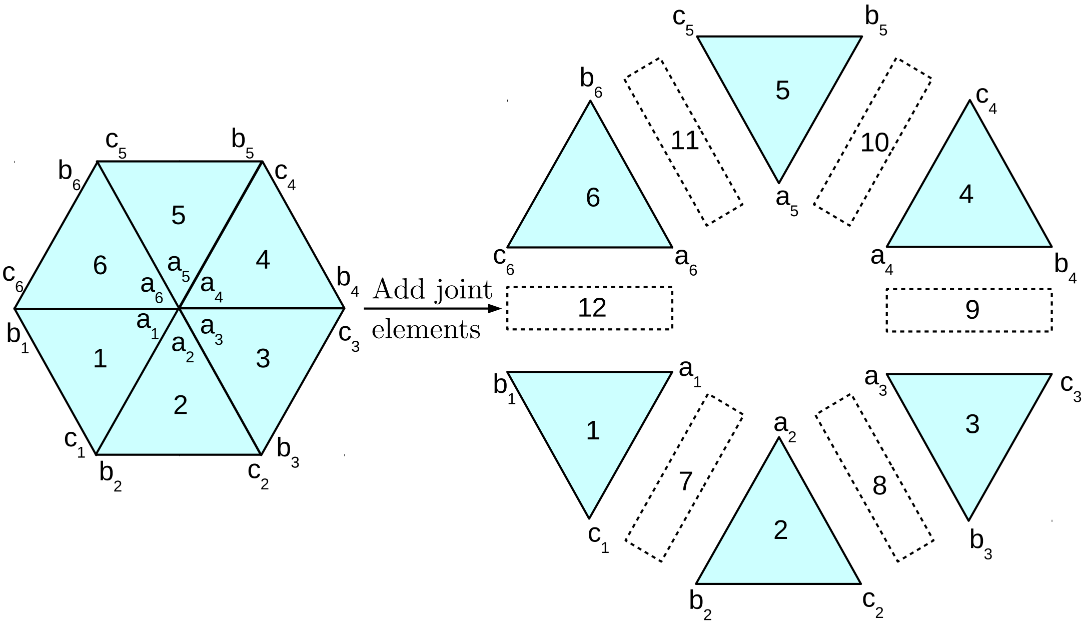

Figure 4.1 Six solid discontinuous elements with joint elements. Elements 1–6 are six adjacent discontinuous elements, and elements 7–12 are the six joint elements added among them.

criterion with a tension cut-off:

$$f_s = \begin{cases} -\sigma_n tan\phi + c, & when \quad \sigma_n < f_t; \\ -f_t tan\phi + c, & when \quad \sigma_n \geqslant f_t, \end{cases} \tag{4.1}$$

where σ_n is the normal stress, ϕ is the angle of internal friction and c is the cohesion. Based on Equation (4.1), the shear strength f_s can be calculated by σ_n or f_t. When $\sigma > f_t$, the tensile failure occurs whilst when $\tau > f_s$, the shear failure occurs.

The physical meanings of δ_p and δ_c in a single mode I tensile fracture are described in Fig. 4.3. For three different displacement ranges, the normal stress σ can be calculated by Equation (4.2).

$$\sigma = \begin{cases} zf_t, & \text{when} \quad \delta_{np} < \delta_n \leqslant \delta_{nc}; \\ f_t\left[2\frac{\delta_n}{\delta_{np}} - \left(\frac{\delta_n}{\delta_{np}}\right)^2\right], & \text{when} \quad 0 \leqslant \delta_n \leqslant \delta_{np}; \\ 2\frac{\delta_n}{\delta_{np}} f_t, & \text{when} \quad \delta_n < 0, \end{cases} \tag{4.2}$$

where δ_{np} is the maximum elastic displacement in the normal direction, δ_{nc} is the critical displacement at failure in the normal direction, z is an empirical parameter,

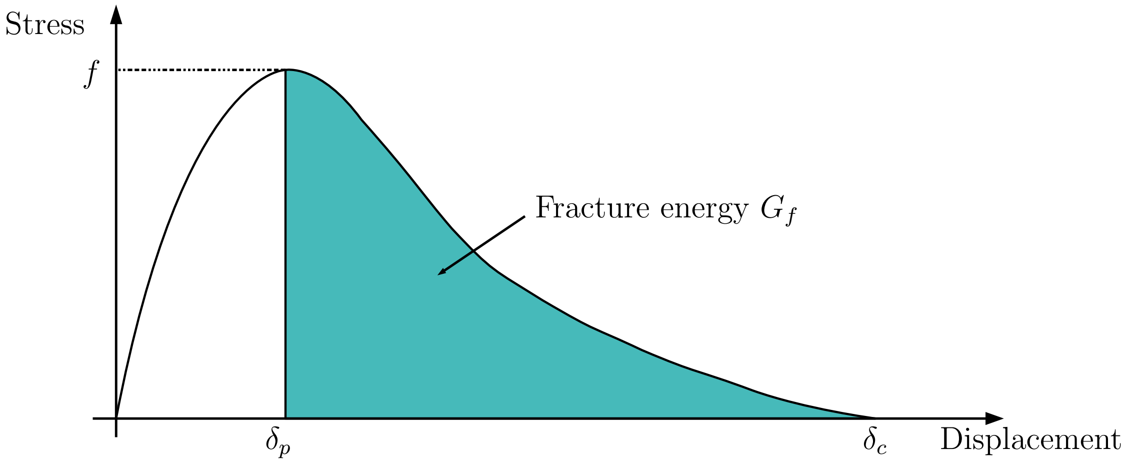

Figure 4.2 The stress for different displacements.

which comes from the curve fitting of experimental data (more details can be found in the literature (Guo *et al.*, 2015; Munjiza *et al.*, 1999; Xian *et al.*, 1991)). The failure criterion used in the 2D fracture model is a Mohr-Coulomb failure criterion with a tension cut-off. It is important to note that the fracture model is based on a fixed mesh, which results in fractures only propagating along triangular element boundaries since fracturing follows the routes of joint elements (Guo *et al.*, 2015). Hence the solid mesh size could affect the fracture pattern when the solid mesh size is not small enough.

4.3 The equation of state

The equation of state (EOS) is a thermodynamic equation to close the fluid governing equations. It links the fluid temperature, pressure, density and internal energy together by introducing the thermodynamic relationship of fluids. There are a number of EOS for explosive gases (Braithwaite *et al.*, 1996). However, the JWL-EOS is the most widely used one in blasting applications (Itoh *et al.*, 2002; Sazid & Singh, 2013). The JWL equation is:

$$p = A\cdot\left(1-\frac{\omega}{R_1\cdot V}\right)\cdot\exp(-R_1\cdot V)+B\cdot\left(1-\frac{\omega}{R_2\cdot V}\right)\cdot\exp\left(-R_2\cdot V\right)+\frac{\omega\cdot e_0}{V}, \quad (4.3)$$

where parameters A , B , R_1 , R_2, ω and e_0 are material constants, which are obtained by fitting the JWL-EOS to experimental results; p is the pressure; the volume ratio V is defined by $V = \rho_e/\rho_f$, where ρ_e is the density of the explosive

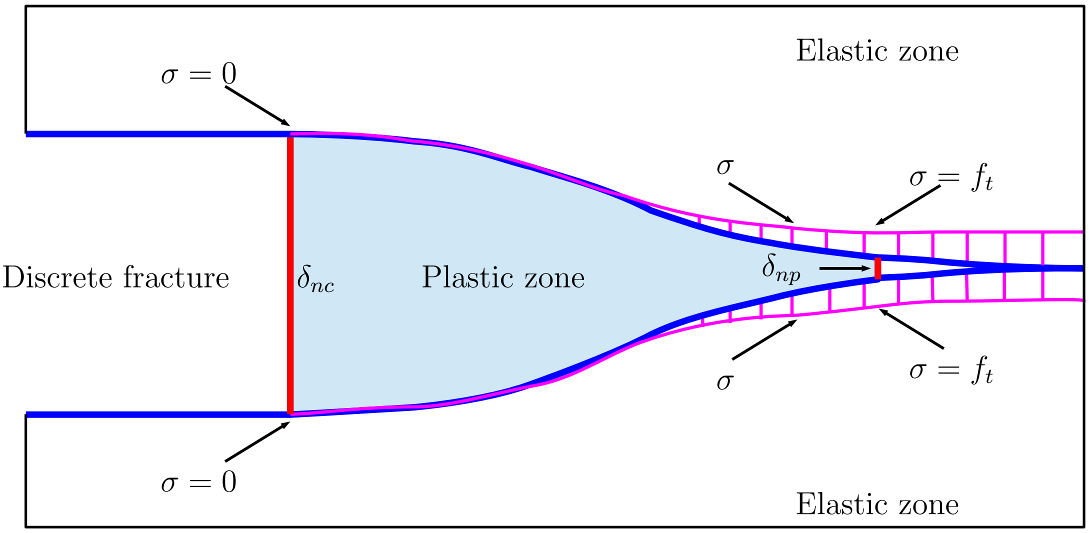
Elastic zone
$\sigma = 0$
σ
$\sigma = f_t$
Discrete fracture
δ_{nc}
Plastic zone
δ_{np}
σ
$\sigma = f_t$
$\sigma = 0$
Elastic zone

Figure 4.3 Different zones in a single mode I fracture tip. δ_{np} and δ_{nc} represent δ_p and δ_c, respectively. The left open white area refers to a physically discrete fracture; the middle light-blue area is the plastic zone; the top and bottom white area represent the continuous solid without any cracks; the short vertical pink bars between the pink and blue lines represent the magnitudes of the normal stress σ.

(solid part) and ρ_f is the density of the detonation products; ρ_0 is the initial density (solid part). By using the JWL-EOS, I assume the temperature is constant, same assumption can be see from the literature (Mohammadi & Pooladi, 2007; Munjiza *et al.*, 2000). Under this assumption, the internal energy e in the energy Equation (2.14) should also be constant. Thus, in order to implement the JWL-EOS, I use the perturbation pressure method to obtain the sound speed of the explosive gas $c = \sqrt{\frac{\delta p}{\delta \rho_f}}$, which is the approximation of $c = \sqrt{\frac{\partial p}{\partial \rho_f}}$.

4.4 Coupled gas-solid interaction

4.4.1 The coupling term $\boldsymbol{s}_c$ and the exchange force $\boldsymbol{F}_v$ and $\boldsymbol{F}_p$ including the Q-scheme

After the gas viscosity μ_t, pressure p and velocity $\boldsymbol{u}_f^f$ are solved by Equation (2.13, 2.12, 2.14 and 4.3) on the gas mesh. They are projected on the solid surface through a shell mesh (more details about the projection method can be found in the literature (Viré *et al.*, 2015)), and the exchange force $\boldsymbol{F}_v^s$ and $\boldsymbol{F}_p^s$ on the solid surface are:

$$\boldsymbol{F}_v^s + \boldsymbol{F}_p^s = \int\limits_{\Gamma_{solid}} N_i n \cdot (\tau + Ip)\, d\Gamma, \tag{4.4}$$

in which Γ_{solid} represents the solid surface. The extension form of $\int_{\Gamma_{solid}} N_i n \cdot \tau d\Gamma$ in u and v directions are:

$$\begin{aligned} &\int\limits_{V_{shell}} N_i \left(a_{xx} u_{sl} + a_{xy} v_{sl} \right) dV, \\ &\int\limits_{V_{shell}} N_i \left(a_{yx} u_{sl} + a_{yy} v_{sl} \right) dV, \end{aligned} \tag{4.5}$$

where, V_{shell} stands for the volume of the shell mesh, the slip velocity $\boldsymbol{u}_{sl} = \boldsymbol{u}_s - \boldsymbol{u}_f$. The components of velocity in 2D are u and v. The coefficient $\boldsymbol{a}$ has four components $(a_{xx}, a_{xy}, a_{yx}, a_{yy})$ in 2D. They are:

$$\begin{aligned} a_{xx} &= \frac{\mu_t}{\Delta r \Delta x_{wall}} \left[n_x \left(2 - \frac{2}{3} \right) n_x + n_y n_y \right], \\ a_{xy} &= \frac{\mu_t}{\Delta r \Delta x_{wall}} \left(-n_x \frac{2}{3} n_y + n_y n_x \right), \\ a_{yx} &= \frac{\mu_t}{\Delta r \Delta x_{wall}} \left(n_x n_y - n_x \frac{2}{3} n_y \right), \\ a_{yy} &= \frac{\mu_t}{\Delta r \Delta x_{wall}} \left[n_x n_x + n_y \left(2 - \frac{2}{3} \right) n_y \right], \end{aligned} \tag{4.6}$$

$\mu_t = \mu_p + \mu_a$, in which μ_p is the dynamic viscosity, μ_a is the Q-scheme artificial viscosity (Castro *et al.*, 2001). The μ_a used here is,

$$\mu_a = -c_q h^2 \rho_f \, min\{0, \nabla \cdot \boldsymbol{u}_f\} \quad - \quad c\, c_l h \rho_f \, min\{0, \nabla \cdot \boldsymbol{u}_f\}, \tag{4.7}$$

in which c_q, c_l are scalar and $c_q = 1, c_l = 0.05$ are used here, where h is a length scale measured across each element. Also the speed of sound c is obtained from:

$$c = \sqrt{\frac{\partial p}{\partial \rho_f}}. \tag{4.8}$$

The exchange force $\boldsymbol{F}_v$ and $\boldsymbol{F}_p$ is used in Equation (2.1) to compute the solid velocity $\boldsymbol{u}_s = (u_s, v_s)$.

The coupling term $\boldsymbol{s}_c$ can be formed as:

$$\begin{aligned} s^f_{c,x} &= a_{xx}u_s + a_{xy}v_s; \\ s^f_{c,y} &= a_{yx}u_s + a_{yy}v_s, \end{aligned} \tag{4.9}$$

then the solid-fluid coupling term $\boldsymbol{s}_c = \left(s^f_{c,x}, s^f_{c,y}\right)^T$ in Equation (2.13).

4.4.2 Update of solid boundary after fracturing

After fractures are generated in the fracture model (see Section 4.2), the new fracture boundaries are discontinua. These discontinuous boundaries cannot be recognised by the fluid model because of the projection method (Viré *et al.*, 2015) cannot project these boundaries from the solid mesh to the fluid mesh through the shell mesh. The projection method (Viré *et al.*, 2015) is designed to project continuous boundaries. In order to enable the fluid to realise the positions of new fractures, these discontinuous boundaries need to be transformed into continuous ones. This algorithm is presented as follows.

According to the joint element method mentioned in Section 4.2.1, there are six unbroken joint elements (element 7–12) among them (see Fig. 4.1, right). When joint elements 7–12 added to the discontinuous elements 1–6, they are given the value 0, which means the joint elements are intact. Once the stress state of the nodes on joint elements meets the fracture criterion, these joint elements are regarded as broken, and the values of these joint elements are changed from 0 to 1. Algorithm 1 is used to determine which group of nodes in nodes $(a_1 - a_6)$, which are shared by the six adjacent joint elements, should be consider as one node. For instance, by using Algorithm 1, if only joint element 9 is broken, then discontinuous node $a_1 - a_6$

Algorithm 1 Transforming fracture boundaries from discontinua to continua.

```
for each discontinuous node $i$ (for example, node $a_1$ in Fig. 4.1) do
    (1) Detect all the discontinuous nodes that have the same coordinates as it has;
    (2) Give these nodes indices $DN_1 - DN_n$ (in Fig. 4.1, these nodes are $a_2 - a_6$);
    (3) Detect all the joint elements that are using nodes $DN_1 - DN_n$ and discrete
        node $i$;
    (4) Give these joint elements indices $JE_1 - JE_m$ (in Fig. 4.1, these joint
        elements are $7 - 12$);
    (5) From node i, go through the joint element $JE_1 - JE_m$;
    (6) In anticlockwise direction (from joint element 7 to 12);
    if the value of the joint element is 0 then
        continue, and remember the discontinuous node indices in $DN_1 - DN_n$ that
        are used by this joint element as node $AC_1 - AC_k$,
    else
        stop;
    end if
    (7) In clockwise direction (from joint element 12 to 7);
    if the value of the joint element is 0 then
        continue, and remember the discontinuous node index in $DN_1 - DN_n$ that
        are used by this joint element as node $C_1 - C_l$,
    else
        stop;
    end if
    (8) Give node $i$, $AC_1 - AC_k$ and $C_1 - C_l$ the same new index, because they
        are the same point in the continuous domain.
end for
```

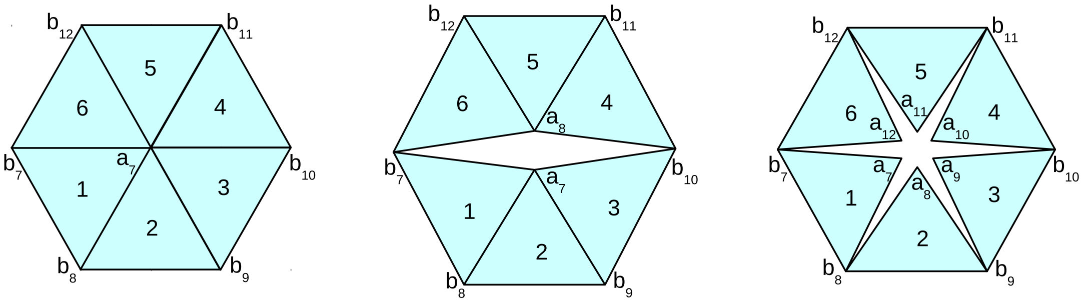

(a) (b) (c)

Figure 4.4 Six solid continuous elements with cracks in different broken patterns: (a) only joint element 9 is broken, (b) both joint element 9 and 12 are broken, (c) all the joint elements $7-12$ are broken.

should be the same point in the continuous domain (see Fig. 4.4, a). When both joint element 9 and 12 are broken, then discontinuous node $a_1 - a_3$ is one point, whilst discontinuous node $a_4 - a_6$ is another point in the continuous domain (see Fig. 4.4, b). Or in an extreme situation, all the joint elements $7-12$ are broken, then each point of discontinuous node $a_1 - a_6$ should be an individual point in the continuous domain (see Fig. 4.4, c).

After all the discontinuous fracture solid boundaries are transformed into continuous ones, the thin shell mesh surrounding the solid surface can be generated on the new solid continuous boundaries. Then new fluid conditions are passed to the solid surface via the shell mesh through the projection method in the literature (Viré *et al.*, 2015).

4.4.3 The theory behind the coupling approach

In this work, the 'Solidity' (Latham *et al.*, 2013a,b), a two-dimensional (2D) FEM-DEM solver is coupled with a finite element fluid code 'Fluidity-Multiphase'. The steps to implement the gas-solid interaction with the fracture model are shown in Algorithm 2.

Algorithm 2 Gas-solid interaction.

```
for Time step in the fluid solver: $n$ do
    (1) Solve fluid velocity $\boldsymbol{u}_f$, pressure $p$, and viscosity $\mu_t$ via equations (2.13, 2.12, 2.14 and 4.3);
    (2) Project $\boldsymbol{u}_f, p, \mu_t$ from fluid to shell mesh (Viré et al., 2015);
    (3) Project $\boldsymbol{u}_f, p, \mu_t$ from shell to solid surface mesh;
    for Time step in the solid solver: $i$ do
        (4) Detect fractures;
        (5) Transforming fracture boundaries from discontinua to continua via Algorithm 1;
        (6) Construct shell mesh;
        (7) Compute $\boldsymbol{F}_v$ and $\boldsymbol{F}_p$ via Equation (4.4);
        (8) Solve for $\boldsymbol{u}_s$ via Equation (2.1);
        (9) $i = i + 1$;
    end for
    (10) Compute $\boldsymbol{s}_c$ , and $(a_{xx}, a_{xy}, a_{yx}, a_{yy})$ via $\boldsymbol{u}_s$ and $\boldsymbol{u}_f$;
    (11) Project $\boldsymbol{s}_c$ , and $(a_{xx}, a_{xy}, a_{yx}, a_{yy})$ from solid surface to shell mesh;
    (12) Project $\boldsymbol{s}_c$, and $(a_{xx}, a_{xy}, a_{yx}, a_{yy})$ from shell to fluid mesh;
    (13) Implicitly solve $\boldsymbol{u}_f$ via Equation (2.13);
    (14) $n = n + 1$.
end for
```

4.5 Results

In this section, two benchmark test cases and a complex blasting application are presented to validate and evaluate the performance of this method. The two benchmark test cases are the blasting cylinder test and the projectile fire test. The complicated blasting application test is the masonry block fragmentation due to an internal explosion.

4.5.1 Blasting cylinder

The blasting cylinder test case simulates an explosion occurring inside a solid cylindrical chamber (see Fig. 4.5). This test case has been used many times to verify gas-solid interaction formulations (Munjiza, 1992; Mohammadi & Bebamzadeh, 2005, 2007; Mohammadi & Pooladi, 2007). This cylindrical metal chamber is 1220 mm in length, and its diameter is 25.4 mm. The chamber is filled with 0.148 kg ANFO (ammonium nitrate/fuel oil) with density 240 kg/m^3. The JWL-EOS parameters for ANFO used here are as follow: $A = 266.799$ GPa, $B = 3.435$ GPa, $R_1 = 7.037$, $R_2 = 1.159$, $\omega = 0.39$ and $E_0 = 6.4365$ GPa. More information about ANFO can be found in the literature (Sanchidrian *et al.*, 2015).

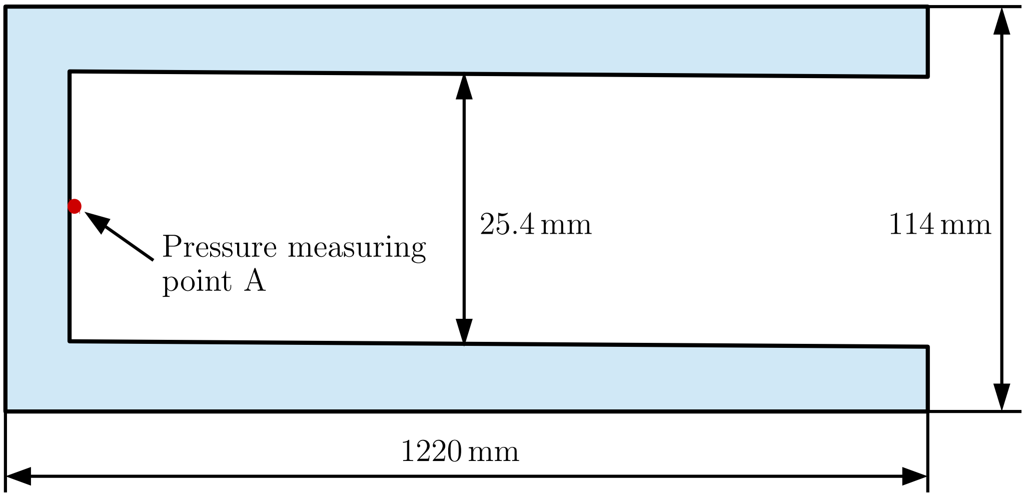

Figure 4.5 The geometry of the cylindrical chamber. Point A is where the gas pressure is measured.

In this simulation, open boundary conditions are applied on all boundaries of the fluid computational domain. The fluid element edge length is 0.0033 m and the fluid time step size Δt_f is set to 10^{-7} s. The solid element edge length is 0.005 m and the solid time step size Δt_s is set to 0.4×10^{-7} s. The simulation is based on the assumption that the change in gas pressure is due to the gas loss from the right end of the chamber. As a result, the internal pressure decreases sharply after the gas starts to escape from the chamber. The internal pressure history measured at the left end of the chamber (the point A in Fig. 4.5) can be found in Fig. 4.6, a. The pressure in the simulation is in good agreement with the experimental data presented in the literature (Munjiza, 1992) (see Fig. 4.6, a). The drop in density is shown in Fig. 4.6, b. It is seen that the gas pressure and density time-series follow a similar pattern that begins with the maximum value after the ignition point, following with the continuous decrease due to the loss of the gas at the right end of the chamber. It is worth to mention that all the simulations start after the ignition point when the detonation gas fills the whole chamber because the model proposed here does not take the ignition stage into consideration.

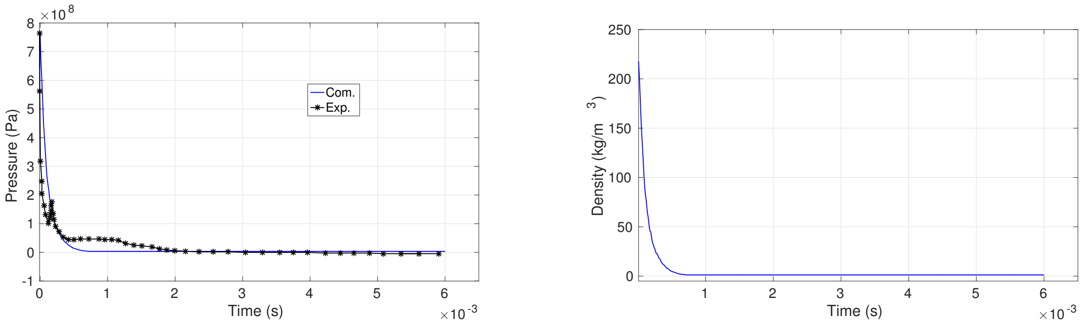

(a) The pressure history of the blasting cylinder test in comparison with the experimental results (Munjiza, 1992). The comparison does not take the ignition stage into consideration.

(b) The density history of the blasting cylinder test.

Figure 4.6 The pressure and density history at point A of the blasting cylinder test.

4.5.2 Projectile

The second benchmark test is a projectile fire test case. This test is designed to validate the presented solid-gas interaction model under a sudden change in gas volume. There are experimental data for this test case in (Johanson & Persson, 1970), and other two models developed by Mohammadi & Pooladi (2007, 2012) have already used the same test case to assess their models. In the experiment, a 180 mm × 127 mm projectile of 18 kg mass (see Fig. 4.7) is fired when various masses of explosive materials are detonated. The maximum velocity of the projectile is measured in order to calculate the maximum kinetic energy, which is used to compare with the simulation results.

The firing system is shown in Fig. 4.7. This projectile system is composed of two compartments. One is the right part, which holds the 18 kg projectile. Another is the left explosive chamber, which is used for the explosion. The total volume (the left and right chambers) and the volume of the explosive chamber are $1913\,\mathrm{cm}^3$ and $295\,\mathrm{cm}^3$, respectively. In this simulation, open boundary conditions are applied on all the boundaries of the fluid computational domain. The fluid element edge length is 0.005 m and the fluid time step size Δt_f is set to 4.0×10^{-7} s. The solid element edge length is 0.003 m and the solid time step size Δt_s is set to 0.5×10^{-7} s. The explosive material used here is nitroglycerin with the specified parameters of JWL-EOS as follow: $A = 190.7\,\mathrm{GPa}$, $B = 7.58\,\mathrm{GPa}$, $R_1 = 4.4$, $R_2 = 1.4$, $\omega = 0.23$

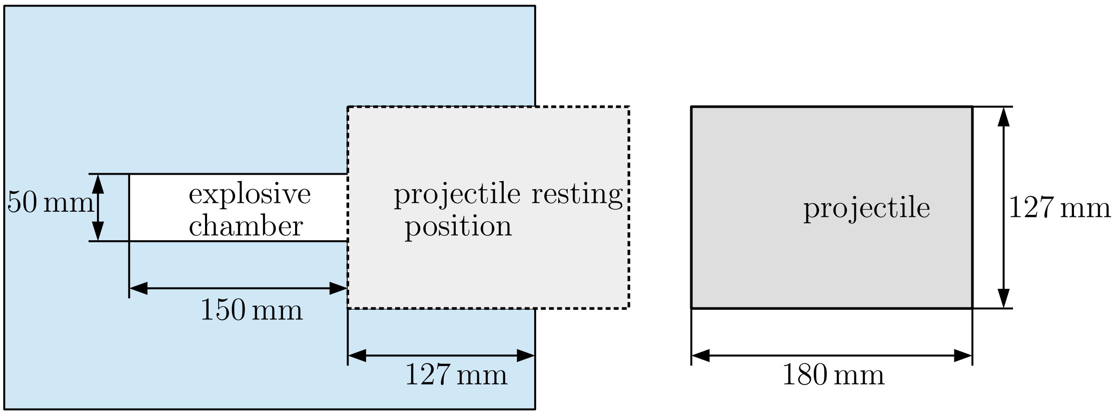

Figure 4.7 The geometry of the firing system.

and $E_0 = 7.237\,\mathrm{GPa}$. In this work, three different masses of nitroglycerin, as listed in Table 4.2, are simulated by the presented gas-solid interaction model.

Table 4.2 The density, maximum gas pressure, maximum projectile velocity and maximum kinetic energy for three different masses of explosives.

$M_e(g)$	ρ_{exp} (kg/m^3)	p_{exp} (Pa)	V_{max} (m/s)	E_{Cmax} (kNm)	E_{Emax} (kNm)	e_r^E
5.0	16.9	2.20×10^7	31.9	9.16	8.51	0.0764
10.0	33.9	4.41×10^7	43.6	17.11	17.02	0.0053
15.0	50.8	6.62×10^7	52.7	25.00	25.53	-0.0208

The production of a mixed gas with a high pressure is due to the detonation of the explosive material. When the high pressure acts on the left side of the projectile, it starts to accelerate. After the projectile moves rightwards (see Fig. 4.8), there is some space between the explosive chamber and the projectile's left surface. The gas expands and fills in this space immediately when the space appears. As the gas expands and propagates, the gas pressure and density are reduced. This process stops when the projectile reaches its terminal velocity.

The variations of the gas pressure and density; projectile velocity and kinetic energy in time of the three different explosive masses are shown in Fig. 4.9. For the gas pressure and density patterns, they are very similar and continuously decrease. Projectile velocity and kinetic energy time-series follow a similar pattern that begins with zero then increase non-linearly, reaching a maximum value, which remains

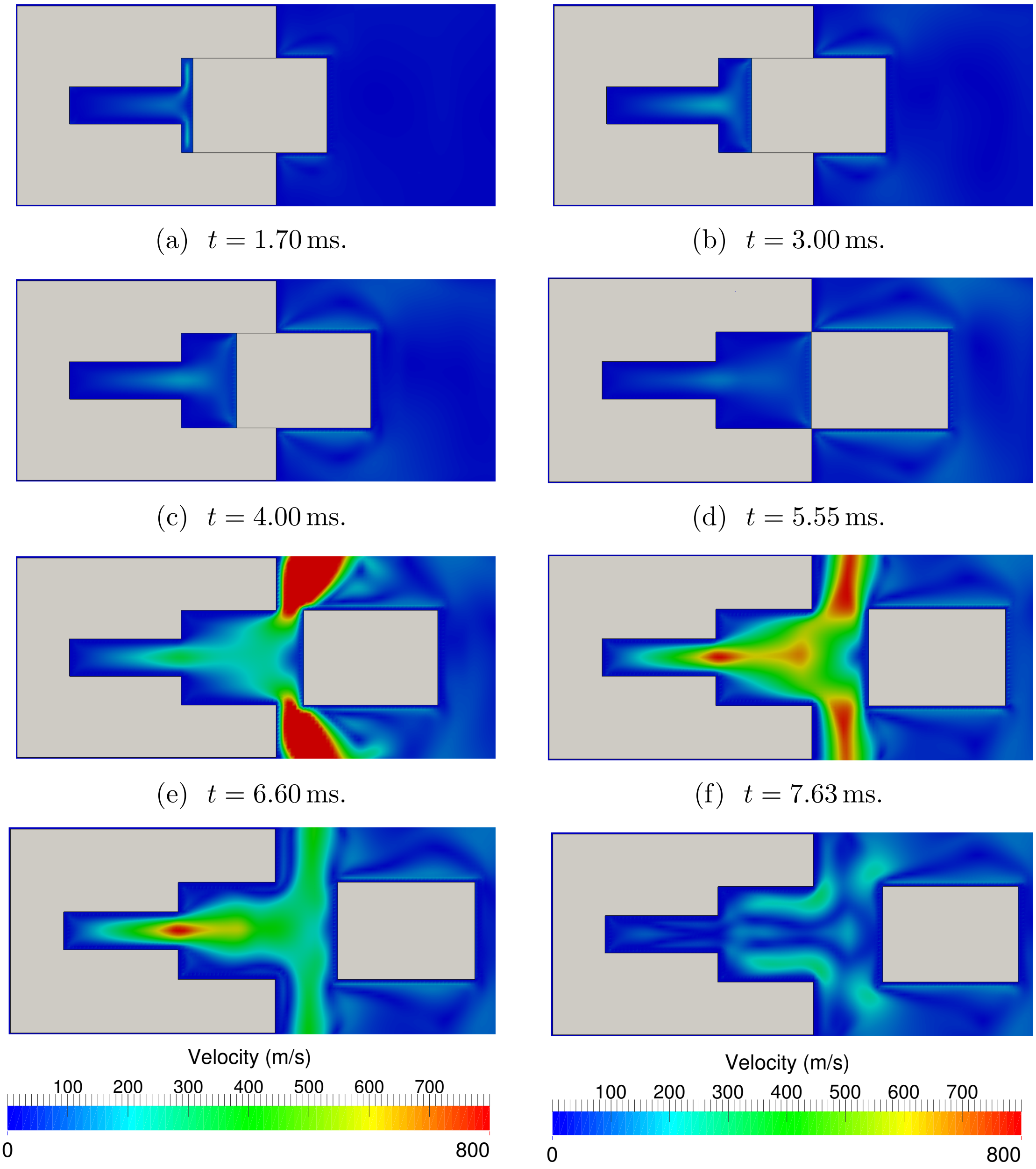

(a) $t = 1.70\,\mathrm{ms}$.
(b) $t = 3.00\,\mathrm{ms}$.
(c) $t = 4.00\,\mathrm{ms}$.
(d) $t = 5.55\,\mathrm{ms}$.
(e) $t = 6.60\,\mathrm{ms}$.
(f) $t = 7.63\,\mathrm{ms}$.
(g) $t = 7.81\,\mathrm{ms}$.
(h) $t = 8.10\,\mathrm{ms}$.

Figure 4.8 The snapshots of projectile position and gas velocity when the mass of the explosive material is 0.005 kg. Figure (a), (b), (c), (d), (e), (f), (g) and (h) refer to the snapshots at 1.70 ms, 3.00 ms, 4.00 ms, 5.55 ms, 6.60 ms ,7.63 ms , 7.81 ms and 8.10 ms, respectively.

constant shortly after the projectile leaves the projectile system.

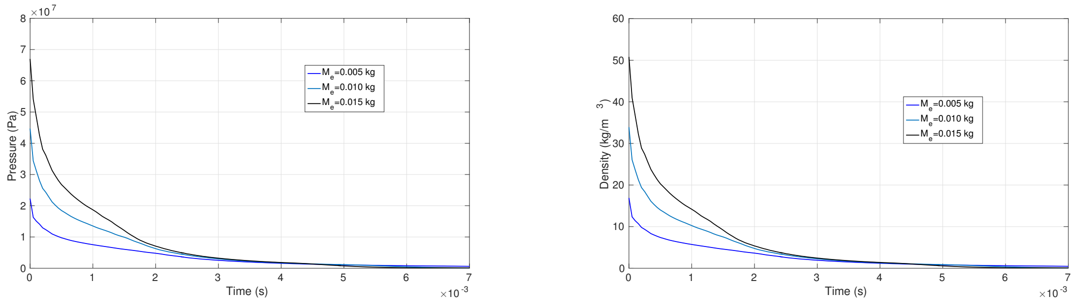

(a) Pressure history within the projectile system.

(b) Density history within the projectile system.

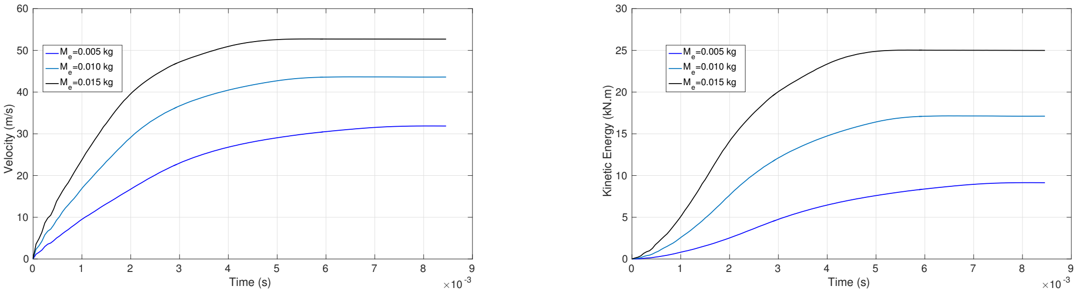

(c) Projectile velocity history.

(d) Projectile kinetic energy history.

Figure 4.9 Thermodynamic quantity histories for different values of M_e in the projectile system.

Fig. 4.8 shows the history of the projectile position and gas velocity profile when the mass of the explosive material is 0.005 kg. At $t = 1.70$ ms, the projectile has moved slightly rightwards, meanwhile, a small space occurred behind the left surface of the projectile. Following the expansion of the high-pressure gas into space, high gas velocity areas are found at the top and bottom sides in the space behind the projectile (see Fig. 4.8, a). When the projectile continues to move further to the right, the high gas velocity areas become much larger and concentrate on the centre of the chamber and the space behind the projectile (see Fig. 4.8, b and c). Extremely high gas velocity appears when the projectile departs from its compartment (see Fig. 4.8, d and e).

The contours of the stress inside the solid and the gas pressure when the mass of the explosive material is 0.005 kg are shown in Fig. 4.10 and Fig. 4.11. In the beginning, because of the high gas pressure on the surface of the chamber and the projectile left surface, high solid stresses are found near these surfaces (see Fig. 4.10, a–f). From

Fig. 4.10 a–f, we can clearly see the stress wave reflection inside the solid chamber and the projectile. As expected, large stresses inside the solid chamber appear at the two inner left vertices (see Fig. 4.10, a, b, d and e). As the projectile moves further rightwards, the vibration of the stress inside the solid appears. It is clear when comparing Fig. 4.11, k and l. At $t = 4.00\,\mathrm{ms}$ (see Fig. 4.11, k), the high stress area focuses on the upside and downside of the left chamber, whilst the high stress area transfers to the right-side of the chamber at $t = 5.55\,\mathrm{ms}$ (see Fig. 4.11, l). Importantly, when the projectile leaves its compartments, the stress inside the projectile immediately reduces to a low value (see Fig. 4.11, m).

The density, maximum gas pressure, maximum projectile velocity and maximum kinetic energy for three different masses of explosives are listed in Table 4.2. In this table, E_{Cmax} is the maximum kinetic energy calculated by the solid-gas interaction model, whilst E_{Emax} is the maximum kinetic energy presented in the literature (Johanson & Persson, 1970). The relative error e_r^E between E_{Cmax} and E_{Emax} is defined as:

$$e_r^E = \frac{E_{Cmax} - E_{Emax}}{E_{Emax}}. \tag{4.10}$$

Simulation results of the maximum kinetic energy are in good agreement with the experimental as can be seen in Table 4.2.

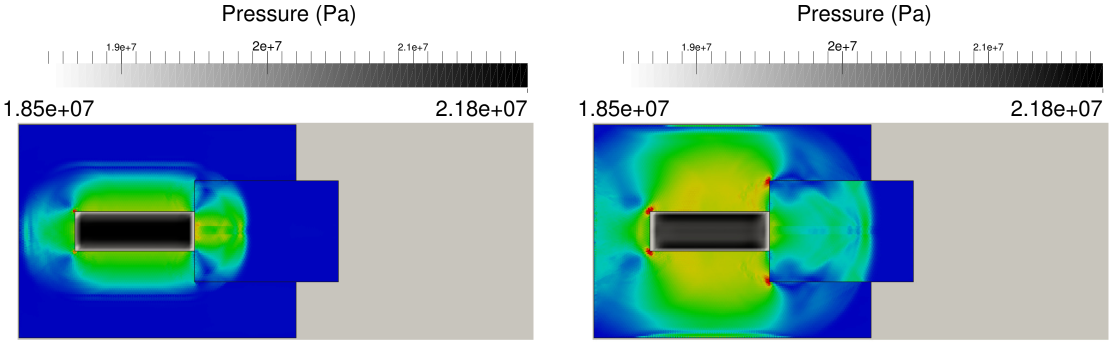

(a) $t = 0.01$ ms. (b) $t = 0.02$ ms.

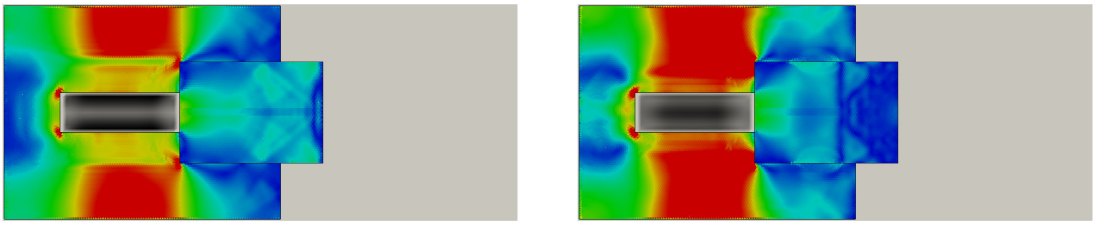

(c) $t = 0.03$ ms. (d) $t = 0.04$ ms.

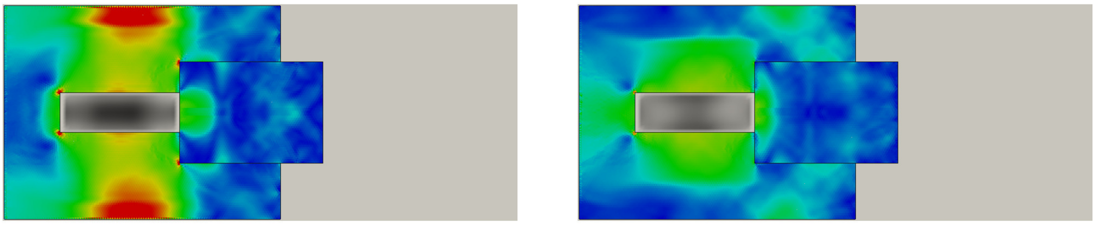

(e) $t = 0.05$ ms. (f) $t = 0.06$ ms.

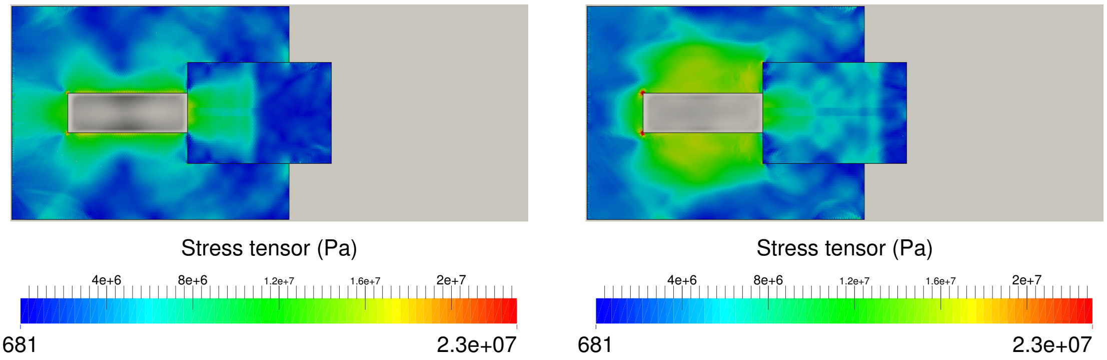

(g) $t = 0.07$ ms. (h) $t = 0.08$ ms.

Figure 4.10 The snapshots of projectile stress and gas pressure when the mass of the explosive material is 0.005 kg. Figure (a), (b), (c), (d), (e), (f), (g) and (h) refer to the snapshots at 0.01 ms, 0.02 ms, 0.03 ms, 0.04 ms, 0.05 ms, 0.06 ms, 0.07 ms and 0.08 ms, respectively.

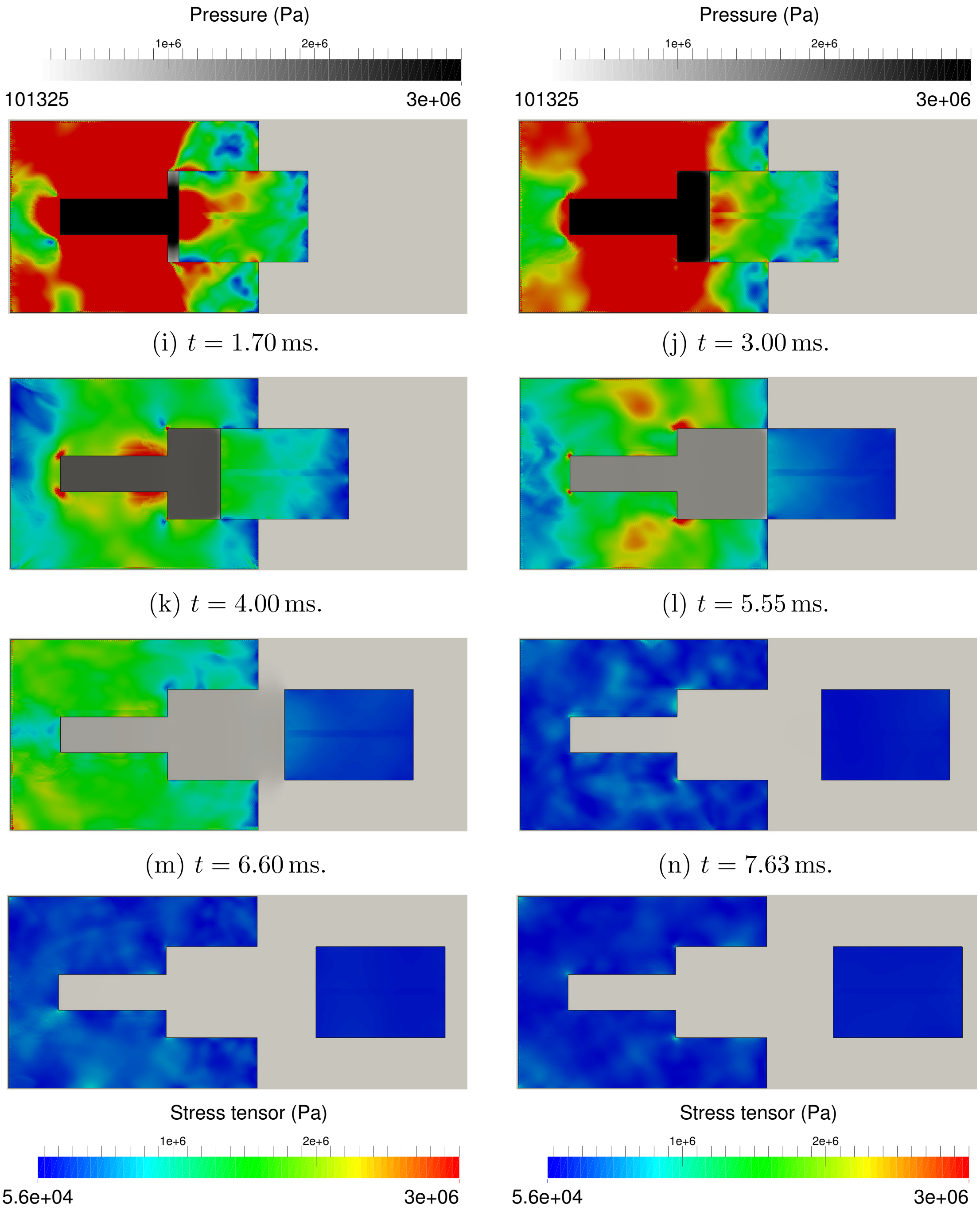

(i) $t = 1.70\,\mathrm{ms}$.

(j) $t = 3.00\,\mathrm{ms}$.

(k) $t = 4.00\,\mathrm{ms}$.

(l) $t = 5.55\,\mathrm{ms}$.

(m) $t = 6.60\,\mathrm{ms}$.

(n) $t = 7.63\,\mathrm{ms}$.

(o) $t = 7.81\,\mathrm{ms}$.

(p) $t = 8.10\,\mathrm{ms}$.

Figure 4.11 The snapshots of projectile stress and gas pressure when the mass of the explosive material is 0.005 kg. Figure (i), (j), (k), (l), (m), (n), (o) and (p) refer to the snapshots at 1.70 ms, 3.00 ms, 4.00 ms, 5.55 ms, 6.60 ms 7.63 ms, 7.81 ms and 8.10 ms, respectively.

4.5.3 Masonry block fragmentation due to an internal explosion

The final test case is that of bore-hole blasting in a square rock-block, which was previously studied by Mohammadi & Bebamzadeh (2005); Mohammadi & Pooladi (2012) and Sazid & Singh (2013). Mohammadi & Bebamzadeh (2005) firstly proposed a simplified square gas mesh coupled with a single solid mesh method. More recently, they extended this method to an unstructured solid mesh coupled with three different gas meshes. However, all the gas meshes are structured. In the presented approach, both the fluid and solid meshes are unstructured and use triangular elements (see Fig. 4.12). The fluid mesh is initially refined at the gas-solid interface (see Fig. 4.12, c), which enables an accurate simulation of the bore-hole test with different hole shapes to be performed. In this bore-hole blasting test case, a circular hole with the diameter 0.1 m is located at the centre of a 1 m × 1 m square rock-block (see Fig. 4.12). The meshes for the block and the gas are also shown in Fig. 4.12. In this simulation, open boundary conditions are applied on all the boundaries of the fluid computational domain. The largest fluid element edge length L is 0.02 m and the smallest fluid element edge length l is 0.005 m. The fluid time step size Δt_f is set to 0.5×10^{-7} s. The solid element edge length is 0.01 m and the solid time step size Δt_s is set to 0.5×10^{-7} s. The properties of the rock are as follow: density $\rho_s = 2340.0\,\mathrm{kg/m^3}$, Young's modulus $E = 2.66 \times 10^{10}$ Pa, penalty number $Pe = 2.0 \times 10^{10}$, fracture energy release rate $G_f = 200.0$, Poisson ratio $\nu = 0.205$, tensile strength $f_t = 4.0 \times 10^6$ Pa and shear strength $f_s = 1.4 \times 10^7$ Pa. In the centre hole, the explosive material, nitroglycerin is initially loaded. However, apart from the bore-hole area, the background space beyond the block is assumed to be a low pressure and density gas, which is given the pressure and density of the air but is modelled by the JWL-EOS of nitroglycerin. The initial pressure levels in the bore-hole and background are 1.8×10^8 Pa and 1.0×10^5 Pa, respectively. The initial gas densities in the bore-hole and the background are $70\,\mathrm{kg/m^3}$ and $1.205\,\mathrm{kg/m^3}$, respectively. The gas dynamic viscosity is $0.1\,\mathrm{Pa \cdot s}$.

In this blasting test case, the generation of the first set of cracks is due to the high bore-hole pressure. Initially, the crack tips are behind the front of the stress wave in the square rock when the stress wavefront moves from the centre to the boundaries of the square block (see Fig. 4.14). Subsequently, the stress wave is reflected by the boundaries, existing cracks are further propagated and the fragments are pushed to the edges of the computational domain (see Fig. 4.14, d). Before big cracks are

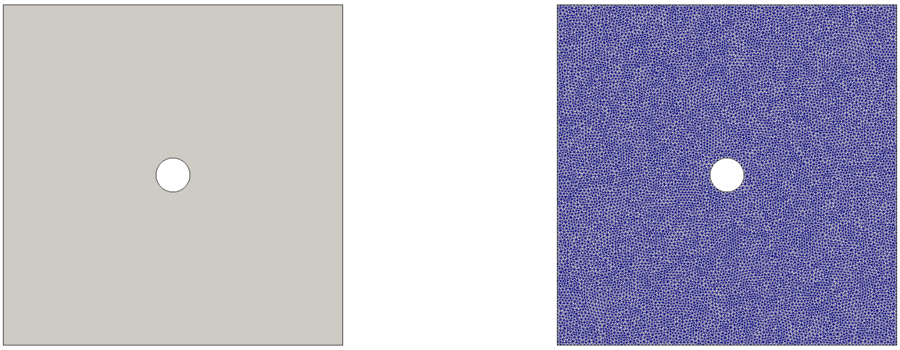

(a) The geometry of the square rock block. (b) The mesh of the square rock block.

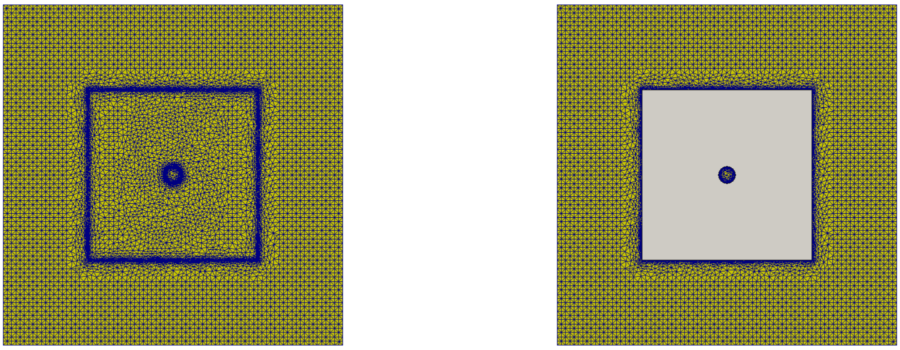

(c) The fluid mesh. (d) The square rock block immersed in the fluid mesh.

Figure 4.12 The geometry and mesh for the square rock block, and the gas mesh.

created, the highly pressurized gas remains in the centre bore-hole, which results in a low rate of reduction of thermodynamic quantities including pressure, density and mass.

The profile of the solid velocity inside the block is shown in Fig. 4.14. From $t = 0.14\,\text{ms}$ (Fig. 4.14, a) to $t = 0.30\,\text{ms}$ (Fig. 4.14, b), the stress wave inside the square rock moves from the inner core to the boundaries. Then it is reflected back by the boundaries at $t = 0.30\,\text{ms}$ (Fig. 4.14, b), and high solid velocity areas are found near boundaries. Following, the high solid velocity areas are always found near the bore-hole (see Fig. 4.14, e and f).

The time history of the bore-hole gas pressure near the internal surface of the block is shown in Fig. 4.13, a. The exponential reduction in pressure is as would be expected for an internal blast. It can be seen that similar results have been obtained

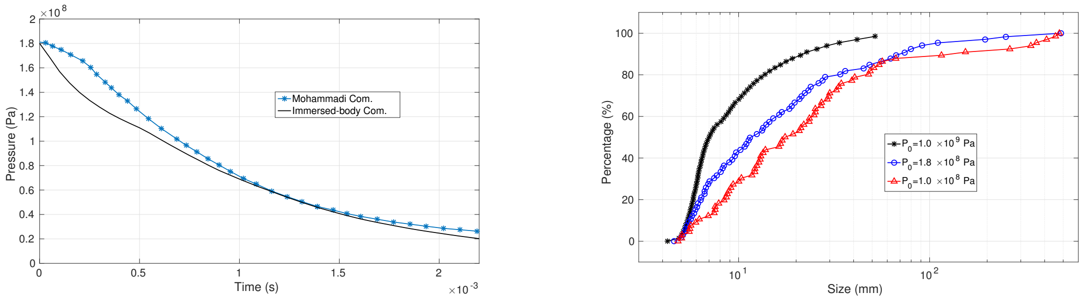

(a) Gas pressure history of bore-hole blasting test at the blasting core for $p_0 = 1.8 \times 10^8$ Pa.

(b) Fragment size distribution for different initial pressures at $t = 1.86$ ms.

Figure 4.13 (a) The black line and the blue star line represent the numerical results of the immersed-body method and Mohammadi two-mesh coupled model (Mohammadi & Pooladi, 2012), respectively. (b) The black, blue, red lines stand for three different initial pressures: $p_0 = 1.0 \times 10^9$ Pa, $p_0 = 1.8 \times 10^8$ Pa and $p_0 = 1.0 \times 10^8$ Pa, respectively.

by Mohammadi using a two-mesh coupled model (Mohammadi & Pooladi, 2012).

In order to evaluate the influence of the initial pressure on the blasting process, three simulations are performed using different initial pressure levels in the bore-hole: $p_0 = 1.0 \times 10^9$ Pa, $p_0 = 1.8 \times 10^8$ Pa and $p_0 = 1.0 \times 10^8$ Pa. For the very high pressure test case, $p_0 = 1.0 \times 10^9$ Pa, the crack pattern and solid velocity are given in Fig. 4.15, which are very close to the results that Munjiza *et al.* (2000) obtained. From comparison of the fracture patterns for $p_0 = 1.8 \times 10^8$ Pa (Fig. 4.14, d) and $p_0 = 1.0 \times 10^9$ Pa (Fig. 4.15, d) at $t = 1.86$ s, we can see that the big cracks first appear at boundaries for the high pressure test case, since the stress wave dominates at $p_0 = 1.0 \times 10^9$ Pa test case. We also show the tensile and shear failure in Fig. 4.14 and 4.15. It is seen that lots of cracks are generated by the stress wave during the fragmentation phase, where the shear failure occurs. The fragment size distribution for these three test cases is shown in Fig. 4.13, b. It is seen that the higher the initial pressure, the more small fragments are produced.

Based on this solid-gas interaction model, we can extend this work to fragmentation analysis, for instance, evaluate size distributions (Xiang *et al.*, 2010). Furthermore, we can apply this model to simulate the growth of pre-existing fractures (Lei *et al.*, 2014) and stresses on the boundaries.

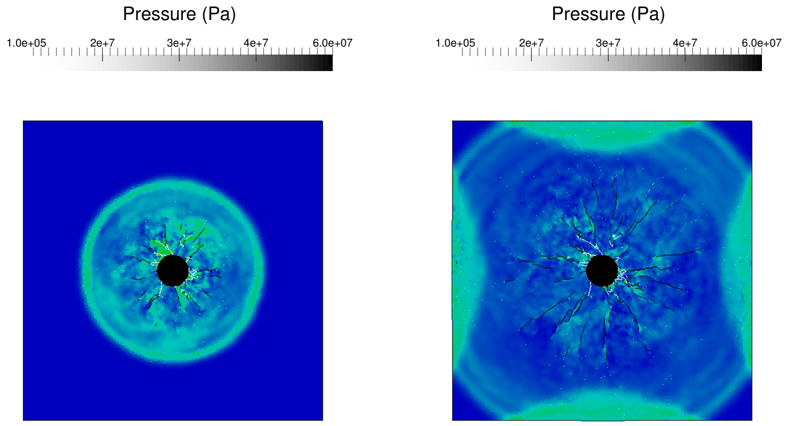

(a) $t = 0.14\,\mathrm{ms}$. (b) $t = 0.30\,\mathrm{ms}$.

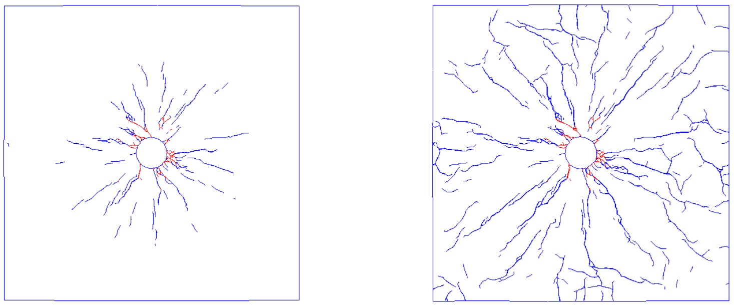

(c) $t = 0.30\,\mathrm{ms}$. (d) $t = 0.64\,\mathrm{ms}$.

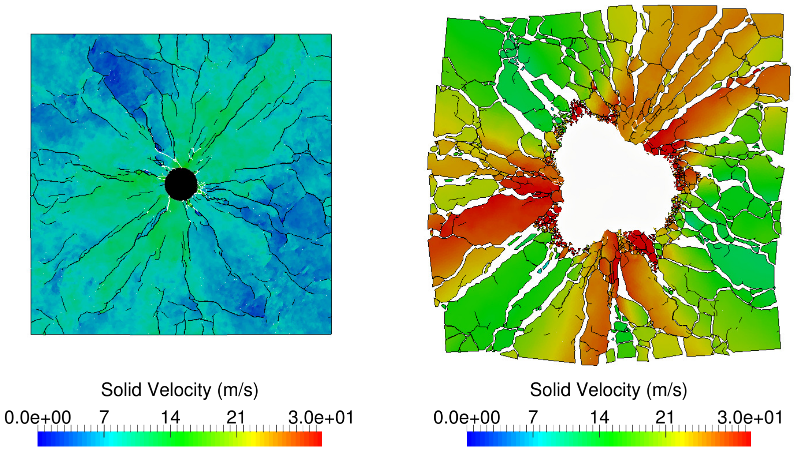

(e) $t = 0.64\,\mathrm{ms}$. (f) $t = 5.70\,\mathrm{ms}$.

Figure 4.14 The snapshots of the crack and solid velocity inside the square rock block for test case $p_0 = 1.8 \times 10^8\,\mathrm{Pa}$. Figure (a), (b), (e) and (f) refer to the snapshots at $0.14\,\mathrm{ms}$, $0.30\,\mathrm{ms}$, $0.64\,\mathrm{ms}$ and $5.70\,\mathrm{ms}$. Figure (c) and (d) show different fracture type at $0.30\,\mathrm{ms}$ and $0.64\,\mathrm{ms}$, where blue and red crack stand for the tensile and shear failure, respectively.

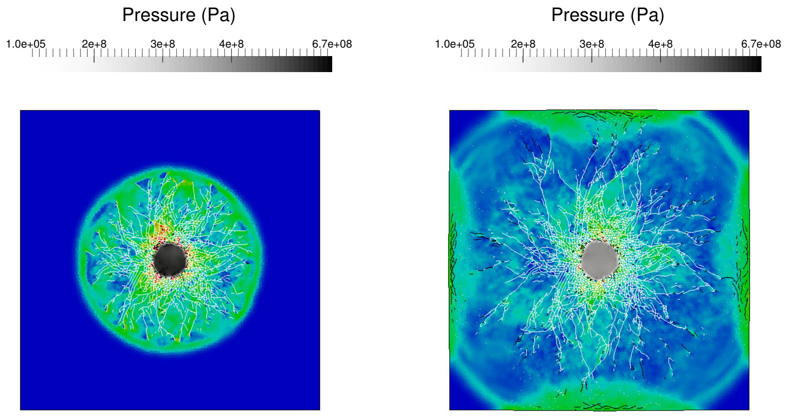

(a) $t = 0.14\,\text{ms}$. (b) $t = 0.30\,\text{ms}$.

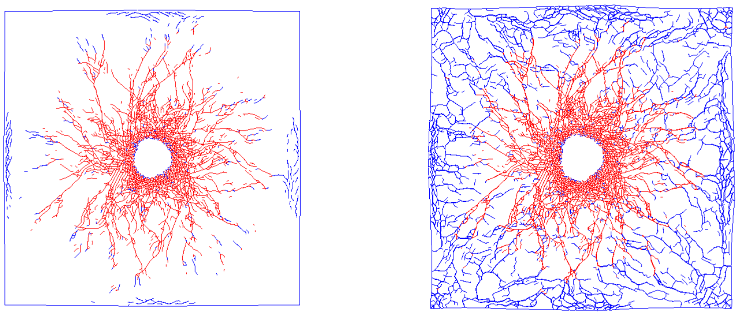

(c) $t = 0.30\,\text{ms}$. (d) $t = 0.64\,\text{ms}$.

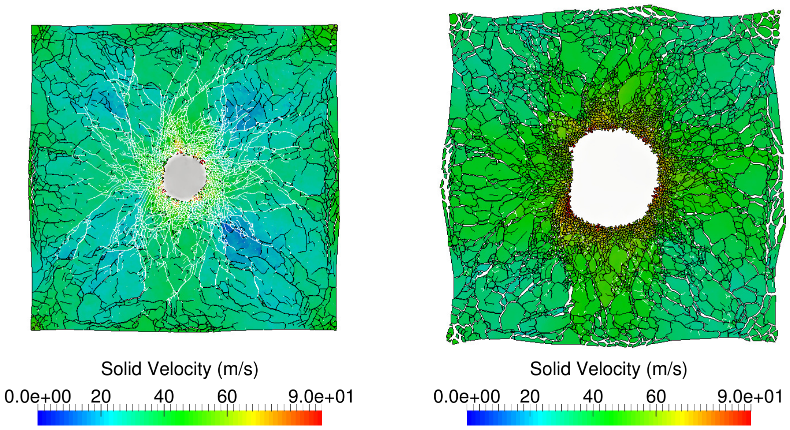

(e) $t = 0.64\,\text{ms}$. (f) $t = 1.86\,\text{ms}$.

Figure 4.15 The snapshots of the crack and solid velocity inside the square rock block for test case $p_0 = 1.0 \times 10^9\,\text{Pa}$. Figure (a), (b), (e) and (f) refer to the snapshots at 0.14 ms, 0.30 ms, 0.64 ms and 1.86 ms. Figure (c) and (d) show different fracture type at 0.30 ms and 0.64 ms, where blue and red crack stand for the tensile and shear failure, respectively.

4.6 Concluding remarks

The FSI model coupled with a cohesive zone fracture model is presented and validated in this Chapter. This coupling model combines an immersed-body method and a cohesive zone fracture model. The whole complex blasting process including both fragmentation and burden movement phases is simulated in this complete coupling model. A new mesh conversion algorithm to convert discontinuous meshes to continuous meshes has been implemented and demonstrated in section 4.4.2. The detonation gas in the model is resolved by the JWL-EOS as a highly compressible fluid, which is close to the realistic behaviour of the detonation gas in common mining explosions. Importantly, it is easy to extend the equation of state in this model to more practical equation of states. Additionally, this model in combination with the Q-scheme is stable when dealing with extremely high pressure and velocity situations. Two benchmark cases, the blasting cylinder and projectile fire, are used to validate this gas-solid interaction model. The numerical simulation results of these two test cases are in good agreement with the available experimental data. A practical complicated blasting engineering simulation with shock waves, fracture propagation, gas-solid interaction and flying fragments is simulated to demonstrate the ability of the gas-solid interaction model. At the following chapter, the benchmark and validation test cases of the developed FSI model for turbulent flows are going to be presented.

Chapter

FIVE

Turbulence flow FSI model

Before apply the developed URANS FSI model for turbulent flows to industrial applications, detailed validation is required. Thus, this chapter validates the FSI model developed in chapter 2 for turbulent flows in both 2D and 3D. The validation includes five series of test cases. Both the 2D and 3D test cases have obtained comparable results with those numerical and experimental data in the literature. Some of the test cases have obtained the same results as the numerical data in the literature, others have achieved better results than the numerical data in the literature compared to the experimental data. The results show that the immersed-body method is an effective, accurate and reliable approach for two-way solid-fluid coupling in turbulent flows.

5.1 Introduction

This chapter validates the solid-fluid coupling model for turbulent flows using both 2D and 3D cases. It is organised as follows. Section 5.2 presents the first test case: the flow over a circular cylinder at $Re = 3900$. The second test case of turbulent flow over a static NACA0015 aerofoil with an attack angle of $\alpha = 60°$ at $Re = 5200$ is given in section 5.3. Section 5.4 shows the third test case of a free rising circular cylinder in a fluid at rest with $Re = 5000$ and $Re = 3800$. The fourth test case of a free rising sphere in a fluid at rest with $Re = 6000$ and 10000 is also presented in section 5.5. Section 5.6 presents the final test case: flow bending a 3D elastic plate. The list of the test cases in this chapter is shown in Table 5.1. I discuss the strength and weaknesses of this approach and draw conclusions in Section 5.8. To make all the simulations stable, the Courant-Friedrichs-Lewy (CFL) number is controlled under 1.0 in all the following test cases.

Table 5.1 Turbulence flow test cases

Section	Case name	Case purpose
Section 5.2	Flow over a circular cylinder at $Re = 3900$	Validation
Section 5.3	Turbulent flow over a static NACA0015 aerofoil with an attack angle of $\alpha = 60°$ at $Re = 5200$	Qualitative comparison
Section 5.4	A free rising circular cylinder in a fluid at rest with $Re = 5000$ and $Re = 3800$	Validation
Section 5.5	A free rising sphere in a fluid at rest with $Re =$ 6000 and 10000	Validation
Section 5.6	Flow bending a 3D elastic plate	Validation

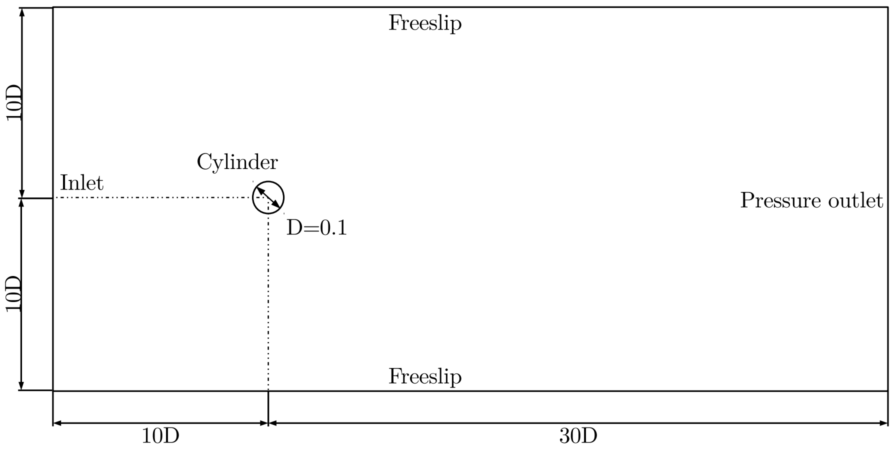

Figure 5.1 The computational domain and settings of the flow over a cylinder at $Re = 3900$.

5.2 Flow over a circular cylinder at $Re = 3900$

The following test case is the flow over a circular cylinder at $Re = 3900$. A schematic of the computational domain is shown in Fig. 5.1. This is a benchmark test case for validating turbulence models and an abundance of reference data exists, see Refs. (Meyer *et al.*, 2010b,a; Ong & Wallace, 1996; Breuer, 1998; Kravchenko & Moin, 2000; Franke & Frank, 2002; Parnaudeau *et al.*, 2008; Gnanaskandan & Mahesh, 2016). The Reynolds number for this test case is defined as:

$$Re = \frac{\rho_\infty U_\infty D}{\mu_\infty}, \tag{5.1}$$

where, ρ_∞ is the reference density, U_∞ is the free stream velocity, D is the diameter of the cylinder and μ_∞ is the reference dynamic viscosity. Here, $\rho_\infty = 1.0$, $D = 0.1$, $U_\infty = 1.0$ and $\mu_\infty = 2.5641 \times 10^{-5}$.

The fixed fluid mesh used in this case is shown in Fig. 5.2. The minimum and maximum mesh edge lengths are 0.002 and 0.1, respectively. Fig. 5.3a shows the instantaneous vorticity field of the turbulent wake behind the cylinder. Similar qualitative results are found in (Singh & Mittal, 2005; Breuer, 1998; Kravchenko & Moin, 2000).

For quantitative comparison, all parameters are obtained after the steady vortex

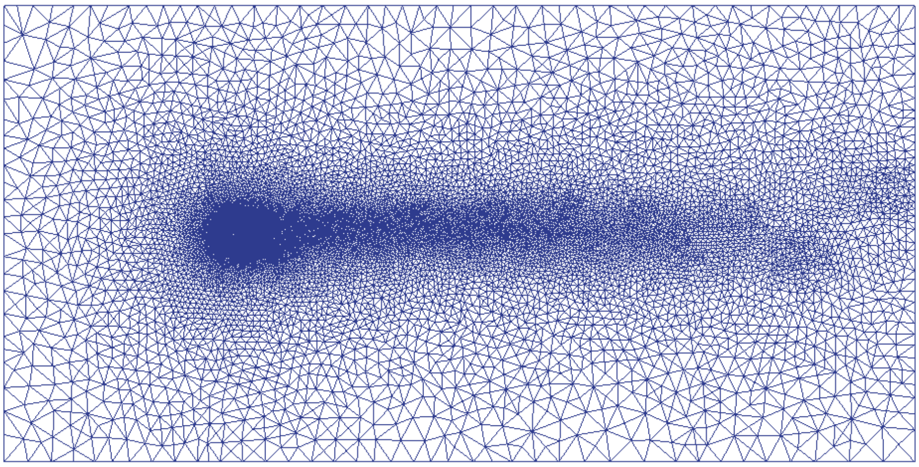

Figure 5.2 The computational mesh of the flow over a cylinder at $Re = 3900$.

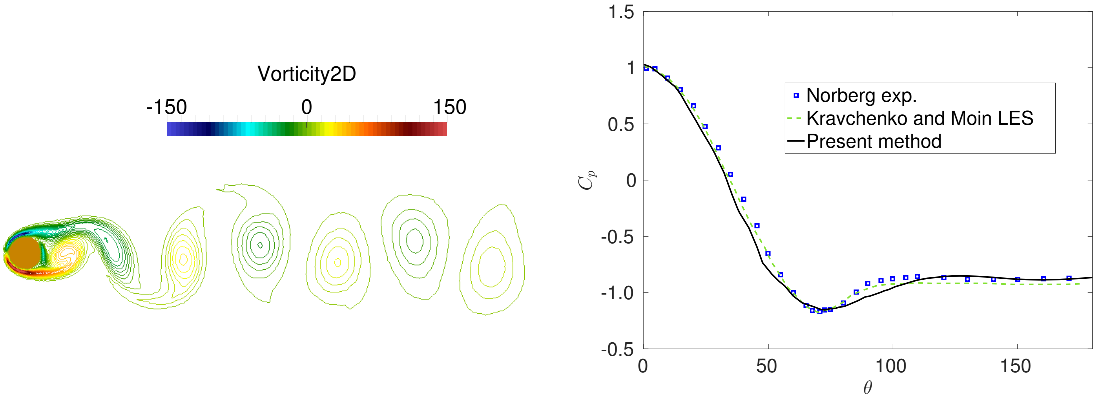

(a) (b)

Figure 5.3 (a) The instantaneous vorticity field of the turbulent wake behind the cylinder at $Re = 3900$. (b) Pressure coefficient C_p around the circular cylinder surface from the stagnation point where $\theta = 0$ at $Re = 3900$; □: Norberg (1987) (experiment); – –: Kravchenko & Moin (2000) (LES); –: Present immersed-body URANS model.

shedding was established. The surface pressure coefficient is defined as:

$$C_p = 2\frac{p - p_\infty}{\rho_\infty U_\infty^2}, \tag{5.2}$$

where p_∞ is the pressure value in the far field. the results of pressure coefficient are compared with the experimental data by Norberg extracted from Kravchenko & Moin (2000) and the numerical results found in (Meyer *et al.*, 2010b,a). Fig. 5.3b shows that the pressure coefficient C_p obtained by the presented immersed-body URANS model is in good agreement with the experimental data of Kravchenko & Moin (2000) and numerical results of Kravchenko & Moin (2000).

Table 5.2 summaries the mean flow parameters from Refs. (Kravchenko & Moin, 2000; Parnaudeau *et al.*, 2008; Dröge, 2007; Meyer *et al.*, 2010b,a; Ong & Wallace, 1996) and the present FSI model, i.e. the mean drag coefficient $C_D = 2\frac{F_D}{\rho_\infty U_\infty^2 D}$ (F_D is the drag force), Strouhal number $S_t = \frac{fD}{U_\infty}$ (f is the frequency of the vortex shedding), bulk suction coefficient, mean separation angle and mean recirculation length. It shows that all quantities calculated from the present model are in the range of experimental data and the previous results of direct numerical simulations (DNS) in (Ma *et al.*, 2000; Dröge, 2007) and large eddy simulations (LES) in (Beaudan & Moin, 1994; Mittal, 1996; Fröhlich *et al.*, 1998; Franke & Frank, 2002; Kravchenko & Moin, 2000; Park *et al.*, 2004; Mahesh *et al.*, 2004; Meyer *et al.*, 2010b).

The flow over a circular cylinder has been investigated both numerically and experimentally, e.g. the particle-image velocimetry (PIV) data of Parnaudeau *et al.* (2008) and Dröge (2007), the hot-wire measurements (HWA) of Parnaudeau *et al.* (2008) and Ong & Wallace (1996), and the LES results from Kravchenko & Moin (2000). The present numerical results are compared with the results in (Parnaudeau *et al.*, 2008; Dröge, 2007; Parnaudeau *et al.*, 2008; Kravchenko & Moin, 2000). Fig. 5.4a shows the mean streamwise velocity $\bar{u}/U_\infty$ along the centreline and is found to be a good agreement with the PIV experimental data (Parnaudeau *et al.*, 2008) and the numerical simulation data in (Meyer *et al.*, 2010b,a; Kravchenko & Moin, 2000). It seems that there were some uncontrolled factors that caused a dip at $x/D = 3$ in Lourenco and Shih's experiment (Lourenco & Shih, 1993), since none of our results and the simulation results in (Meyer *et al.*, 2010b,a; Kravchenko & Moin, 2000) capture the dip at $x/D = 3$. The mean velocity profiles at different locations of x/D and the Reynolds normal stresses $u'u'/U_\infty^2$ are shown in Fig. 5.4b-d. These results are also in good agreement with simulation data in (Meyer *et al.*, 2010b,a; Kravchenko & Moin, 2000) and the experimental data in (Parnaudeau *et al.*, 2008).

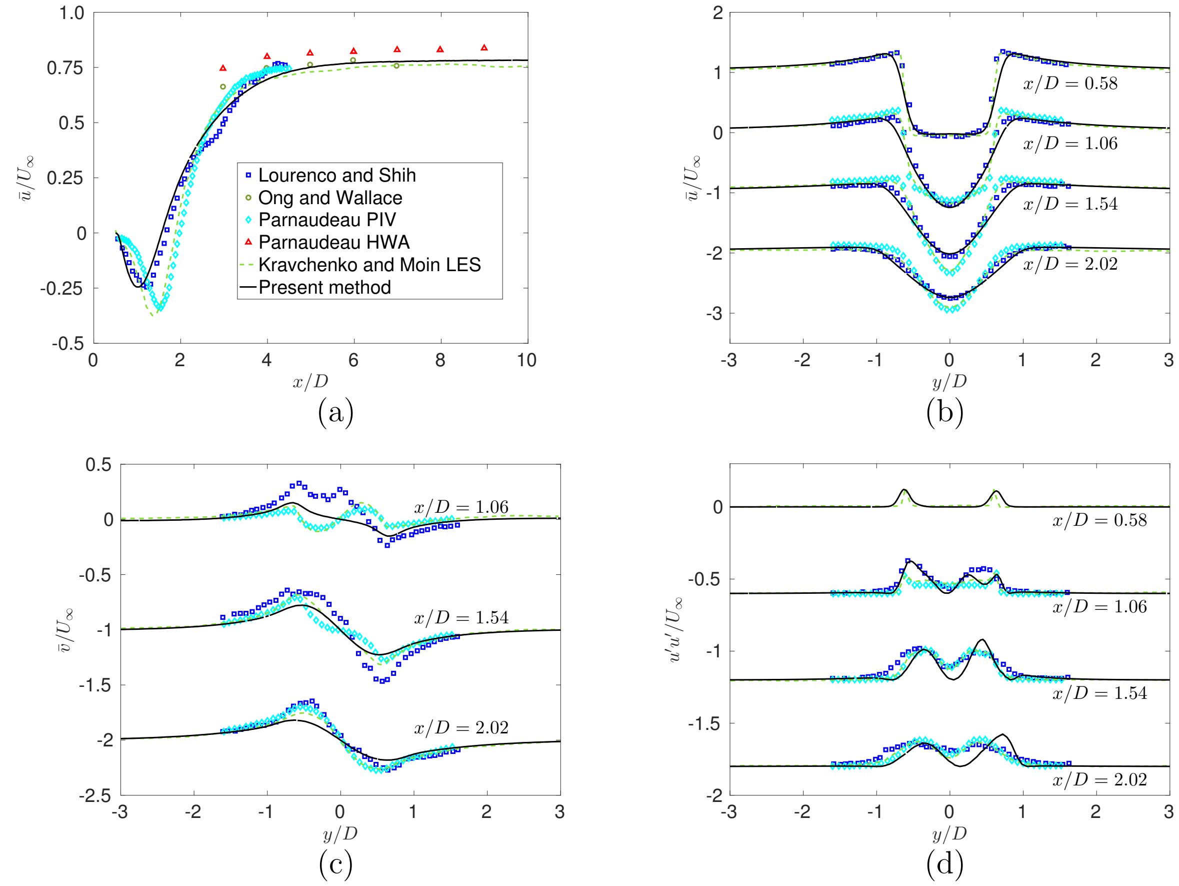

(a)

(b)

(c)

(d)

Figure 5.4 Comparison of velocity fields with experimental data and numerical results in literature for the flow over a circular cylinder at $Re = 3900$ test case. (a) Mean streamwise velocity along the centreline of the circular cylinder; (b) Mean streamwise velocity along four different vertical lines at $x/D = 0.58$, $x/D = 1.06$, $x/D = 1.54$ and $x/D = 2.02$, respectively; (c) Mean transverse velocity along three different vertical lines at $x/D = 1.06$, $x/D = 1.54$ and $x/D = 2.02$, respectively; (d) Streamwise velocity fluctuations along four different vertical lines at $x/D = 0.58$, $x/D = 1.06$, $x/D = 1.54$ and $x/D = 2.02$, respectively; in the wake of the flow over circular cylinder at $Re = 3900$. □: Lourenco & Shih (1993) (experiment); ○: Ong & Wallace (1996) (experiment); ♢: Parnaudeau *et al.* (2008) (experiment, PIV); △: Parnaudeau *et al.* (2008) (experiment, HWA); – –: Kravchenko & Moin (2000) (LES); –: Present immersed-body URANS model.

Table 5.2 Global flow quantity comparisons for the flow over a cylinder at $Re = 3900$ test case. This table includes mean pressure drag coefficient C_D. mean base pressure coefficient (bulk suction coefficient) C_{pb}, mean separation angle θ_{sep}, mean recirculation bubble length L_r/D, Strouhal number S_t, and minimum mean streamwise velocity U_{min}. The first group is the experimental data. The second and third groups are the LES and DNS model data in the previous literature, respectively. The last group is simulation results of present immersed-body URANS model.

Research	C_D	C_{pb}	θ_{sep}	L_r/D	S_t	U_{min}
Son & Hanratty (1969) (experiment)	–	–	85°/86°	–	–	–
Norberg (1987) (experiment)	0.98	-0.9	–	–	0.210	–
Cardell (1993) (experiment)	–	–	–	1.33	0.215	–
Lourenco & Shih (1993) (experiment)	0.99	–	86°	1.19	0.215	-0.24
Ong & Wallace (1996) (experiment)	–	–	–	–	0.210	–
Parnaudeau *et al.* (2008) (experiment)	–	–	–	1.51	0.208	–
Beaudan & Moin (1994) (LES)	1.01	-0.94	84.8°	1.36	0.203	-0.31
Mittal (1996) (LES)	1.0	-0.93	86.9°	1.4	0.207	-0.35
Fröhlich *et al.* (1998) (LES)	1.08	-1.03	88.1°	1.09	0.216	-0.24
Kravchenko & Moin (2000) (LES)	1.04	-0.94	88°	1.35	0.210	-0.37
Franke & Frank (2002) (LES)	0.98	-0.85	88.2°	1.64	0.209	–
Mahesh *et al.* (2004) (LES)	1.00	–	87.6°	1.35	0.218	-0.31
Park *et al.* (2004) (LES)	1.02	-0.89	–	1.37	0.209	-0.33
Meyer *et al.* (2010b) (LES)	1.05	-0.92	88°	1.38	0.210	–
Ma *et al.* (2000) (DNS)	0.96	-0.96	89.1°	1.12	0.203	–
Dröge (2007) (DNS)	1.01	-0.88	87.7°	1.26	0.210	-0.32
Present immersed-body URANS model	1.04	-0.92	87.7°	1.1	0.208	-0.283

5.3 Turbulent flow over a static NACA0015 aerofoil with an attack angle of $\alpha = 60°$ at $Re = 5200$

The following test case is the turbulent flow over a static NACA0015 aerofoil with an attack angle of $\alpha = 60°$ at $Re = 5200$. This test case has been studied both experimentally (Freymuth, 1985; Freymuth *et al.*, 1985; Sengupta *et al.*, 2007) and numerically (Sengupta *et al.*, 2007; Milthaler, 2014). It was first set up by Freymuth (1985) who studied accelerated flows over static NACA0015 aerofoils at various Reynolds numbers experimentally.

The configuration of this computational case is the same as in the literature (Freymuth, 1985). The inlet velocity is given as:

$$u_{inlet} = at, \tag{5.3}$$

where t is the time, and $a = 2.4$ is the acceleration. The Reynolds number in the literature (Freymuth, 1985) is defined as:

$$Re = \frac{\rho_\infty a^{\frac{1}{2}} c^{\frac{3}{2}}}{\mu_\infty}, \tag{5.4}$$

where the reference fluid density $\rho_\infty = 1.0$, the chord length of the NACA0015 aerofoil $c = 0.152$, and the reference dynamic viscosity $\mu = 1.5387 \times 10^{-5}$ (see Fig. 5.5).

Using the anisotropic mesh adaptivity, the mesh is refined in the turbulent wake according to the velocity field. The mesh is also refined at the immersed-body surface to resolve the flows generated by the presence of the solid object. In Fig. 5.6, it is clear that the use of mesh adaptivity enables resolving the solid object and evolving velocity field. The minimum mesh edge length is 5.0×10^{-4} and the maximum mesh edge length is 0.4. In Fig. 5.6, it is found that the use of mesh adaptivity can resolve the details of vorticities near the aerofoil wake.

The stream-wise visualization profiles at every $1/64\,\mathrm{s}$ are given at Freymuth's experiment (Freymuth, 1985) in the time range $t = [24/64, 64/64]\,\mathrm{s}$. Sengupta *et al.* (2007) carried out a numerical simulation of this experiment using a structured, fixed mesh. In their simulations, only 8 snapshots were shown and compared with the experimental data in (Freymuth, 1985). Later, Milthaler (2014) performed the same simulation by DNS. The simulation results of the presented model are compared

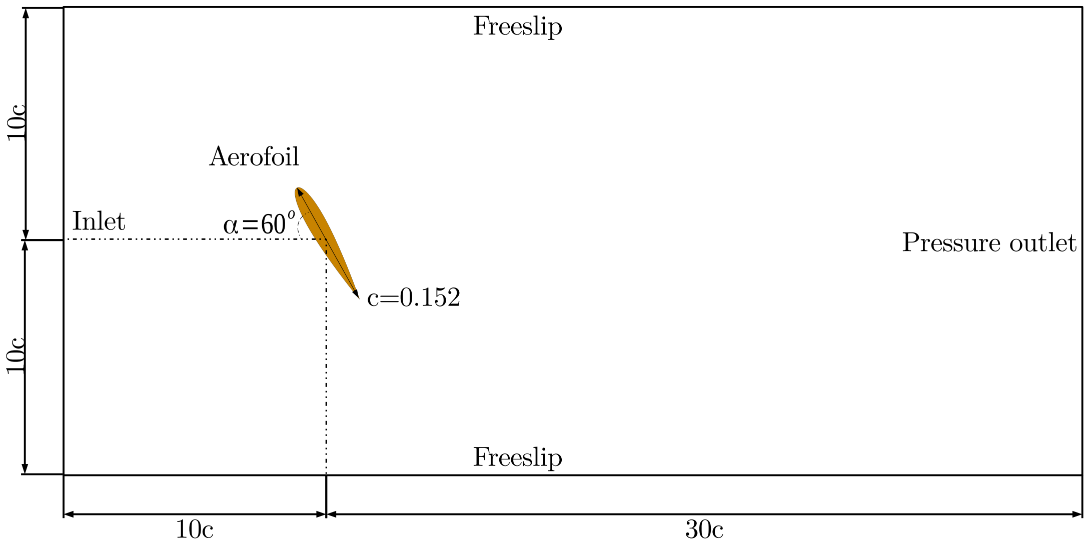

Figure 5.5 The computational domain and settings of the flow over a static NACA0015 aerofoil with an attack angle of $\alpha = 60°$ at $Re = 5200$.

with both the numerical (Sengupta *et al.*, 2007; Milthaler, 2014) and experimental (Freymuth, 1985) data.

The pressure contours are shown in Fig. 5.7. The results obtained from the present model are in good agreement with the pressure contours in Fig. 14 in (Sengupta *et al.*, 2007) and Fig. 4.5 in (Milthaler, 2014). The present model captures the developing of the pressure contours along both the rear and leading edges of aerofoil very well. From Fig. 5.7, it can be clearly seen that the low-pressure contours along the upper surface of the aerofoil. From Fig. 5.7a-c, it can be found that a low-pressure centre is generated at the back of the leading edge on the aerofoil. Then this low-pressure centre grows larger and larger when it moves to the downstream. When this low pressure centre moves downstream, two small low pressure centres appear at the leading edge and another one at the rear edge at $t = \frac{40}{64}$ s (see Fig. 5.7d). These small low-pressure centres then move to the downstream and more small ones are created one after another at the back of the leading edge (see Fig. 5.7e-f). However, the small pressure centre at the back of the rear edge continues to increase its size and move downstream, while no more small pressure centres appear at the back of the rear edge (see Fig. 5.7e-f).

The velocity profiles and streamlines obtained from the present model are given in Figs. 5.8 and 5.9. For the velocity profiles, the larger velocity areas are found near

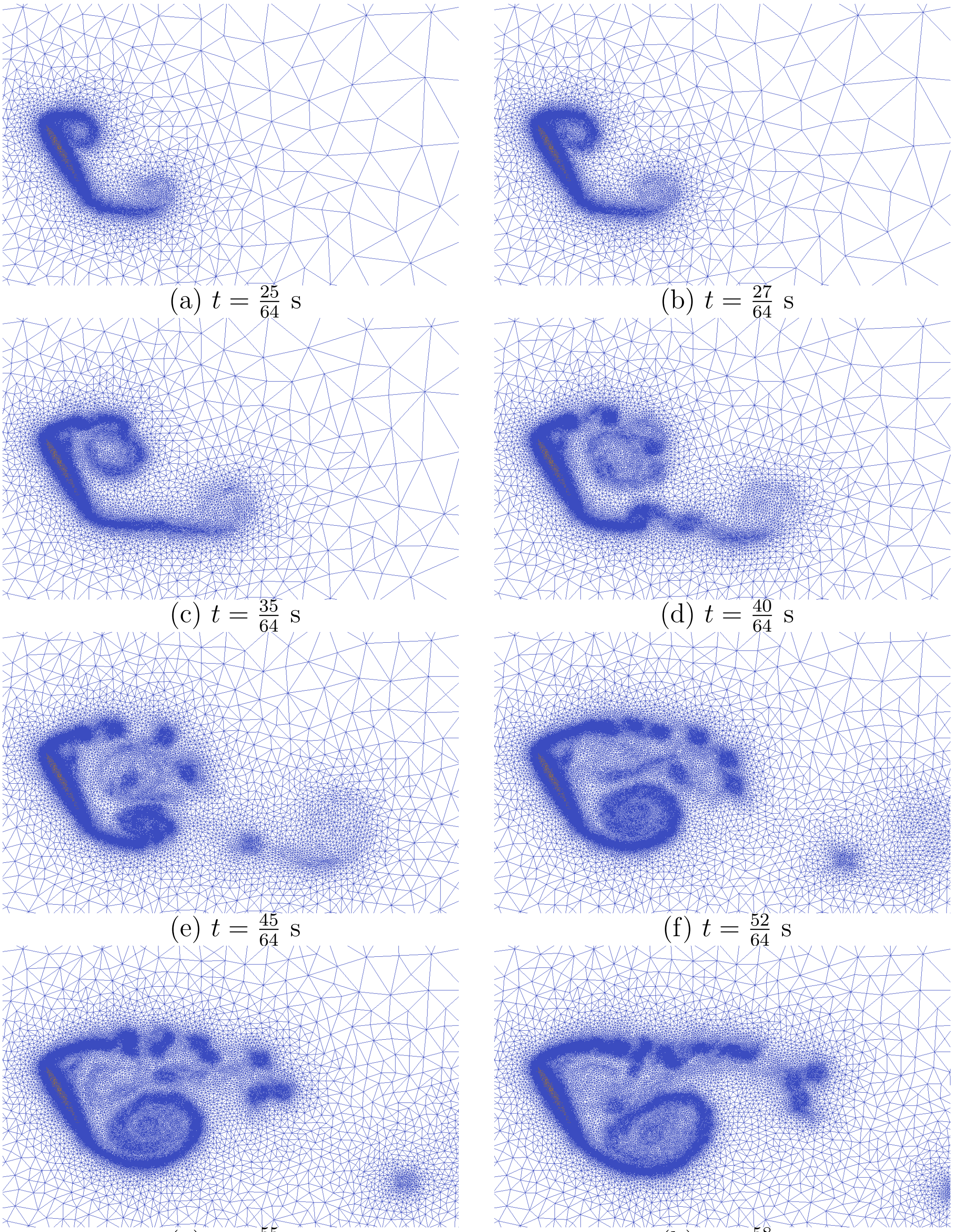

(a) $t = \frac{25}{64}$ s

(b) $t = \frac{27}{64}$ s

(c) $t = \frac{35}{64}$ s

(d) $t = \frac{40}{64}$ s

(e) $t = \frac{45}{64}$ s

(f) $t = \frac{52}{64}$ s

(g) $t = \frac{55}{64}$ s

(h) $t = \frac{58}{64}$ s

Figure 5.6 The fluid mesh at different times of the flow over a NACA0015 aerofoil at $Re = 5200$ and attack angle $\alpha = 60°$: (a) $t = \frac{25}{64}$ s, (b) $t = \frac{27}{64}$ s, (c) $t = \frac{35}{64}$ s, (d) $t = \frac{40}{64}$ s, (e) $t = \frac{45}{64}$ s, (f) $t = \frac{52}{64}$ s, (g) $t = \frac{55}{64}$ s and (h) $t = \frac{58}{64}$ s.

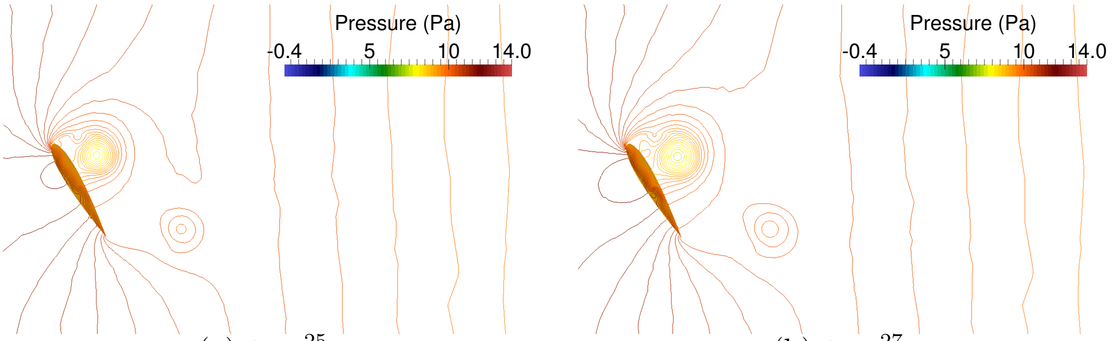

(a) $t = \frac{25}{64}$ s (b) $t = \frac{27}{64}$ s

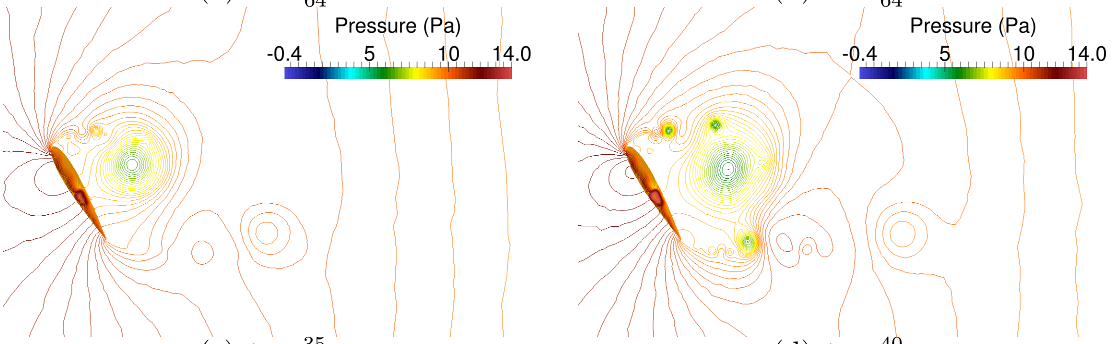

(c) $t = \frac{35}{64}$ s (d) $t = \frac{40}{64}$ s

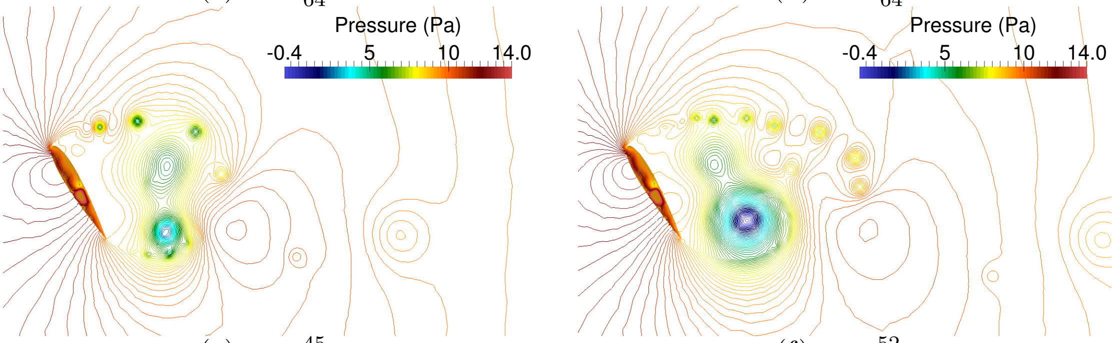

(e) $t = \frac{45}{64}$ s (f) $t = \frac{52}{64}$ s

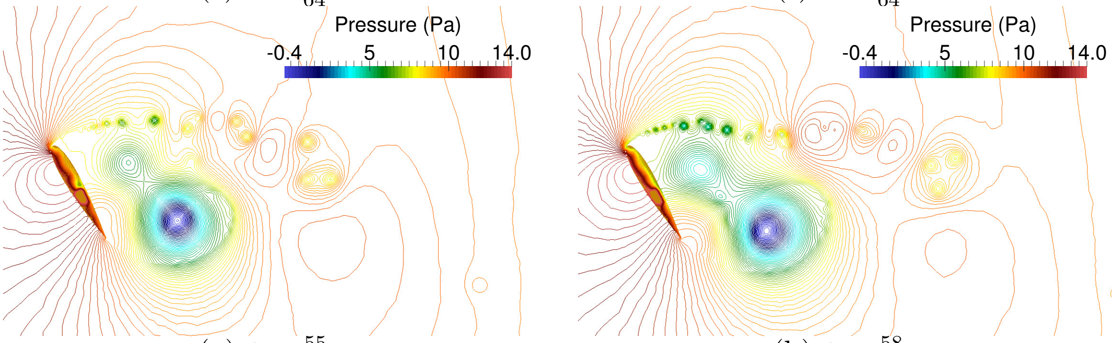

(g) $t = \frac{55}{64}$ s (h) $t = \frac{58}{64}$ s

Figure 5.7 The pressure contours of flow over a NACA0015 aerofoil at $Re = 5200$ and attack angle $\alpha = 60°$ obtained from the present model in different times: (a) $t = \frac{25}{64}$ s, (b) $t = \frac{27}{64}$ s, (c) $t = \frac{35}{64}$ s, (d) $t = \frac{40}{64}$ s, (e) $t = \frac{45}{64}$ s, (f) $t = \frac{52}{64}$ s, (g) $t = \frac{55}{64}$ s and (h) $t = \frac{58}{64}$ s. Similar results have been found in Figure 14 in the literature (Sengupta *et al.*, 2007) and Fig. 4.5 in the literature (Milthaler, 2014).

the rear and leading edges of the aerofoil. The streamlines generated by the present method are in good agreement with the streamlines from Ref. (Sengupta *et al.*, 2007) and Fig. 4.6 in (Milthaler, 2014). In Figs. 5.8a and b, one big and one small bubbles are generated one after another near the leading edge of the aerofoil. The big bubble is the main vortex, and the small bubble is the secondary vortex, which always attaches to the leading edge. The main big bubble keeps growing bigger and bigger (see Figs. 5.8a-d). As the secondary vortex increases the size, the main larger vortex detaches from the leading edge but still attaches to the upper surface of the aerofoil (see Fig. 5.8c and d). Meanwhile, a minor bubble appears at the rear of the aerofoil at $t = \frac{40}{64}$ s (see Fig. 5.8d). When the minor bubble is generated, it is already detached from the rear edge and locates at the downstream of the rear edge. Subsequently, the rear-edge minor bubble continues to grow, while the top big bubble starts to reduce in size (see Figs. 5.8d, 5.9e-g). During this period (from $t = \frac{45}{64}$ s to $t = \frac{55}{64}$ s), it can be clearly seen that two big vortices above each other positioning downstream of aerofoil upper surface. Soon after the bottom bubble growing bigger than the top one, the bottom one is detached from the rear edge (see Fig. 5.9h). At all time frames, the streamlines obtained from the present model match these from Ref. (Sengupta *et al.*, 2007) (shown in Figs. 5.8 and 5.9). From Figs. 5.8 and 5.9, it can be found that all the bubbles captured by Sengupta *et al.* (2007) are also obtained by the present model. At every time snapshot, the positions of all the bubbles are in good agreement between the present model streamlines and these from Ref. (Sengupta *et al.*, 2007). Additionally, by comparing the streamlines obtained from the present model and these from Ref. (Sengupta *et al.*, 2007), it is clear that there are more details in the present model results (see Fig. 5.9). Similar streamline results have also been found in Fig. 4.6 in (Milthaler, 2014). Moreover, the turbulent kinetic energy profiles are also shown in Fig. 5.10.

The comparison of present vorticity contours with experimental visualization pictures from Freymuth (1985) at different times is shown in Figs. 5.11 and 5.12. Sengupta *et al.* (2007) and Milthaler (2014) also compared their numerical vorticity results with the experimental visualization pictures from the literature (Freymuth, 1985) in Fig. 12 in (Sengupta *et al.*, 2007) and Figure 4.7 in (Milthaler, 2014). As it can be seen from Figs. 5.11 and 5.12, the vorticity contours obtained from the present immersed-body URANS model are in good agreement with these experimental visualization pictures from the literature (Freymuth, 1985). The eddies near the leading and rear edges are both very close to the experimental visualization pictures. And the details of the small shedding eddies are captured in Figs. 5.12f-h.

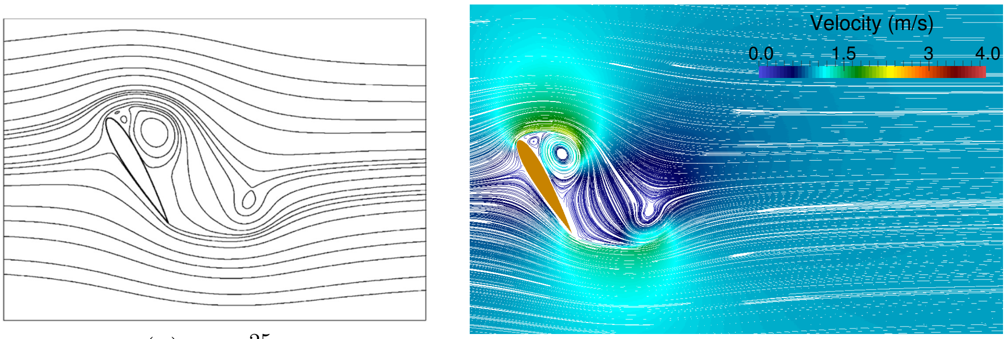

(a) $t = \frac{25}{64}$ s

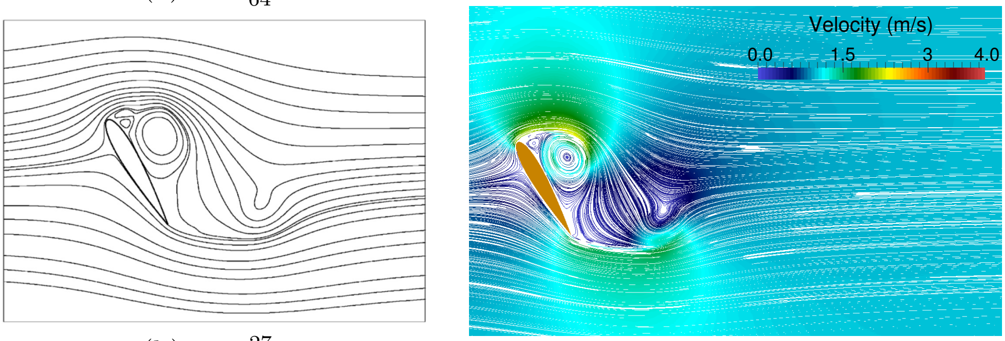

(b) $t = \frac{27}{64}$ s

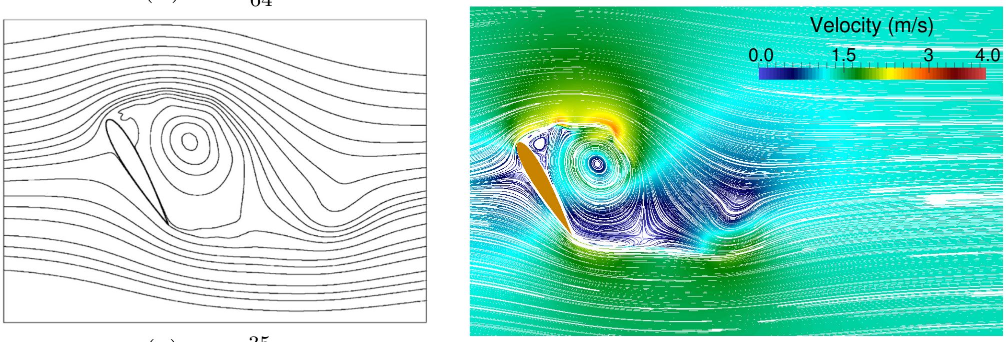

(c) $t = \frac{35}{64}$ s

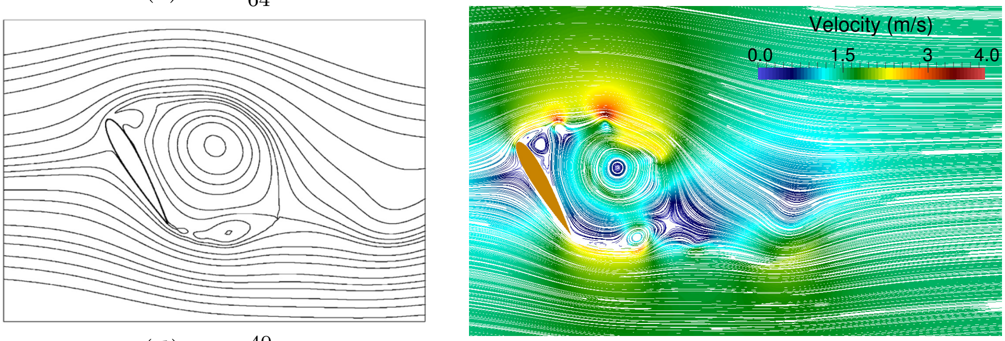

(d) $t = \frac{40}{64}$ s

Figure 5.8 Comparison of present streamlines (right) of flow over a NACA0015 aerofoil at $Re = 5200$ and attack angle $\alpha = 60°$ with the numerical streamlines in (Sengupta *et al.*, 2007) at different times: (a) $t = \frac{25}{64}$ s, (b) $t = \frac{27}{64}$ s, (c) $t = \frac{35}{64}$ s and (d) $t = \frac{40}{64}$ s. . Similar results have been found in Fig. 4.6 in (Milthaler, 2014).

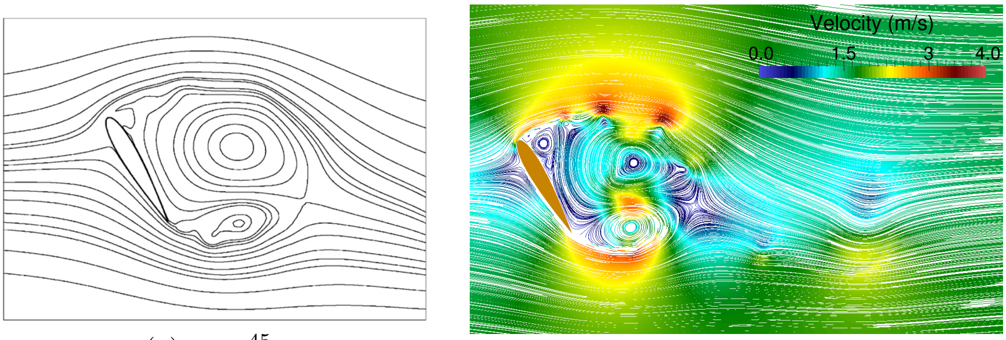

(e) $t = \frac{45}{64}$ s

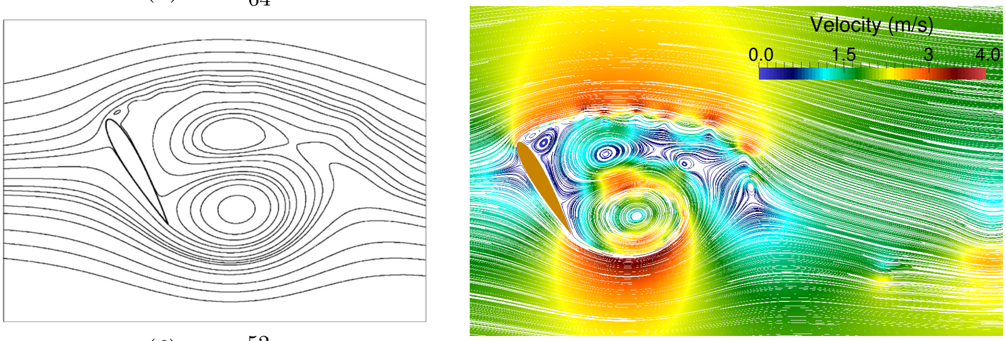

(f) $t = \frac{52}{64}$ s

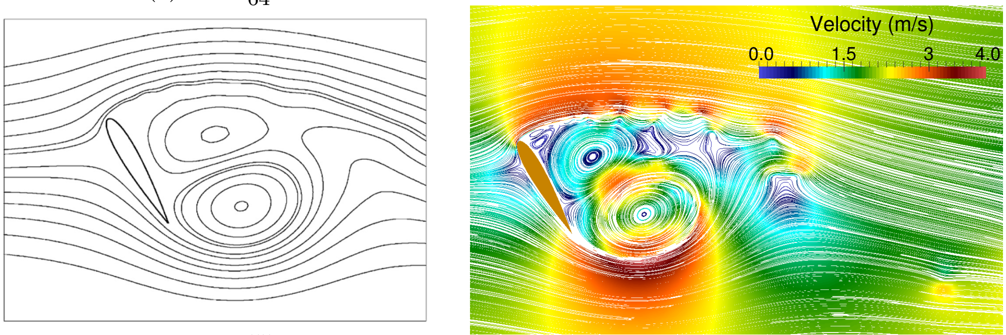

(g) $t = \frac{55}{64}$ s

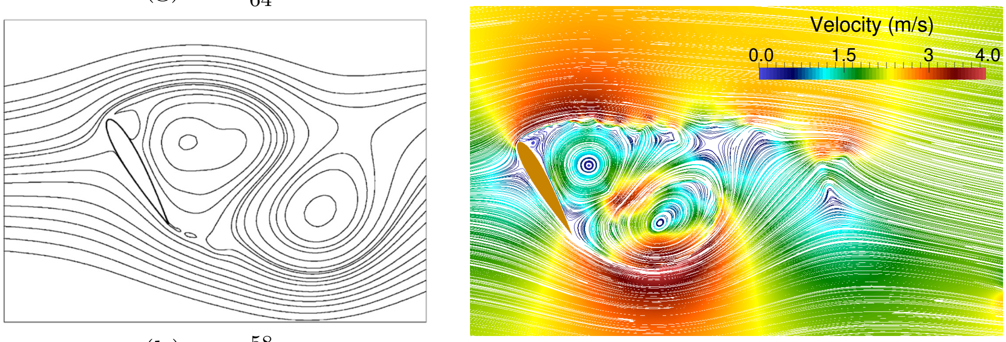

(h) $t = \frac{58}{64}$ s

Figure 5.9 Comparison of present streamlines (right) of flow over a NACA0015 aerofoil at $Re = 5200$ and attack angle $\alpha = 60°$ with the numerical streamlines in (Sengupta *et al.*, 2007) at different times: (e) $t = \frac{45}{64}$ s, (f) $t = \frac{52}{64}$ s, (g) $t = \frac{55}{64}$ s and (h) $t = \frac{58}{64}$ s. Similar results have been found in Fig. 4.6 in (Milthaler, 2014).

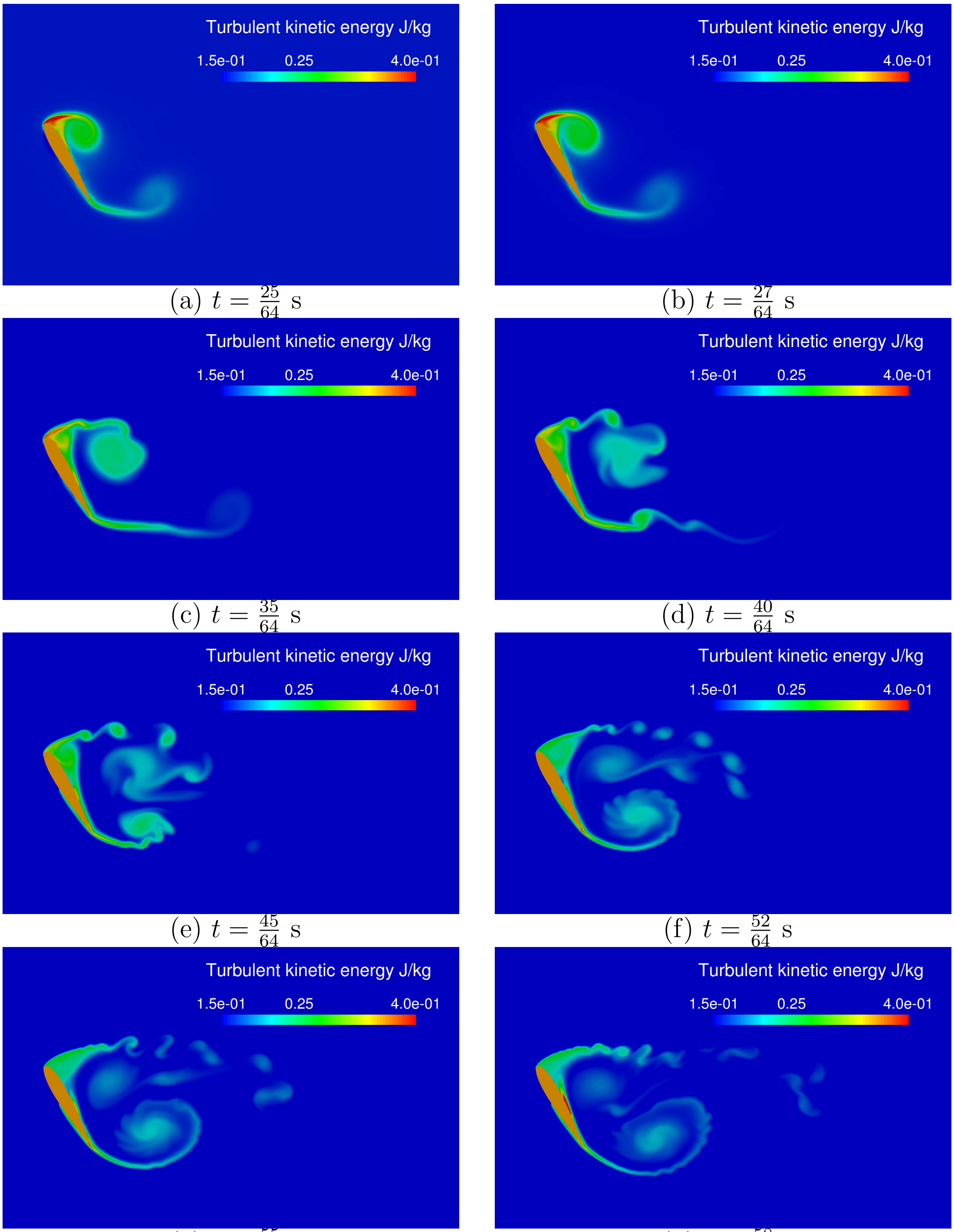

(a) $t = \frac{25}{64}$ s (b) $t = \frac{27}{64}$ s (c) $t = \frac{35}{64}$ s (d) $t = \frac{40}{64}$ s (e) $t = \frac{45}{64}$ s (f) $t = \frac{52}{64}$ s (g) $t = \frac{55}{64}$ s (h) $t = \frac{58}{64}$ s

Figure 5.10 The turbulent kinetic energy profiles of flow over a NACA0015 aerofoil at $Re = 5200$ and attack angle $\alpha = 60°$ obtained from the present model in different times: (a) $t = \frac{25}{64}$ s, (b) $t = \frac{27}{64}$ s, (c) $t = \frac{35}{64}$ s, (d) $t = \frac{40}{64}$ s, (e) $t = \frac{45}{64}$ s, (f) $t = \frac{52}{64}$ s, (g) $t = \frac{55}{64}$ s and (h) $t = \frac{58}{64}$ s.

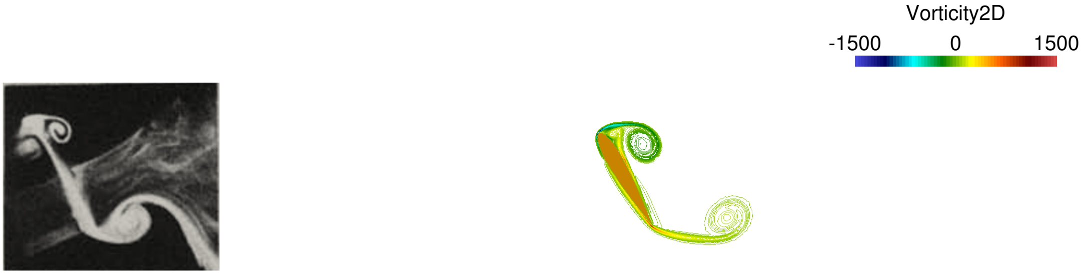

(a) $t = \frac{25}{64}$ s

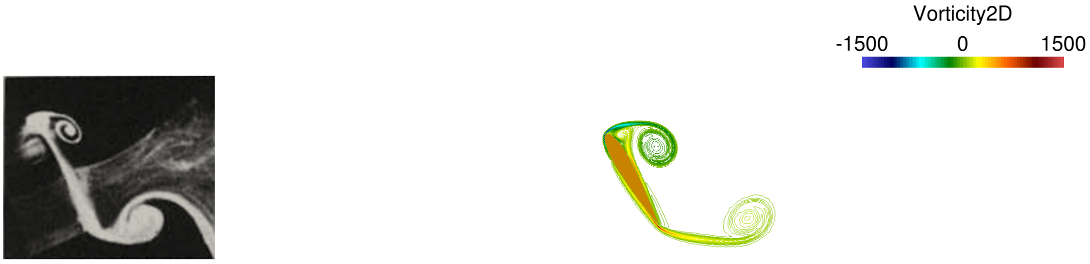

(b) $t = \frac{27}{64}$ s

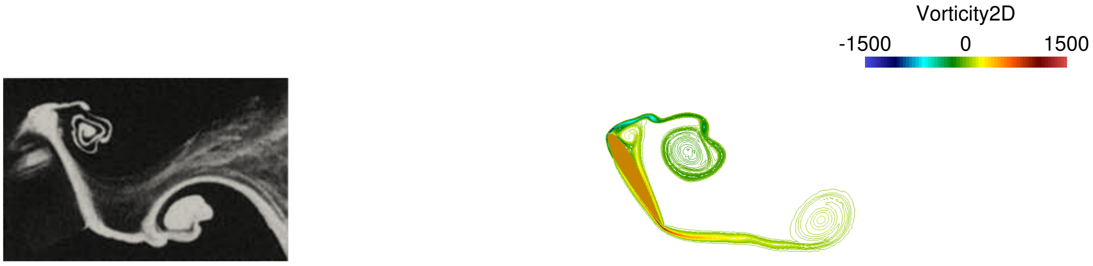

(c) $t = \frac{35}{64}$ s

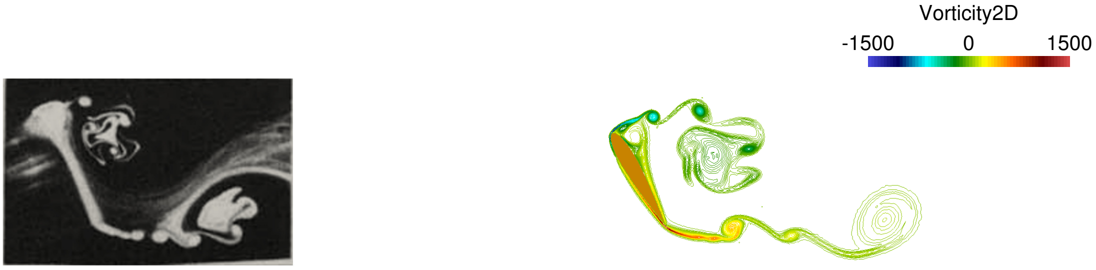

(d) $t = \frac{40}{64}$ s

Figure 5.11 Comparison of present vorticity contours (right) of flow over a NACA0015 aerofoil at $Re = 5200$ and attack angle $\alpha = 60°$ with visualization pictures (left) from the literature (Freymuth, 1985) at different times: (a) $t = \frac{25}{64}$ s, (b) $t = \frac{27}{64}$ s, (c) $t = \frac{35}{64}$ s and (d) $t = \frac{40}{64}$ s. Similar results have been found in Fig. 12 in the literature (Sengupta *et al.*, 2007) and Fig. 4.7 in (Milthaler, 2014).

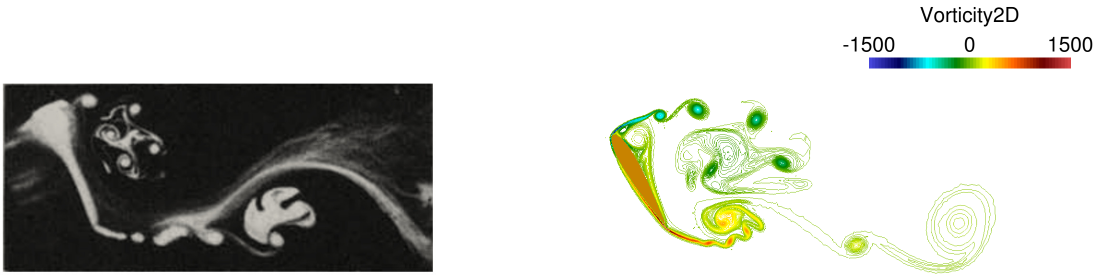

(e) $t = \frac{45}{64}$ s

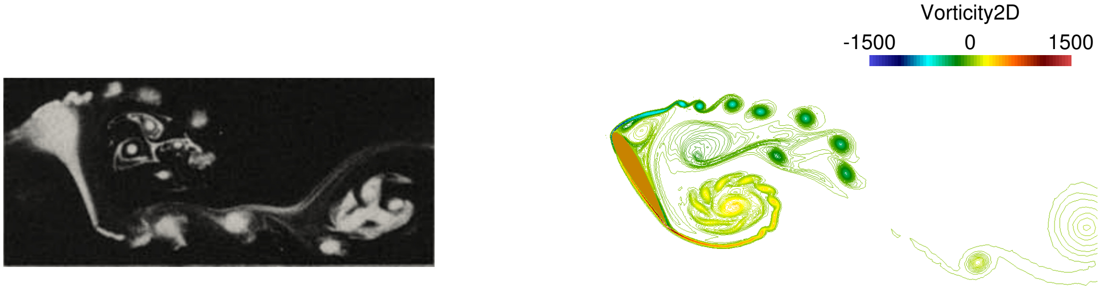

(f) $t = \frac{52}{64}$ s

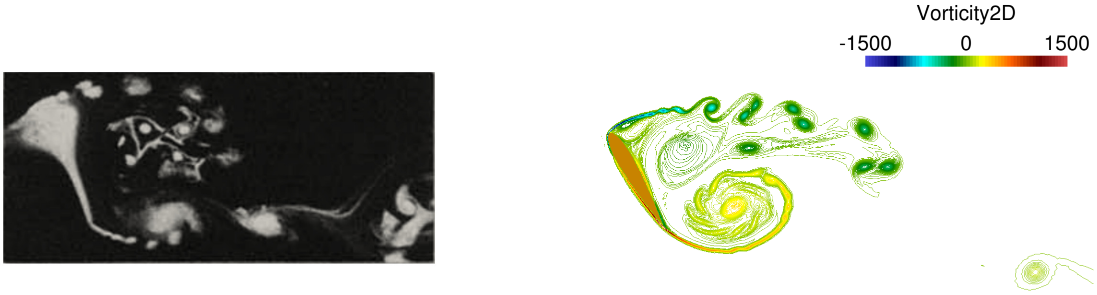

(g) $t = \frac{55}{64}$ s

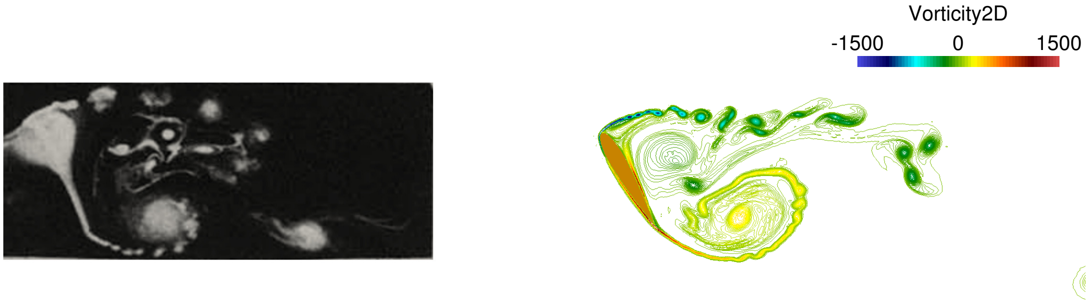

(h) $t = \frac{58}{64}$ s

Figure 5.12 Comparison of present vorticity contours (right) of flow over a NACA0015 aerofoil at $Re = 5200$ and attack angle $\alpha = 60^\circ$ with visualization pictures (left) from the literature (Freymuth, 1985) at different times: (e) $t = \frac{45}{64}$ s, (f) $t = \frac{52}{64}$ s, (g) $t = \frac{55}{64}$ s and (h) $t = \frac{58}{64}$ s. Similar results have been found in Fig. 12 in Sengupta et al. (Sengupta *et al.*, 2007) and Fig. 4.7 in (Milthaler, 2014).

The eddies presented here are closer to the experimental visualization pictures than those in Fig. 12 in (Sengupta *et al.*, 2007) and Fig. 4.7 in (Milthaler, 2014).

The comparison of pressure contours, streamlines and the vorticity contours with both the experimental visualization pictures from the literature (Freymuth, 1985) and numerical results in (Sengupta *et al.*, 2007; Milthaler, 2014) indicates that the immersed-body URANS model is able to simulate complex turbulent flows for large flow separations.

5.4 A free rising circular cylinder in a fluid at rest with $Re = 5000$ and $Re = 3800$

In practical engineering applications, turbulent flows around geometrically complex bodies are commonly used in many fields. In most cases, the solids are in motion driven by the fluid pressure and drag loads on the structures. This section focuses on the turbulent flows coupling with moving solids.

For free falling or rising cylinder in a fluid under the influence of gravity, there are many experimental data in (Horowitz & Williamson, 2006, 2010; Jayaweera & Mason, 1965; Stringham *et al.*, 1969). In this section, a free rising cylinder case is carried out. It has the same setting as the experiment in (Horowitz & Williamson, 2006). The computational domain and settings of the free rising cylinder case are shown in Fig. 5.13. The dimensions of the computational domain is $0.4\,\mathrm{m} \times 1.5\,\mathrm{m}$. No slip-condition is prescribed on the left, right and the bottom boundaries while the top is defined as having an open boundary condition. The kinematic viscosity ν of this fluid is $0.95 \times 10^{-6}\,\mathrm{m}^2/\mathrm{s}$. The diameter D of the cylinder is $0.0191\,\mathrm{m}$. In the beginning, the centre of the buoyant cylinder is located at the point $(0.2, 0.0191)\,\mathrm{m}$.

The density ratio of the cylinder to the fluid is defined as m^*, which is given as a constant of 0.78 and 0.45 for test R1 and R2, respectively. The Reynolds numbers of test R1 and R2 are about 5000 and 3800, respectively. The same setting experiment of this case was presented in (Horowitz & Williamson, 2006). In the present simulations, the anisotropic mesh adaptivity is used (see Fig. 5.14). The minimum and maximum mesh edge lengths are $7.5 \times 10^{-4}\,\mathrm{m}$ and $0.12\,\mathrm{m}$ respectively.

In order to know the response of a free rising cylinder to the vortex shedding dynamics, Horowitz & Williamson (2006) measured the vorticity pattern near the

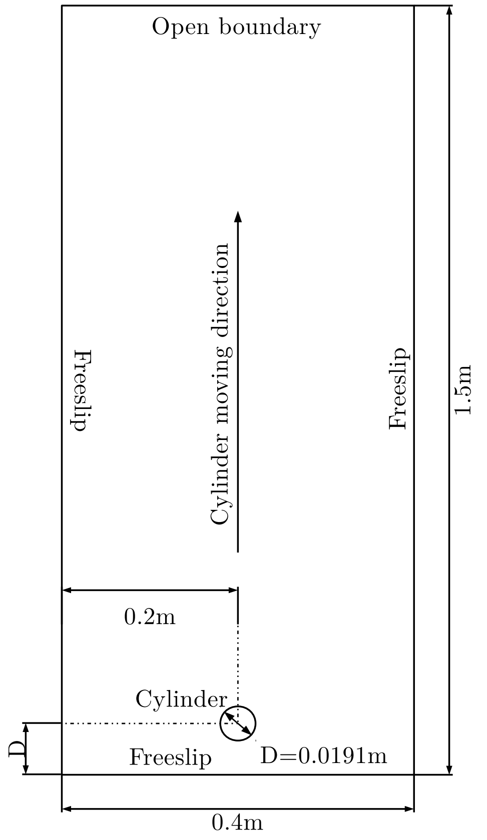
Open boundary
Freeslip
Cylinder moving direction
Freeslip
1.5m
0.2m
Cylinder
D
Freeslip
D=0.0191m
0.4m

Figure 5.13 The computational domain and settings of the rising cylinder.

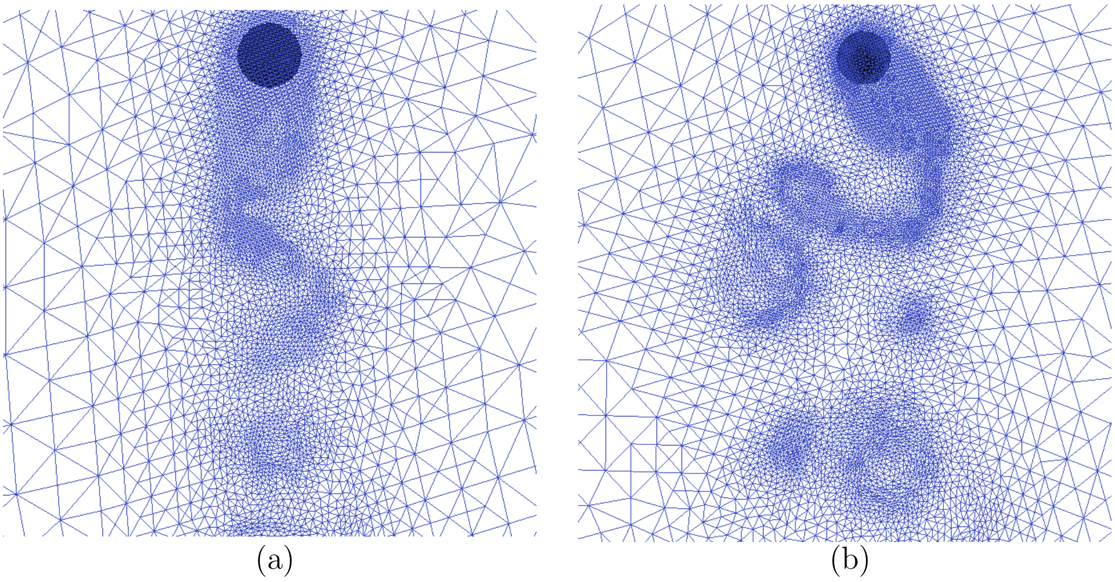

Figure 5.14 (a) The fluid mesh of a free rising cylinder at $m^* = 0.78$, (b) The fluid mesh of a free rising cylinder at $m^* = 0.45$.

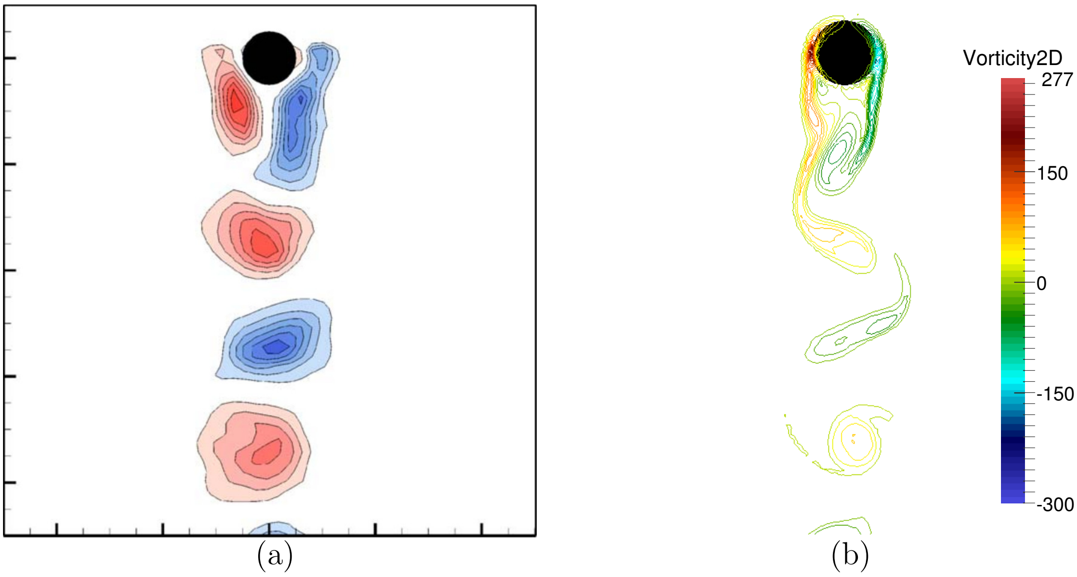

Figure 5.15 Comparison of present vorticity contours (b) of free rising cylinder at $Re = 5000$ with experimental measurements (a) from the literature (Horowitz & Williamson, 2006) when $m* = 0.78$.

wake of rising cylinder at their experiment. The vorticity obtained from the present immersed-body URANS model is compared with the measured vorticity in Figs. 5.15 and 5.16. The rising cylinder with $m^* = 0.78$ moves upward straightly with negligible transverse motion. However, the rising cylinder with $m^* = 0.45$ moves upward with significant vibrations. In both experimental measurements and the numerical contours of the vorticity, the same 2S mode of vortex formation was observed for $m^* = 0.78$ (see Fig. 5.15). In the meantime, the same 2P mode of vortex were observed for $m^* = 0.45$ (see Fig. 5.16).

The trajectories of the rising cylinder for test R1 and R2 are shown in Fig. 5.17. They are in good agreement with the experimental trajectories. Fig. 5.17a shows that the rising cylinder has negligible transverse motion in the simulation for test R1 (same situation observed in the experiment (Horowitz & Williamson, 2006)). But for test R2, there is non-negligible transverse motion. Our simulations have repeated these vibrating motions (see Fig. 5.17b). The eddy viscosity of the free rising cylinder is shown in Fig. 5.18.

The comparison of present vorticity contours and trajectories of free rising cylinder at $Re = 5000$ & $Re = 3800$ with experimental measurements from the literature (Horowitz & Williamson, 2006) in Figs. 5.15, 5.16 and 5.17 shows a good agreement. Since the free rising cylinder is a two-way coupling case, this demonstrates that the

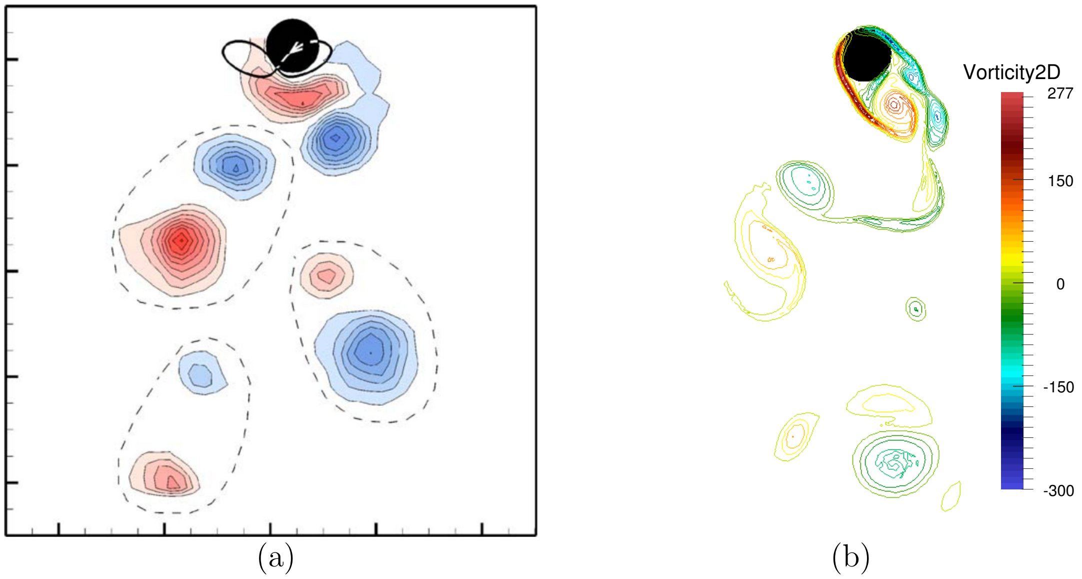

(a) (b)

Figure 5.16 Comparison of present vorticity contours (b) of free rising cylinder at $Re = 3800$ with experimental measurements (a) from the literature (Horowitz & Williamson, 2006) when $m* = 0.45$.

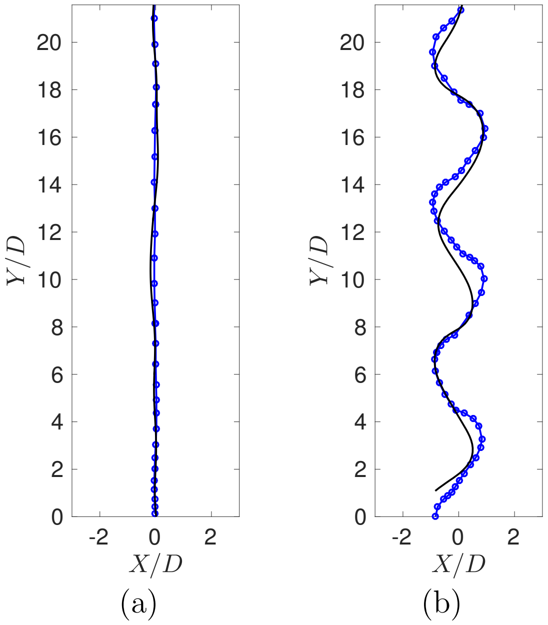

(a) (b)

Figure 5.17 The blue lines with circles are experimental data from Ref. (Horowitz & Williamson, 2006), and the black solid lines are trajectories of the rising cylinders in the simulations obtained from the present immersed-body URANS model. (a) The trajectories of a rising cylinder at $m^* = 0.78$, (b) The trajectories of a rising cylinder at $m^* = 0.45$.

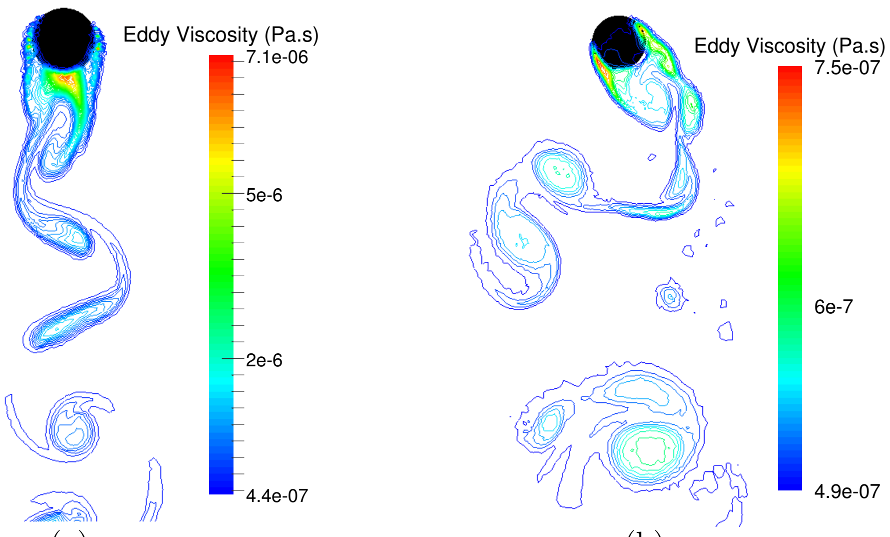

(a) (b)

Figure 5.18 (a) The contours of eddy viscosity for a free rising cylinder at $m^* = 0.78$, (b) The contours of eddy viscosity for a free rising cylinder at $m^* = 0.45$.

presented immersed-body URANS model is able to correctly simulate two-way solid-fluid coupling at high Reynolds number situations.

5.5 A free rising sphere in a fluid at rest with $Re = 6000$ and 10000

In this section, simulations of a free rising sphere in a fluid at rest with $Re = 6000$ and 10000 have been undertaken for validation of the URANS FSI model.

The computational domain with dimensions $10D \times 10D \times 150D$ is shown in Fig. 5.19a. The centre of the sphere is initially set at $5D$ distance to the bottom, left, right, front and back of the domain. The top surface of this computational domain is given the open boundary condition, other surfaces: bottom, right, left, front and back of the domain are all given free-slip boundary conditions. Adaptive fluid meshes are used in this test case with the maximum and minimum mesh edge length $L_{max} = 5D$ and $L_{min} = 0.025D$, respectively (see Fig. 5.19b).

Using equation 3.10, the empirical solutions of the terminal velocity for free setting spheres can be obtained. The terminal velocity comparison between the empirical

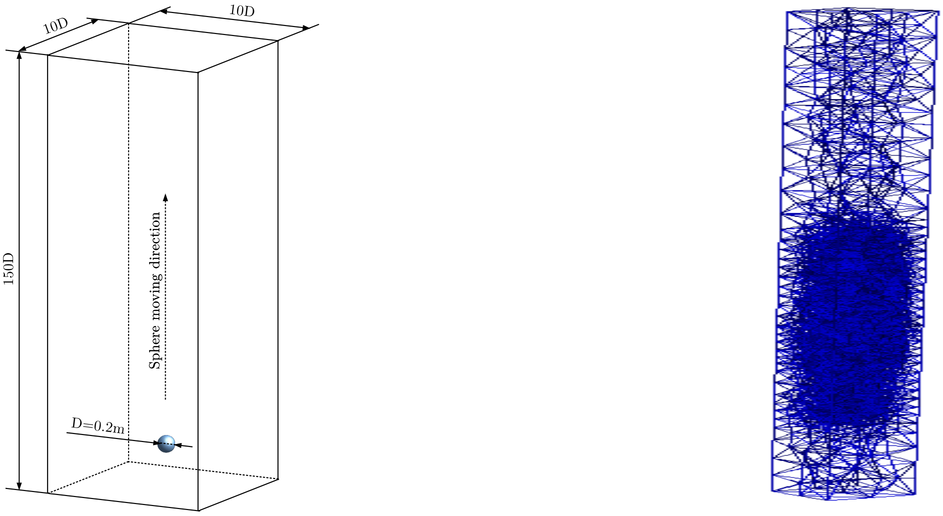

(a) (b)

Figure 5.19 (a) The computational domain of the rising sphere test case, (b) The computational mesh of the rising sphere test case.

solutions and the simulation results obtained from the presented model for $m^* = 0.55$ and $m^* = 0.8$ are listed in Table 5.3. It can be found that the absolute values of all relative errors are less than 0.03. This indicates the present model is accurate for two-way FSI simulations at high Reynolds number regime.

Table 5.3 Free rising sphere test cases for different m^*.

Case	m^*	ν	Re	U_t^{sf}	U_t^{is}	E_r^{Ut}
Rising-sphere-r41	0.55	5.43×10^{-5}	6000	1.63686	1.6282	0.0053
Rising-sphere-r42	0.55	3.29×10^{-5}	10000	1.66824	1.6448	0.0143
Rising-sphere-r43	0.8	3.62×10^{-5}	6000	1.11216	1.0855	0.0245

The Q-criterion of the free rising sphere cases is shown in Fig. 5.20. It is worth to note that the vortex shedding patterns of Rising-sphere-r42 and Rising-sphere-r43 are different, while Rising-sphere-r41 and Rising-sphere-r42 have a similar pattern. Horowitz & Williamson (2010) have carried out a large number of experiment tests of the free rising sphere and drew three vortex shedding patterns i.e. ‘R’ , ‘2R’ and ‘4R’. The parameters determining the vortex shedding patterns are Re and m^*. Different free rising sphere near weak patterns on the $\{m^*, Re\}$ plane are given in Fig. 5.21. This shedding vortex map is drawn based on a large number of experiments test case. To define different patterns, the ‘R’ , ‘2R’ and ‘4R’ modes are introduced

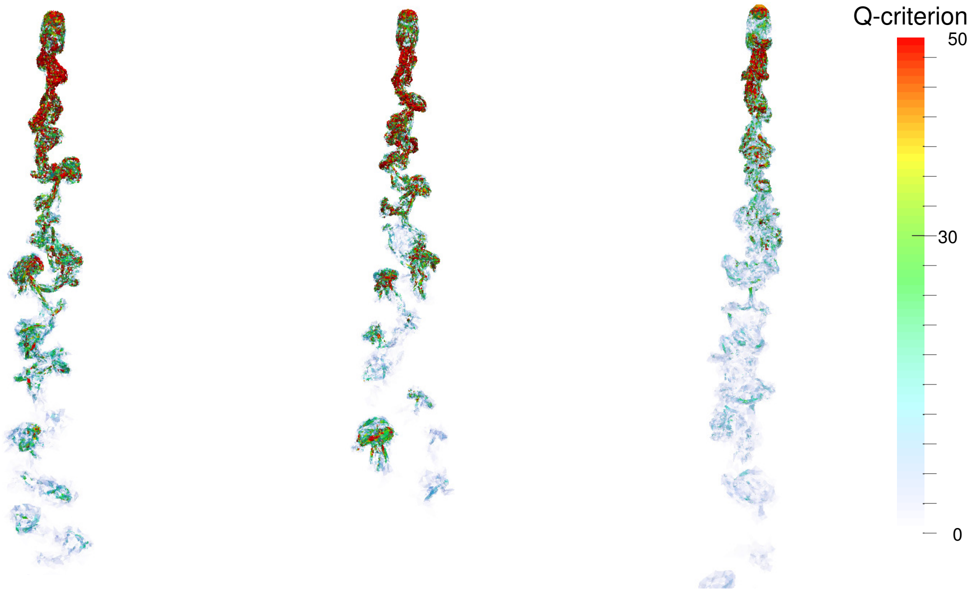
Q-criterion
50
30
0

(a) (b) (c)

Figure 5.20 The Q-criterion of the free rising sphere cases: (a) Rising-sphere-r41: $m^* = 0.55$ and $Re = 6000$, (b) Rising-sphere-r42: $m^* = 0.55$ and $Re = 10000$, and (c) Rising-sphere-r43 $m^* = 0.8$ and $Re = 6000$.

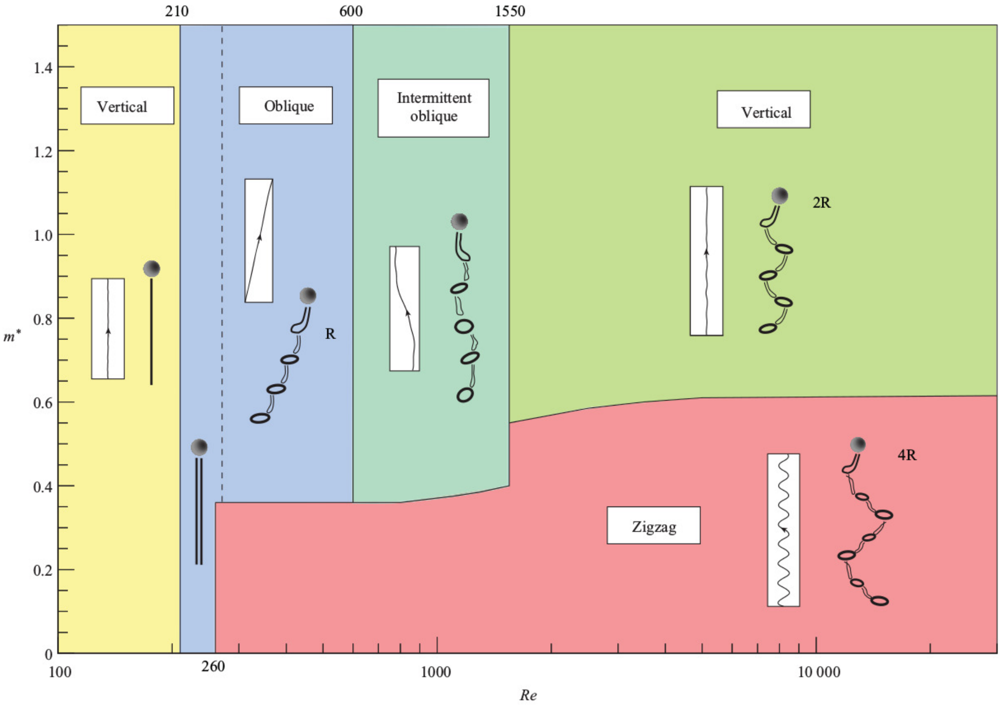
210
600
1550
Vertical
Oblique
Intermittent oblique
Vertical
2R
R
4R
Zigzag
1.4
1.2
1.0
0.8
0.6
0.4
0.2
0
m*
100
260
1000
10 000
Re

Figure 5.21 Different free rising sphere near weak patterns on the $\{m^*, Re\}$ plane from Ref. (Horowitz & Williamson, 2010).

(Horowitz & Williamson, 2010). The 'R' and '2R' modes are the vortex rings with single-sided and double-sided periodic sequences, respectively. The '4R' mode is the shedding vortex that including four vortex rings at every cycle of oscillation. From the definitions, it can be found that Rising-sphere-r41 and Rising-sphere-r42 generate the '4R' mode of vortex rings, while Rising-sphere-r42 creates the '2R' mode vortex rings. By checking the vortex map in Fig. 5.21, in the test case: Rising-sphere-r41 and Rising-sphere-r42, $m^* = 0.55$, $Re = 6000$ and 10000, thus the '4R' mode vortex rings could be found. For the Rising-sphere-r43 test case, $m^* = 0.8$ and $Re = 6000$, the '2R' mode vortex rings could be found based on the vortex map. By comparing the vortex pattern modes obtained from the present model and the vortex map, the present model successfully regenerate the '2R' and '4R' modes for different m^* and Re.

5.6 Flow bending a 3D elastic plate

In this section, flow bending a flexible plate test case is used to validate the model when dealing with elasticity in FSI. The results obtained by the present model are compared with the experimental data in (Luhar & Nepf, 2011) and the numerical data in (Tian *et al.*, 2014).

The schematic of the flexible plate is shown in Fig. 5.22a. This flexible plate of length L, width b, and thickness h is vertically placed in a cross flow. The relationships between L, b and h are $L/b = 5$ and $h/b = 0.2$. The computational domain and boundary conditions of this case are defined in Fig. 5.23b. The dimensions of this domain are $21b \times 16b \times 17b$. As shown in Fig. 5.23b, the left and right sides are set as the velocity inlet and pressure outlet boundary conditions. The inlet velocity is U_i and the outlet pressure is P_0. The front, back, top and bottom sides are all given free-slip boundary conditions. The centre of the plate is set at $5b$ to the left side, $8b$ to the front side and $8.5b$ to the bottom side. The dimensionless parameters used in this case are: $Re = U_i b/\nu = 1600$, $E^* = E/\rho_f U_0^2 = 19054.9$, $m* = \rho_s/\rho_f = 0.678$, and $f_b^* = (\rho_f - \rho_s)gh/(\rho_f U_0^2) = 0.2465$. Adaptive meshes with the minimum and maximum mesh edge lengths $l = 0.075b$ and $L = 2.5b$ are used in this case (see Fig. 5.23a).

Fig. 5.24 shows the motion of the flexible plate. From Fig. 5.24a-d, it can be found that the tip of plate first moves to the right-hand side from $t = 0$ to $t = 155$.

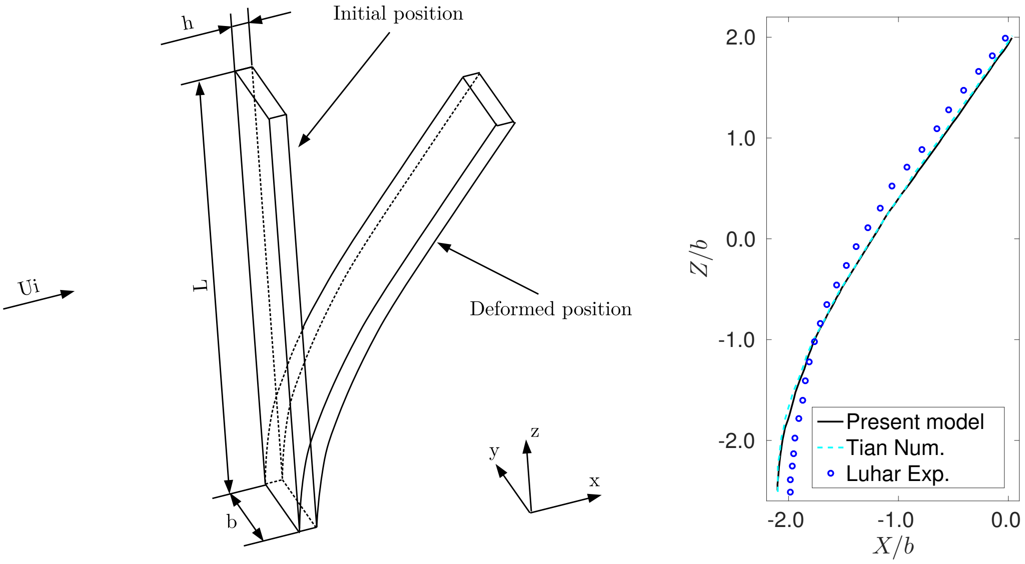

(a) (b)

Figure 5.22 (a) Schematic of a flexible plate. (b) The comparison of baselines computed by the present model with the numerical data in (Tian *et al.*, 2014) and experimental data in (Luhar & Nepf, 2011).

Then the plate experiences a period of vibrating from $t = 170$ to $t = 700$ (see Fig. 5.24e-m). During this vibrating period, the tip of the plate moves back to the left-hand side at $t = 170$ and quickly moves to the right-hand side again at $t = 265$ and $t = 330$. After this, the second pullback happens at $t = 470$ and $t = 575$ that pulling the plate tip moving back to the left-hand side again. Finally, after $t = 750$, the plate moves slowly and stabilizes at $t = 840$ (see Fig. 5.24p).

After the plate is stabilizes at $t = 840$ (see Fig. 5.24p), the baseline of the plate is compared with the numerical data in (Tian *et al.*, 2014) and experimental data in (Luhar & Nepf, 2011). From Fig. 5.22b, it can be found that the baseline computed by the present model is in good agreement with the experimental data in (Luhar & Nepf, 2011) and the numerical data in (Tian *et al.*, 2014). This proves that the present model is good at capturing the elastic structure response in FSI.

Figs. 5.25-5.26 plot the pressure contours surrounding the plate at different time snapshots. From Fig. 5.25a-c, there is no clear pressure contour shell and the plate tip gently moves to the right-hand side from $t = 0$ to $t = 80$. Even when $t = 155$, the pressure difference between the right and left sides of the plate is relatively small and the plate continues moving to the right-hand side (see Fig. 5.25d). However,

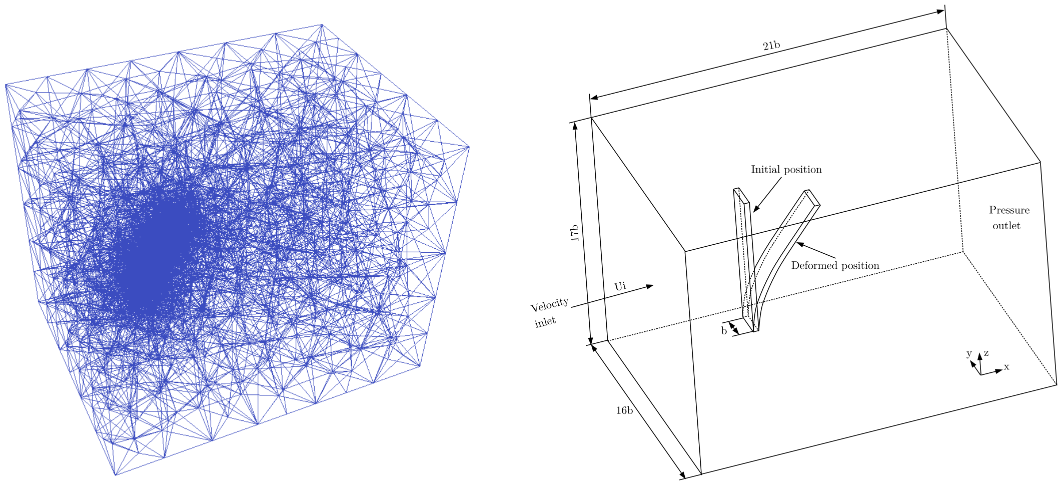

(a) (b)

Figure 5.23 (a) The mesh the flow bending a flexible plate case. (b) The computational domain and boundary settings of the flow bending a flexible plate case.

from $t = 170$ to $t = 700$, there are huge pressure differences between the left and right side surrounding the plate (see Figs. 5.25e-i and 5.26j-m), which drive the plate vibrate frequently. Taking for an example, from $t = 470$ to $t = 575$, the pressure on the right-hand side is much larger than that on the left-hand side, thus the tip of the plate is moving the left-hand side at these time snapshots (see Fig. 5.25h-i). At $t = 590$, since the pressure on the left-hand side is bigger than that on the right-hand side, the plate tip is driven to move right-hand side. After this strong vibrating period, the pressure differences decreased to very small value from $t = 750$ to $t = 840$ and the plate moves slowly and finally stabilizes at $t = 840$ (see Fig. 5.26p).

Additionally, the streamlines of the flow bending a 3D elastic plate test case at different time snapshots are shown in Figs. 5.27 and 5.28. As the plate moves to the right-hand side gently from $t = 0$ to $t = 155$ (see Fig. 5.27), the streamlines at this time period are smooth and relatively few with large curvatures. From $t = 170$ to $t = 700$, the plate is in the mode of vibration. The streamlines are mixed by the frequent moving plate. At the same time, many streamlines with large curvatures appear and lots of streamlines cross with each other (see Figs. 5.27g-h and 5.28i-l). After this vibration phase, the flexible plate stabilises. The streamlines become ordered and the curvatures become smaller than these during the vibration phase (see Fig. 5.28n-p).

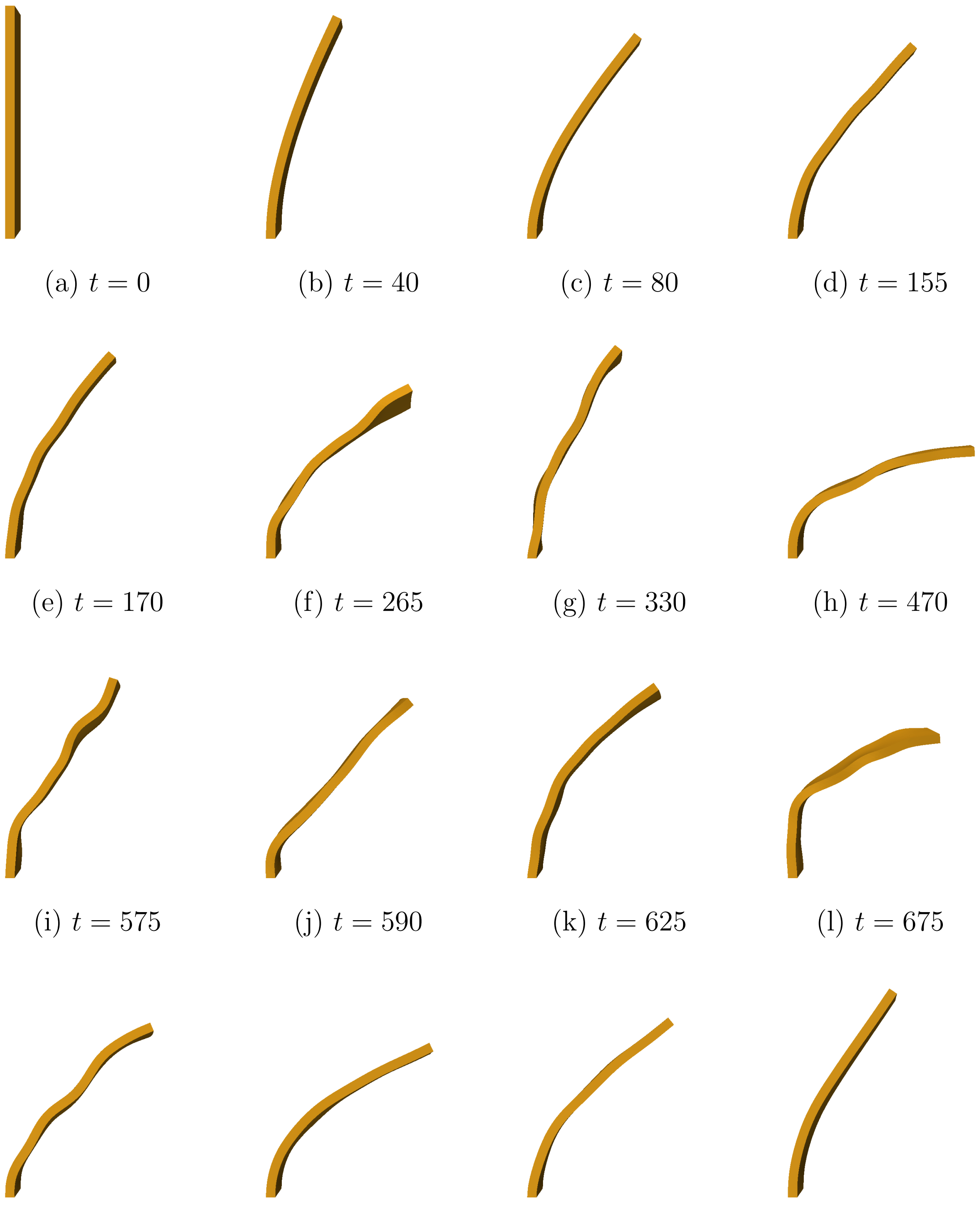

(a) $t = 0$ (b) $t = 40$ (c) $t = 80$ (d) $t = 155$

(e) $t = 170$ (f) $t = 265$ (g) $t = 330$ (h) $t = 470$

(i) $t = 575$ (j) $t = 590$ (k) $t = 625$ (l) $t = 675$

(m) $t = 700$ (n) $t = 750$ (o) $t = 800$ (p) $t = 840$

Figure 5.24 The bending plate positions at different times: (a) $t = 0$, (b) $t = 40$, (c) $t = 80$, (d) $t = 155$, (e) $t = 170$, (f) $t = 265$, (g) $t = 330$, (h) $t = 470$, (i) $t = 575$, (j) $t = 590$, (k) $t = 625$, (l) $t = 675$, (m) $t = 700$, (n) $t = 750$, (o) $t = 800$ and (p) $t = 840$.

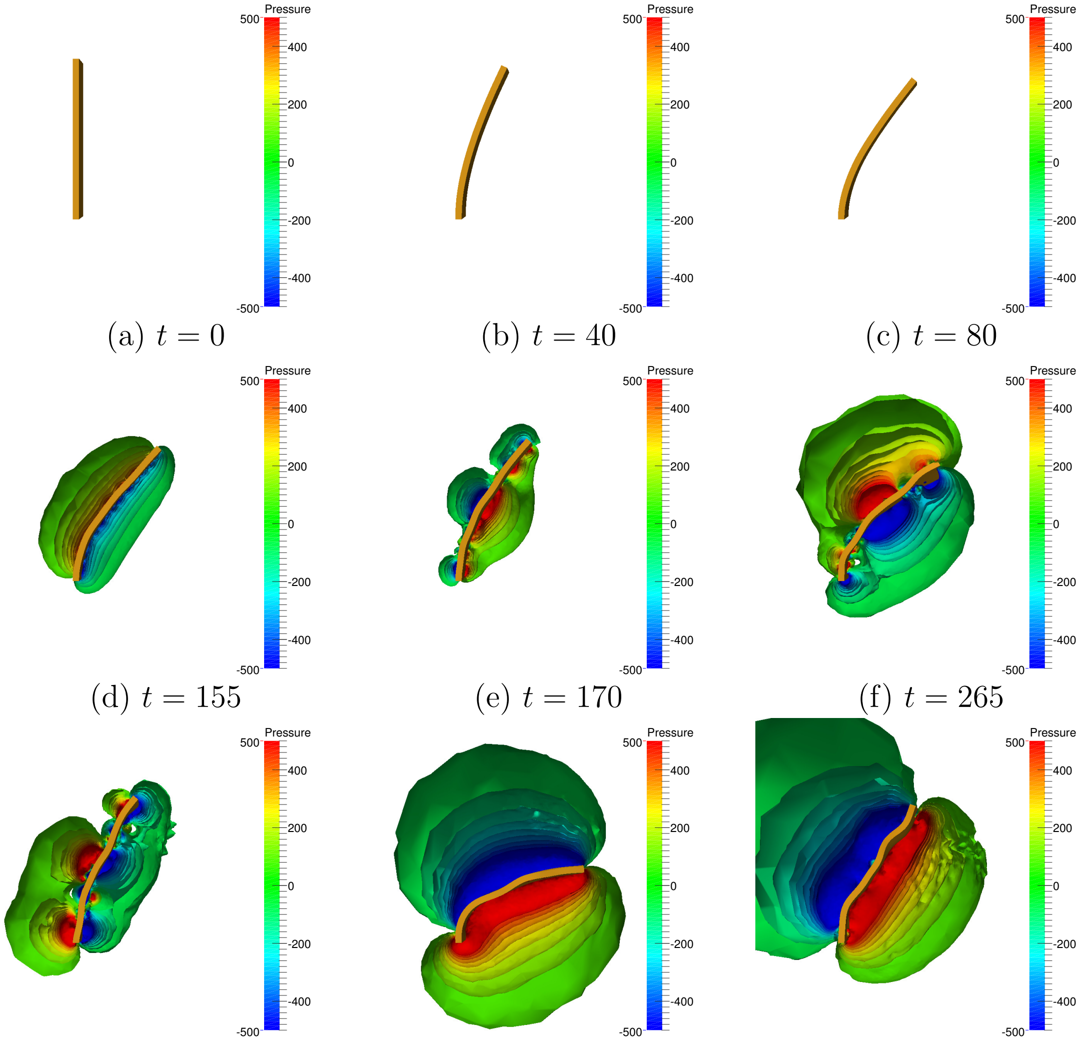
Pressure
500
400
200
0
-200
-400
-500

(a) $t = 0$ (b) $t = 40$ (c) $t = 80$

(d) $t = 155$ (e) $t = 170$ (f) $t = 265$

(g) $t = 330$ (h) $t = 470$ (i) $t = 575$

Figure 5.25 The pressure contour of the flow bending a 3D elastic plate case at different times: (a) $t = 0$, (b) $t = 40$, (c) $t = 80$, (d) $t = 155$, (e) $t = 170$, (f) $t = 265$, (g) $t = 330$, (h) $t = 470$ and (i) $t = 575$.

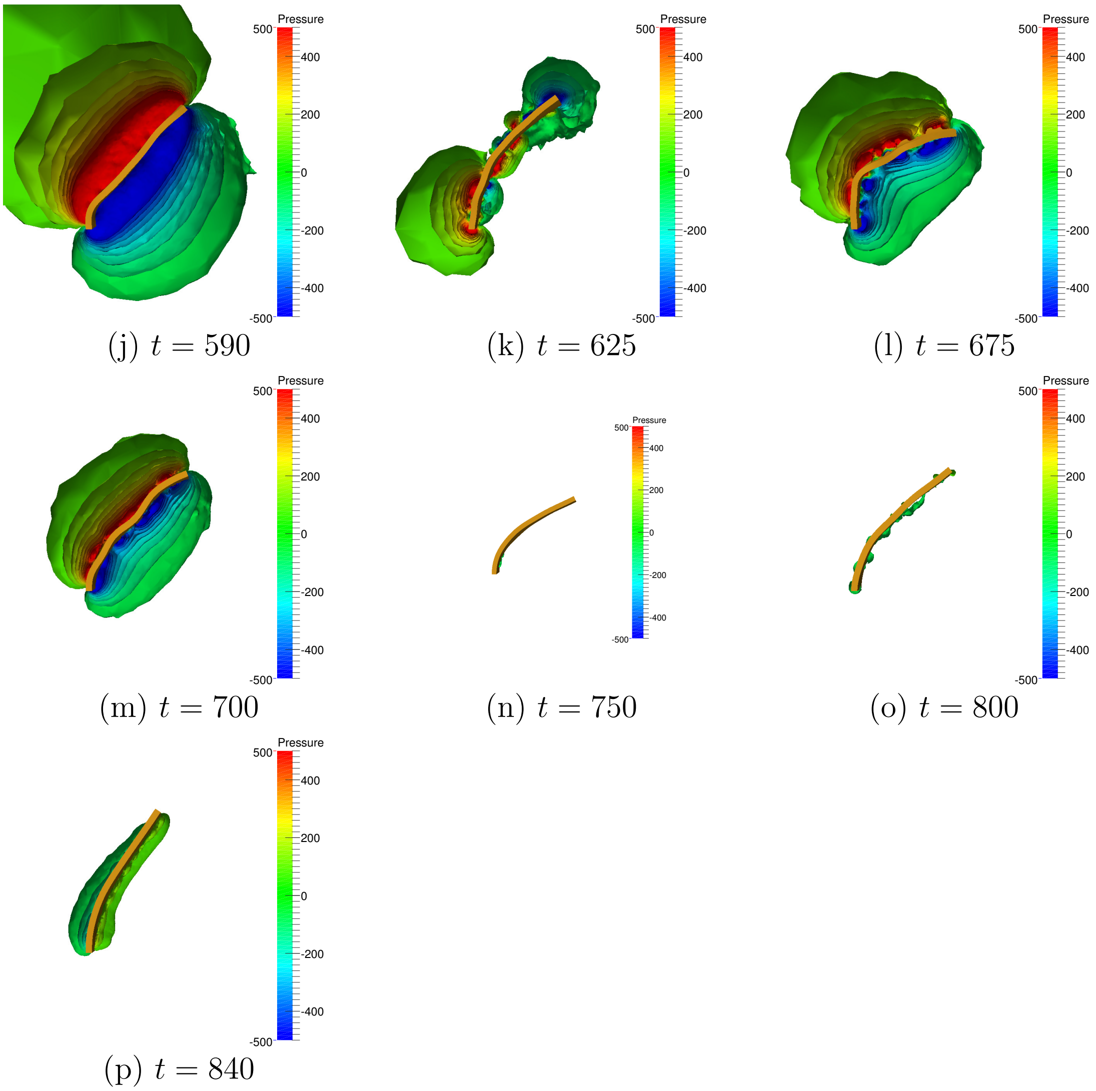
Pressure
500
400
200
0
-200
-400
-500

(j) $t = 590$ (k) $t = 625$ (l) $t = 675$

(m) $t = 700$ (n) $t = 750$ (o) $t = 800$

(p) $t = 840$

Figure 5.26 The pressure contour of the flow bending a 3D elastic plate case at different times: (j) $t = 590$, (k) $t = 625$, (l) $t = 675$, (m) $t = 700$, (n) $t = 750$, (o) $t = 800$ and (p) $t = 840$.

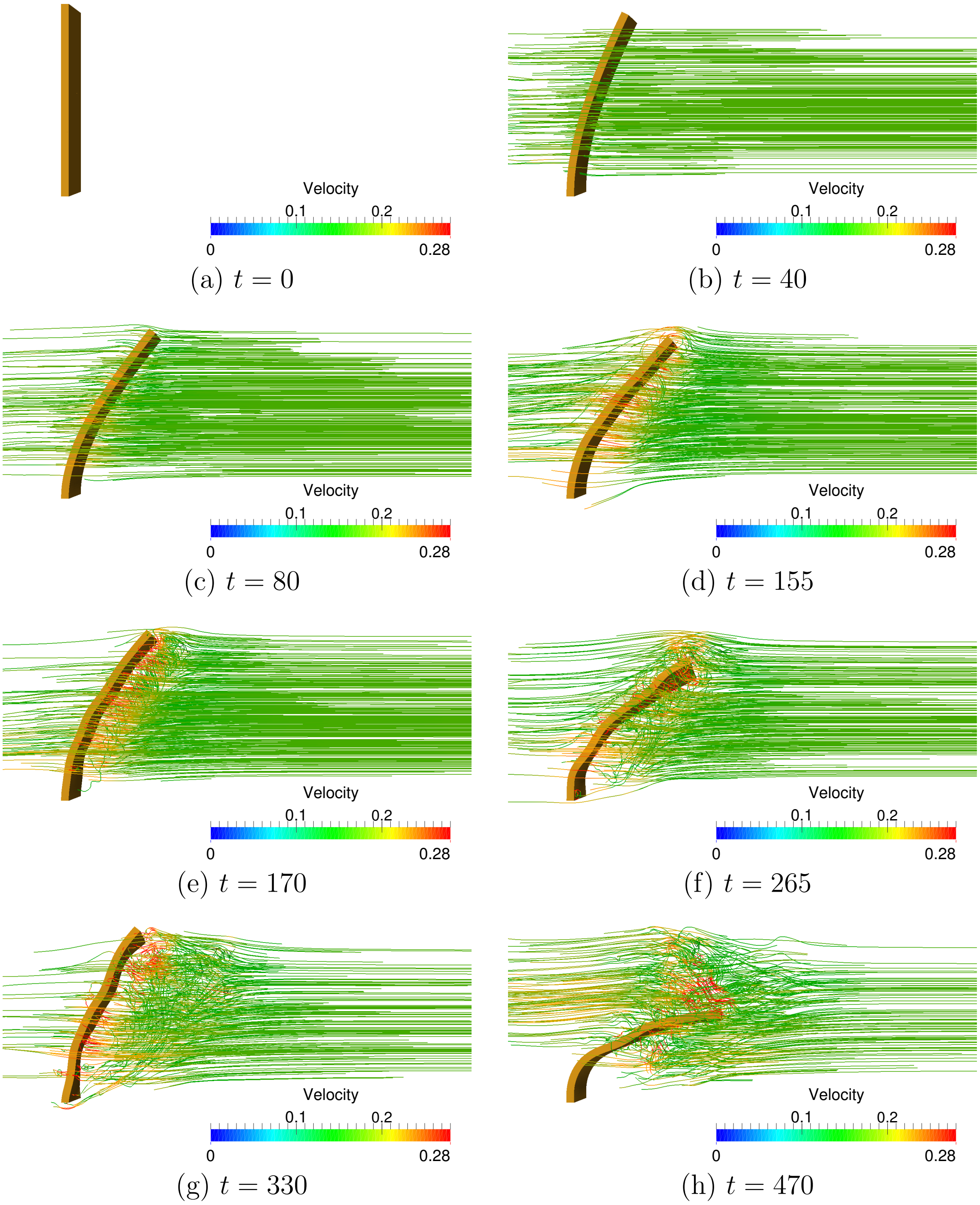

(a) $t = 0$ (b) $t = 40$ (c) $t = 80$ (d) $t = 155$ (e) $t = 170$ (f) $t = 265$ (g) $t = 330$ (h) $t = 470$

Figure 5.27 The streamline of the flow bending a 3D elastic plate case at different times: (a) $t = 0$, (b) $t = 40$, (c) $t = 80$, (d) $t = 155$, (e) $t = 170$, (f) $t = 265$, (g) $t = 330$ and (h) $t = 470$.

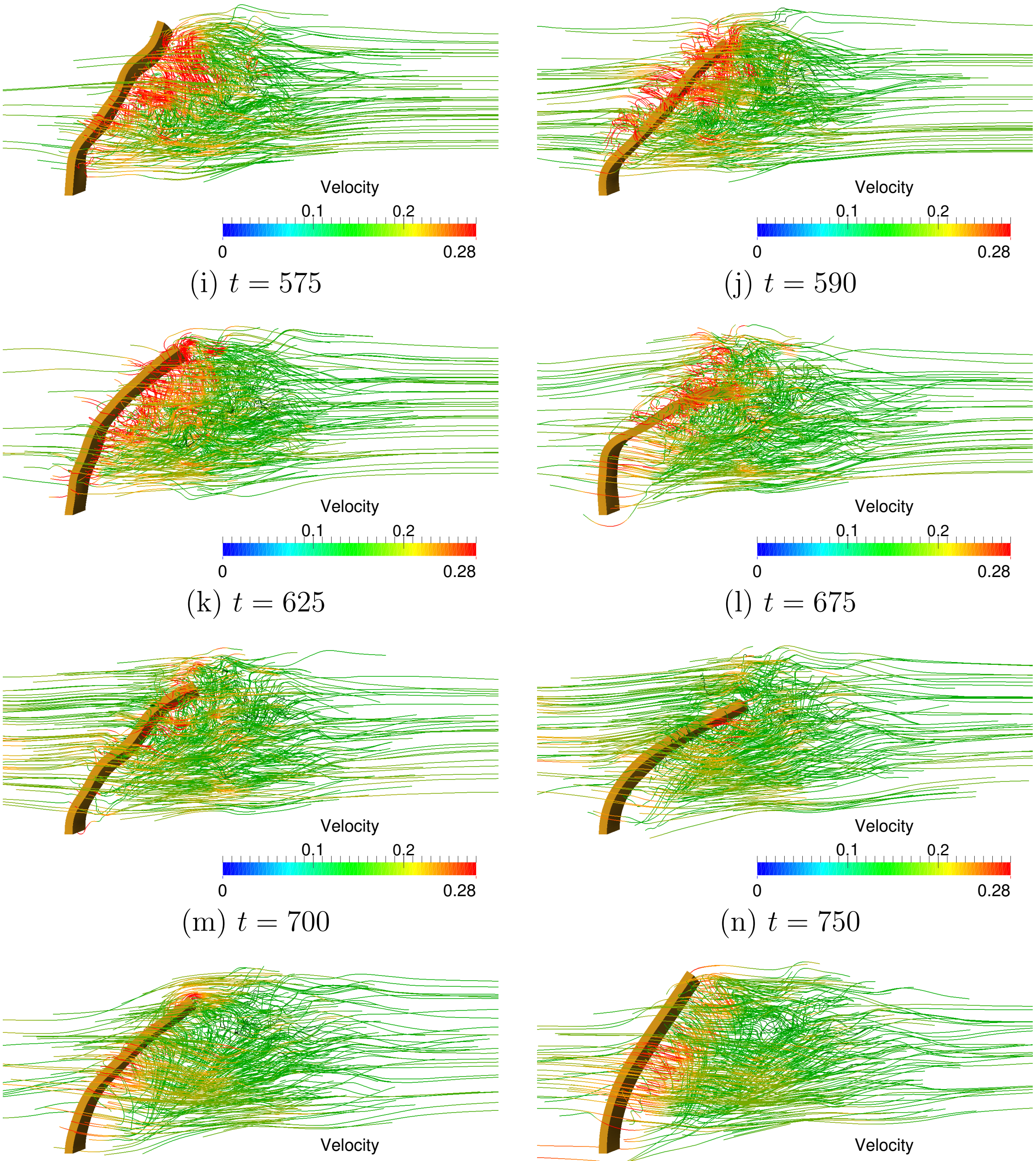

(i) $t = 575$ (j) $t = 590$

(k) $t = 625$ (l) $t = 675$

(m) $t = 700$ (n) $t = 750$

(o) $t = 800$ (p) $t = 840$

Figure 5.28 The streamline of the flow bending a 3D elastic plate case at different times: (i) $t = 575$, (j) $t = 590$, (k) $t = 625$, (l) $t = 675$, (m) $t = 700$, (n) $t = 750$, (o) $t = 800$ and (p) $t = 840$.

5.7 Computational time

A brief software profile of the computational time in this coupled code has been done (see Table 5.4). From Table 5.4, we can see that the two longest computational time expenditures are caused by the nonlinear iterations in the fluid solver and the projection process between the fluid, shell and solid meshes. The computational time cost on projection would be very expensive when the structure surface is relatively large and fine meshes concentrate on fluid-structure interfaces. For the projection process, the search algorithm R-TREE (Guttman, 1984) is used. The R-TREE algorithm is a dynamic indexing algorithm using certain related bounding boxes/rectangles. More advanced search algorithm, such as NBS contact detection algorithm (Munjiza & Andrews, 1998), may be implemented in the projection process to improve the efficiency of the coupled code.

Table 5.4 The time cost in different functions in percentage.

case name	speed test 1	speed test 2	speed test 3
fluid mesh size	0.05	0.05	0.025
solid mesh size	0.01	0.02	0.01
normal loop	0.0308	0.0829	0.0174
$k - \varepsilon$	9.9598	30.0661	23.0384
nonlinear loop	6.2902	17.6752	17.7783
interpolate fields out r	34.8882	22.1566	20.7009
interpolate fields out v	15.9157	8.8122	11.7213
interpolate fields in v	7.0613	3.2523	5.4534
interpolate fields in r	7.7176	3.9821	5.9789
calculate solid volume fraction	5.2977	2.6778	4.6359
calculate shell volume fraction	5.8158	2.9319	4.5574
y3dfemdem	1.9054	0.7722	0.6935

5.8 Concluding remarks

In this chapter, detailed validation of the FSI model for turbulent flows is presented. The immersed-body URANS turbulence model is validated by several test cases, and the results show good agreements with both experimental data and previous numerical data in the literature. The first two test cases are flow over a circular cylinder at $Re = 3900$ and turbulent flow over a static NACA0015 aerofoil with an attack angle of $\alpha = 60^\circ$ at $Re = 5200$. The comparison between the experimental and numerical results shows that the model has the accuracy and reliability to resolve the turbulent flow coupled with fixed solids. The third and fourth test cases are a free rising circular cylinder in a fluid at rest with $Re = 5000$ and $Re = 3800$ and a free rising sphere in a fluid at rest with $Re = 6000$ and 10000. These two benchmark test cases indicate that the immersed-body URANS model has the ability to simulate moving bodies coupled with the turbulent flow. The structural elastic response in a cross flow is also validated by the flow bending a 3D elastic plate test case. The simulation results obtained from the present FSI model are in good agreement with the experimental data and previous numerical results in the literature. Finally, this chapter presents the software profile, which could be used for further code optimisation. The developed FSI model has been validated from incompressible, compressible to turbulent flows at chapter 3 to chapter 6. The next chapter will show a complex application case for a tidal turbine.

Chapter

SIX

Application: FSI model for tidal turbine

The present FSI model is applied to vertical axis tidal turbines (VATTs) in this chapter. Numerical simulations for vertical axis tidal turbines are carried out based on the developed 2D and 3D fidelity fluid-structure turbulence model. This model is capable of simulating the fluid dynamics of the flow, as well as the stress, vibration, deformation, fracture, and motion of structures at the same time. Most importantly, this model is able to capture the structure response and fluid dynamics of rotating vertical axis tidal turbines in turbulent flows, since a URANS $k-\varepsilon$ *model is implemented in this model. In order to improve the computational efficiency, an extremely anisotropic mesh adaptivity is used here. To validate the present model, the test of flow past a rigid rotating vertical tidal turbine is considered. The simulation results of these complex practical test cases are all in good agreement with experimental and numerical data in the literature. Finally, the elasticity of a vertical axis turbine test case is presented to demonstrate the model's capabilities when analysing the elasticities for realistic vertical axis tidal turbines. More importantly, flow-induced fractures in a vertical axis turbine are presented to predict the worst scenarios.*

6.1 Introduction

Recently, an advanced FSI turbulent model is developed by Yang *et al.* (2016, 2017a) based an immersed-body method. This model couples a combined finite-discrete element solid model (FEMDEM) with a finite element CFD model (Fluidity-Multiphase). The interaction between the moving solids and turbulent flow is modelled in a very thin shell mesh surrounding the solid surface. This thin shell is acted as a delta function to implement the boundary conditions for both the turbulence model and the fluid momentum equation.

The 2D & 3D URANS FSI model has been developed in this work. In this chapter, this model is applied to simulate 2D & 3D vertical axis turbines. To validate the model, the power coefficients are compared to those measured in (Maître *et al.*, 2013). Additionally, the model has been applied to analyze the elastic response of vertical axis turbines in turbulent flows. More importantly, this model can be used to predict some worst scenarios, for instance, flow-induced fractures in a vertical axis turbine. An extremely anisotropic mesh adaptivity is used here to reduce the total number of nodes in the computational mesh. This enables the model to run relatively fast.

The remainder of this chapter is organised as follows. Flow past 2D and 3D rotating vertical axis turbine test cases are presented in section 6.2 and section 6.3, respectively. In section 6.4, the elastic response of a vertical axis turbine with the tower in turbulent flow is given out. Flow-induced fractures in a vertical axis turbine test case is presented to predict the worst scenarios in section 6.5 The list of the test cases in this chapter is shown in Table 6.1. The strengths and weaknesses of this model are discussed in Section 6.6. The conclusions are presented in Section 6.6.

Table 6.1 Tidal turbine test cases

Section	Case name	Case purpose
Section 6.2	Flow past a 2D rotating vertical axis turbine	Validation
Section 6.3	Flow past a 3D rotating vertical axis turbine	Validation
Section 6.4	Flow past a 3D flexible vertical axis turbine	Application
Section 6.5	Flow-induced fractures in a 3D vertical axis turbine	Application

6.2 Flow past a 2D rotating vertical axis turbine

In this section, a 2D vertical axis turbine rotating in turbulent flow is simulated. The power coefficients calculated in the simulations are compared with the numerical and experimental data in (Maître *et al.*, 2013). Maître *et al.* (2013) developed a sliding mesh method based on a flow solver, ANSYS-Fluent V13, to complete the simulations of the flow past a 2D rotating vertical axis marine turbine. The sliding mesh allows the fine mesh to be used near the blade surfaces. The test cases in (Maître *et al.*, 2013) are fluid only simulations. It is worth noting that Maître *et al.* (2013) used ANSYS-Fluent as a pure CFD solver (without solid-fluid coupling) to simulate the flow past a VATT.

The present URANS $k - \varepsilon$ FSI model is a solid-fluid coupling model. An adaptive mesh can ensure the mesh quality near the blade surfaces. Meantime, the solid stress, motion, deformation and fracture can be computed inside the turbine structure.

6.2.1 The setup of the vertical axis turbine

A horizontal slice of the vertical axis turbine (Maître *et al.*, 2013) is used to set up a 2D numerical simulation. The height of the vertical axis turbine is H=0.175m and the radius of the vertical axis turbine is R=0.5H (see Fig. 6.1). The physical rotating axis of the vertical axis turbine is a cylinder with diameter $D_c = 0.022\,\mathrm{m}$ (see Fig. 6.1). The blade profiles used on this vertical axis turbine are based on NACA0018 (Maître *et al.*, 2013) aerofoil with the chord length $c = 0.032\,\mathrm{m}$. The fluid with inlet velocity $U_i = 2.3\,\mathrm{m/s}$ and kenimatic viscosity $\nu = 1 \times 10^{-6}\,\mathrm{m}^2/\mathrm{s}$ passes the rotating vertical axis turbine from the left to right hand side. The rotating angular velocity of the vertical axis turbine is $\Omega = 52.5714\,\mathrm{rad}/s$. Then the Reynolds number of this case can be given as:

$$Re = \frac{\Omega R c}{\nu} = 147200. \qquad (6.1)$$

The tip-speed ratio is defined as:

$$\lambda = \frac{\Omega R c}{U_i} = 2.0. \qquad (6.2)$$

The on-coming fluid velocity vector on the turbine blade is combined by two components: U_i and ΩR (see Fig. 6.2b). Thus the on-coming fluid velocity vector W

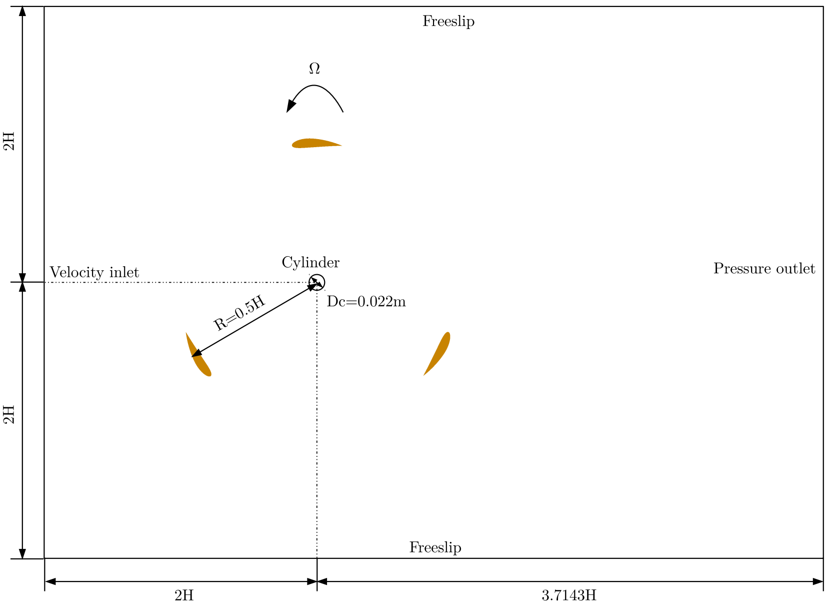

Figure 6.1 The computational domain and settings of flow past a 2D rotating vertical axis turbine.

can be obtained via:

$$\vec{W} = \vec{U_i} - \vec{\Omega} R. \tag{6.3}$$

Then the on-coming velocity modulus, W, and the incidence angle, α_i can be expressed as:

$$W = U_i \sqrt{1 + 2\lambda cos\theta_b + \lambda^2}, \tag{6.4}$$

$$\alpha_i = tan^{-1}\left(\frac{sin\theta_b}{cos\theta_b + \lambda}\right). \tag{6.5}$$

The incidence angle α_i of the flow past a 2D rotating vertical axis turbine at different blade position θ_b at $\lambda = 2.0$ are drawn on Fig. 6.2a. There are two components of forces on the vertical axis turbine blade (see Fig. 6.2b). They are f_x and f_y that represent forces on x and y direction, respectively. f_x and f_y are calculated by the following equations:

$$f_x = \int_{blade\_surfce} f_s \bullet n_x dS, \tag{6.6}$$

$$f_y = \int_{blade\_surfce} f_s \bullet n_y dS, \tag{6.7}$$

where f_s is the force applied to the blade surface in unit normal vector, n_x and n_y

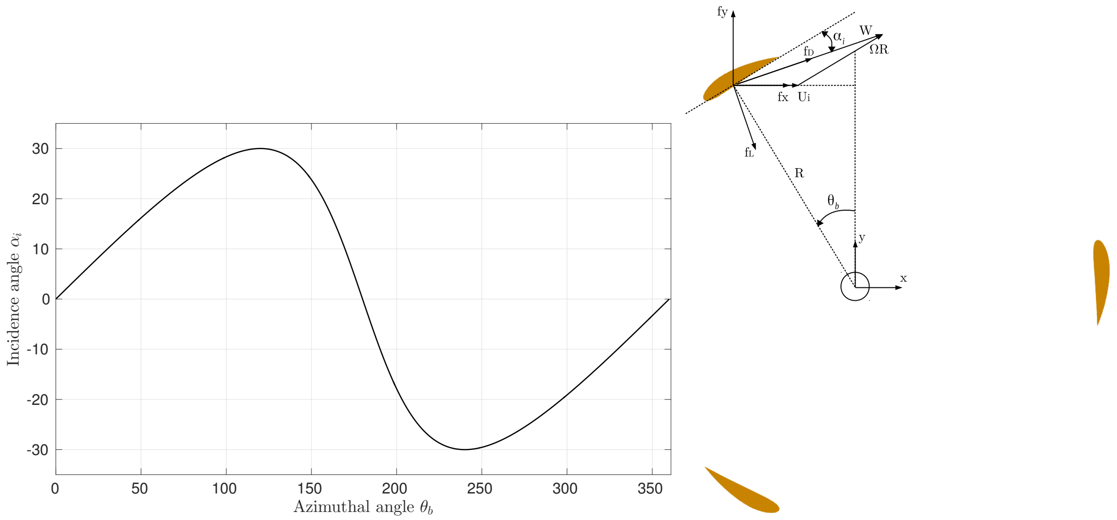

(a) (b)

Figure 6.2 (a) The incidence angle α_i of the flow past a 2D rotating vertical axis turbine at different blade position θ_b at $\lambda = 2.0$. (b) Velocities triangles and forces in a vertical axis turbine.

are the unit normal vector in x and y direction, dS is the unit surface. Then the drag and lift forces on the blade can be computed using f_x and f_y via (Maître *et al.*, 2013; McNaughton *et al.*, 2014):

$$f_D = f_x cos\gamma + f_y sin\gamma, \tag{6.8}$$

$$f_L = f_x sin\gamma - f_y cos\gamma, \tag{6.9}$$

$$\gamma = \theta_b - \alpha_i. \tag{6.10}$$

The power coefficient of the vertical axis turbine is calculated by:

$$C_{pow} = \frac{T\Omega}{\rho_f H R U_i^3}, \tag{6.11}$$

where $\rho_f = 1000\,\mathrm{kg/m^3}$, T is the torque.

6.2.2 The fluid dynamics of the flow past a 2D rotating vertical axis turbine

The computational domain with the boundary conditions of the flow past a 2D rotating vertical turbine test case is shown in Fig. 6.1. The dimensions of this domain are $5.7143H \times 4H$ and the centre of the cylinder axis locating at $2H$ to the left and bottom boundaries. A velocity inlet condition is given at the left wall and a pressure outlet with $P_o = 0.0\,\mathrm{Pa}$ is given at the right wall. A free slip condition is given at the bottom and the top boundaries.

The vorticity field and contour of the flow past a rotating vertical axis turbine are shown in Figs. 6.3 and 6.4, respectively. In order to link the fluid separation to the incidence angle (also called as the attack angle) α_i, Table 6.2 lists the relationship between the attack angle α_i and the blade positions θ_b using equation 6.5 and Fig. 6.2a. From Table 6.2, it can be found that the attack angle moves from $\alpha_i = 0°$ to $\alpha_i = 19.11°$ when the blade position moves from $\theta_b = 0°$ to $\theta_b = 60°$ (see Fig. 6.3a, c and d). In this period, no flow separation and smaller vortices are detaching from the rears of the blades (see Fig. 6.3a, c and d). Here, this stage is named as ‘no separation stage’. In the ‘no separation stage’ the flow passes through the blade surface smoothly without reverse flow and small vortices detaching from the rear of the blade. As the blade moves from $\theta_b = 90°$ to $\theta_b = 150°$, the attack angle moves from $\alpha_i = 26.57°$ to $\alpha_i = 23.79°$ (see Table 6.2, Fig. 6.3a, b and d). This period is called as the ‘pressure surface separation stage’ since there are large flow separations on the pressure surface of the blade in this stage. It is worth to mention that the attack angle α_i changes to its maximum value $\alpha_i = 30°$ when blade position at $\theta_b = 90°$ (see Table 6.2, Fig. 6.3a). At the attack angle $\alpha_i = 30°$, the largest separation vortex appears (see Fig. 6.3a) on the blade pressure surface. At the attack angle $\alpha_i = 26.57°$ and $\alpha_i = 23.79°$, there are clear flow separations on the blade pressure surface (see Fig. 6.3b and d). Then there is a short period near the attack angle $\alpha_i = 0°$ when the blade position at $\theta_b = 180°$ (see Table 6.2, Fig. 6.3c). In this period, the attached eddies in the ‘pressure surface separation stage’ reattach the blade surface (see Fig. 6.3c). This period is then named as the ‘transition stage’ due to the linkage between two large operation stages: ‘pressure surface separation stage’ and ‘suction surface separation stage’. The ‘suction surface separation stage’ ranges from the attack angle $\alpha_i = -23.79°$ to the $\alpha_i = -26.57°$ (see Table 6.2, Fig. 6.3a, b and d). In this stage, the separations are found at the suction surface of the blade (see Fig. 6.3a, b and d). It can be found that the largest suction surface separation happens at attack angle $\alpha_i = -30°$ and the blade position at $\theta_b = 270°$ (see Fig. 6.3d). In the meantime, flow separations on the suction surface of the blade are also found at attack angle $\alpha_i = -23.79°$ and $\alpha_i = -26.57°$ (see Fig. 6.3a and b). After the ‘suction surface separation stage’, there is a final stage in which the flow separations become less and less till to the ‘no separation stage’. this final stage is named as the 'reattaching stage'. In summary, the blade experience five stages in a circular movement, i.e. 'no separation stage', 'pressure surface separation stage', 'transition stage', 'suction surface separation stage' and 'reattaching stage'. Similar vortex shedding patterns are also obtained by Maître *et al.* (2013).

Table 6.2 The relationship between the blade position θ_b and the attack angle α_i.

Blade position θ_b	Attack angle α_i
0°	0°
30°	9.90°
60°	19.11°
90°	26.57°
120°	30°
150°	23.79°
180°	0°
210°	−23.79°
240°	−30°
270°	−26.57°
300°	−19.11°
330°	−9.90°

There are breaking and merging eddies during the turbine rotation (see Fig. 6.4). From Fig. 6.4a, it can be found that the blade at position $\theta_b = 0°$ breaks the eddies detaching from the blade at position $\theta_b = 120°$. The broken eddies move to the downstream and meet with the eddies detaching from the blade at position $\theta_b = 0°$. Among these broken eddies and new eddies, some of them merge into bigger eddies and others interact with each other and generate smaller ones. However, the eddy motions near the blade at the position $\theta_b = 240°$ are different from these at $\theta_b = 0°$ and $\theta_b = 120°$. The eddies detaching from the blade at the position $\theta_b = 240°$ interact with the blade itself. Since the eddies detaching from the blade at the position $\theta_b = 240°$ are relatively big, the blade mainly changes the shape of the eddies from a circle to an ellipse. Similar breaking and merging patterns are also found in Fig. 6.4b-d. It is worth noting that larger eddies are generated by merging small eddies at the central far downstream because most of the eddies move to this area.

An unstructured anisotropic adaptive fluid mesh is used in this study case (see Fig. 6.5). The minimum and maximum mesh edge lengths are $5 \times 10^{-4}\,\mathrm{m}$ and $0.3\,\mathrm{m}$, respectively. The fluid mesh is always automatically refined near the blade surfaces

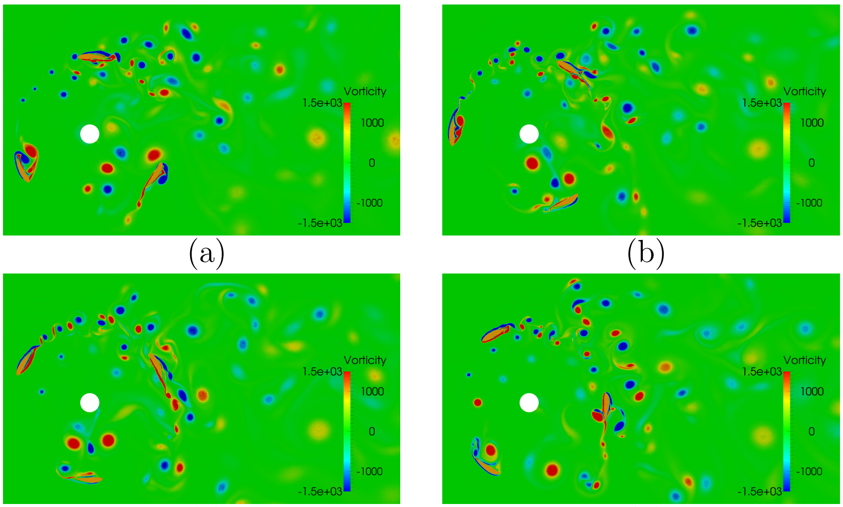

(a) (b)

(c) (d)

Figure 6.3 The vorticity of flow past a rotating vertical axis turbine obtained by the presented model at $\lambda = 2$ at different blade positions. (a) The positions of the three blades are $\theta_b = 0°$, $\theta_b = 120°$ and $\theta_b = 240°$. (b) The positions of the three blades are $\theta_b = 90°$, $\theta_b = 210°$ and $\theta_b = 330°$. (c) The positions of the three blades are $\theta_b = 180°$, $\theta_b = 300°$ and $\theta_b = 60°$. (d) The positions of the three blades are $\theta_b = 270°$, $\theta_b = 30°$ and $\theta_b = 150°$.

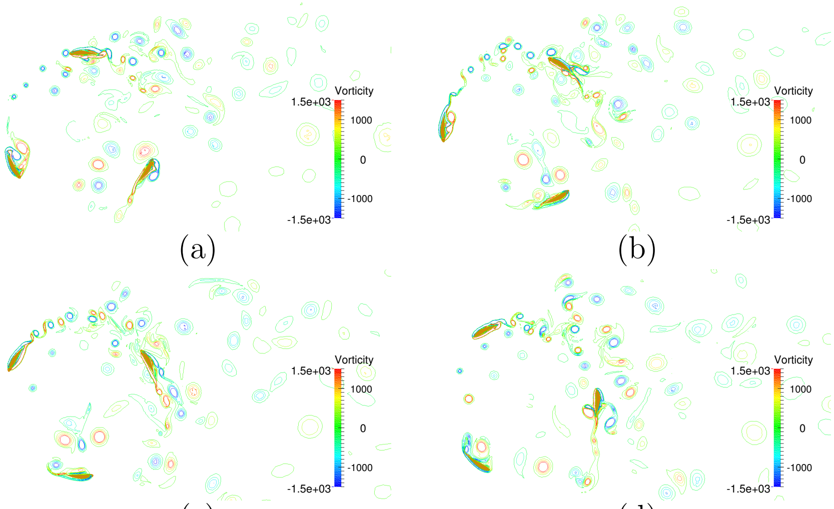

(a) (b)

(c) (d)

Figure 6.4 The vorticity contours of flow past a rotating vertical axis turbine obtained by the presented model at $\lambda = 2$ at different blade positions. (a) The positions of the three blades are $\theta_b = 0°$, $\theta_b = 120°$ and $\theta_b = 240°$. (b) The positions of the three blades are $\theta_b = 90°$, $\theta_b = 210°$ and $\theta_b = 330°$. (c) The positions of the three blades are $\theta_b = 180°$, $\theta_b = 300°$ and $\theta_b = 60°$. (d) The positions of the three blades are $\theta_b = 270°$, $\theta_b = 30°$ and $\theta_b = 150°$.

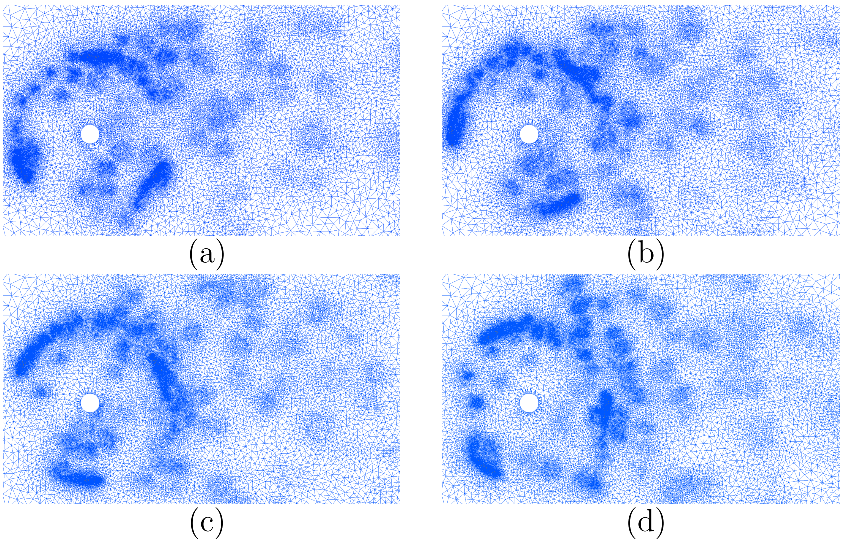
(a) (b) (c) (d)

Figure 6.5 The meshes of flow past a rotating vertical axis turbine obtained by the presented model at $\lambda = 2$ at different blade positions. (a) The positions of the three blades are $\theta_b = 0°$, $\theta_b = 120°$ and $\theta_b = 240°$. (b) The positions of the three blades are $\theta_b = 90°$, $\theta_b = 210°$ and $\theta_b = 330°$. (c) The positions of the three blades are $\theta_b = 180°$, $\theta_b = 300°$ and $\theta_b = 60°$. (d) The positions of the three blades are $\theta_b = 270°$, $\theta_b = 30°$ and $\theta_b = 150°$.

in order to ensure the fluid mesh capture the exact positions of the blade surfaces. Additionally, the adaptive mesh is also refined in the area with the large velocity gradient to accurately resolve the vortex shedding at the weak. This adaptive mesh allows a small number of the total mesh nodes to be used in this test case without the reduction of the ability to capture the eddies and the sharp solid-fluid interfaces. This results in the reduction of the computational expense both in memory and CPU time.

The pressure contours of flow past a rotating vertical axis turbine case at different blade positions are shown in Fig. 6.6. The high-pressure areas are moving when the blade position changes. From the blade position $\theta_b = 0°$ to $\theta_b = 30°$, the high-pressure areas are at the leading edge of the blade (see Fig. 6.6a and d). When the blade position moves from $\theta_b = 60°$ to $\theta_b = 120°$, the high-pressure areas transfer to the suction surface of the blade (see Fig. 6.6a-c). However, the high-pressure areas quickly change to the pressure surface of the blade at the position $\theta_b = 150°$ to $\theta_b = 240°$ (see Fig. 6.6a-d). At the end, the high-pressure change back to the suction surface of the blade at $\theta_b = 270°$ and $\theta_b = 330°$ (see Fig. 6.6b and d). There is one strange thing happening at the blade position $\theta_b = 300°$ that the high-pressure

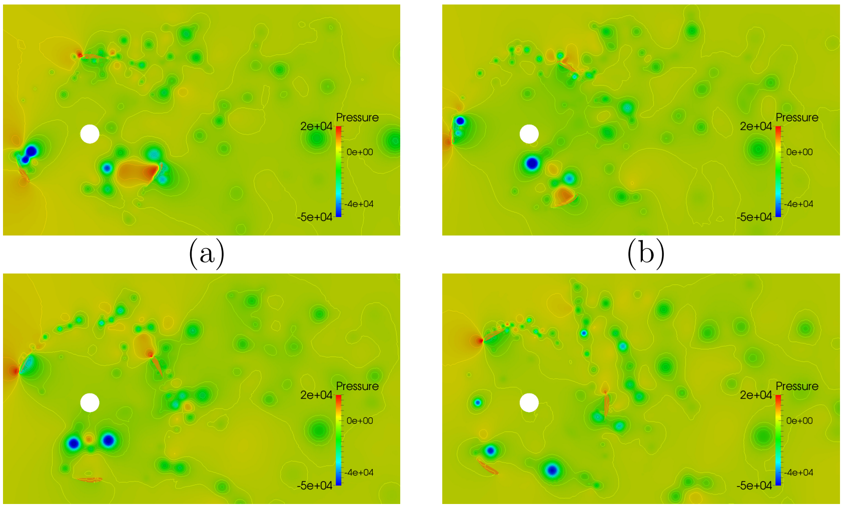

(a) (b)

(c) (d)

Figure 6.6 The pressure contours of flow past a rotating vertical axis turbine obtained by the presented model at $\lambda = 2$ at different blade positions. (a) The positions of the three blades are $\theta_b = 0°$, $\theta_b = 120°$ and $\theta_b = 240°$. (b) The positions of the three blades are $\theta_b = 90°$, $\theta_b = 210°$ and $\theta_b = 330°$. (c) The positions of the three blades are $\theta_b = 180°$, $\theta_b = 300°$ and $\theta_b = 60°$. (d) The positions of the three blades are $\theta_b = 270°$, $\theta_b = 30°$ and $\theta_b = 150°$.

area is on the leading edge of the blade (see Fig. 6.6c). According to blade position at $\theta_b = 270°$ and $\theta_b = 330°$ (see Fig. 6.6b and d), the high-pressure on the suction surface should be expected. To further explain why the high-pressure area moves to the leading edge of the blade, let us look at the vortex pattern in Fig. 6.3c. In Fig. 6.3c, it is found that the flow separation starts from the leading edge of the blade. This results in the high-pressure area moving from the suction surface to the leading edge of the blade. Similar pressure contours can be found in (Milthaler, 2014).

The turbulent kinetic energy profiles of flow past a rotating vertical axis turbine case at different blade positions are given in Fig. 6.7. The turbulent kinetic energy diffuses when it transfers to the downstream of the turbine. The highest turbulent kinetic energy is found near the surface of the blade. As the vortex shedding from the blade surface, the turbulent kinetic energy reduces. Since the eddies move to the far downstream of the turbine, the turbulent kinetic energy reduces a lot. Although the eddies at the far downstream are very large (see Fig. 6.4), they have the lowest turbulent kinetic energy. This means the flow mixing in this area could be very low.

Finally, the total power coefficient of the turbine obtained from the present model

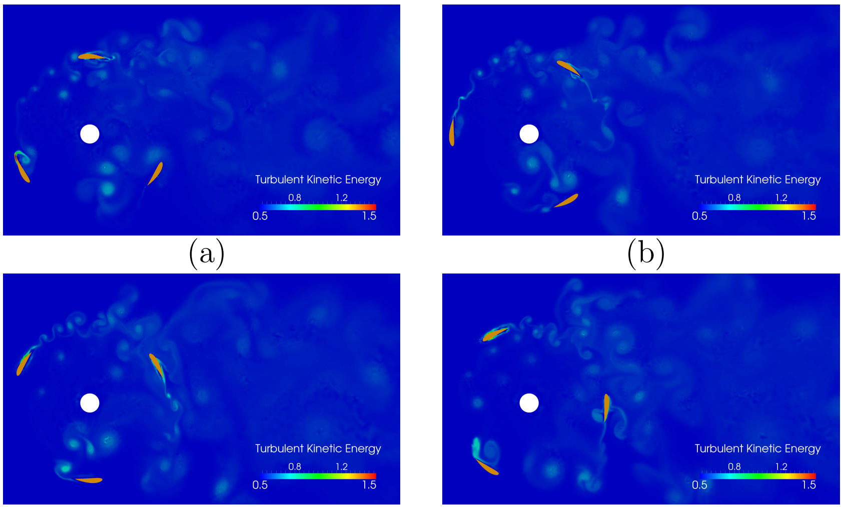

(a) (b) (c) (d)

Figure 6.7 The turbulent kinetic energy of flow past a rotating vertical axis turbine obtained by the presented model at $\lambda = 2$ at different blade positions. (a) The positions of the three blades are $\theta_b = 0^\circ$, $\theta_b = 120^\circ$ and $\theta_b = 240^\circ$. (b) The positions of the three blades are $\theta_b = 90^\circ$, $\theta_b = 210^\circ$ and $\theta_b = 330^\circ$. (c) The positions of the three blades are $\theta_b = 180^\circ$, $\theta_b = 300^\circ$ and $\theta_b = 60^\circ$. (d) The positions of the three blades are $\theta_b = 270^\circ$, $\theta_b = 30^\circ$ and $\theta_b = 150^\circ$.

is compared with the experimental data in (Maître *et al.*, 2013) and numerical simulation results in (McNaughton *et al.*, 2014) in Fig. 6.8. From Fig. 6.8, it can be found that the power coefficient computed via the present model is in good agreement with the experimental data (McNaughton *et al.*, 2014). The present URANS FSI model overestimates the total power coefficient. McNaughton *et al.* (2014) also found the same error in the $k-\omega$ SST model and $k-\omega$ SST LRE models. This overestimate could be caused by zero diffusion of the energy loss in the 2D numerical simulations. In a real 3D numerical model, there is the blade tip loss, the arm (the beam linking the blades and the central rotating cylinder) friction loss and the shaft bearing system loss. However, the results obtained by the present model are closer to the experimental data in (Maître *et al.*, 2013) than these numerical data in (McNaughton *et al.*, 2014). This indicates the present URANS FSI model using adaptive mesh are good at solving fluid dynamics for moving solids in turbulent flows for industry application.

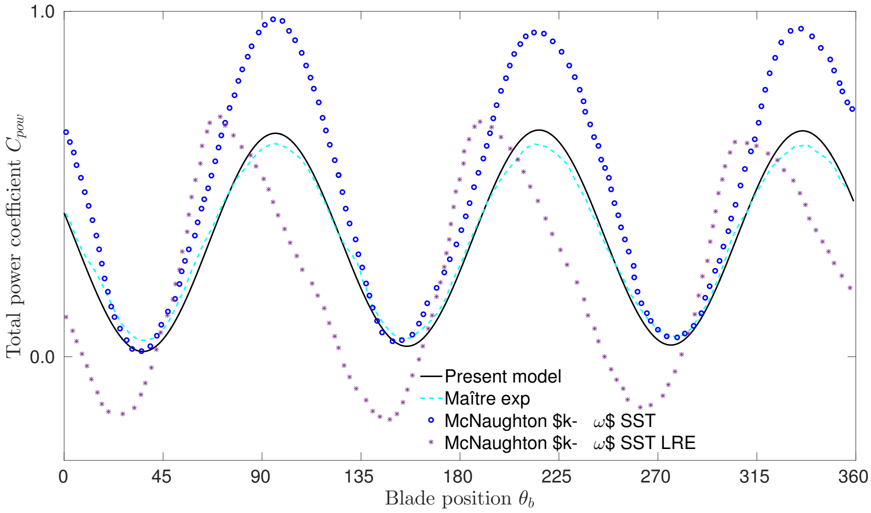

Figure 6.8 The comparison of total power coefficient C_{pow} of flow past a rotating vertical axis turbine at $\lambda = 2$. The black solid line is the simulation result obtained from the present model. The green dash line is the experimental data in (Maître *et al.*, 2013). The blue circle line is the simulation result of $k - \omega$ SST model in (McNaughton *et al.*, 2014). The purple star line is the simulation result of $k - \omega$ SST LRE model in (McNaughton *et al.*, 2014).

6.3 Flow past a 3D rotating vertical axis turbine

The 3D rotating vertical axis turbine structure and solid mesh are shown in Fig. 6.9. The 3D computational domain with dimensions $5.7143H \times 4H \times 2H$ is given in Fig. 6.10. The left and right sides are set as velocity inlet and pressure outlet boundary conditions. The front, back, top and bottom sides are all given free-slip boundary conditions. The centre of the cylinder axis is set at 2H to the left side, 2H to the front side and 1H to the bottom side.

An unstructured anisotropic adaptive fluid mesh with the minimum and maximum edge lengths of 0.002 m and 0.2 m is used in this simulation. Here, 3D unstructured tetrahedral elements are used for fluid flow. The anisotropic mesh edge length ratio is set as 10.0. This means that the maximum edge length in one tetrahedron can be 10.0 times of the minimum edge length in this tetrahedron. This anisotropic mesh setting can extremely reduce the total mesh node number required in this test case. Combining with the dynamic mesh adaptivity as required, the total node number used here is decreased again. This enables me to run the complex 3D simulation in an acceptable timescale. In Fig. 6.11, the fluid velocity and adaptive meshes are

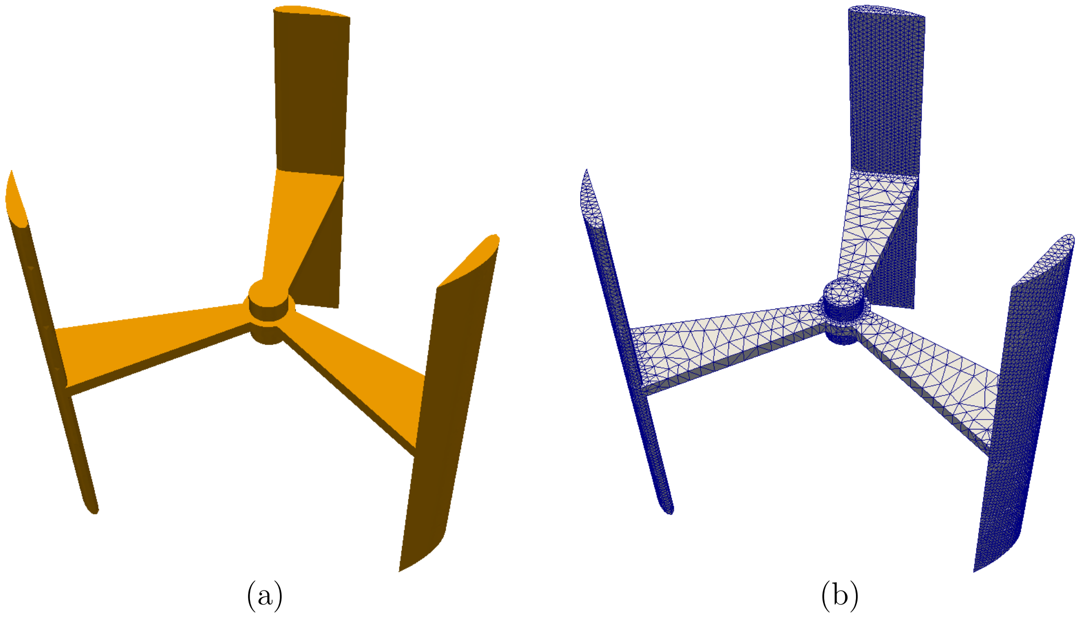

Figure 6.9 (a) The geometry of the vertical axis turbine. (b) The solid mesh of the vertical axis turbine.

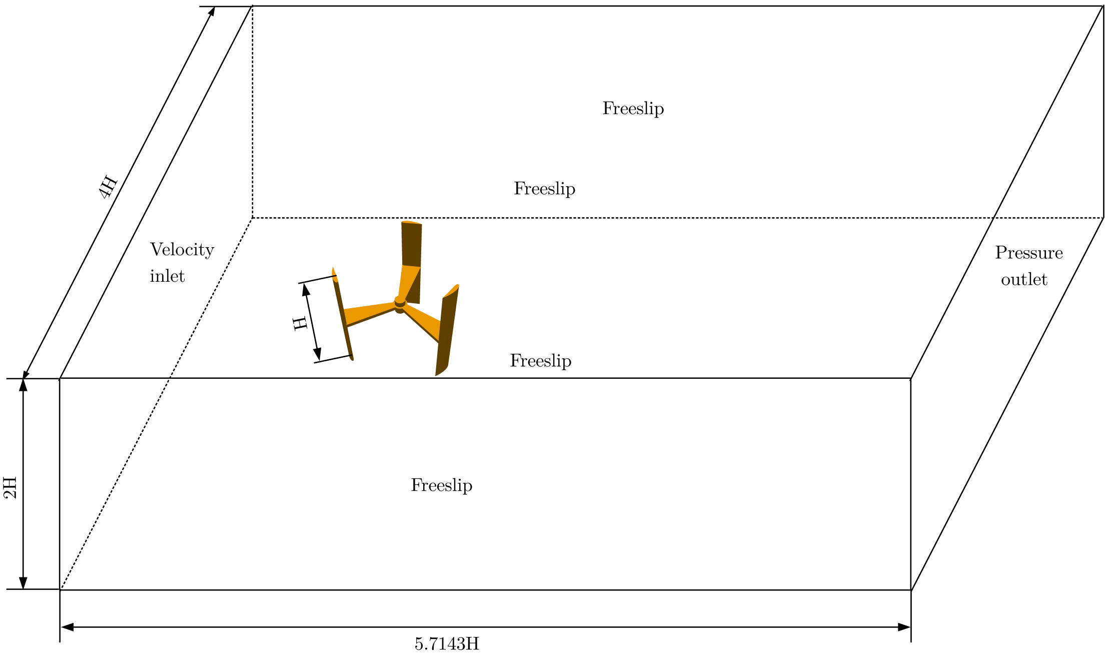
Freeslip
Freeslip
4H
Velocity inlet
Pressure outlet
H
Freeslip
2H
Freeslip
5.7143H

Figure 6.10 The computational domain and settings of flow past a 3D rotating vertical axis turbine.

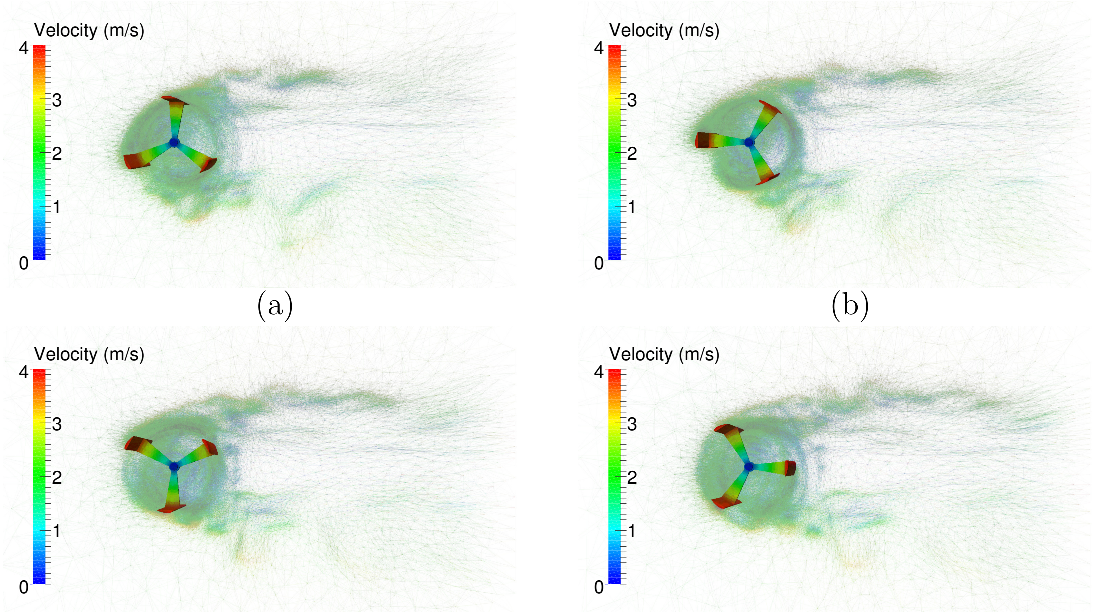

(a) (b)

(c) (d)

Figure 6.11 The velocity and adaptive mesh of flow past a 3D rotating vertical axis turbine obtained by the presented model at $\lambda = 2$ at different blade positions. (a) The positions of the three blades are $\theta_b = 0°$, $\theta_b = 120°$ and $\theta_b = 240°$. (b) The positions of the three blades are $\theta_b = 90°$, $\theta_b = 210°$ and $\theta_b = 330°$. (c) The positions of the three blades are $\theta_b = 180°$, $\theta_b = 300°$ and $\theta_b = 60°$. (d) The positions of the three blades are $\theta_b = 270°$, $\theta_b = 30°$ and $\theta_b = 150°$.

given out at four different blade positions: (a) $\theta_b = 0°$, $\theta_b = 120°$ and $\theta_b = 240°$; (b) $\theta_b = 90°$, $\theta_b = 210°$ and $\theta_b = 330°$; (c) $\theta_b = 180°$, $\theta_b = 300°$ and $\theta_b = 60°$; (d) $\theta_b = 270°$, $\theta_b = 30°$ and $\theta_b = 150°$. From Fig. 6.11, it can be found that the meshes are always refined at the turbine structural surface and the area with large velocity gradients. In Fig. 6.11, it can be found that the 3D adaptive meshes mainly concentrate around the rotating blades because there are lots of mixing flows in the central area. The adaptive mesh captures this mixing process caused by the rotating arms and the blades. Unlike the 2D simulation (see Fig. 6.5), there are more mesh nodes in the centre of the turbine because by the rotating arms in the 3D simulation requires a high-resolution mesh to capture their structures. Additionally, the 3D arms further mix the flow in the centre of the turbine. Importantly, the meshes at the downstream of the upbound and down-bound of the turbine are also refined because there are a large number of shedding vortices.

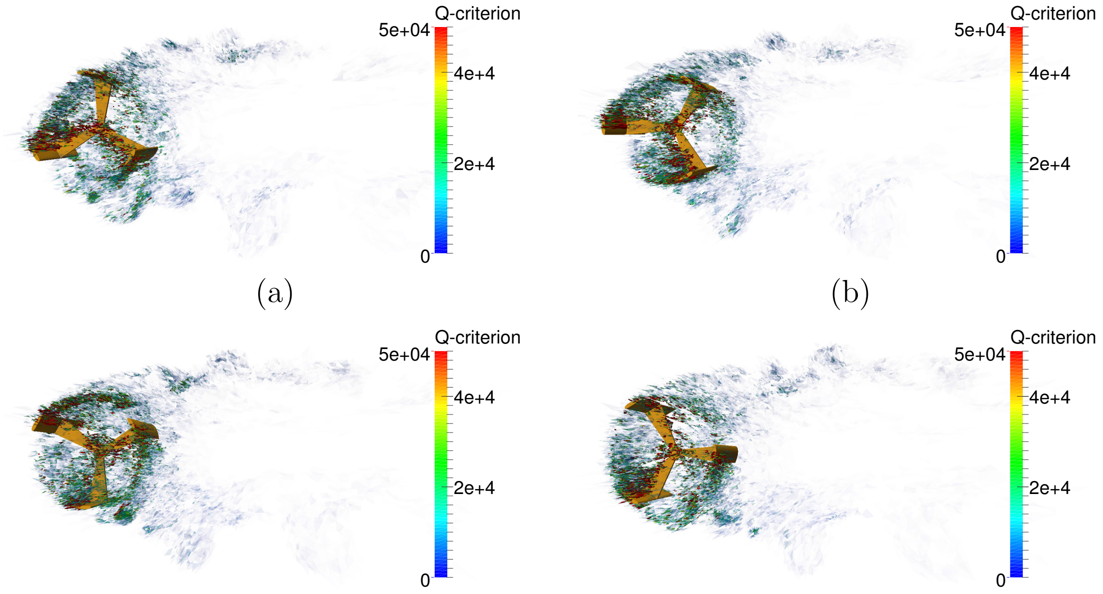

(a) (b)

(c) (d)

Figure 6.12 The Q-criterion of flow past a 3D rotating vertical axis turbine obtained by the presented model at $\lambda = 2$ at different blade positions. (a) The positions of the three blades are $\theta_b = 0°$, $\theta_b = 120°$ and $\theta_b = 240°$. (b) The positions of the three blades are $\theta_b = 90°$, $\theta_b = 210°$ and $\theta_b = 330°$. (c) The positions of the three blades are $\theta_b = 180°$, $\theta_b = 300°$ and $\theta_b = 60°$. (d) The positions of the three blades are $\theta_b = 270°$, $\theta_b = 30°$ and $\theta_b = 150°$.

The Q-criterion patterns at different blade positions of the 3D rotating vertical axis turbine are shown in Fig. 6.12. From Fig. 6.12, it can be found that the vortex rings are shedding from the rear of the three blades and the tower to the downstream. The vortex rings detached from each blade are mixed with each other. During rotating, the larger vortex rings are broken by the following blade and generating many smaller vortex rings. These small vortex rings merge and impact with each other. It is worth noting that the rotating arms and blades break the vortices in the centre into lots of small ones. This makes it difficult to identify some structured vortex shedding patterns in the centre of the turbine. However, it is relatively easy to find the shedding patterns at the upbound and down-bound of the turbine downstream. It can be found that the periodic vortices are detaching from the turbine.

In Fig. 6.13, the total power coefficient for this 3D rotating turbine in this simulation is compared with the experimental data in (Maître *et al.*, 2013) and numerical sim-

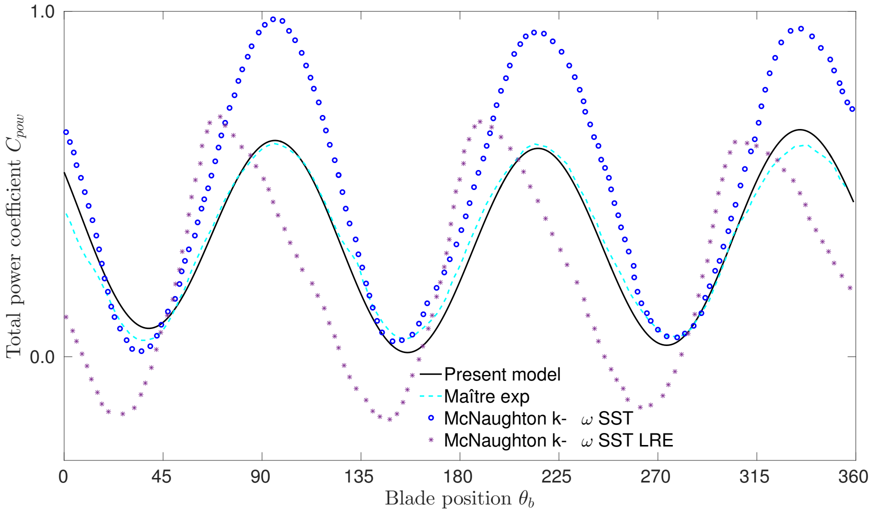

Figure 6.13 The comparison of total power coefficient C_{pow} of flow past a 3D rotating vertical axis turbine at $\lambda = 2$. The black solid line is the simulation result obtained from the present model. The green dash line is the experimental data in (Maître *et al.*, 2013). The blue circle line is the simulation result of $k - \omega$ SST model in (McNaughton *et al.*, 2014). The purple star line is the simulation result of $k - \omega$ SST LRE model in (McNaughton *et al.*, 2014).

ulation results in (McNaughton *et al.*, 2014). Good agreement is obtained between the experimental data (McNaughton *et al.*, 2014) and the numerical data from the present model. Like the 2D results (see Fig. 6.8), the overestimates are also found at $\theta = 150$ and $\theta = 270$. However, unlike the 2D results (see Fig. 6.8), it can be found that there are some underestimates of the total power coefficient at $\theta = 40$ and $\theta = 225$. The mixing of underestimates and overestimates in the 3D results obtained from the present URANS FSI model proves that the 3D model is closer to the reality. In Fig. 6.13, the numerical data in (McNaughton *et al.*, 2014) are obtained from 2D $k - \omega$ SST model and $k - \omega$ SST LRE models. To sum up, the 3D results are better than the 2D results obtained from the present model, since the 3D model simulates the 3D rotating arms and takes the blade tip loss into account.

6.4 Flow past a 3D flexible vertical axis turbine

This section focuses on the elastic response of a 3D vertical axis turbine with tower facing a constant inlet velocity flow. The structure of the 3D vertical axis turbine

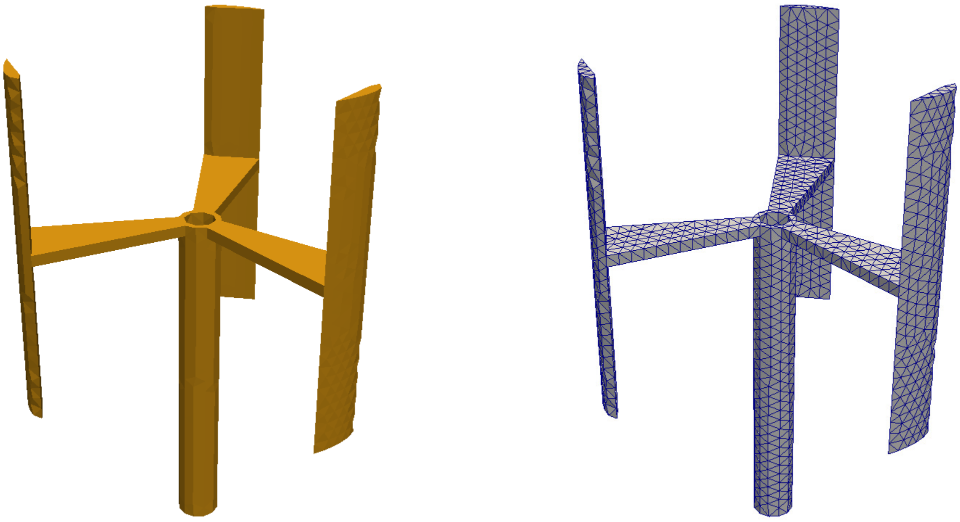
(a) (b)

Figure 6.14 (a) The geometry of the vertical axis turbine with tower. (b) The solid mesh of the vertical axis turbine with tower.

and the solid mesh are shown in Fig. 6.14. This flexible vertical axis turbine has three components: the three turbine blades, the three arms, and the tower. The tower is vertically installed on the ground with a fixed bottom. The three turbine blades are linked with the tower by the three arms. The geometry of the arms and the turbine blades are the same as those in Section 6.3. The tower is a hollow cylinder with the outer radius $r_o = 0.011\,\text{m}$ and the inner radius $r_i = 0.0081\,\text{m}$, respectively. The height of the tower is H.

The 3D computational domain of the tower bottom fixed vertical axis turbine with dimensions $5.7143H \times 4H \times 2H$ is given in Fig. 6.15. The left and right sides are set as the velocity inlet and pressure outlet boundary conditions, respectively. The front, back, top and bottom sides are all given free-slip boundary conditions. The centre of the cylinder tower top is set at 2H to the left side, 2H to the front side and 1H to the bottom side. The bottom of the turbine tower is fixed (see Fig. 6.15). The inlet velocity is given as a constant value of $2.3\,\text{m/s}$.

The solid mesh size in this simulation is $0.006\,\text{m}$. The material properties of the turbine are listed in Table 6.3. The adaptive fluid meshes with the minimum and maximum edge lengths of $0.002\,\text{m}$ and $0.2\,\text{m}$ are used in this simulation. The anisotropic mesh edge length ratio is set as 10.0. From Fig. 6.16, it can be found that the fluid meshes are always refined at the turbine structural surface (on the blades, the arms

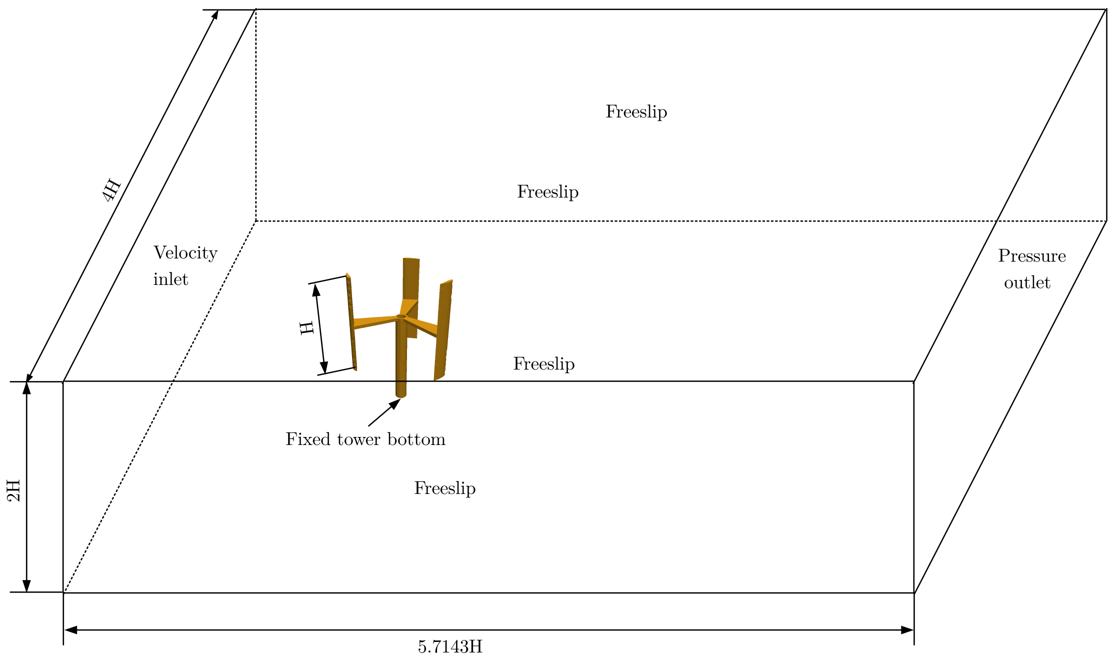

Figure 6.15 The 3D computational domain of a tower bottom fixed vertical axis turbine.

and the tower) and the area with large velocity gradients. Importantly, in Fig. 6.16, the varies in velocity along the tower and blades height at the z direction can be found. There are 3D effects that cause the secondary flows at the top and bottom tips of the blades.

Table 6.3 The material properties of the turbine.

Turbine conditions	values
Density (kg/m^3)	2100
Young's modulus E (Pa)	3.86×10^{10}
Penalty number	3.86×10^{10}
Fracture energy release rate G_f	100.0
Poisson ratio	0.26
Tensile strength (Pa)	1.062×10^{9}
Shear Strength (Pa)	2.124×10^{9}

The vortex-induced vibration of the vertical axis turbine happens in this simulation. The results of the largest displacement of the turbine in this simulation are given in Fig. 6.17a. In this figure, the maximum displacements of the vertical axis turbine compared to the initial position are presented. The yellow geometry represents the

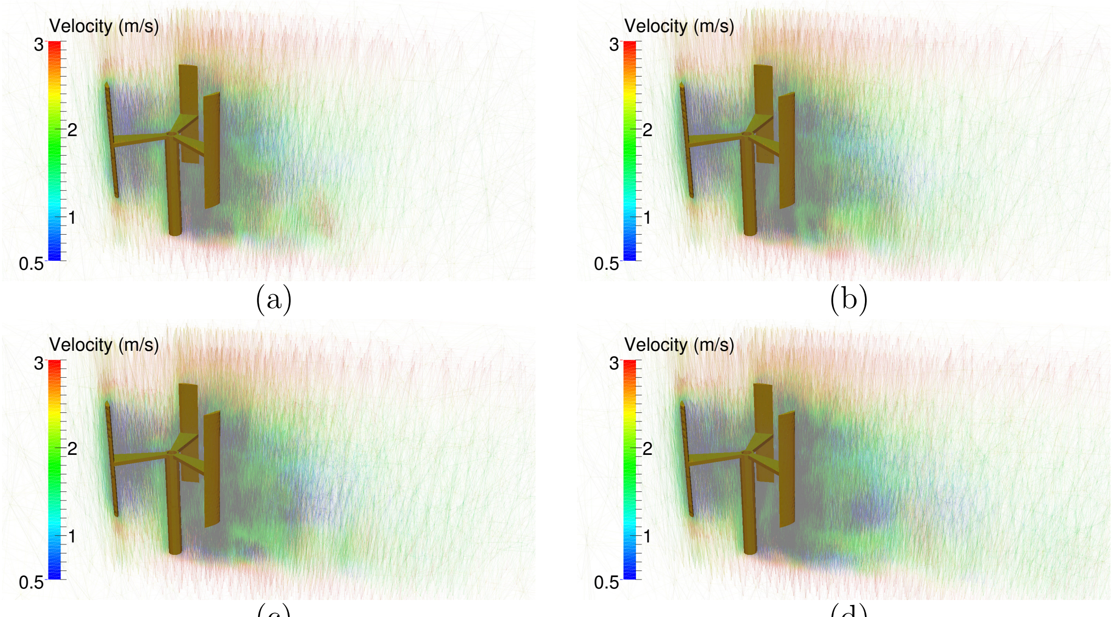

(a) (b) (c) (d)

Figure 6.16 The velocity and adaptive mesh of the vibrating vertical axis turbine at different times: (a) t=0.2 s, (b) t=0.25 s, (c) t=0.3 s and (d) t=0.35 s.

initial position and the white one with the blue meshes shows the position of the largest displacement at time $t = 0.003\,\mathrm{s}$. From the Fig. 6.17a, it can be found that the bottom of the tower does not have displacement because it is fixed. From the tower bottom to the top tips of the three blade, the displacements increase. The largest displacements are found on the tips of the blades. Thus three points on the tip of each blade are marked on Fig. 6.17b. The displacements of these three points are drawn in Fig. 6.18. From Fig. 6.18, it can be found that the largest displacements of every blade are generated when the inlet flow impact on the turbine at $t = 0.003\,\mathrm{s}$. Then the vibration magnitudes attenuate immediately from $t = 0.003\,\mathrm{s}$ to $t = 0.025\,\mathrm{s}$. In the first vibration cycle, the maximum magnitude is 0.025H, while it is halved in the second vibration cycle. Then at the third vibration cycle, the vibration magnitude drops to one-fourth of that at the first vibration cycle. In the fourth variation cycle, the vibration magnitude is almost one-eighth of that at the first vibration cycle. After the fourth vibration cycle, the vibration magnitude is controlled and decreased to a stable level.

The Q-criterion patterns at different times of the 3D vibrating turbine are shown in Fig. 6.19. From Fig. 6.19, it can be found that the vortex rings are shedding from rears of the three blades and the tower to the downstream. The vortex rings detached from blade No. 3 are mixed with the vortex rings detached from the tower and the

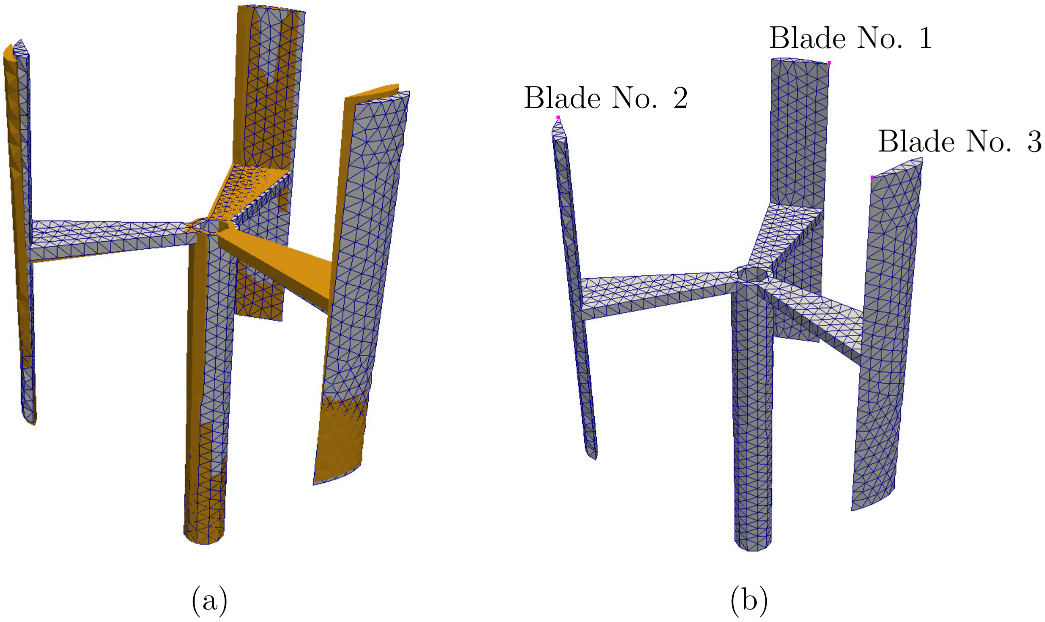

Figure 6.17 (a)The displacement of the vertical axis turbine compared to the initial position. The yellow one without mesh is the initial position. The white one with blue mesh is the position at the largest displacement. (b) The displacement measurement points on each blade. The three red points on each blade are the points where the displacement is plotted out in Fig. 6.18.

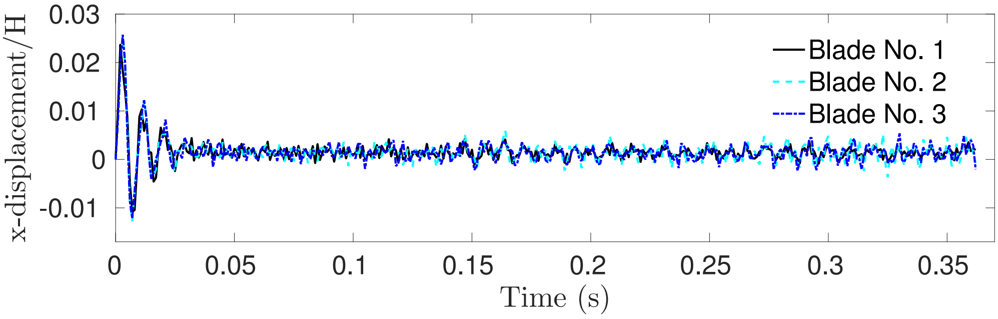

Figure 6.18 The displacements of three points marked in Fig. 6.17b.

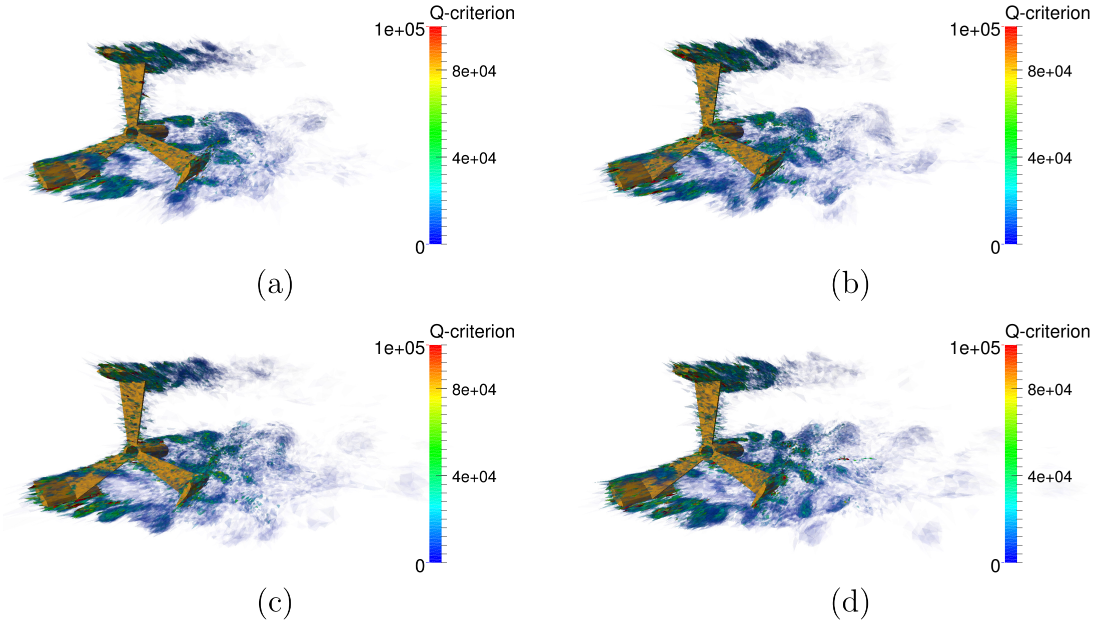
Q-criterion
1e+05
8e+04
4e+04
0

(a) (b)

(c) (d)

Figure 6.19 The Q-criterion of the vibrating vertical axis turbine at different times: (a) t=0.2 s, (b) t=0.25 s, (c) t=0.3 s and (d) t=0.35 s.

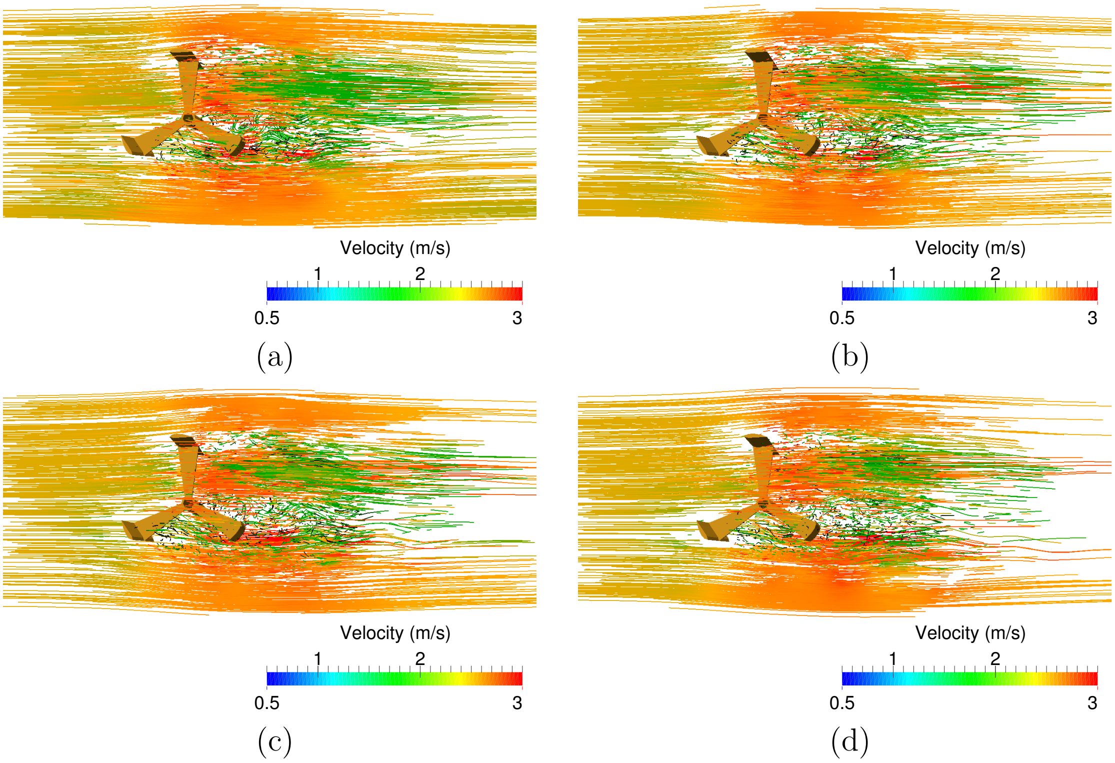
Velocity (m/s)
1
2
0.5
3

(a) (b)

(c) (d)

Figure 6.20 The streamline of the vibrating vertical axis turbine at different times: (a) t=0.2 s, (b) t=0.25 s, (c) t=0.3 s and (d) t=0.35 s.

blade No. 2. These vortex rings merge and impact with each other. Some smaller shedding rings are created by the impact, while some bigger ones are generated by merging several small vortex rings. In the downstream of blade No. 1 (see Fig. 6.19b-d), there are clear vortex ring patterns. The pattern is 2-3 uniform vortex rings shedding on after another. However, this is not the case for the downstream of blade No. 1 in Fig. 6.19a. In Fig. 6.19a, the first vortex ring at the downstream of the blade No. 1 is not clear and breaks into 3 three rings. It could be caused by the secondary flows at the top and bottom tips of the blade No. 1. Along the blade height z direction, the vortex rings are not uniform cylinders, some of them are with thick centres and some are with thick tips. This kind of vortex shapes is caused by the 3D effects because there is flow in the z direction in 3D simulations compared to the 2D ones. Similar patterns can also be found at the downstream of the blade No. 2 in Fig. 6.19 In Fig. 6.19a-b, the vortex rings at the downstream of the blade No. 2 are mixed, while the vortex rings become obvious in Fig. 6.19c-d. These vortex shedding patterns indicate that the present FSI model is able to model 3D complex cases.

The streamlines of the flow past a 3D flexible vertical axis turbine case are given in Fig. 6.20. In these streamlines, these go around the turbine up-bound and down-bound are smooth and they are not cut and mixed by the turbine. However, these go directly through the turbine are mixed and bent a lot. For these streamlines go directly through the turbine, they have shown the vortex patterns in the downstream of the turbine. These streamlines demonstrate that the present FSI model is good at capturing the flow details at the downstream of complicated vibrating structures.

6.5 Flow-induced fractures in a 3D vertical axis turbine

Since the horizontal axis wind turbine have been widely used, there are various flow-induced structural failures in wind turbines (Chou & Tu, 2011; Chen & Xu, 2016). Chou & Tu (2011) reported a collapsed large wind turbine tower in Typhoon Jangmi on September 28, 2008. This wind turbine was located on the shore of Taichung Harbor. The total height of the turbine tower is 62.0 m, the tower was fractured at 17.3 m height to the ground when the typhoon struck the wind turbine. After the turbine tower failure, the blades impacted the ground and two of the three

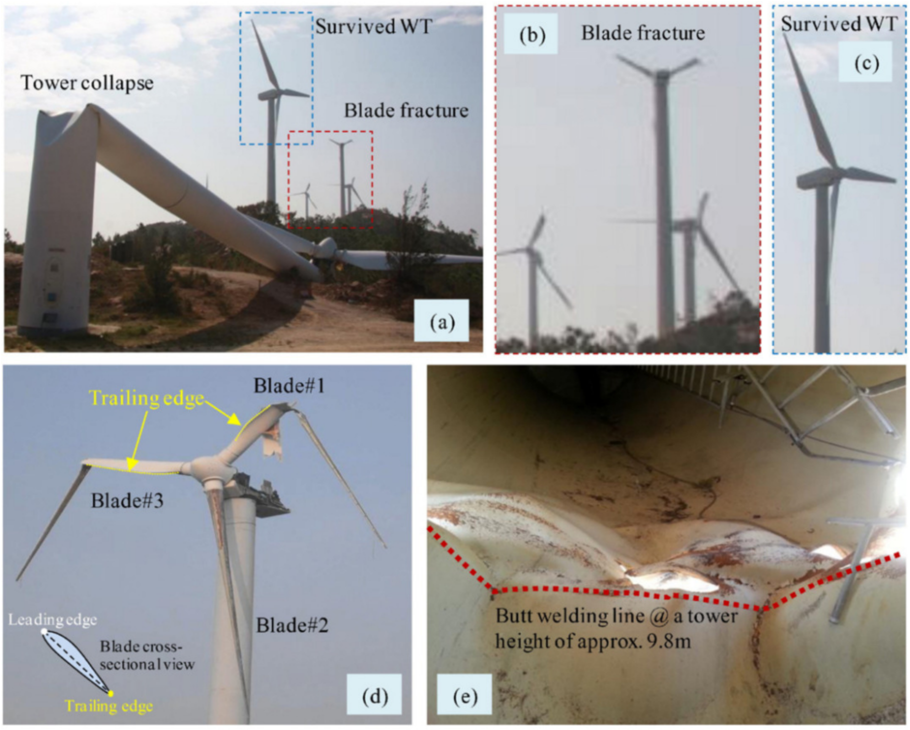
Tower collapse
Survived WT
Blade fracture
(a)
(b)
Blade fracture
Survived WT
(c)
Trailing edge
Blade#1
Blade#3
Blade#2
Leading edge
Blade cross-sectional view
Trailing edge
(d)
Butt welding line @ a tower height of approx. 9.8m
(e)

Figure 6.21 Different fracture patterns of wind turbines damaged by the super typhoon Usagi in 2013. (a) Tower collapse at the bottom. (b) Fractured blades. (c) Intact wind turbine. (d) Two fractured blades in one turbine. (e) The details at the collapsed tower location. This figure is from Ref. (Chen & Xu, 2016).

blades were fractured at the bottom of the blade where is very close to the rotating shaft. Chen & Xu (2016) have showed various fracture patterns in wind turbines in the super typhoon Usagi in 2013 (see Fig. 6.21). Many of the turbines are reported having collapsed tower and some of them have the fractured blades (see Fig. 6.21a, b and d). The locations on the collapsed towers are mainly at the bottom of the towers (see Fig. 6.21a). Some blades are broken near the shaft, while others are cracked in the middle of the blades (see Fig. 6.21b and d). Comparing to the wind turbine, the tidal turbine blades are suffering much more thrust and torsional loadings than the wind turbines because the tidal turbines are facing high-density seawater flows (Grogan *et al.*, 2013). Hence tidal turbines are more likely to be damaged than the wind turbine. Critical damage and economic loss have been caused by tidal turbine blade fractures and failures (Liu & Veitch, 2012). Therefore it is necessary to investigate flow-induced fractures in a 3D vertical axis turbine.

The settings of the test case flow-induced fractures in a 3D vertical axis turbine are

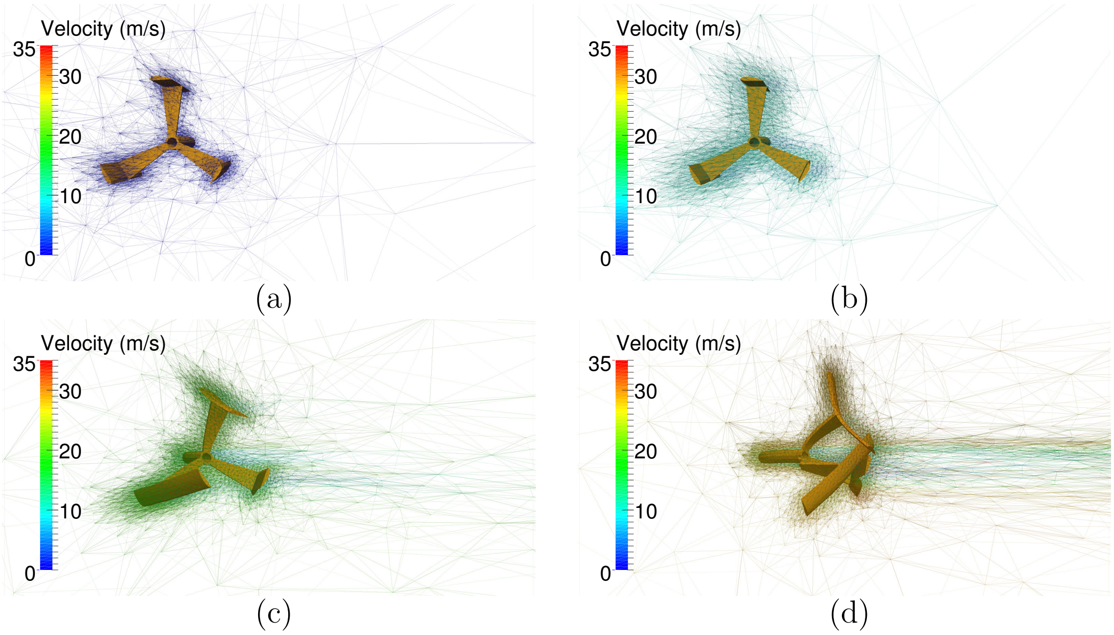

Figure 6.22 The fluid velocity and adaptive mesh of the fracturing vertical axis turbine at different times: (a) t=0.0 s, (b) t=0.1 s, (c) t=0.2 s and (d) t=0.277 s.

the same as Fig. 6.4 except for the boundary condition for the inlet velocity U_i. Unlike the constant inlet velocity in the test of flow past a 3D flexible vertical axis turbine case in Section 6.4, the inlet velocity U_i is given as an accelerating velocity as the following equation:

$$U_i = a_f t, \tag{6.12}$$

where a_f is the acceleration with the constant value of 100.0 m/s^2.

Fig. 6.22 shows the turbine structure, fluid velocity and adaptive meshes of the fracturing vertical axis turbine. The adaptive fluid meshes with minimum and maximum edge length 0.002 m and 0.2 m are used in this simulation. The anisotropic mesh edge length ratio is set as 10.0. At $t = 0.0\,\mathrm{s}\,(U_i = 0.0\,\mathrm{m/s})$ and $t = 0.1\,\mathrm{s}\,(U_i = 10.0\,\mathrm{m/s})$, the meshes are relatively coarse compared to those at $t = 0.2\,\mathrm{s}\,(U_i = 20.0\,\mathrm{m/s})$ and $t = 0.277\,\mathrm{s}\,(U_i = 27.7\,\mathrm{m/s})$, since the mesh is gradually refined to make the simulation run fast at the beginning. This gradually refining mesh setting further speeds up the simulations. Because there are no fractures in the start stage of the simulation, this part can be completed with high speed by using relatively coarse mesh. When the blade starts to fracture, the mesh is refined rapidly to capture the details of the fracture process. In total, the simulation could be complete 4-6 times

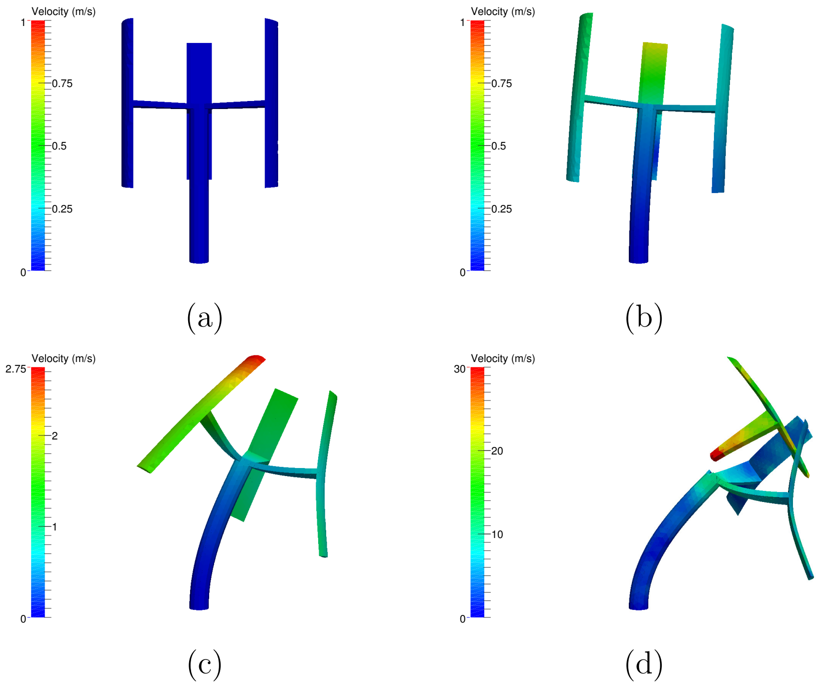

(a) (b)

(c) (d)

Figure 6.23 The solid velocity of the fracturing vertical axis turbine at different times: (a) t=0.0 s, (b) t=0.1 s, (c) t=0.2 s and (d) t=0.277 s.

faster than those are not applied this generally refining mesh setting.

The solid velocities inside the turbine are shown in Fig. 6.23. Comparing with the fluid velocity in Fig. 6.22, the solid velocities increase as the fluid velocities accelerate. Since the fluid velocity accelerates constantly, the top of turbine moves to the right-hand side and the turbine is bent accordingly. At $t = 0.1\,\mathrm{s}\,(U_i = 10.0\,\mathrm{m/s})$ and $t = 0.2\,\mathrm{s}\,(U_i = 20.0\,\mathrm{m/s})$, the maximum solid velocity of the turbine is about $1.0\,\mathrm{m}/s$ and $2.75\,\mathrm{m}/s$ which is much lower than the fluid inlet fluid velocity $U_i = 10.0\,\mathrm{m/s}$ and $U_i = 20.0\,\mathrm{m/s}$ (see Fig. 6.23a). However, at $t = 0.277\,\mathrm{s}\,(U_i = 27.7\,\mathrm{m/s})$, the maximum solid velocity found in the turbine is more than $30\,\mathrm{m}/s$ which is higher than the inlet fluid velocity $U_i = 27.7\,\mathrm{m/s}$. This is because fractures are initiated in the turbine that makes the turbine more unstable. It is worth noting that the maximum solid velocity is normally found at the tips of the blades.

Figs. 6.24 gives out the solid stress component σ_1 of the turbine. As the turbine is bent, the maximum magnitude of solid stress at each time appears at the joints between the blades and the tower. It is worth noting that at $t = 0.2\,\mathrm{s}\,(U_i = 20.0\,\mathrm{m/s})$ and $t = 0.277\,\mathrm{s}\,(U_i = 27.7\,\mathrm{m/s})$, relatively larger stress is found at the bottom of the tower as well. The stress hot spots are where the fractures appear (see Figs. 6.24d.

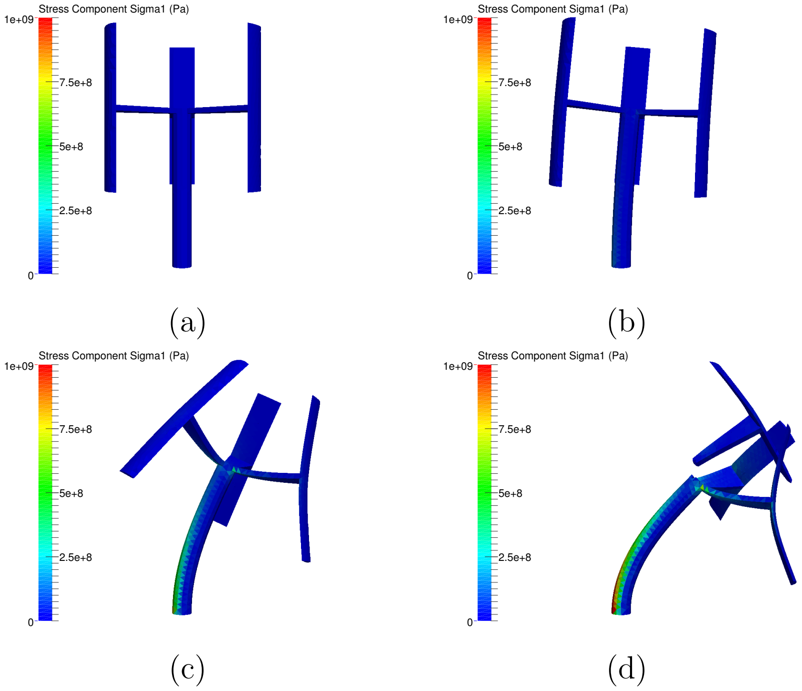

Figure 6.24 The solid stress component σ_1 of the fracturing vertical axis turbine at different times: (a) t=0.0 s, (b) t=0.1 s, (c) t=0.2 s and (d) t=0.277 s.

Although there are no fractures at the bottom of the tower, the hot spots are found at the right side of the tower bottom (see Figs. 6.24c and 6.24d). In some other circumstances, e.g. unsteady turbulent flows, these locations with stress hot spots are highly likely to fracture or collapse.

From Fig. 6.25, it can be found that fractures initiate and propagate at the joint between the blade No. 2 and the tower at $t = 0.277\,\mathrm{s}\,(U_i = 27.7\,\mathrm{m/s})$ and then the blade No. 2 flies away from the tower (see Fig. 6.25d). Importantly, this fracture in blade No. 2 is caused by tensile failure.

The displacements of three points marked on Fig. 6.17b are given in Fig. 6.26. From Fig. 6.26, it can be found that the displacements increase gradually before $t = 0.15\,\mathrm{s}\,(U_i = 15.0\,\mathrm{m/s})$. After that, the turbine becomes unstable and the displacements grow faster. This kind of the vibration mode is called as the unstable vibration. At $t = 0.277\,\mathrm{s}\,(U_i = 27.7\,\mathrm{m/s})$, the displacement of blade No. 2 sharply increases. This indicates the joint between blade No. 2 and the tower has already fractured and the blade No. 2 separates from the tower at this time.

As the stress hot spots are found near the arm bottom (see Fig. 6.24, three points near the stress hot spot areas are marked in Fig. 6.27. Fig. 6.28 draws the stress

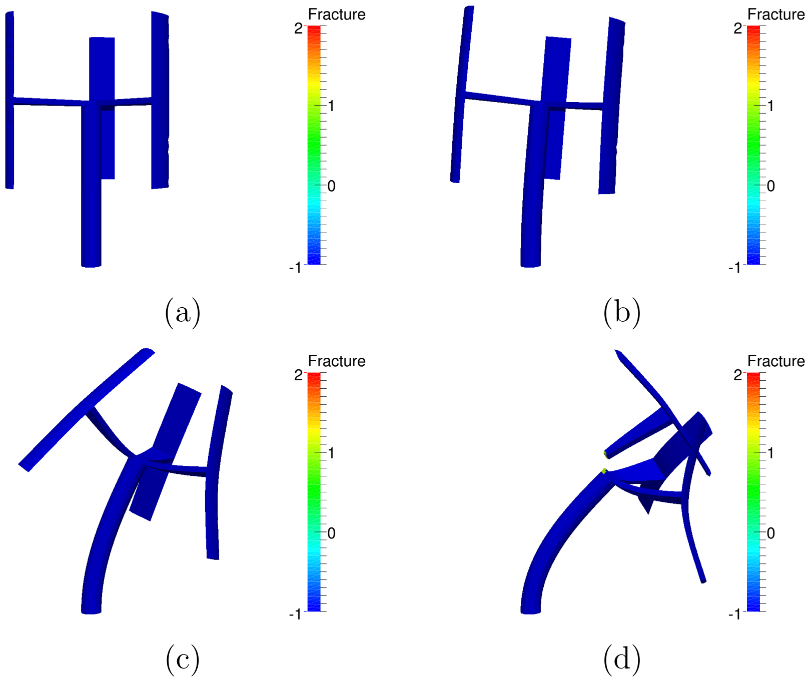

Figure 6.25 The solid cracks of the fracturing vertical axis turbine at different times. (a) t=0.0 s, (b) t=0.1 s, (c) t=0.2 s and (d) t=0.277 s. The blue parts are fractured and the yellow parts are intact. Here, the fracture bar value=-1 means preexisting boundaries or fractures, the fracture bar value=2 means shear failure, while the fracture bar value=2 means tensile failure.

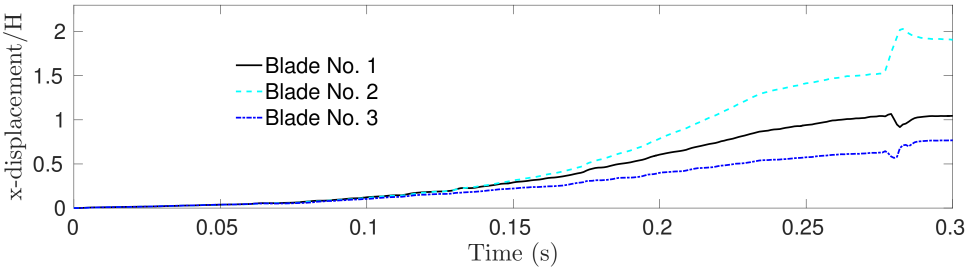

Figure 6.26 The displacements of three points marked in Fig. 6.17b.

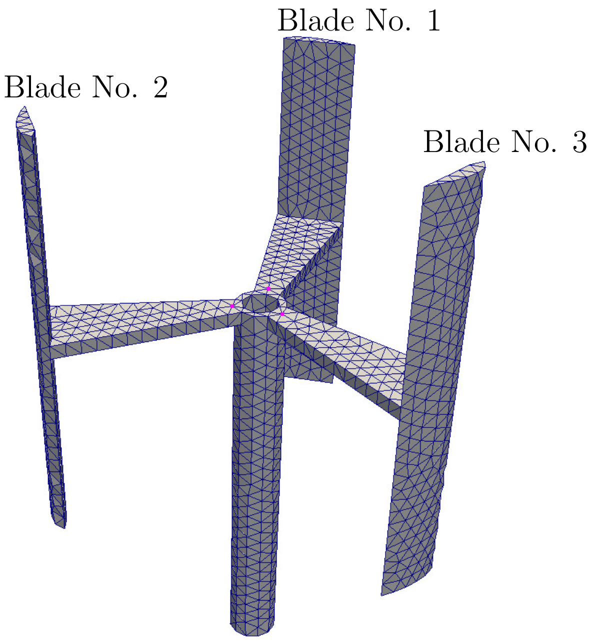

Figure 6.27 The stress measurement points on each blade.The three red points on each blade are the points where the stress is plotted out in Fig. 6.28.

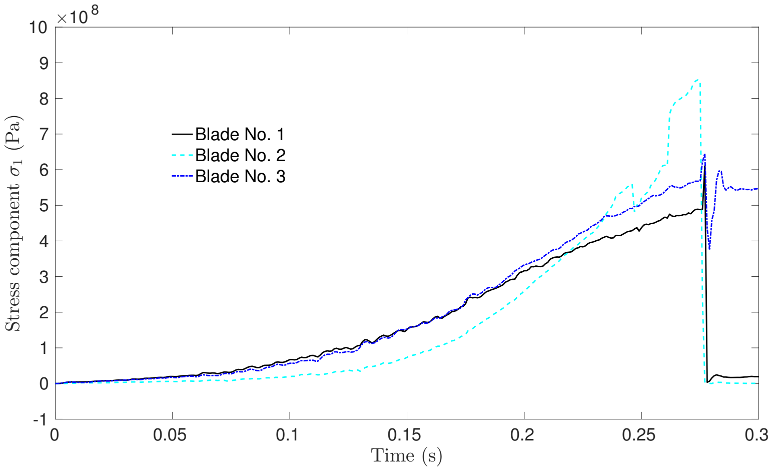

Figure 6.28 The stress component σ_1 of three points marked in Fig. 6.27. The black solid line is the stress component σ_1 on the joint between the tower and the arm which links the tower and the Blade No. 1. The green dash line is the stress component σ_1 on the joint between the tower and the arm which links the tower and the Blade No. 2. The blue dash line is the stress component σ_1 on the joint between the tower and the arm which links the tower and the Blade No. 3.

component σ_1 of the stress hot spots near the three points marked in Fig. 6.27. The black solid line is the stress component σ_1 on the joint between the tower and the arm which links the tower and the Blade No. 1. The green dash line is the stress component σ_1 on the joint between the tower and the arm which links the tower and the Blade No. 2. The blue dash line is the stress component σ_1 on the joint between the tower and the arm which links the tower and the Blade No. 3. From this figure, it can be found that the stress component σ_1 near these three points are increasing slowly before $t = 0.15\,\mathrm{s}\,(U_i = 15.0\,\mathrm{m/s})$. After this time, the stresses increase sharply. Then at $t = 0.277\,\mathrm{s}\,(U_i = 27.7\,\mathrm{m/s})$, the stress in blade No. 2 sharply increases to a very high value and then sharply drops to near zero. This means the blade No. 2 is fractured and blew away, then the bottom of the arm becomes a free tip where there is tiny stress.

6.6 Concluding remarks

In this chapter, the 3D fidelity fluid-structure interaction turbulence model developed in chapter 2 is applied to vertical axis tidal turbines. The fluid dynamics of turbulent flows, and the stress, vibration, deformation, fracture and motion in structures are computed in this model at the same time. The URANS $k-\varepsilon$ FSI model developed in this work is used here to capture the structural response of a rotating vertical axis turbine in turbulent flows. Large aspect ratio anisotropic mesh adaptivity is used here to make the simulations run fast in 3D. Two benchmark cases flow past a 2D and 3D rotating vertical axis tidal turbines are carried out to validate the URANS FSI model for complex industrial applications. The simulation results from all the benchmark test cases are in good agreement with experimental and numerical data in the literature. This indicates the developed URANS FSI model is capable for industrial applications. The flow past a 3D flexible vertical axis turbine is simulated to model the flow-induced vibration in complex structures. This demonstrates that the model is capable of analysing the elasticities for complex 3D problems. Most importantly, the flow-induced fractures in a 3D vertical axis turbine with the tower are presented to predict the worst scenarios: the blades are fractured by typhoon or tsunami. Thus this 3D fidelity fluid-structure interaction turbulence model is a fully two-way solid-fluid coupling model, which is suitable to simulate complex moving, deforming, vibrating and fracturing structures in turbulent flows for industrial applications.

Chapter

SEVEN

Discussion and Conclusion & Future Work

7.1 Discussion and Conclusion

In this thesis, I have developed a high fidelity fluid-structure model for incompressible, compressible and turbulent flows based on an immersed-body method. I have coupled a finite element multiphase fluid model with a combined finite-discrete element solid model. Three separate meshes are used in this model: fluid, solid and a novel thin shell mesh surrounding solid surfaces. The thin shell mesh acts as a numerical delta function in order to help apply the solid-fluid boundary conditions.

First of all, an unsteady Reynolds-averaged Navier-Stokes (URANS) $k-\varepsilon$ turbulence model is coupled with an immersed-body method to model fluid-structure interaction (FSI) via a thin shell mesh. The interface boundary conditions for both the turbulence model and the fluid momentum equation are applied to the thin shell mesh. Secondly, in order to reduce the computational cost, a log-law wall function is used within the thin shell to resolve the flow near the solid surface. At the same time, the solid-fluid coupling terms are treated implicitly to enable larger time steps to be used. Thirdly, in order to improve the accuracy of the wall function, a novel shell mesh external-surface intersection approach is introduced to identify sharp solid-fluid interfaces. Fourthly, unstructured anisotropic mesh adaptivity is used to refine the mesh according to the interface and the velocity solutions. Last but not least, the model has been extended to model highly compressible gas coupled with fracturing solids. The John-Wilkins-Lee equation of state is introduced to resolve the relationship between pressure and density of the highly compressible gas in blasts and explosions. A Q-scheme is used to stabilise the model when solving extremely high-pressure situations. A cohesive zone fracture model is used in the solid model to simulate fracture propagation.

The present FSI model for incompressible flow has been validated using a free falling circular cylinder and a free falling sphere in a fluid at rest with Reynolds number up to about 1800. The benchmark case, a collapsing column of water moving an initially stationary solid square, has been used to help validate this immersed-body method. The simulation results are in good agreement with the experimental data. Importantly, the mesh sensitivity analysis in this work indicates that the simulation results are converged when then fluid and shell mesh sizes are decreased. As described in Chapter 3, this immersed-body method can be applied to multiphase viscous flows, for example, the water-air flows and FSI of ships, floating wind-turbine platforms, and oil platforms. The immersed-body method is a promising approach for modelling multiphase viscous flows coupled with dynamic solids, especially for phenomena with multiple-interfaces e.g solid-water, solid-air, water-air, which is useful for ocean dynamics.

Moreover, I have extended the FSI model in this work to a gas-solid interaction model for simulating blast-induced fractures. This coupling model combines an immersed-body method and a cohesive zone fracture model. The whole complex blasting process including both fragmentation and burden movement phases is simulated in this complete coupling model. A new mesh conversion algorithm to convert discontinuous meshes to continuous meshes has been implemented and demonstrated in section 4.4.2. The detonation gas in the model is resolved by the JWL-EOS as a highly compressible fluid, which is close to the realistic behaviour of the detonation gas in common mining explosions. Importantly, it is easy to extend the equation of state in this model to more practical equation of states. Additionally, this model in combination with the Q-scheme is stable when dealing with extremely high pressure and velocity situations. Two benchmark cases, the blasting cylinder and projectile fire, are used to validate this gas-solid interaction model. The numerical simulation results of these two test cases are in good agreement with the available experimental data. A practical complicated blasting engineering simulation with shock waves, fracture propagation, gas-solid interaction and flying fragments is used to demonstrate the ability of the gas-solid interaction model.

Importantly, detailed validation of the FSI model for turbulent flows is presented. The immersed-body URANS turbulence model is validated by several test cases, and the results show good agreements with both experimental data and previous numerical results in the literature. The first two test cases are the flow over a circular cylinder at $Re = 3900$ and turbulent flow past a static NACA0015 aerofoil with an attack angle of $\alpha = 60°$ at $Re = 5200$. The comparison between the experimental and numerical results shows that the model has the accuracy and reliability to resolve turbulent flows coupled with fixed solids. The third and fourth test cases are a free rising circular cylinder in a fluid at rest with $Re = 5000$ and $Re = 3800$ and a free rising sphere in a fluid at rest with $Re = 6000$ and 10000. These two benchmark test cases indicate that the immersed-body URANS model has the ability to simulate moving bodies coupled with turbulent flows. The structural elastic response in the flow is also validated by the flow bending a 3D plate test case. All the simulation results obtained from the present FSI model are in good agreement with the experimental data and previous numerical results in the literature.

Finally, I have applied the developed FSI model to tidal turbines for the analysis of fluid dynamics and structure elastic and fracturing response. The hydrodynamics in fluids, and the stress, vibration, deformation, fracture and motion in structures are computed in this model at the same time. The developed URANS $k - \varepsilon$ FSI model is used here to capture the structural response of a full-scale rotating vertical axis turbine in turbulent flows. Large aspect ratio anisotropic mesh adaptivity is used here to make the simulations run fast in 3D. The test cases - flow across a 2D & 3D operating vertical axis tidal turbine are presented. The simulation results from all these test cases are in good agreement with experimental and numerical data in the literature. The vortex-induced vibration of a full-scale 3D vertical axis turbine with the tower is presented in this work. This demonstrates the model ability in analysing the elasticities for complex 3D problems. Most importantly, the flow-induced fractures in a 3D vertical axis turbine with the tower are simulated to predict the worst scenarios: the vertical axis turbine being fractured by typhoon or tsunami.

7.2 Future Work

The new developed FSI model has been validated by many test cases. Its applications have included moving structures in multiphase flows, fracturing solid coupled with the compressible flow in blasting, and the operating tidal turbine in turbulent flows. However, there are some further developments and possible applications.

7.2.1 Further validation

The highest Reynolds number simulated by the FSI model in this work is $Re = 147200$, which is not high enough. The range of scales by Reynolds number can be as large as $10^6 - 10^8$ in many industrial applications, for example, a flow over airfoil at high Reynolds number (Johnson *et al.*, 2014). More advanced turbulent models, for instance, LES and VLES (Bull, 2013) can be implemented to simulate the turbulent flows. When dealing with different turbulent models, it must ensure that the wall distance from the fluid mesh nodes to the moving structure surfaces is calculated accurately and efficiently. These distances should be updated frequently especially for loosely coupling methods. With the increasing of Reynolds number, the computational cost would increase. In the future, further validation with much high Reynolds number will be undertaken.

7.2.2 Numerical model improvement

In this FSI model, while the fluid solver “Fluidity-Multiphase” is parallelised with Message Passing Interface (MPI) and the solid solver “FEMDEM” is parallelised with Open Multi-Processing (OpenMP). However, the coupling process is not parallelised. In order to parallelise the whole coupling system, a new parallel structure needs to be developed by considering the characters of the coupling process. First of all, the solid solver “Fluidity-Multiphase” should be parallelised with MPI as it is only parallelised with OpenMP. Secondly, a good dynamic domain decomposition strategy with dynamic loading balance should be taken into consideration because “FEMDEM” combines Lagrangian DEM and Eulerian FEM methods and in some applications, the CPU load can be highly unbalanced. To obtain good scalability, hybrid MPI/OpenMP should be considered to be implemented. In the future, parallelisation of the coupling code would be important.

7.2.3 Moving mesh

Moving mesh method (Bazilevs *et al.*, 2015) would a good choice for the present FSI model when dealing with fast-moving solids in turbulent flows. In the present model, the adaptive mesh is used to capture sharp fluid-structure interfaces for moving solids in fluids. However, the adaptive mesh could limit the fluid time step when the solids are moving with high velocities in fluids. This results in costing more CPU time. To make the FSI model run fast, the moving mesh method (Bazilevs *et al.*, 2015) would be taken into consideration. By using a very fine moving mesh surrounding structure surfaces, large CFL numbers can be used. In the present FSI model, the one layer thin shell mesh can be extended to certain layers and play the role of the moving mesh. When the multi-layer shell mesh is defined as the moving fluid mesh, the fluid governing equations should be solved on the multi-layer shell mesh and the results obtained on the multi-layer shell mesh should be projected on the fluid mesh at every fluid time step.

7.2.4 Possible applications

One of the potential applications of the developed FSI model is landslides into a lake (Yin *et al.*, 2015). In this kind of applications, the water wave height and propagation, rockslides and fracturing can be simulated by using this FSI model. This model can be used to predict the landslide disaster and give out some suggestions about prevention. In order to simulate the real-world landslides into a lake, the field investigation data should be used here to build the initial geometry. If necessary, in some stages of the simulation, the data assimilation technique may be used to make the FSI model more accurate and reliable.

Another possible extension of the FSI model is in cardiac mechanics (Borazjani, 2013). Since the 3D elastic body coupled with the turbulent model has been modelled by using the FSI model, it would be possible to model blood flows through elastic heart valves via this model. However, the blood is a non-Newton fluid that can not be directly modelled by the present fluid model in this thesis. Some modifications should be made in the fluid model to make it adapt to non-Newton fluid, for instance, some empirical phase change equations can be used to model the rheology of the blood.

Bibliography

Ai, HA, & Ahrens, TJ. 2006. Simulation of dynamic response of granite: a numerical approach of shock-induced damage beneath impact craters. *International Journal of Impact Engineering*, **33**(1), 1–10.

Alotto, Piergiorgio, Freschi, Fabio, Repetto, Maurizio, & Rosso, Carlo. 2013. *The Cell Method for Electrical Engineering and Multiphysics Problems: An Introduction.* Vol. 230. Springer Science & Business Media.

ANSYS, AQWA. 2013. Version 15.0; ANSYS. *Inc.: Canonsburg, PA, USA November.*

Apte, Sourabh V, Martin, Mathieu, & Patankar, Neelesh A. 2009. A numerical method for fully resolved simulation (FRS) of rigid particle–flow interactions in complex flows. *Journal of Computational Physics*, **228**(8), 2712–2738.

Banadaki, MM Dehghan, & Mohanty, B. 2012. Numerical simulation of stress wave induced fractures in rock. *International Journal of Impact Engineering*, **40**, 16–25.

Bauchau, Olivier A, & Craig, James I. 2009. *Structural analysis: with applications to aerospace structures.* Vol. 163. Springer Science & Business Media.

Bazilevs, Y, Hsu, M-C, Akkerman, I, Wright, S, Takizawa, K, Henicke, B, Spielman, T, & Tezduyar, TE. 2011a. 3D simulation of wind turbine rotors at full scale. Part I: Geometry modeling and aerodynamics. *International Journal for Numerical Methods in Fluids*, **65**(1-3), 207–235.

Bazilevs, Y, Hsu, M-C, Kiendl, J, Wüchner, R, & Bletzinger, K-U. 2011b. 3D simulation of wind turbine rotors at full scale. Part II: Fluid–structure interaction modeling with composite blades. *International Journal for Numerical Methods in Fluids*, **65**(1-3), 236–253.

Bazilevs, Y, Korobenko, A, Deng, X, & Yan, J. 2015. Novel structural modeling and mesh moving techniques for advanced fluid–structure interaction simulation of wind turbines. *International Journal for Numerical Methods in Engineering*, **102**(3-4), 766–783.

Beaudan, Patrick, & Moin, Parviz. 1994. *Numerical experiments on the flow past a circular cylinder at sub-critical Reynolds number.* Tech. rept. DTIC Document.

Berg, J, & Resor, B. 2012. Numerical manufacturing and design tool (NuMAD V2. 0) for wind turbine blades: Users guide. *Sandia National Laboratories, Albuquerque, NM, Technical Report No. SAND2012-728.*

Borazjani, Iman. 2013. Fluid–structure interaction, immersed boundary-finite element method simulations of bio-prosthetic heart valves. *Computer Methods in Applied Mechanics and Engineering*, **257**, 103–116.

Borg, Michael, Shires, Andrew, & Collu, Maurizio. 2014. Offshore floating vertical axis wind turbines, dynamics modelling state of the art. Part I: aerodynamics. *Renewable and Sustainable Energy Reviews*, **39**, 1214–1225.

Braithwaite, M, Brown, WB, & Minchinton, A. 1996. The use of ideal detonation computer codes in blast modelling. *Proc. 5th Int. Sym. Rock Fragmentation by Blasting (FRAGBLAST 5), Montreal, Quebec, Canada. Rotterdam, Balkema*, **3744**.

Breuer, Michael. 1998. Large eddy simulation of the subcritical flow past a circular cylinder: numerical and modeling aspects. *International Journal for Numerical Methods in Fluids*, **28**(9), 1281–1302.

Brown, Phillip P, & Lawler, Desmond F. 2003. Sphere drag and settling velocity revisited. *Journal of environmental engineering*, **129**(3), 222–231.

Buchan, AG, Farrell, PE, Gorman, GJ, Goddard, AJH, Eaton, MD, Nygaard, ET, Angelo, PL, Smedley-Stevenson, RP, Merton, SR, & Smith, PN. 2014. The immersed body supermeshing method for modelling reactor physics problems with complex internal structures. *Annals of Nuclear Energy*, **63**, 399–408.

Bull, Jonathan R. 2013. *Turbulence models with adaptive meshing for industrial CFD.* Ph.D. thesis, Imperial College London.

Bungartz, Hans-Joachim, & Schäfer, Michael. 2006. *Fluid-structure interaction: modelling, simulation, optimisation.* Vol. 53. Springer Science & Business Media.

Capizzano, Francesco. 2011. Turbulent wall model for immersed boundary methods. *AIAA journal*, **49**(11), 2367–2381.

Cardell, Gregory Scott. 1993. *Flow past a circular cylinder with a permeable wake splitter plate.* Ph.D. thesis, California Institute of Technology.

Cardona, José L. 1984. Flow curvature and dynamic stall simulated with an aerodynamic free-vortex model for VAWT. *Wind Engineering*, 135–143.

Castro, Manuel, Macías, Jorge, & Parés, Carlos. 2001. A Q-scheme for a class of systems of coupled conservation laws with source term. Application to a two-layer 1-D shadow water system. *ESAIM: Mathematical Modelling and Numerical Analysis-Modélisation Mathématique et Analyse Numérique*, **35**(1), 107–127.

Cate, Andreas Ten, Derksen, Jos J, Portela, Luis M, & Van Den Akker, Harry EA. 2004. Fully resolved simulations of colliding monodisperse spheres in forced isotropic turbulence. *Journal of Fluid Mechanics*, **519**, 233–271.

Chapman, David Leonard. 1899. VI. On the rate of explosion in gases. *The London, Edinburgh, and Dublin Philosophical Magazine and Journal of Science*, **47**(284), 90–104.

Chen, Long, Sun, Pengtao, & Xu, Jinchao. 2007. Optimal anisotropic meshes for minimizing interpolation errors in L^p-norm. *Mathematics of Computation*, **76**(257), 179–204.

Chen, Xiao, & Xu, Jian Zhong. 2016. Structural failure analysis of wind turbines impacted by super typhoon Usagi. *Engineering Failure Analysis*, **60**, 391–404.

Cho, Yong, Boluriaan, Said, & Morris, Philip. 2006. Immersed boundary method for viscous flow around moving bodies. *Page 1089 of: 44th AIAA Aerospace Sciences Meeting and Exhibit.*

Cho, Yong, Chopra, Jogesh, & Morris, Philip. 2007. Immersed boundary method for compressible high-Reynolds number viscous flow around moving bodies. *Page 125 of: 45th AIAA Aerospace Sciences Meeting and Exhibit.*

Chou, Jui-Sheng, & Tu, Wan-Ting. 2011. Failure analysis and risk management of a collapsed large wind turbine tower. *Engineering Failure Analysis*, **18**(1), 295–313.

Clift, Roland, Grace, John R, & Weber, Martin E. 2005. *Bubbles, drops, and particles*. Courier Corporation.

Coquerelle, Mathieu, & Cottet, G-H. 2008. A vortex level set method for the two-way coupling of an incompressible fluid with colliding rigid bodies. *Journal of Computational Physics*, **227**(21), 9121–9137.

Cotter, Colin J, Ham, David A, & Pain, Christopher C. 2009. A mixed discontinuous/continuous finite element pair for shallow-water ocean modelling. *Ocean Modelling*, **26**(1), 86–90.

Cristallo, Antonio, & Verzicco, Roberto. 2006. Combined immersed boundary/large-eddy-simulations of incompressible three dimensional complex flows. *Flow, Turbulence and Combustion*, **77**(1), 3–26.

Danao, Louis Angelo, Edwards, Jonathan, Eboibi, Okeoghene, & Howell, Robert. 2014. A numerical investigation into the influence of unsteady wind on the performance and aerodynamics of a vertical axis wind turbine. *Applied Energy*, **116**, 111–124.

De Palma, Pietro, De Tullio, MD, Pascazio, Giuseppe, & Napolitano, Michele. 2006. An immersed-boundary method for compressible viscous flows. *Computers & Fluids*, **35**(7), 693–702.

De Tullio, Marco D, De Palma, Pietro, Iaccarino, Gianluca, Pascazio, Giuseppe, & Napolitano, Michele. 2007. An immersed boundary method for compressible flows using local grid refinement. *Journal of Computational Physics*, **225**(2), 2098–2117.

Dröge, Marc Theodoor. 2007. *Cartesian grid methods for turbulent flow simulation in complex geometries*. Ph.D. thesis, University of Groningen.

Dunne, Thomas, & Rannacher, Rolf. 2006. Adaptive finite element approximation of fluid-structure interaction based on an Eulerian variational formulation. *Fluid-structure interaction*, 110–145.

Engels, Thomas, Kolomenskiy, Dmitry, Schneider, Kai, & Sesterhenn, Jörn. 2015. Numerical simulation of fluid–structure interaction with the volume penalization method. *Journal of Computational Physics*, **281**, 96–115.

Farhat, Charbel, Lesoinne, Michael, & Le Tallec, P. 1998. Load and motion transfer algorithms for fluid/structure interaction problems with non-matching discrete interfaces: Momentum and energy conservation, optimal discretization and application to aeroelasticity. *Computer Methods in Applied Mechanics and Engineering*, **157**(1), 95–114.

Farnam, Yaghoob, Mohammadi, Soheil, & Shekarchi, Mohammad. 2010. Experimental and numerical investigations of low velocity impact behavior of high-performance fiber-reinforced cement based composite. *International Journal of Impact Engineering*, **37**(2), 220–229.

Farrell, P. E., & Maddison, J. R. 2011. Conservative interpolation between volume meshes by local Galerkin projection. *Computer Methods in Applied Mechanics and Engineering*, **200**(1-4), 89–100.

Farrell, Patrick E. 2011. The addition of fields on different meshes. *Journal of Computational Physics*, **230**(9), 3265–3269.

Farrell, PE, Piggott, MD, Pain, CC, Gorman, GJ, & Wilson, CR. 2009. Conservative interpolation between unstructured meshes via supermesh construction. *Computer Methods in Applied Mechanics and Engineering*, **198**(33-36), 2632–2642.

Feng, James, Hu, Howard H, & Joseph, Daniel D. 1994. Direct simulation of initial value problems for the motion of solid bodies in a Newtonian fluid Part 1. Sedimentation. *Journal of Fluid Mechanics*, **261**, 95–134.

Feng, Zhi-Gang, & Michaelides, Efstathios E. 2005. Proteus: a direct forcing method in the simulations of particulate flows. *Journal of Computational Physics*, **202**(1), 20–51.

Ferziger, Joel H, & Peric, Milovan. 2012. *Computational methods for fluid dynamics*. Springer Science & Business Media.

Field, JE, & Ladegaard-Pedersen, A. 1971. The importance of the reflected stress wave in rock blasting. *Pages 213–226 of: International Journal of Rock Mechanics and Mining Sciences & Geomechanics Abstracts*, vol. 8. Elsevier.

Firth, IR, & Taylor, DL. 2001. Bench blast modeling using numerical simulation and mine planning software. *In: SME Annual Meeting, Denver, Colorado*. Citeseer.

Franke, J, & Frank, W. 2002. Large eddy simulation of the flow past a circular cylinder at Re_D= 3900. *Journal of Wind Engineering and Industrial Aerodynamics*, **90**(10), 1191–1206.

Freymuth, P, Bank, W, & Palmer, M. 1985. Reynolds number dependence of vortex patterns in accelerated flow around airfoils. *Experiments in fluids*, **3**(2), 109–112.

Freymuth, Peter. 1985. The vortex patterns of dynamic separation: a parametric and comparative study. *Progress in Aerospace Sciences*, **22**(3), 161–208.

Fröhlich, J, Rodi, W, Kessler, Ph, Parpais, S, Bertoglio, JP, & Laurence, D. 1998. Large eddy simulation of flow around circular cylinders on structured and unstructured grids. *Pages 319–338 of: Numerical Flow Simulation I*. Springer.

Gabitto, Jorge, & Tsouris, Costas. 2008. Drag coefficient and settling velocity for particles of cylindrical shape. *Powder Technology*, **183**(2), 314–322.

García, Xavier, Pavlidis, Dimitrios, Gorman, Gerard J, Gomes, Jefferson LMA, Piggott, Matthew D, Aristodemou, Elsa, Mindel, Julian, Latham, John-Paul, Pain, Christopher C, & ApSimon, Helen. 2011. A two-phase adaptive finite element method for solid–fluid coupling in complex geometries. *International Journal for Numerical Methods in Fluids*, **66**(1), 82–96.

Ghias, Reza, Mittal, Rajat, & Dong, Haibo. 2007. A sharp interface immersed boundary method for compressible viscous flows. *Journal of Computational Physics*, **225**(1), 528–553.

Ghosh, Santanu, Choi, Jung-Il, & Edwards, Jack. 2008. RANS and hybrid LES/RANS Simulation of the Effects of Micro Vortex Generators using Immersed Boundary Methods. *Page 3728 of: 38th Fluid Dynamics Conference and Exhibit*.

Ghosh, Santanu, Choi, Jung-Il, & Edwards, Jack R. 2010. Numerical simulations of effects of micro vortex generators using immersed-boundary methods. *AIAA journal*, **48**(1), 92–103.

Gibou, Frédéric, & Min, Chohong. 2012. Efficient symmetric positive definite second-order accurate monolithic solver for fluid/solid interactions. *Journal of Computational Physics*, **231**(8), 3246–3263.

Glowinski, R, Pan, TW, Hesla, TI, Joseph, DD, & Periaux, J. 2001. A fictitious domain approach to the direct numerical simulation of incompressible viscous flow past moving rigid bodies: application to particulate flow. *Journal of Computational Physics*, **169**(2), 363–426.

Glowinski, Roland, Pan, Tsorng-Whay, & Periaux, Jacques. 1994. A fictitious domain method for external incompressible viscous flow modeled by Navier-Stokes equations. *Computer Methods in Applied Mechanics and Engineering*, **112**(1), 133–148.

Glowinski, Roland, Pan, T-W, Hesla, Todd I, & Joseph, Daniel D. 1999. A distributed Lagrange multiplier/fictitious domain method for particulate flows. *International Journal of Multiphase Flow*, **25**(5), 755–794.

Gnanaskandan, Aswin, & Mahesh, Krishnan. 2016. Numerical investigation of near-wake characteristics of cavitating flow over a circular cylinder. *Journal of Fluid Mechanics*, **790**, 453–491.

Gresho, Philip M, & Sani, Robert L. 1998. Incompressible flow and the finite element method. Volume 1: Advection-diffusion and isothermal laminar flow.

Griffith, Boyce E, Hornung, Richard D, McQueen, David M, & Peskin, Charles S. 2007. An adaptive, formally second order accurate version of the immersed boundary method. *Journal of Computational Physics*, **223**(1), 10–49.

Grogan, David M, Leen, Sean B, Kennedy, CR, & Brádaigh, CM Ó. 2013. Design of composite tidal turbine blades. *Renewable energy*, **57**, 151–162.

Guerri, Ouahiba, Hamdouni, Aziz, & Sakout, Anas. 2008. Fluid structure interaction of wind turbine airfoils. *Wind Engineering*, **32**(6), 539–557.

Gui, Yi-Lin, Bui, Ha H, Kodikara, Jayantha, Zhang, Qian-Bing, Zhao, Jian, & Rabczuk, Timon. 2016. Modelling the dynamic failure of brittle rocks using a hybrid continuum-discrete element method with a mixed-mode cohesive fracture model. *International Journal of Impact Engineering*, **87**, 146–155.

Guo, Liwei, Latham, John-Paul, & Xiang, Jiansheng. 2015. Numerical simulation of breakages of concrete armour units using a three-dimensional fracture model in the context of the combined finite-discrete element method. *Computers & Structures*, **146**, 117–142.

Guttman, Antonin. 1984. *R-trees: A dynamic index structure for spatial searching*. Vol. 14. ACM.

Hao, H, Wu, C, & Seah, CC. 2002a. Numerical analysis of blast-induced stress waves in a rock mass with anisotropic continuum damage models Part 2: Stochastic approach. *Rock Mechanics and Rock Engineering*, **35**(2), 95–108.

Hao, Ho, Wu, Chengqing, & Zhou, Yinxing. 2002b. Numerical analysis of blast-induced stress waves in a rock mass with anisotropic continuum damage models Part 1: equivalent material property approach. *Rock Mechanics and Rock Engineering*, **35**(2), 79–94.

Hesch, C, Gil, AJ, Carreno, A Arranz, & Bonet, J. 2012. On continuum immersed strategies for Fluid–Structure Interaction. *Computer Methods in Applied Mechanics and Engineering*, **247**, 51–64.

Hirsch, Ir H, & Mandal, AC. 1987. A cascade theory for the aerodynamic performance of Darrieus wind turbines. *Wind Engineering*, 164–175.

Hodges, Dewey H. 2003. Geometrically exact, intrinsic theory for dynamics of curved and twisted anisotropic beams. *AIAA journal*, **41**(6), 1131–1137.

Horowitz, M, & Williamson, CHK. 2006. Dynamics of a rising and falling cylinder. *Journal of Fluids and Structures*, **22**(6), 837–843.

Horowitz, M, & Williamson, CHK. 2010. The effect of Reynolds number on the dynamics and wakes of freely rising and falling spheres. *Journal of Fluid Mechanics*, **651**, 251–294.

Hsu, Ming-Chen, & Bazilevs, Yuri. 2012. Fluid–structure interaction modeling of wind turbines: simulating the full machine. *Computational Mechanics*, **50**(6), 821–833.

Hübner, Björn, Walhorn, Elmar, & Dinkler, Dieter. 2004. A monolithic approach to fluid–structure interaction using space–time finite elements. *Computer Methods in Applied Mechanics and Engineering*, **193**(23), 2087–2104.

Hunt, Julian CR, Wray, Alan A, & Moin, Parviz. 1988. Eddies, streams, and convergence zones in turbulent flows.

Idelsohn, SR, Onate, E, & Del Pin, F. 2003. A Lagrangian meshless finite element method applied to fluid–structure interaction problems. *Computers & Structures*, **81**(8), 655–671.

Ikeno, Tsutomu, & Kajishima, Takeo. 2007. Finite-difference immersed boundary method consistent with wall conditions for incompressible turbulent flow simulations. *Journal of Computational Physics*, **226**(2), 1485–1508.

Islam, Mazharul, Ting, David S-K, & Fartaj, Amir. 2008. Aerodynamic models for Darrieus-type straight-bladed vertical axis wind turbines. *Renewable and Sustainable Energy Reviews*, **12**(4), 1087–1109.

Itoh, S, Hamashima, H, Murata, K, & Kato, Y. 2002. Determination of JWL parameters from underwater explosion test. *Page 0 of: 12th International Detonation Symposium*, vol. 281. Citeseer.

Jaiman, Rajeev K, Jiao, Xiangmin, Geubelle, Philippe H, & Loth, Eric. 2006. Conservative load transfer along curved fluid–solid interface with non-matching meshes. *Journal of Computational Physics*, **218**(1), 372–397.

Jayaweera, KOLF, & Mason, BJ. 1965. The behaviour of freely falling cylinders and cones in a viscous fluid. *Journal of Fluid Mechanics*, **22**(04), 709–720.

Jewer, S, Buchan, AG, Pain, CC, & Cacuci, DG. 2014. An immersed body method for coupled neutron transport and thermal hydraulic simulations of PWR assemblies. *Annals of Nuclear Energy*, **68**, 124–135.

Ji, C, Munjiza, A, & Williams, JJR. 2012. A novel iterative direct-forcing immersed boundary method and its finite volume applications. *Journal of Computational Physics*, **231**(4), 1797–1821.

Jindal, Shailesh, Khalighi, Bahram, & Iaccarino, Gianluca. 2005. Numerical investigation of road vehicle aerodynamics using immersed boundary RANS approach. *Page 0546 of: SAE World Congress, Detroit, MI, SAE Paper.*

Johanson, CH, & Persson, PA. 1970. Detonics of High Explosives. *Academic Press, London, UK.*

Johnson, James P, Iaccarino, Gianluca, Chen, Kuo-Huey, & Khalighi, Bahram. 2014. Simulations of high Reynolds number air flow over the NACA-0012 airfoil using the immersed boundary method. *Journal of Fluids Engineering*, **136**(4), 040901.

Jouguet, E. 1905. Sur la propagation des réactions chimiques dans les gaz. *Journal des Mathématiques Pures et Appliquées, série*, **6**, 347–425.

Kajishima, Takeo, Takiguchi, Satoshi, Hamasaki, Hiroyuki, & Miyake, Yutaka. 2001. Turbulence structure of particle-laden flow in a vertical plane channel due to vortex shedding. *JSME International Journal Series B Fluids and Thermal Engineering*, **44**(4), 526–535.

Kang, Seokkoo, Borazjani, Iman, Colby, Jonathan A, & Sotiropoulos, Fotis. 2012. Numerical simulation of 3D flow past a real-life marine hydrokinetic turbine. *Advances in Water Resources*, **39**, 33–43.

Kang, Seongwon, Iaccarino, Gianluca, & Moin, Parviz. 2009. Accurate immersed-boundary reconstructions for viscous flow simulations. *AIAA journal*, **47**(7), 1750–1760.

Kawasaki, Koji, & Mizutani, Norimi. 2007. Numerical simulation of bore-induced dynamic behavior of rigid body using 2-D multiphase flow numerical model. *Pages 1477–1488 of: Proceedings of International Conference on Coastal Structures*. World Scientific.

Kempe, Tobias, & Fröhlich, Jochen. 2012. An improved immersed boundary method with direct forcing for the simulation of particle laden flows. *Journal of Computational Physics*, **231**(9), 3663–3684.

Kravchenko, Arthur G, & Moin, Parviz. 2000. Numerical studies of flow over a circular cylinder at Re_D= 3900. *Physics of Fluids*, **12**(2), 403–417.

Krawczyk, Piotr, Beyene, Asfaw, & MacPhee, David. 2013. Fluid structure interaction of a morphed wind turbine blade. *International Journal of Energy Research*, **37**(14), 1784–1793.

Larcher, Martin. 2009. Development of discrete cracks in concrete loaded by shock waves. *International Journal of Impact Engineering*, **36**(5), 700–710.

Latham, John-Paul, Mindel, Julian, Xiang, Jiansheng, Guises, Romain, Garcia, Xavier, Pain, Chris, Gorman, Gerard, Piggott, Matthew, & Munjiza, Antonio. 2009. Coupled FEMDEM/Fluids for coastal engineers with special reference to armour stability and breakage. *Geomechanics and Geoengineering: An International Journal*, **4**(1), 39–53.

Latham, John-Paul, Xiang, Jiansheng, Belayneh, Mandefro, Nick, Hamidreza M, Tsang, Chin-Fu, & Blunt, Martin J. 2013a. Modelling stress-dependent permeability in fractured rock including effects of propagating and bending fractures. *International Journal of Rock Mechanics and Mining Sciences*, **57**, 100–112.

Latham, John-Paul, Anastasaki, Eleni, & Xiang, Jiansheng. 2013b. New modelling and analysis methods for concrete armour unit systems using FEMDEM. *Coastal Engineering*, **77**, 151–166.

Launder, Brian Edward, & Spalding, DB. 1974. The numerical computation of turbulent flows. *Computer Methods in Applied Mechanics and Engineering*, **3**(2), 269–289.

Le, DV, Khoo, BC, & Lim, KM. 2008. An implicit-forcing immersed boundary method for simulating viscous flows in irregular domains. *Computer Methods in Applied Mechanics and Engineering*, **197**(25), 2119–2130.

Lee, Long, & LeVeque, Randall J. 2003. An Immersed Interface Method for Incompressible Navier–Stokes Equations. *SIAM Journal on Scientific Computing*, **25**(3), 832–856.

Lee, Ya-Jung, Jhan, Yu-Ti, & Chung, Cheng-Hsien. 2012. Fluid–structure interaction of FRP wind turbine blades under aerodynamic effect. *Composites Part B: Engineering*, **43**(5), 2180–2191.

Lei, Qinghua, Latham, John-Paul, Xiang, Jiansheng, Tsang, Chin-Fu, Lang, Philipp, & Guo, Liwei. 2014. Effects of geomechanical changes on the validity of a discrete fracture network representation of a realistic two-dimensional fractured rock. *International Journal of Rock Mechanics and Mining Sciences*, **70**, 507–523.

LeVeque, Randall J, & Li, Zhilin. 1997. Immersed interface methods for Stokes flow with elastic boundaries or surface tension. *SIAM Journal on Scientific Computing*, **18**(3), 709–735.

Li, SH, Wang, JG, Liu, BS, & Dong, DP. 2007. Analysis of critical excavation depth for a jointed rock slope using a face-to-face discrete element method. *Rock Mechanics and Rock Engineering*, **40**(4), 331–348.

Liu, Pengfei, & Veitch, Brian. 2012. Design and optimization for strength and integrity of tidal turbine rotor blades. *Energy*, **46**(1), 393–404.

Löhner, Rainald, Cebral, Juan R, Camelli, Fernando E, Appanaboyina, S, Baum, Joseph D, Mestreau, Eric L, & Soto, Orlando A. 2008. Adaptive embedded and immersed unstructured grid techniques. *Computer Methods in Applied Mechanics and Engineering*, **197**(25), 2173–2197.

Loseille, Adrien, & Alauzet, Frédéric. 2011a. Continuous mesh framework part I: well-posed continuous interpolation error. *SIAM Journal on Numerical Analysis*, **49**(1), 38–60.

Loseille, Adrien, & Alauzet, Frédéric. 2011b. Continuous mesh framework part II: validations and applications. *SIAM Journal on Numerical Analysis*, **49**(1), 61–86.

Lourenco, LM, & Shih, C. 1993. Characteristics of the plane turbulent near wake of a circular cylinder, a particle image velocimetry study. *private communication.*

Luhar, Mitul, & Nepf, Heidi M. 2011. Flow-induced reconfiguration of buoyant and flexible aquatic vegetation. *Limnology and Oceanography*, **56**(6), 2003–2017.

Luo, Kun, Wang, Zeli, & Fan, Jianren. 2007. A modified immersed boundary method for simulations of fluid–particle interactions. *Computer Methods in Applied Mechanics and Engineering*, **197**(1), 36–46.

Ma, X, Karamanos, G-S, & Karniadakis, GE. 2000. Dynamics and low-dimensionality of a turbulent near wake. *Journal of Fluid Mechanics*, **410**, 29–65.

Mahesh, Krishnan, Constantinescu, George, & Moin, Parviz. 2004. A numerical method for large-eddy simulation in complex geometries. *Journal of Computational Physics*, **197**(1), 215–240.

Maître, Thierry, Amet, Ervin, & Pellone, Christian. 2013. Modeling of the flow in a Darrieus water turbine: Wall grid refinement analysis and comparison with experiments. *Renewable Energy*, **51**, 497–512.

McNaughton, J, Billard, F, & Revell, A. 2014. Turbulence modelling of low Reynolds number flow effects around a vertical axis turbine at a range of tip-speed ratios. *Journal of Fluids and Structures*, **47**, 124–138.

Mei, Renwei. 1994. Flow due to an oscillating sphere and an expression for unsteady drag on the sphere at finite Reynolds number. *Journal of Fluid Mechanics*, **270**, 133–174.

Meyer, Mar, Hickel, S, & Adams, NA. 2010a. Assessment of implicit large-eddy simulation with a conservative immersed interface method for turbulent cylinder flow. *International Journal of Heat and Fluid Flow*, **31**(3), 368–377.

Meyer, Marcel, Devesa, A, Hickel, Stefan, Hu, XY, & Adams, NA. 2010b. A conservative immersed interface method for large-eddy simulation of incompressible flows. *Journal of Computational Physics*, **229**(18), 6300–6317.

Michler, C, Hulshoff, SJ, Van Brummelen, EH, & De Borst, René. 2004. A monolithic approach to fluid–structure interaction. *Computers & Fluids*, **33**(5), 839–848.

Milthaler, Frank Fritz Michael. 2014. *The Immersed Body Method and Its Use in Modelling Vertical Axis Turbines*. Ph.D. thesis.

Mindel, Julian E, Collins, Gareth S, Latham, John Paul, Pain, Christopher C, & Munjiza, A. 2007. Towards a numerical wave simulator using the two-fluid interface tracking approach combined with a novel ALE scheme. *In: Proceedings of the fifth international conference on coastal structures, Venice*. World Scientific.

Mittal, R. 1996. Progress on LES of flow past a circular cylinder. *Center for Turbulence Research Annual Research Briefs*, 233–241.

Mohammadi, S, & Bebamzadeh, A. 2005. A coupled gas–solid interaction model for FE/DE simulation of explosion. *Finite Elements in Analysis and Design*, **41**(13), 1289–1308.

Mohammadi, S, & Bebamzadeh, A. 2007. Analysis of fractured rock and gas flow interaction in explosion simulations. *Combustion, Explosion, and Shock Waves*, **43**(4), 482–491.

Mohammadi, S, & Pooladi, A. 2007. Non-uniform isentropic gas flow analysis of explosion in fractured solid media. *Finite Elements in Analysis and Design*, **43**(6), 478–493.

Mohammadi, S, & Pooladi, A. 2012. A two-mesh coupled gas flow–solid interaction model for 2D blast analysis in fractured media. *Finite Elements in Analysis and Design*, **50**, 48–69.

Morris, Joseph P, Rubin, MB, Block, GI, & Bonner, MP. 2006. Simulations of fracture and fragmentation of geologic materials using combined FEM/DEM analysis. *International Journal of Impact Engineering*, **33**(1), 463–473.

Mostaghimi, Peyman, Percival, James R, Pavlidis, Dimitrios, Ferrier, Richard J, Gomes, Jefferson LMA, Gorman, Gerard J, Jackson, Matthew D, Neethling, Stephen J, & Pain, Christopher C. 2015. Anisotropic mesh adaptivity and control volume finite element methods for numerical simulation of multiphase flow in porous media. *Mathematical Geosciences*, **47**(4), 417–440.

Munjiza, A, & Andrews, KRF. 1998. NBS contact detection algorithm for bodies of similar size. *International Journal for Numerical Methods in Engineering*, **43**(1), 131–149.

Munjiza, A, Andrews, KRF, & White, JK. 1999. Combined single and smeared crack model in combined finite-discrete element analysis. *International Journal for Numerical Methods in Engineering*, **44**(1), 41–57.

Munjiza, A, Latham, John-Paul, & Andrews, KRF. 2000. Detonation gas model for combined finite-discrete element simulation of fracture and fragmentation. *International Journal for Numerical Methods in Engineering*, **49**(12), 1495–1520.

Munjiza, Ante. 1992. *Discrete elements in transient dynamics of fractured media.* Ph.D. thesis, Swansea University.

Munjiza, Ante. 2004. *The combined finite-discrete element method.* John Wiley & Sons.

Nilson, RH. 1986. An integral method for predicting hydraulic fracture propagation driven by gases or liquids. *International Journal for Numerical and Analytical Methods in Geomechanics*, **10**(2), 191–211.

Ning, Youjun, Yang, Jun, Ma, Guowei, & Chen, Pengwan. 2011. Modelling rock blasting considering explosion gas penetration using discontinuous deformation analysis. *Rock Mechanics and Rock Engineering*, **44**(4), 483–490.

Nobari, MRH, Mirzaee, E, & Nosratollahi, M. 2016. Improvement of wind turbine performance using a novel tip plate structure. *Energy Conversion and Management*, **123**, 592–609.

Norberg, Christoffer. 1987. Effects of Reynolds number and a low-intensity freestream turbulence on the flow around a circular cylinder. *Chalmers University, Gothenburg, Sweden, Technological Publications*, **87**(2).

Oñate, Eugenio. 2013. *Structural analysis with the finite element method. Linear statics: volume 2: beams, plates and shells.* Springer Science & Business Media.

Ong, L, & Wallace, J. 1996. The velocity field of the turbulent very near wake of a circular cylinder. *Experiments in fluids*, **20**(6), 441–453.

Pain, CC, Mansoorzadeh, S, De Oliveira, CRE, & Goddard, AJ. 2001a. Numerical modelling of gas–solid fluidized beds using the two-fluid approach. *International Journal for numerical methods in fluids*, **36**(1), 91–124.

Pain, CC, Umpleby, AP, De Oliveira, CRE, & Goddard, AJH. 2001b. Tetrahedral mesh optimisation and adaptivity for steady-state and transient finite element calculations. *Computer Methods in Applied Mechanics and Engineering*, **190**(29), 3771–3796.

Pain, CC, Piggott, MD, Goddard, AJH, Fang, F, Gorman, GJ, Marshall, DP, Eaton, MD, Power, PW, & De Oliveira, CRE. 2005. Three-dimensional unstructured mesh ocean modelling. *Ocean Modelling*, **10**(1), 5–33.

Park, Noma, Yoo, Jung Yul, & Choi, Haecheon. 2004. Discretization errors in large eddy simulation: on the suitability of centered and upwind-biased compact difference schemes. *Journal of Computational Physics*, **198**(2), 580–616.

Parnaudeau, Philippe, Carlier, Johan, Heitz, Dominique, & Lamballais, Eric. 2008. Experimental and numerical studies of the flow over a circular cylinder at Reynolds number 3900. *Physics of Fluids*, **20**(8), 085101.

Pavlidis, Dimitrios, Gomes, Jefferson LMA, Xie, Zhihua, Percival, James R, Pain, Christopher C, & Matar, Omar K. 2016. Compressive advection and multi-component methods for interface-capturing. *International Journal for Numerical Methods in Fluids*, **80**(4), 256–282.

Peskin, Charles S. 1972. Flow patterns around heart valves: a numerical method. *Journal of Computational Physics*, **10**(2), 252–271.

Piggott, MD, Gorman, GJ, Pain, CC, Allison, PA, Candy, AS, Martin, BT, & Wells, MR. 2008. A new computational framework for multi-scale ocean modelling based on adapting unstructured meshes. *International Journal for Numerical Methods in Fluids*, **56**(8), 1003.

Piggott, MD, Farrell, PE, Wilson, CR, Gorman, GJ, & Pain, CC. 2009. Anisotropic mesh adaptivity for multi-scale ocean modelling. *Philosophical Transactions of the Royal Society of London A: Mathematical, Physical and Engineering Sciences*, **367**(1907), 4591–4611.

Pope, Stephen B. 2000. *Turbulent flows*. Cambridge University Press.

Preece, Dale S, & Taylor, Lee M. 1989. *Complete computer simulation of crater blasting including fragmentation and rock motion*. Tech. rept. Sandia National Labs., Albuquerque, NM (USA).

Preece, Dale S, Tidman, J Paul, & Chung, Stephen H. 1996. *Expanded rock blast modeling capabilities of DMC_BLAST, including buffer blasting*. Tech. rept. Sandia National Labs., Albuquerque, NM (United States).

Pruppacher, HR, Le Clair, BP, & Hamielec, AE. 1970. Some relations between drag and flow pattern of viscous flow past a sphere and a cylinder at low and intermediate Reynolds numbers. *Journal of Fluid Mechanics*, **44**(04), 781–790.

Rafiee, Ashkan, & Thiagarajan, Krish P. 2009. An SPH projection method for simulating fluid-hypoelastic structure interaction. *Computer Methods in Applied Mechanics and Engineering*, **198**(33), 2785–2795.

Rasheed, Adil, Holdahl, Runar, Kvamsdal, Trond, & Åkervik, Espen. 2014. A Comprehensive Simulation Methodology for Fluid-structure Interaction of Offshore Wind Turbines. *Energy Procedia*, **53**, 135–145.

Renani, Hossein Rafiei, Martin, C Derek, & Hudson, Richard. Back analysis of rock mass displacements around a deep shaft using two-and three-dimensional continuum modeling. *Rock Mechanics and Rock Engineering*, 1–15.

Rezaeiha, Abdolrahim, Kalkman, Ivo, & Blocken, Bert. 2017. Effect of pitch angle on power performance and aerodynamics of a vertical axis wind turbine. *Applied Energy*, **197**, 132–150.

Robinson-Mosher, Avi, Schroeder, Craig, & Fedkiw, Ronald. 2011. A symmetric positive definite formulation for monolithic fluid structure interaction. *Journal of Computational Physics*, **230**(4), 1547–1566.

Roman, F, Armenio, V, & Fröhlich, J. 2009. A simple wall-layer model for large eddy simulation with immersed boundary method. *Physics of Fluids*, **21**(10), 101701.

Rougier, E, Knight, EE, Broome, ST, Sussman, AJ, & Munjiza, A. 2014. Validation of a three-dimensional finite-discrete element method using experimental results of the Split Hopkinson Pressure Bar test. *International Journal of Rock Mechanics and Mining Sciences*, **70**, 101–108.

Ryzhakov, PB, Rossi, Riccardo, Idelsohn, SR, & Oñate, E. 2010. A monolithic Lagrangian approach for fluid–structure interaction problems. *Computational Mechanics*, **46**(6), 883–899.

Saharan, Mani Ram, & Mitri, HS. 2008. Numerical procedure for dynamic simulation of discrete fractures due to blasting. *Rock Mechanics and Rock Engineering*, **41**(5), 641–670.

Sanchidrian, Jose A, Segarra, Pablo, & López, Lina M. 2007. Energy components in rock blasting. *International Journal of Rock Mechanics and Mining Sciences*, **44**(1), 130–147.

Sanchidrian, Jose A, Castedo, Ricardo, Lopez, Lina M, Segarra, Pablo, & Santos, Anastasio P. 2015. Determination of the JWL Constants for ANFO and Emulsion Explosives from Cylinder Test Data. *Central European Journal of Energetic Materials*, **12**(2), 177–194.

Sazid, M, & Singh, TN. 2013. Two-dimensional dynamic finite element simulation of rock blasting. *Arabian Journal of Geosciences*, **6**(10), 3703–3708.

Sengupta, TK, Lim, TT, Sajjan, Sharanappa V, Ganesh, S, & Soria, Julio. 2007. Accelerated flow past a symmetric aerofoil: experiments and computations. *Journal of Fluid Mechanics*, **591**, 255–288.

Singh, SP, & Mittal, S. 2005. Flow past a cylinder: shear layer instability and drag crisis. *International Journal for Numerical Methods in Fluids*, **47**(1), 75–98.

Smith, M, Wilkin, P, & Williams, M. 1996. The advantages of an unsteady panel method in modelling the aerodynamic forces on rigid flapping wings. *Journal of Experimental Biology*, **199**(5), 1073–1083.

Son, Jaime S, & Hanratty, Thomas J. 1969. Velocity gradients at the wall for flow around a cylinder at Reynolds numbers from 5×10^3 to 10^5. *Journal of Fluid Mechanics*, **35**(02), 353–368.

Sotiropoulos, Fotis, & Yang, Xiaolei. 2014. Immersed boundary methods for simulating fluid–structure interaction. *Progress in Aerospace Sciences*, **65**, 1–21.

Strickland, James H, Webster, BT, & Nguyen, T. 1979. A vortex model of the Darrieus turbine: an analytical and experimental study. *Journal of Fluids Engineering*, **101**(4), 500–505.

Stringham, GE, Simons, Daryl B, & Guy, Harold P. 1969. *The behavior of large particles falling in quiescent liquids.* US Government Printing Office.

Su, Kai, Latham, J-P, Pavlidis, Dimitrios, Xiang, Jiansheng, Fang, Fangxin, Mostaghimi, Peyman, Percival, James R, Pain, Christopher C, & Jackson, Matthew D. 2015. Multiphase flow simulation through porous media with explicitly resolved fractures. *Geofluids*, **15**(4), 592–607.

Tan, Zhijun, Le, Duc-Vinh, Li, Zhilin, Lim, KM, & Khoo, Boo Cheong. 2008. An immersed interface method for solving incompressible viscous flows with piecewise constant viscosity across a moving elastic membrane. *Journal of Computational Physics*, **227**(23), 9955–9983.

Tessicini, F, Iaccarino, G, Fatica, M, Wang, M, & Verzicco, R. 2002. Wall modeling for large-eddy simulation using an immersed boundary method. *Annual Research Briefs, Stanford University Center for Turbulence Research, Stanford, CA*, 181–187.

Tezduyar, Tayfun E, Behr, Mittal, Mittal, S, & Liou, J. 1992a. A new strategy for finite element computations involving moving boundaries and interfacesthe deforming-spatial-domain/space-time procedure: II. Computation of free-surface flows, two-liquid flows, and flows with drifting cylinders. *Computer methods in applied mechanics and engineering*, **94**(3), 353–371.

Tezduyar, TE, Behr, M, & Liou, J. 1992b. A new strategy for finite element computations involving moving boundaries and interfaces–the DSD/ST procedure: I. The concept and the preliminary numerical tests. *Computer Methods in Applied Mechanics and Engineering*, **94**(3), 339–351.

Tian, Fang-Bao, Dai, Hu, Luo, Haoxiang, Doyle, James F, & Rousseau, Bernard. 2014. Fluid–structure interaction involving large deformations: 3D simulations and applications to biological systems. *Journal of computational physics*, **258**, 451–469.

Tseng, Yu-Heng, & Ferziger, Joel H. 2003. A ghost-cell immersed boundary method for flow in complex geometry. *Journal of Computational Physics*, **192**(2), 593–623.

Tu, Cheng, & Peskin, Charles S. 1992. Stability and instability in the computation of flows with moving immersed boundaries: a comparison of three methods. *SIAM Journal on Scientific and Statistical Computing*, **13**(6), 1361–1376.

Tyagi, Mayank, & Acharya, Sumanta. 2005. Large eddy simulation of turbulent flows in complex and moving rigid geometries using the immersed boundary method. *International Journal for Numerical Methods in Fluids*, **48**(7), 691–722.

Tyagi, Mayank, Roy, Somnath, Harvey Iii, Albert D, & Acharya, Sumanta. 2007. Simulation of laminar and turbulent impeller stirred tanks using immersed boundary method and large eddy simulation technique in multi-block curvilinear geometries. *Chemical Engineering Science*, **62**(5), 1351–1363.

Uhlmann, Markus. 2005. An immersed boundary method with direct forcing for the simulation of particulate flows. *Journal of Computational Physics*, **209**(2), 448–476.

Van Loon, R, Anderson, PD, Van de Vosse, FN, & Sherwin, SJ. 2007. Comparison of various fluid–structure interaction methods for deformable bodies. *Computers & Structures*, **85**(11), 833–843.

Van Loon, Raoul, Anderson, Patrick D, & van de Vosse, Frans N. 2006. A fluid–structure interaction method with solid-rigid contact for heart valve dynamics. *Journal of Computational Physics*, **217**(2), 806–823.

Versino, Daniele, Mourad, Hashem M, Williams, Todd O, & Addessio, Francis L. 2015. A global–local discontinuous Galerkin finite element for finite-deformation analysis of multilayered shells. *Computer Methods in Applied Mechanics and Engineering*, **283**, 1401–1424.

Version, ABAQUS. 2013. 6.12 Documentation Collection. *ABAQUS/CAE User's Manual.*

Versteeg, Henk Kaarle, & Malalasekera, Weeratunge. 2007. *An introduction to computational fluid dynamics: the finite volume method.* Pearson Education.

Viré, A, Xiang, J, & Pain, CC. 2015. An immersed-shell method for modelling fluid–structure interactions. *Philosophical Transactions of the Royal Society of London A: Mathematical, Physical and Engineering Sciences*, **373**(2035), 20140085.

Viré, Axelle, Xiang, Jiansheng, Milthaler, Frank, Farrell, Patrick Emmet, Piggott, Matthew David, Latham, John-Paul, Pavlidis, Dimitrios, & Pain, Christopher Charles. 2012. Modelling of fluid–solid interactions using an adaptive mesh fluid model coupled with a combined finite–discrete element model. *Ocean Dynamics*, **62**(10-12), 1487–1501.

Wang, Hongwu, Chessa, Jack, Liu, Wing K, & Belytschko, Ted. 2008. The immersed/fictitious element method for fluid-structure interaction: Volumetric consistency, compressibility and thin members. *International Journal for Numerical Methods in Engineering*, **74**(1), 32–55.

Wang, Ming, Hao, Hong, Ding, Yang, & Li, Zhong-Xian. 2009. Prediction of fragment size and ejection distance of masonry wall under blast load using homogenized masonry material properties. *International Journal of Impact Engineering*, **36**(6), 808–820.

Wiens, Jeffrey K, & Stockie, John M. 2015. Simulating flexible fiber suspensions using a scalable immersed boundary algorithm. *Computer Methods in Applied Mechanics and Engineering*, **290**, 1–18.

Wilcox, David C, *et al.* . 1998. *Turbulence modeling for CFD*. Vol. 2. DCW industries La Canada, CA.

Xian, L, Bicanic, N, Owen, DRJ, & Munjiza, A. 1991. Rock blasting simulation by rigid body dynamic analysis and rigid brittle fracturing model. *Pages 477–587 of: Prcoceedings of the International Conference on Nonlinear Engineering Computations, NEC-91, Pineridge Press, Swansea, UK.*

Xiang, J, Latham, John-Paul, Zhang, ZQ, *et al.* . 2010. A numeric simulation of rock avalanches using the combined finite-discrete element method, FEMDEM. *In: 44th US Rock Mechanics Symposium and 5th US-Canada Rock Mechanics Symposium*. American Rock Mechanics Association.

Xiang, Jiansheng, Munjiza, Antonio, & Latham, John-Paul. 2009. Finite strain, finite rotation quadratic tetrahedral element for the combined finite–discrete element method. *International Journal for Numerical Methods in Engineering*, **79**(8), 946–978.

Xiang, Jiansheng, Latham, John-Paul, Vire, Axelle, Anastasaki, Elena, & Pain, Christopher C. 2012. Coupled FLUIDITY/Y3D technology and simulation tools for numerical breakwater modeling. *Coastal Engineering Proceedings*, **1**(33), structures–66.

Xiao, D, Yang, P, Fang, F, Xiang, J, Pain, CC, & Navon, IM. 2016. Non-intrusive reduced order modelling of fluid–structure interactions. *Computer Methods in Applied Mechanics and Engineering*, **303**, 35–54.

Xiao, D, Yang, P, Fang, F, Xiang, J, Pain, CC, Navon, IM, & Chen, M. 2017. A non-intrusive reduced-order model for compressible fluid and fractured solid coupling and its application to blasting. *Journal of Computational Physics*, **330**, 221–244.

Yan, Peng, Zhou, Wangxiao, Lu, Wenbo, Chen, Ming, & Zhou, Chuangbing. 2016. Simulation of bench blasting considering fragmentation size distribution. *International Journal of Impact Engineering*, **90**, 132–145.

Yang, Jianming, & Balaras, Elias. 2006. An embedded-boundary formulation for large-eddy simulation of turbulent flows interacting with moving boundaries. *Journal of Computational Physics*, **215**(1), 12–40.

Yang, Jianming, & Stern, Frederick. 2009. Sharp interface immersed-boundary/level-set method for wave–body interactions. *Journal of Computational Physics*, **228**(17), 6590–6616.

Yang, Liang. 2017. One-fluid formulation for fluid–structure interaction with free surface. *Computer Methods in Applied Mechanics and Engineering.*

Yang, Liang, Gil, Antonio J, Carreño, Aurelio Arranz, & Bonet, Javier. 2018. Unified one-fluid formulation for incompressible flexible solids and multiphase flows: Application to hydrodynamics using the immersed structural potential method (ISPM). *International Journal for Numerical Methods in Fluids*, **86**(1), 78–106.

Yang, P, Xiang, J, Fang, F, Pavlidis, D, Latham, J-P, & Pain, CC. 2016. Modelling of fluid–structure interaction with multiphase viscous flows using an immersed-body method. *Journal of Computational Physics*, **321**, 571–592.

Yang, P., Xiang, J., Fang, F., Pavlidis, D., & Pain, C.C. 2017a. Modelling of fluid-structure interaction for moderate Reynolds number flows using an immersed-body method. *Submited to Computers & Fluids.*

Yang, P, Xiang, J, Chen, M, Fang, F, Pavlidis, D, Latham, J-P, & Pain, CC. 2017b. The immersed-body gas-solid interaction model for blast analysis in fractured solid media. *International Journal of Rock Mechanics and Mining Sciences*, **91**, 119–132.

Yin, Yue-ping, Huang, Bolin, Chen, Xiaoting, Liu, Guangning, & Wang, Shichang. 2015. Numerical analysis on wave generated by the Qianjiangping landslide in Three Gorges Reservoir, China. *Landslides*, **12**(2), 355–364.

Yu, Zhaosheng, Phan-Thien, Nhan, Fan, Yurun, & Tanner, Roger I. 2002. Viscoelastic mobility problem of a system of particles. *Journal of non-newtonian fluid mechanics*, **104**(2), 87–124.

Zhang, Jianping, Guo, Liang, Wu, Helen, Zhou, Aixi, Hu, Danmei, & Ren, Jianxing. 2014. The influence of wind shear on vibration of geometrically nonlinear wind turbine blade under fluid–structure interaction. *Ocean engineering*, **84**, 14–19.

Zhu, Zheming, Mohanty, Bibhu, & Xie, Heping. 2007. Numerical investigation of blasting-induced crack initiation and propagation in rocks. *International Journal of Rock Mechanics and Mining Sciences*, **44**(3), 412–424.

Zienkiewicz, Olgierd Cecil, & Taylor, Robert Leroy. 2000. *The finite element method: Solid mechanics*. Vol. 2. Butterworth-heinemann.

Appendices

Appendix

ONE

Third party material permissions

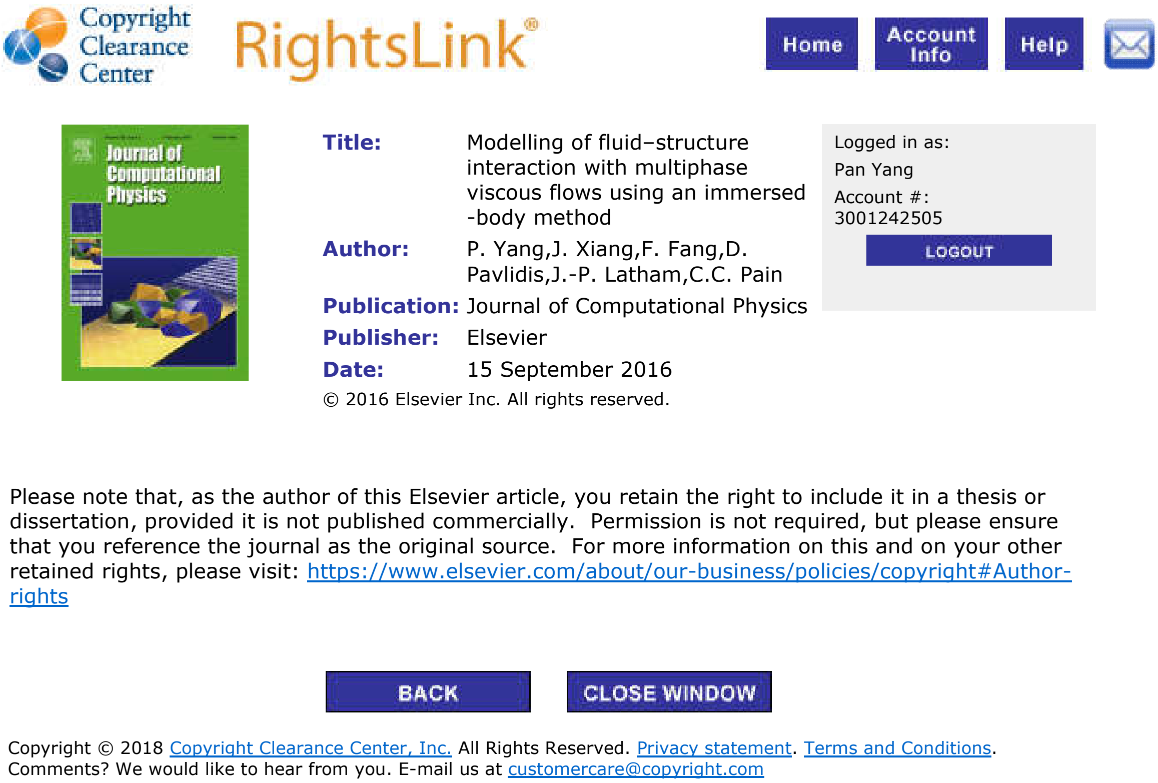
Copyright Clearance Center
RightsLink®
Home
Account Info
Help
Journal of Computational Physics
LOGOUT
BACK
CLOSE WINDOW

Title: Modelling of fluid–structure interaction with multiphase viscous flows using an immersed -body method

Author: P. Yang,J. Xiang,F. Fang,D. Pavlidis,J.-P. Latham,C.C. Pain

Publication: Journal of Computational Physics

Publisher: Elsevier

Date: 15 September 2016

© 2016 Elsevier Inc. All rights reserved.

Logged in as:
Pan Yang
Account #:
3001242505

Please note that, as the author of this Elsevier article, you retain the right to include it in a thesis or dissertation, provided it is not published commercially. Permission is not required, but please ensure that you reference the journal as the original source. For more information on this and on your other retained rights, please visit: https://www.elsevier.com/about/our-business/policies/copyright#Author-rights

Copyright © 2018 Copyright Clearance Center, Inc. All Rights Reserved. Privacy statement. Terms and Conditions.
Comments? We would like to hear from you. E-mail us at customercare@copyright.com

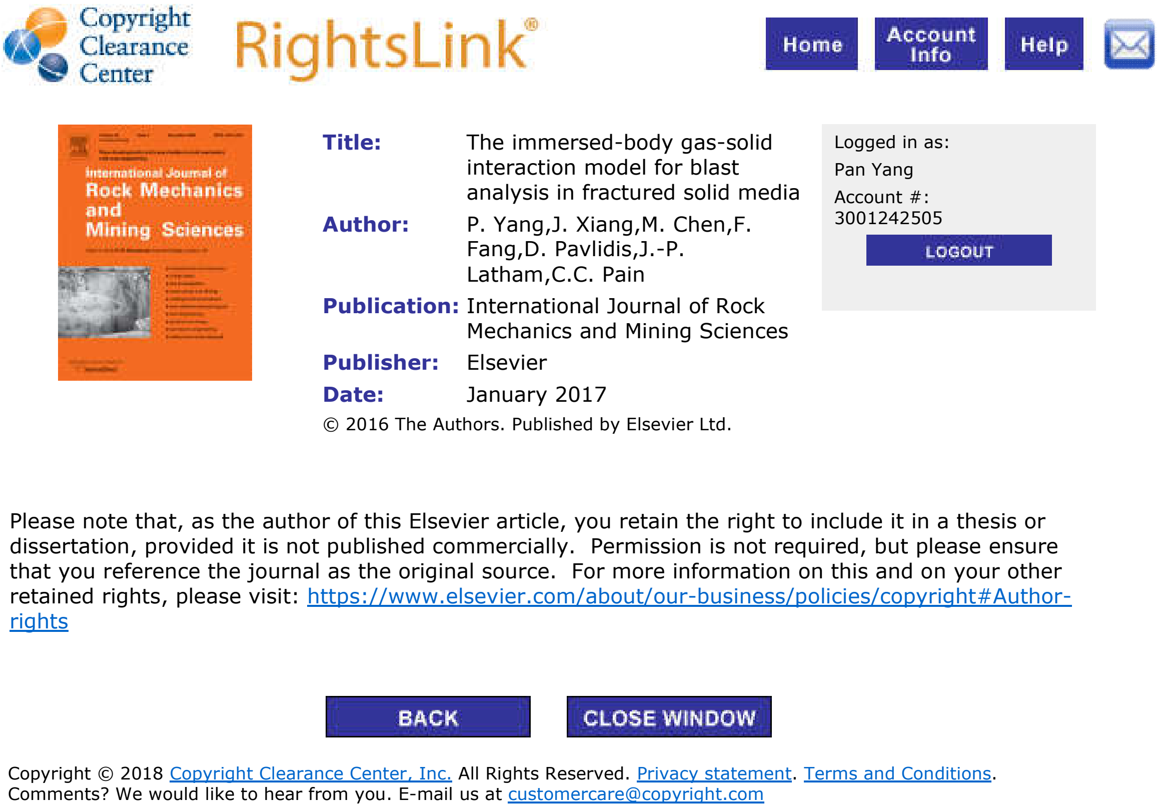

Title: The immersed-body gas-solid interaction model for blast analysis in fractured solid media

Author: P. Yang,J. Xiang,M. Chen,F. Fang,D. Pavlidis,J.-P. Latham,C.C. Pain

Publication: International Journal of Rock Mechanics and Mining Sciences

Publisher: Elsevier

Date: January 2017

© 2016 The Authors. Published by Elsevier Ltd.

Logged in as:
Pan Yang
Account #:
3001242505

Please note that, as the author of this Elsevier article, you retain the right to include it in a thesis or dissertation, provided it is not published commercially. Permission is not required, but please ensure that you reference the journal as the original source. For more information on this and on your other retained rights, please visit: https://www.elsevier.com/about/our-business/policies/copyright#Author-rights

Copyright © 2018 Copyright Clearance Center, Inc. All Rights Reserved. Privacy statement. Terms and Conditions.
Comments? We would like to hear from you. E-mail us at customercare@copyright.com

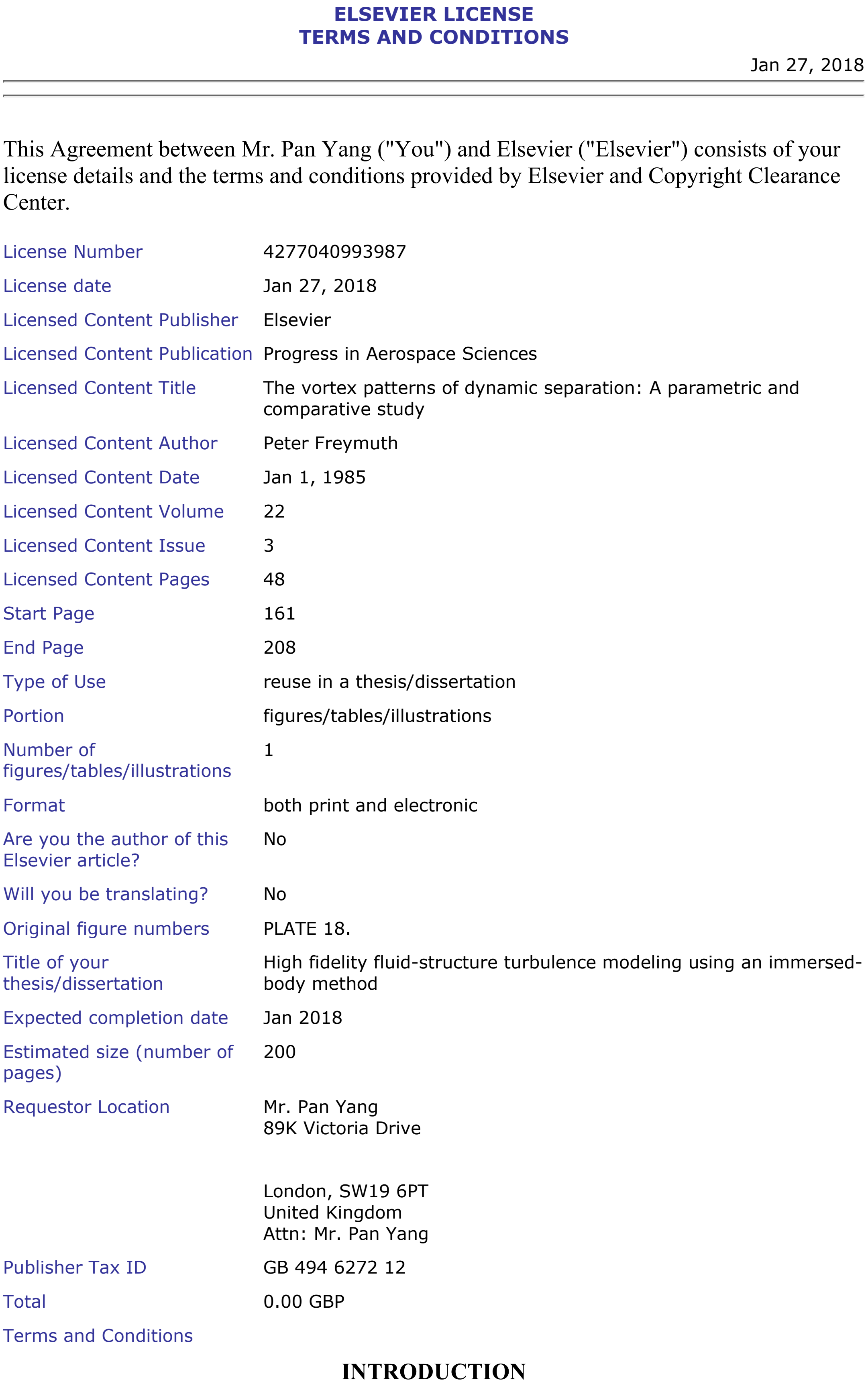

ELSEVIER LICENSE TERMS AND CONDITIONS

Jan 27, 2018

This Agreement between Mr. Pan Yang ("You") and Elsevier ("Elsevier") consists of your license details and the terms and conditions provided by Elsevier and Copyright Clearance Center.

License Number	4277040993987
License date	Jan 27, 2018
Licensed Content Publisher	Elsevier
Licensed Content Publication	Progress in Aerospace Sciences
Licensed Content Title	The vortex patterns of dynamic separation: A parametric and comparative study
Licensed Content Author	Peter Freymuth
Licensed Content Date	Jan 1, 1985
Licensed Content Volume	22
Licensed Content Issue	3
Licensed Content Pages	48
Start Page	161
End Page	208
Type of Use	reuse in a thesis/dissertation
Portion	figures/tables/illustrations
Number of figures/tables/illustrations	1
Format	both print and electronic
Are you the author of this Elsevier article?	No
Will you be translating?	No
Original figure numbers	PLATE 18.
Title of your thesis/dissertation	High fidelity fluid-structure turbulence modeling using an immersed-body method
Expected completion date	Jan 2018
Estimated size (number of pages)	200
Requestor Location	Mr. Pan Yang 89K Victoria Drive London, SW19 6PT United Kingdom Attn: Mr. Pan Yang
Publisher Tax ID	GB 494 6272 12
Total	0.00 GBP
Terms and Conditions	

INTRODUCTION

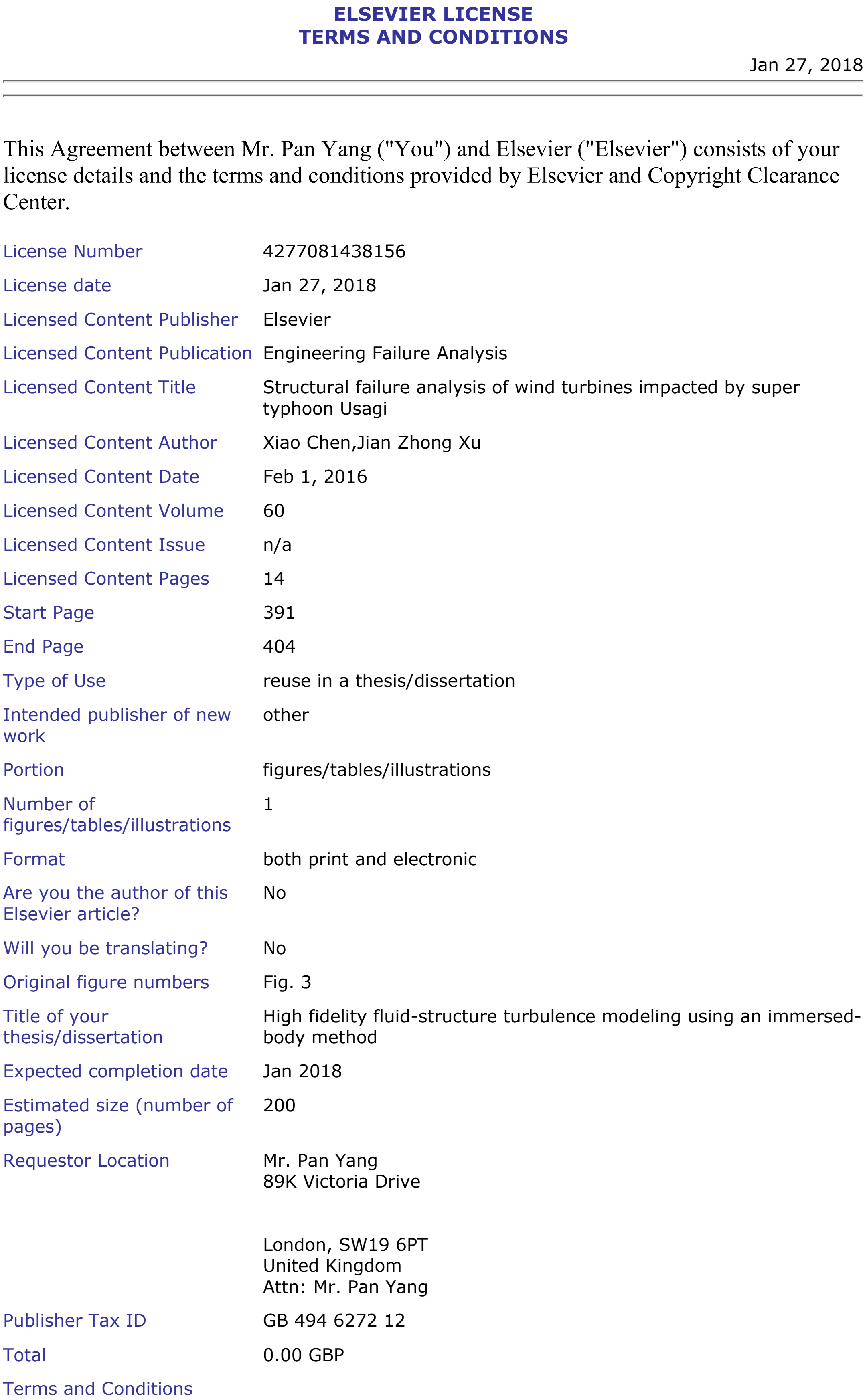

ELSEVIER LICENSE
TERMS AND CONDITIONS

Jan 27, 2018

This Agreement between Mr. Pan Yang ("You") and Elsevier ("Elsevier") consists of your license details and the terms and conditions provided by Elsevier and Copyright Clearance Center.

License Number	4277081438156
License date	Jan 27, 2018
Licensed Content Publisher	Elsevier
Licensed Content Publication	Engineering Failure Analysis
Licensed Content Title	Structural failure analysis of wind turbines impacted by super typhoon Usagi
Licensed Content Author	Xiao Chen,Jian Zhong Xu
Licensed Content Date	Feb 1, 2016
Licensed Content Volume	60
Licensed Content Issue	n/a
Licensed Content Pages	14
Start Page	391
End Page	404
Type of Use	reuse in a thesis/dissertation
Intended publisher of new work	other
Portion	figures/tables/illustrations
Number of figures/tables/illustrations	1
Format	both print and electronic
Are you the author of this Elsevier article?	No
Will you be translating?	No
Original figure numbers	Fig. 3
Title of your thesis/dissertation	High fidelity fluid-structure turbulence modeling using an immersed-body method
Expected completion date	Jan 2018
Estimated size (number of pages)	200
Requestor Location	Mr. Pan Yang 89K Victoria Drive London, SW19 6PT United Kingdom Attn: Mr. Pan Yang
Publisher Tax ID	GB 494 6272 12
Total	0.00 GBP

Terms and Conditions

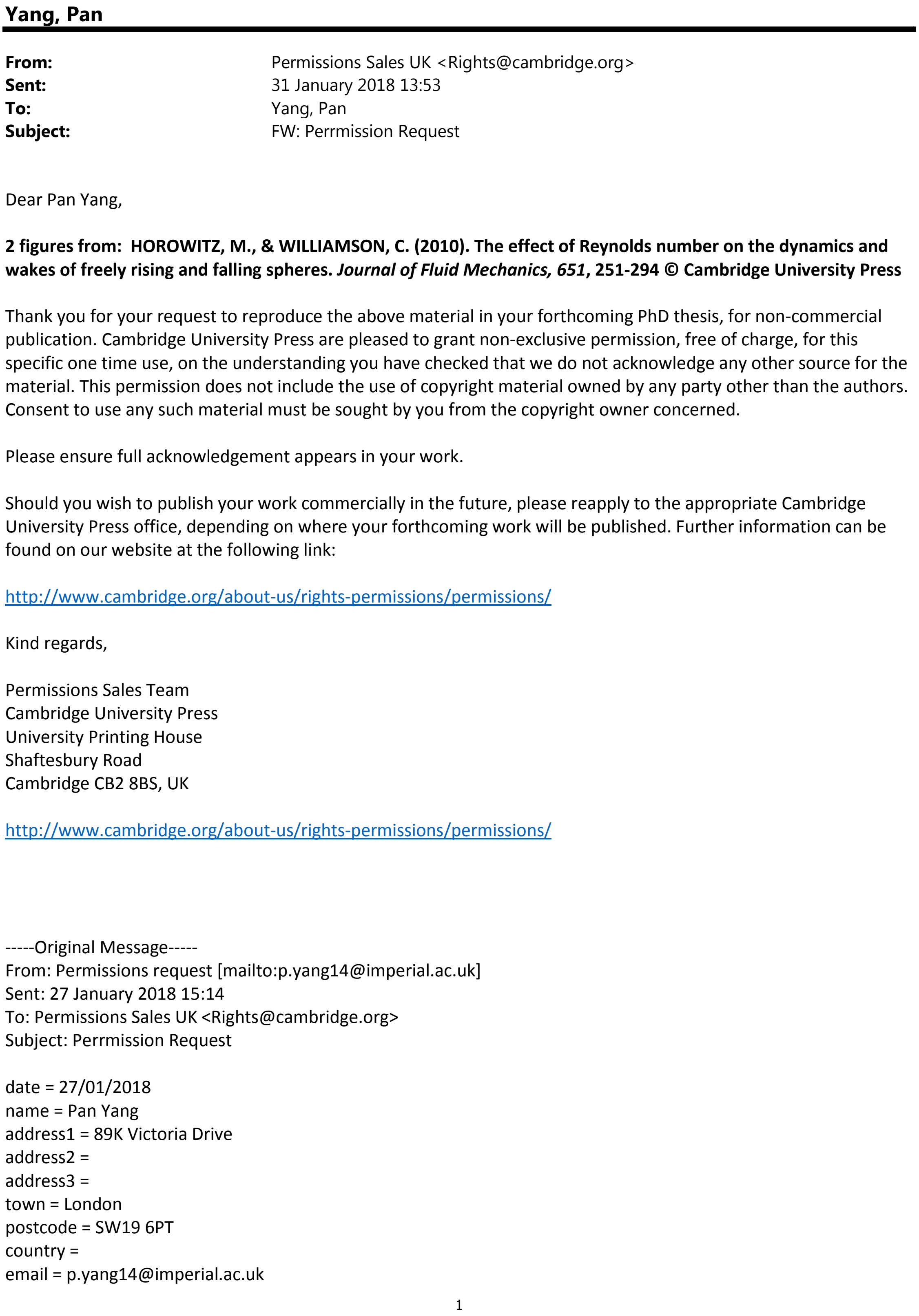

Yang, Pan

From: Permissions Sales UK <Rights@cambridge.org>
Sent: 31 January 2018 13:53
To: Yang, Pan
Subject: FW: Perrmission Request

Dear Pan Yang,

2 figures from: HOROWITZ, M., & WILLIAMSON, C. (2010). The effect of Reynolds number on the dynamics and wakes of freely rising and falling spheres. *Journal of Fluid Mechanics, 651*, 251-294 © Cambridge University Press

Thank you for your request to reproduce the above material in your forthcoming PhD thesis, for non-commercial publication. Cambridge University Press are pleased to grant non-exclusive permission, free of charge, for this specific one time use, on the understanding you have checked that we do not acknowledge any other source for the material. This permission does not include the use of copyright material owned by any party other than the authors. Consent to use any such material must be sought by you from the copyright owner concerned.

Please ensure full acknowledgement appears in your work.

Should you wish to publish your work commercially in the future, please reapply to the appropriate Cambridge University Press office, depending on where your forthcoming work will be published. Further information can be found on our website at the following link:

http://www.cambridge.org/about-us/rights-permissions/permissions/

Kind regards,

Permissions Sales Team
Cambridge University Press
University Printing House
Shaftesbury Road
Cambridge CB2 8BS, UK

http://www.cambridge.org/about-us/rights-permissions/permissions/

-----Original Message-----
From: Permissions request [mailto:p.yang14@imperial.ac.uk]
Sent: 27 January 2018 15:14
To: Permissions Sales UK <Rights@cambridge.org>
Subject: Perrmission Request

date = 27/01/2018
name = Pan Yang
address1 = 89K Victoria Drive
address2 =
address3 =
town = London
postcode = SW19 6PT
country =
email = p.yang14@imperial.ac.uk

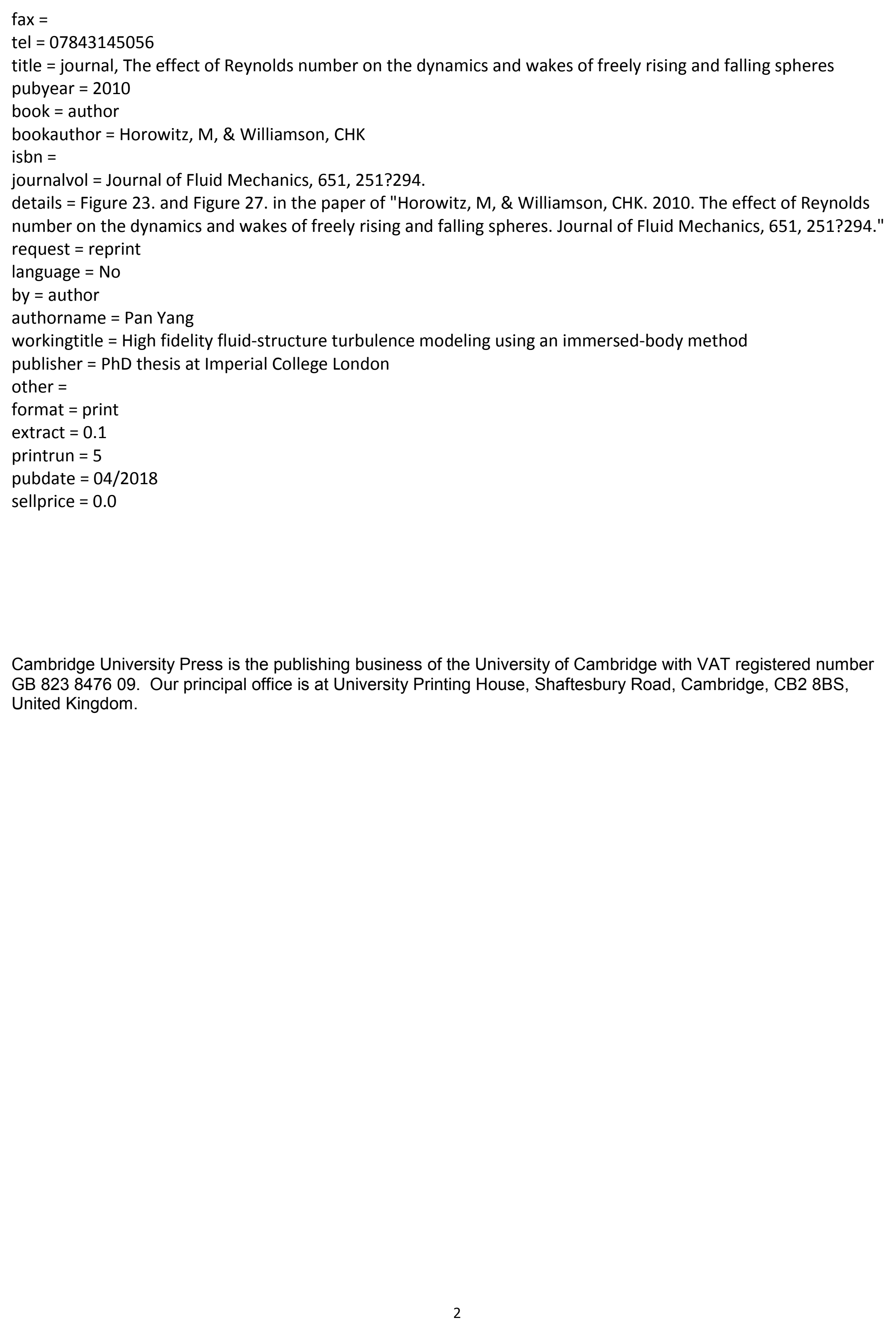

fax =
tel = 07843145056
title = journal, The effect of Reynolds number on the dynamics and wakes of freely rising and falling spheres
pubyear = 2010
book = author
bookauthor = Horowitz, M, & Williamson, CHK
isbn =
journalvol = Journal of Fluid Mechanics, 651, 251?294.
details = Figure 23. and Figure 27. in the paper of "Horowitz, M, & Williamson, CHK. 2010. The effect of Reynolds number on the dynamics and wakes of freely rising and falling spheres. Journal of Fluid Mechanics, 651, 251?294."
request = reprint
language = No
by = author
authorname = Pan Yang
workingtitle = High fidelity fluid-structure turbulence modeling using an immersed-body method
publisher = PhD thesis at Imperial College London
other =
format = print
extract = 0.1
printrun = 5
pubdate = 04/2018
sellprice = 0.0

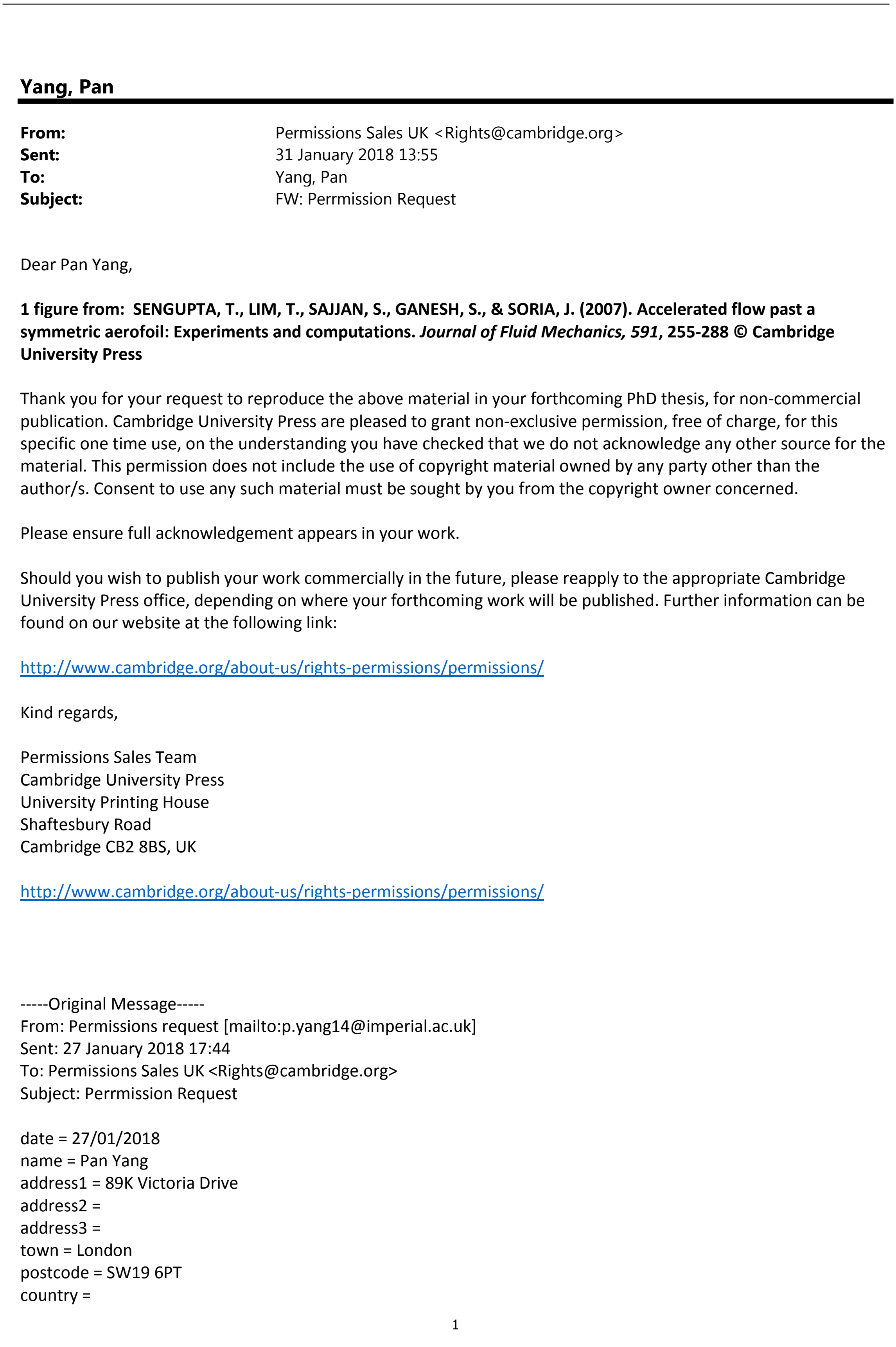

Yang, Pan

From: Permissions Sales UK <Rights@cambridge.org>
Sent: 31 January 2018 13:55
To: Yang, Pan
Subject: FW: Perrmission Request

Dear Pan Yang,

1 figure from: SENGUPTA, T., LIM, T., SAJJAN, S., GANESH, S., & SORIA, J. (2007). Accelerated flow past a symmetric aerofoil: Experiments and computations. *Journal of Fluid Mechanics, 591*, 255-288 © Cambridge University Press

Thank you for your request to reproduce the above material in your forthcoming PhD thesis, for non-commercial publication. Cambridge University Press are pleased to grant non-exclusive permission, free of charge, for this specific one time use, on the understanding you have checked that we do not acknowledge any other source for the material. This permission does not include the use of copyright material owned by any party other than the author/s. Consent to use any such material must be sought by you from the copyright owner concerned.

Please ensure full acknowledgement appears in your work.

Should you wish to publish your work commercially in the future, please reapply to the appropriate Cambridge University Press office, depending on where your forthcoming work will be published. Further information can be found on our website at the following link:

http://www.cambridge.org/about-us/rights-permissions/permissions/

Kind regards,

Permissions Sales Team
Cambridge University Press
University Printing House
Shaftesbury Road
Cambridge CB2 8BS, UK

http://www.cambridge.org/about-us/rights-permissions/permissions/

-----Original Message-----
From: Permissions request [mailto:p.yang14@imperial.ac.uk]
Sent: 27 January 2018 17:44
To: Permissions Sales UK <Rights@cambridge.org>
Subject: Perrmission Request

date = 27/01/2018
name = Pan Yang
address1 = 89K Victoria Drive
address2 =
address3 =
town = London
postcode = SW19 6PT
country =

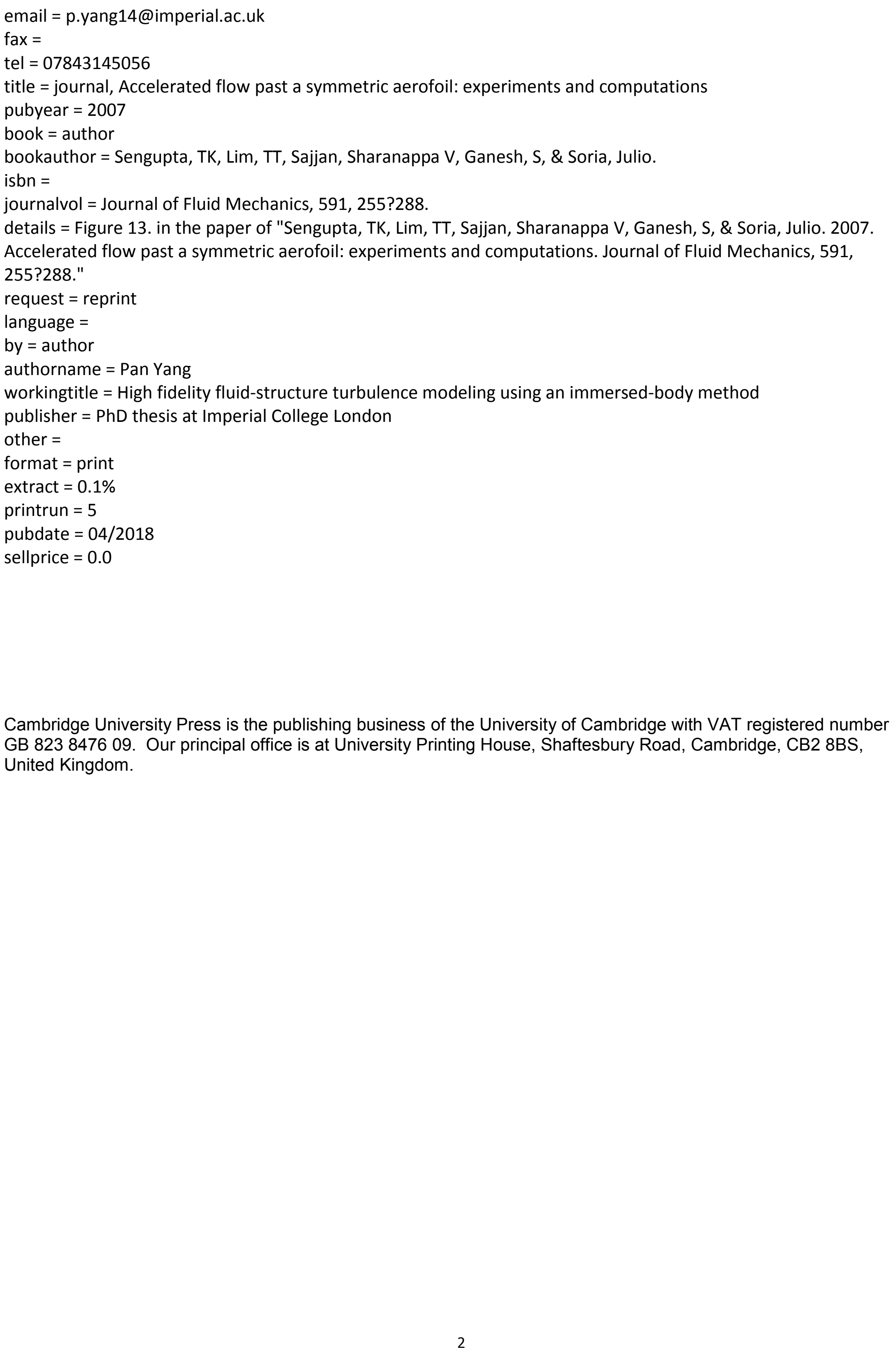

email = p.yang14@imperial.ac.uk
fax =
tel = 07843145056
title = journal, Accelerated flow past a symmetric aerofoil: experiments and computations
pubyear = 2007
book = author
bookauthor = Sengupta, TK, Lim, TT, Sajjan, Sharanappa V, Ganesh, S, & Soria, Julio.
isbn =
journalvol = Journal of Fluid Mechanics, 591, 255?288.
details = Figure 13. in the paper of "Sengupta, TK, Lim, TT, Sajjan, Sharanappa V, Ganesh, S, & Soria, Julio. 2007. Accelerated flow past a symmetric aerofoil: experiments and computations. Journal of Fluid Mechanics, 591, 255?288."
request = reprint
language =
by = author
authorname = Pan Yang
workingtitle = High fidelity fluid-structure turbulence modeling using an immersed-body method
publisher = PhD thesis at Imperial College London
other =
format = print
extract = 0.1%
printrun = 5
pubdate = 04/2018
sellprice = 0.0

Cambridge University Press is the publishing business of the University of Cambridge with VAT registered number GB 823 8476 09. Our principal office is at University Printing House, Shaftesbury Road, Cambridge, CB2 8BS, United Kingdom.